Advances in Civil Engineering

Eco-Friendly and Energy-Saving Cementitious Materials

Lead Guest Editor: Yushi Liu
Guest Editors: Shah Kwok Wei, Shuang Lu, Tuan Anh Nguyen, Xianming Shi, and Yingzi Yang

Eco-Friendly and Energy-Saving Cementitious Materials

Advances in Civil Engineering

Eco-Friendly and Energy-Saving Cementitious Materials

Lead Guest Editor: Yushi Liu
Guest Editors: Shah Kwok Wei, Shuang Lu, Tuan Anh Nguyen, Xianming Shi, and Yingzi Yang

Contents

The Role of Iron Tailing Powder in Ultra-High-Strength Concrete Subjected to Elevated Temperatures
Kexin Huang, Xindan Zhang, Dong Lu, Ning Xu, Yingxin Gan, and Xin Han
Research Article (11 pages), Article ID 6681429, Volume 2021 (2021)

Research on the Infrared Thermographic Detection of Concrete under Solar Heating
Dan Zheng, Shuaishuai Tan, Xinxin Li, and Haonan Cai
Research Article (10 pages), Article ID 6692729, Volume 2021 (2021)

Hindawi
Advances in Civil Engineering
Volume 2021, Article ID 9927910, 11 pages
https://doi.org/10.1155/2021/9927910

Research Article

Experimental and Numerical Investigation of Temperature Development of Ohmic Heating Cured Nonmass Concrete under Subzero Temperature

Beimeng Qi,[1] Zheng Zhou,[2] Weichen Tian,[2] Mingzhe Ouyang,[2] Xiaocheng Wang,[3] Qiang Shi,[3] Ye Wang,[3] Yang Sun,[4] and Wei Wang[2]

[1]*College of Quality & Safety Engineering, China Jiliang University, Hangzhou 310018, China*
[2]*School of Civil Engineering, Harbin Institute of Technology, Harbin 150090, China*
[3]*State Grid Inner Mongolia East Power Co., Ltd., Construction Branch, Hohhot 010000, China*
[4]*State Grid Inner Mongolia East Power Co., Ltd., Institute of Economics and Technology, Hohhot 010000, China*

Correspondence should be addressed to Weichen Tian; tianweichen@hit.edu.cn

Received 3 April 2021; Revised 24 May 2021; Accepted 25 May 2021; Published 15 December 2021

Academic Editor: Xianming Shi

In this paper, carbon fiber/carbon nanofiber strengthening nonmass concrete slab was designed, and ohmic heating (OH) curing was used to promote the strength formation of the slab under −20°C. COMSOL multiphysical field coupling program has been used to simulate the heating process of nonmass concrete slabs under different conditions. COMSOL analysis results showed that the optimal loading power density of OH cured sample under −20°C was 1000 W/m^2~1200 W/m^2. Moreover, numerical analysis results were experimentally validated by the multipoint temperature measurement method. Furthermore, the mechanical properties showed that the compressive strength of the sample cured by 2 days OH curing at −20°C reached up to 48.2 MPa. SEM analysis exhibited that OH curing could improve the interfacial transition zone (ITZ) between the fiber and the matrix, leading to a denser microstructure. This study proved that COMSOL program could provide good theoretical guidance for OH cured nonmass cement concrete under subzero temperature. This work establishes an accurate guideline for electric power supplementation, laying a solid foundation of winter construction with high efficiency and low energy consumption.

1. Introduction

Concrete is a common material, which has attracted wide attention in the construction industry due to its low cost and excellent mechanical properties. However, cementitious materials fail to hydrate under subzero temperature conditions. Therefore, the preparation of concrete structures under subzero temperature is still a serious problem. As a result, the concrete construction in cold region in winter is greatly restricted, which affects the economic development. Traditional curing methods for winter concrete construction mainly include thermal insulation curing and external heating curing method [1, 2]. These methods have been utilized to protect concrete structure from being frozen. However, these methods only can be utilized under moderate conditions and will bring some unpreventable problems. To be specific, external heating curing method works by heating the air around the structure or directly heating the concrete. It is hard to operate and requires much energy consumption. Thermal insulation curing is conducted by covering heating preservation material on the concrete to slow down the heat release. This method is easy and inexpensive to achieve, while it is not suitable for the cold environment with the temperature lower than −10°C [3]. Thus, there is an urgent need for developing a new curing method for curing cementitious materials under ultra-low temperature that is energy-saving and environmentally friendly to meet the structural strength requirements [4, 5].

Ohmic heating (OH) curing method utilizes the ohmic heating generated by the action of electric current to cure cementitious materials. At present, a series of research results proved that OH curing could improve the strength formation of cement-based materials. Kovtun [6, 7] utilized direct current for OH curing of alkali activated cementitious materials containing fly ash under positive temperature. Temperature development was found to be closely related to the formation of strength with different voltage gradient conditions. However, with the progress of hydration, the electric conductivity of the cementitious materials degraded without the addition of conductive fillers, resulting in the decrease of the curing temperature [8]. Under this circumstance, Liu [9] cured cementitious materials incorporated with carbon nanofibers (CNFs) as conductive fillers with 12 h OH curing at −20°C and successfully raised the compressive strength of the sample to 27.7 MPa above the critical frost resistance strength of 3.5 MPa. Furthermore, Liu [10] conducted OH curing on the CF/CNFs reinforced cementitious composites under ultra-low temperature. The compressive strength of the sample reached up to 49.2 MPa with 2 days OH curing under −20°C. Above all, the previous work has solidly shown that OH curing method can be used as a novel and effective curing method for concrete construction under subzero temperature.

However, main researches on OH curing of cementitious materials under subzero temperature focused on the mechanical properties and hydration degree of small size concrete samples (such as 40 mm × 40 mm × 160 mm); the researches on OH cured nonmass concrete structures are still blank. However, the study regarding the properties of nonmass concrete slab has been investigated a lot due to its significance [11]. To be specific, based on the maturity theory of strength development on cement-based materials, the temperature development inside the sample under subzero temperature is crucial to ensure the sufficient strength formation of the sample [12, 13]. According to heat transfer theory, the heating process of small size structure can be regarded as a uniform heating process because of its low internal temperature gradient. However, for the cementitious materials with larger size and different geometries (such as nonmass concrete slab), the internal temperature gradient of the sample cannot be ignored, and the structure is more likely to suffer damage during OH curing process because of the large thermal expansion coefficient differences among the complicated components inside the sample [14–16]. Therefore, it is of vital significance to clarify the regularity of temperature development and corresponding influencing factors of OH cured nonmass concrete structures under subzero temperature. Also, it is essential to establish a numerical model to predict the temperature development of the structure.

COMSOL multiphysical field coupling program based on the solution of partial differential equations has been utilized widely to analyze realistic physical phenomena. For OH curing process, the modeling process is mainly based on Maxwell's equations and fundamental principles of heat transfer. OH curing process is considered to be the application of electrothermal on concrete structure, and COMSOL program has been widely utilized in the field of electrothermal applications and concrete structure. To be specific, Zandi et al. [17] utilized COMSOL program to simulate the photogeneration, electrical properties, and heat distribution of graphene oxide contacting perovskite solar cells and effectively established the three-dimensional model of photo-electric-thermal and determined the promoting effect of graphene on the heating efficiency. Moreover, Li et al. [18] utilized COMSOL program to simulate the heating temperature development of external geothermal bridge system and the results were compared with the field test results. It was found that the simulated results were verified to accurately reflect the bridge heating efficiency in actual winter environment. Larwa et al. [19] simulated the heat flux and temperature distribution of phase change materials enhanced radiant floor systems by 2D model constructed by COMSOL program; it was verified that the utilization of COMSOL program could effectively reflect the heating situation of the system. In summary, COMSOL program can be expected to establish the relationship between different physical fields, especially in the electrothermal physical field. Therefore, COMSOL program has been utilized in this work to establish the model of heat distribution and temperature development within concrete structures cured by OH curing, so as to guide the OH curing process of concrete structures and promise the reasonable temperature distribution under subzero temperature.

In this paper, carbon fibers (CFs) have been utilized as macroscopic conductive fillers and CNFs were utilized as microscopic conductive fillers to synergistically prepare nonmass CFs/CNFs reinforced concrete slab (CFs/CNFs-CS) with the size of 350 mm × 450 mm × 40 mm. COMSOL multiphysical field coupling program was utilized to establish the numerical prediction model of the temperature development and distribution of OH cured slab under subzero temperature. The effects of different influencing factors including loading power densities, environmental temperature, and structure geometric shape on the temperature development and distribution were discussed in detail. Moreover, the temperature development and distribution of the OH cured slab at −20°C were experimentally measured to verify the accuracy of the numerical model. In addition, the mechanical properties of the OH curing nonmass CFs/CNFs-CS samples with optimized loading electric power were measured and SEM analysis was conducted to observe the microstructure of the samples.

2. COMSOL Multiphysical Field Coupling Numerical Simulation

The mutual coupling calculation among different physical fields (such as electric field and heat transfer field) can be realized by the COMSOL multiphysical field coupling program. In this work, OH curing process of nonmass concrete structure is closely related to the curing temperature and the environmental temperature, and the heat generation process is considered to be a transient process. Under this circumstance, COMSOL program was conducted to simulate the OH curing process of CFs/CNFs-CS under

subzero temperature. The detailed modeling process is shown as follows:

(1) Definition of material parameters: the parameters of concrete structure provided by COMSOL database have been utilized to define some relevant parameters.

(2) Establishment of physical field: the OH curing process is a Joule heating process, thus the Joule heating module in COMSOL has been selected, which includes current module and transfer module of solid heating. The current module has also been used to calculate the electric field distribution, current distribution, and potential distribution in the samples cured by OH curing. Based on Ohm's law, the current conservation equation which utilizes scalar potential as the dependent variable has been solved. Its formula [20, 21] is shown as follows:

$$\nabla \cdot J = Q_{j,y},$$
$$J = \sigma E + \frac{\partial D}{\partial t} + J_e, \quad (1)$$
$$E = -\nabla V,$$

where J is the current density vector (A/m^2); $Q_{j,v}$ represents the general current source (A/m^3); E represents the intensity of the electric field (N/C); σ represents the conductivity (S/M); V is the electric potential; and D represents the relative dielectric constant (C2).

The features provided by the solid heating transfer module interface have been utilized to simulate the process of conduction convection and radiation heat transfer through heat flux and the surface settings of environmental radiation, in which, heat flux is defined as convection heat flux, and its expression [22, 23] is shown as follows:

$$Q_D = h(T_{ext} - T), \quad (2)$$

where Q_D is the convective heat transfer; T_{ext} represents the external temperature; and T is the temperature of the sample cured by OH curing. In this simulation, h represents the coefficient of heat transfer.

The transfer of radiant heat is defined by the surface to environment radiation module, and its hypothesis equation [24, 25] is as follows:

$$Q_F = \varepsilon \sigma_1 A(T_{ext} - T), \quad (3)$$

where ε is the surface emissivity of the sample, which is also known as the blackness of the sample, the blackness of concrete value is 0.94; σ_1 represents the Boltzmann constant with the value of 5.67×10^{-8} W/(m^2·K^2); and A is the surface area of the sample.

Electromagnetic-thermal module has been selected to conduct modeling analysis during the COMSOL process of multiphysical field coupling; electromagnetic-thermal module is selected to conduct modeling analysis on the multiphysical field coupling of samples under OH curing condition. Its transient response hypothesis equation [26] is shown as follows:

$$\rho C_p \frac{\partial T}{\partial t} + \rho C_p u \cdot \nabla T = \nabla \cdot (k \nabla T) + Q_e, \quad (4)$$

where ρ is the density of the sample; C_p is the constant pressure heat capacity of the sample (J/(kg ∗ K)); u is the vector field constructed; and K is the thermal conductivity (W/(m ∗ k)).

(3) Division of mesh grid: conventional grid division has been adopted. The size of the cuboid model is 350 mm × 450 mm × 40 mm, and the size of the cylinder model is 200 mm × 1200 mm. The complete grid of the model consists of "1465" domain cells, 600 boundary elements, and 80 edge cells with the condition of conventional grid division. The results of cuboid model mesh division are shown in Figure 1(a), and the results of cylinder model mesh division are shown in Figure 2(a).

(4) Boundary conditions: the interface potential of one side has been set to be 0 in the current boundary conditions, and the electric potential of the opposite section is set to be Vtot, which is converted according to the power required by the experiment. The rest of the interfaces are set to be electrical insulation. The potential distribution diagram of the cuboid model is shown in Figure 1(b), and the potential distribution diagram of the cylinder model is shown in Figure 2(b). As shown below, the red area is considered as of high potential and the blue area is considered to be of low potential.

Solid heat transfer boundary conditions:

(1) It is assumed that the relevant material parameters (specific heat capacity, the coefficient of conductivity, and the conductivity) of the sample cured by OH curing remain unchanged during the process of heat transfer.

(2) Due to the low environmental temperature, no insulation layer is set, and all of the sections in the geometric model are considered to participate in the process of heat exchange.

(5) Output of calculation results: the temperature development of the samples cured by OH curing is considered to be a transient process, the temperature of the sample changes consistently with time, thus the research is determined to be transient. In this work, the length of calculation step was set to be 0.5 min, and the calculation time was set to be 600 min. The temperature probe was set at the center point of the model to record the temperature development during OH curing process.

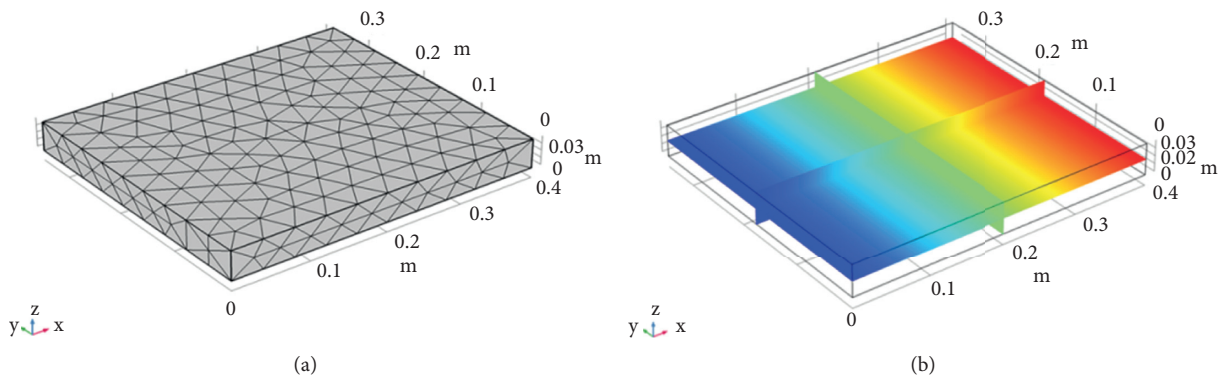

Figure 1: The generation of cuboid model: (a) grid division of cuboid model and (b) electrical potential distribution of cuboid model.

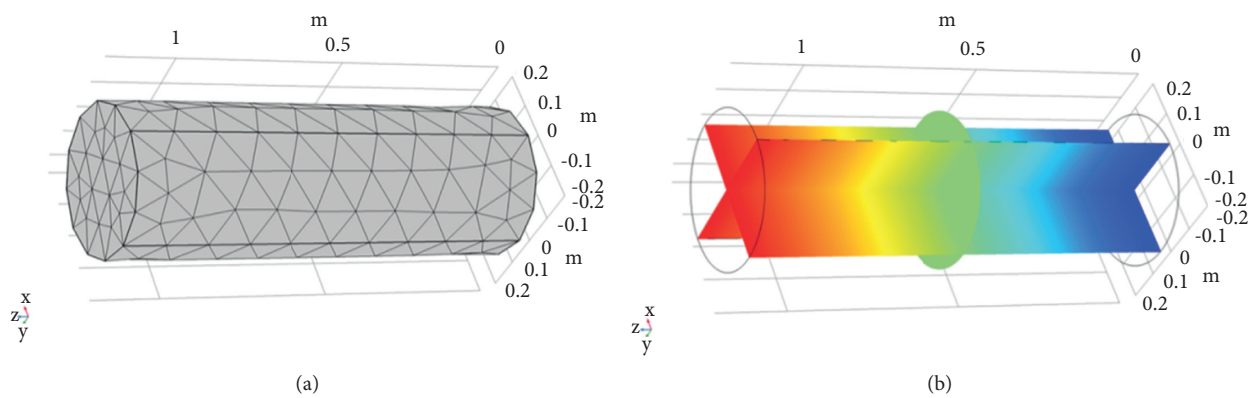

Figure 2: The generation of cylinder model: (a) grid division of cylinder model and (b) electrical potential distribution of cylinder model.

In this paper, COMSOL multiphysical field coupling program has been utilized to simulate OH cured samples under subzero temperature. The temperature development and heating regularity of the sample cured by OH curing under different environmental temperatures, different loading powers, and different sample sizes were mainly studied. The specific physical property parameters of materials used in the simulation process are shown in Table 1.

3. Materials and Experimental Method

3.1. Materials. The cementitious material used in this experiment is PO 42.5 cement. The chemical composition of the cement is shown in Table 2. The aggregate is fine quartz sand with the particle size range of 0.11–0.21 mm, the fineness modulus of fine silica sand is 2.41. CFs produced by Japan Toray have been chosen as the conductive filler; the diameter and the length of CFs are 7 μm and 4 mm, respectively. Detailed physical properties of CFs are shown in Table 3. CNFs have been utilized to construct microscopic conductive paths and the length and average diameter of CNFs are 20 nm and 100 nm, respectively.

Table 1: The physical parameters for simulated materials.

Physical parameter	Value
Thermal conductivity coefficient	1.28 $W \cdot m^{-1} \cdot K^{-1}$
Density	2300 kg/m^2
Constant voltage capacitance	1.26 $kJ \cdot kg^{-1} \cdot K^{-1}$
Relative dielectric constant	4.5
Electric conductivity	3.97 S/m
Radiance	0.94
Thermal expansion coefficient	$10e-6\,1/^{\circ}C$

Table 2: Chemical composition of cement.

Oxide species	SiO_2	Al_2O_3	Fe_2O_3	MgO	CaO	SO_2
The oxide containing (wt.%)	20.86	5.47	3.94	1.73	62.23	2.66

3.2. Sample Preparation and OH Curing Procedures. In this experiment, the mix design of CFs/CNFs-CS is as follows: the ratio of water to cement is 0.3, the ratio of sand to cement is 1 : 1, the CFs addition amount is 0.75 vol%, and the volumetric addition of CNFs is 0.2 vol%. The detailed fabrication process of the samples has been listed as follows: firstly, CNFs and fine silica sand were put into the stirring

Table 3: Physical properties of CFs.

Diameter (μm)	Tensile strength (MPa)	Volume resistivity	Density	Carbon content
7	3800	1.5×10^{-3} Ω·cm	1.76 g/cm^3	>95%

pot, and the CNFs were dispersed by rapid stirring with an eggbeater. Secondly, cement and CFs were sequentially placed in the pot, and the mixture was slowly stirred for 1 min with the mortar mixer and then stirred at high speed for 2 min to fully disperse CFs. Thirdly, the mixed solution of polycarboxylate superplasticizer (SP) and water was slowly added into the stirring pot and stirred for another 3 min to obtain final products. Finally, the mixture was poured into the plastic molds with the size of 350 mm × 450 mm × 40 mm embedded with two copper electrodes. The samples were then surface-smoothed and covered with plastic films. Two-electrode method was used to measure the resistance of CFs/CNFs-CS, the diagram of resistance measurement is depicted in Figure 3, and the resistivity ρ is computed using the formulation as follows:

$$\rho = \frac{RS}{L}, \tag{5}$$

in which R is the measured resistance; S represents the cross-sectional area of the composite; and L is the distance between copper electrodes.

At the same time, fifteen thermocouples were arranged to record the temperature development of CFs/CNFs-CS sample cured by OH curing under subzero temperature. The diagram of the arrangement of thermocouples is shown in Figure 4. Moreover, the newly prepared sample was placed in a refrigerator with the constant temperature of −20°C. To promise the stability of the power P, the voltage was adjusted according to the measured resistivity value every two hours complying with the following equation:

$$P = \frac{SU^2}{L\rho}, \tag{6}$$

in which P is the electric power; U represents the voltage; ρ represents the resistivity; and the cross-sectional area of the sample and the distance between the electrodes are denoted with S and L, respectively.

3.3. Characterization and Test. \The effects of different influencing factors on the temperature development and heating forms can be obtained by COMSOL program. The optimal loading electric power density of OH curing was determined and further utilized to prepare CFs/CNFs-CS sample under −20°C to verify the accuracy of modeling results from the aspect of experiments. CFs/CNFs-CS samples with the size of 350 mm × 450 mm × 40 mm were cured by OH curing with the temperature of −20°C for 1 day and 2 days to figure out the effect of OH curing on strength formation under subzero temperature. While CFs/CNFs-CS samples were also cured by room temperature (RT) curing (with the temperature of 20°C, humidity more than 95%) for 1 day and 2 days, after the curing procedure, the cuboid

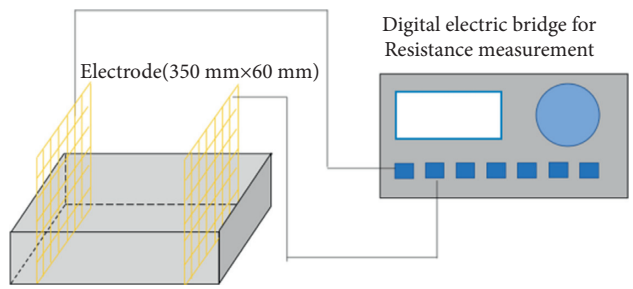

Figure 3: The diagram of resistance measurement.

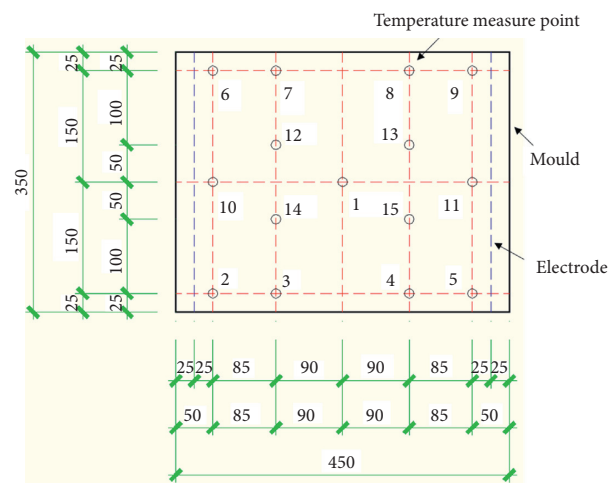

Figure 4: The diagram of the place of thermocouples.

sample with the size of 40 mm × 40 mm × 160 mm was cut from the middle of the slab. The compressive strength measurement of the samples (40 mm × 40 mm × 160 mm) was manufactured according to ISO679:1989 and GB/T 17671-1999 with the loading rate of 2400 ± 200 N/s. The hydration process was terminated by immersing the small pieces of the samples into absolute ethanol. The small pieces were further cold dried for 6 h at −60°C. Scanning electron microscopes (SEM, Hitachi, 9 SU5000) were utilized to obtain the morphology information of the microstructure in CFs/CNFs-CS samples.

4. Results and Discussion

4.1. Numerical Analysis on the Effects of Different Influencing Factors on the Temperature Development and Distribution. In this section, numerical prediction model has been established by COMSOL program to simulate the temperature development and distribution of OH cured CFs/CNFs-CS samples with different influencing factors. The effects of loading power density, environmental temperature, and structure geometric shape are taken into consideration.

4.1.1. Loading Power Density. The temperature development of CFs/CNFs-CS samples is significantly affected by the loading electrical power density. The cuboid model with the geometric size of 350 mm × 450 mm × 40 mm was simulated, and the domain point probe was arranged at the center of the model with the coordinates of (175, 225, 20). The temperature distribution of the model after 600 min has been analyzed under different loading power densities (0 W/m^2, 200 W/m^2, 400 W/m^2, 600 W/m^2, 800 W/m^2, 1000 W/m^2, 1200 W/m^2, and 1400 W/m^2). The results of simulation are shown in Figure 5 and the specific central temperatures of the samples are listed in Table 4. As shown in Figure 5, with the environmental temperature of −20°C, the temperature of the sample with the loading power density of 0 W/m^2 is always at subzero temperature, and this curing temperature cannot promise the hydration reaction of cementitious materials. However, with the loading power density of 200 W/m^2, 400 W/m^2, 600 W/m^2, and 800W/m^2, the final curing temperatures at the center point of the sample reach around 10°C, 27°C, 45°C, and 60°C, respectively. It is worth mentioning that a proper curing temperature is essential to promise ongoing hydration process of cement-based materials [27, 28], leading to the sufficient strength formation, and at these temperatures, although the hydration reaction of concrete can be ensured, the promotion effect on its strength is not obvious. Moreover, with the loading power density of 1400 W/m^2, the peak temperature of the sample reaches up to 110°C. This high curing temperature may lead to the decomposition of ettringite inside the sample, resulting in the degradation of mechanical properties for the sample [29, 30]. Finally, with the loading power density of 1000 W/m^2 and 1200 W/m^2, the final curing temperature at the center of the sample can reach up to 80°C and 90°C, respectively. With these curing temperatures, the strength of the samples can be formed rapidly and the mechanical properties of the samples will not be affected [31, 32]. In conclusion, the optimal loading power density range of OH cured slabs at −20°C has been determined to be 1000 W/m^2~1200 W/m^2.

4.1.2. Environmental Temperature. The environmental temperature also has a great influence on the samples cured by OH curing under ultra-low temperature. The temperature in northern China can reach up to −40°C in winter. Therefore, it is necessary to simulate the temperature development of samples cured with different environmental temperatures. In this section, the loading power density has been determined to be 1000 W/m^2 to analyze the temperature distribution of the model with different environmental temperatures (0°C, −10°C, −20°C, −30°C, and −40°C), and the results are shown in Figure 6. It can be seen from Figure 6 that with the loading power density of 1000 W/m^2, the curing temperature of the sample can be maintained at 70°C~80°C with the environmental temperature range of −20°C~−40°C at the age of 600 min. However, when the environmental temperature is between −10°C and 0°C, the peak temperatures of samples can reach up to 85°C~90°C. The hydration reaction of cementitious materials can be accelerated by properly increasing the curing temperature; this simulation result proves that OH curing can be utilized for concrete construction at severe cold regions in winter with the help of COMSOL numerical analysis.

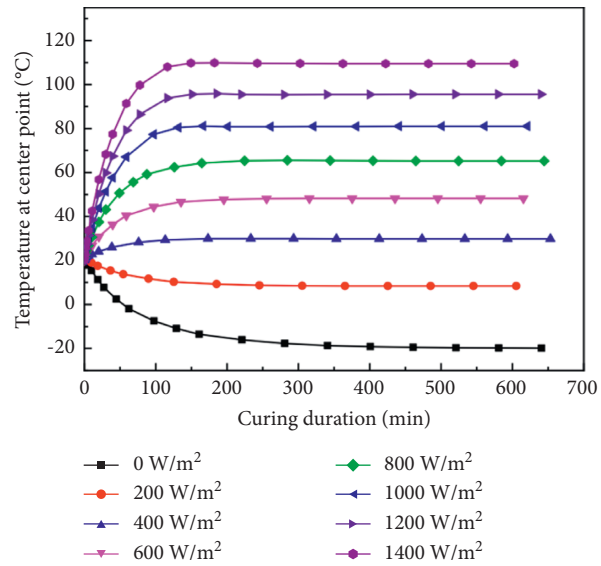

Figure 5: The simulated temperature at center point of the samples with different loading power densities.

Table 4: Simulated central temperatures of the samples with different loading power densities at 600 min.

Power density (W/m^2)	0	200	400	600	800	1000	1200	1400
Central temperature (°C)	−20	10	27	43	61	80	91	108

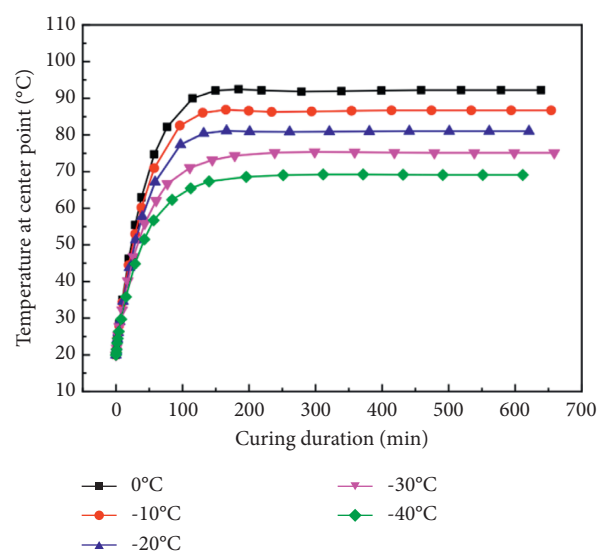

Figure 6: The simulated temperature at the center point of the sample with different environmental temperatures.

4.1.3. Structure Geometric Shape. After the modeling and prediction of the cuboid model, it can be concluded that OH curing can be guaranteed by adjusting the loading power density to reach the proper curing temperature of the sample under subzero temperature. In this section, in order to enhance the application of COMSOL program, the temperature field distributions of both cuboid model and cylinder model with the environmental temperature of −20°C and the loading power density of 1000 W/m^2 were simulated, respectively. The size of the cuboid model is 350 mm × 450 mm × 40 mm, and the size of the cylinder model is Φ200 mm × 1200 mm. The simulation results are shown in Figures 7 and 8. It can be seen from Figure 7 that with the loading power density of 1000 W/m^2, the center temperature of the cuboid model is fairly high, while the temperature decreases gradually from the center point and the temperatures at four corners of the model exhibit lowest values. This phenomenon is due to that the four corners have the largest contact surface with the outside, thus the temperature at the corner decreases quicker. The cylinder model shows the same temperature distribution regularity, the temperature at the center of the sample is high, and the temperature far away from the central area gradually decreases. Moreover, with the increase of temperature, the temperature difference between the central region and the edge area becomes larger. When the curing time exceeds 200 min, the temperature gradually tends to be stable, and the temperature is uniformly distributed in most areas of the whole cylinder. It can be concluded that COMSOL numerical analysis can be utilized to simulate the temperature development of the samples cured by OH curing under subzero temperature with different volumetric shapes.

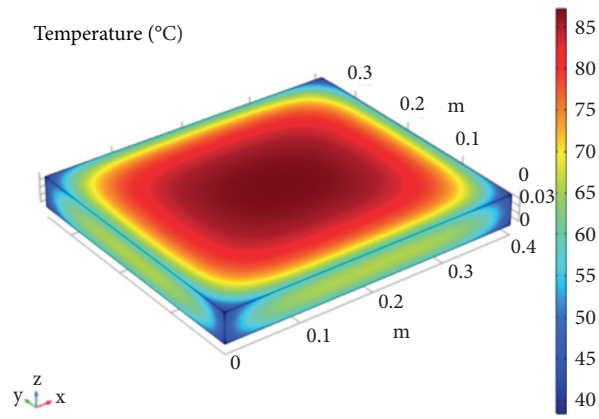

Figure 7: The surface temperature distribution of cuboid model with the loading electric power of 1000 W/m^2.

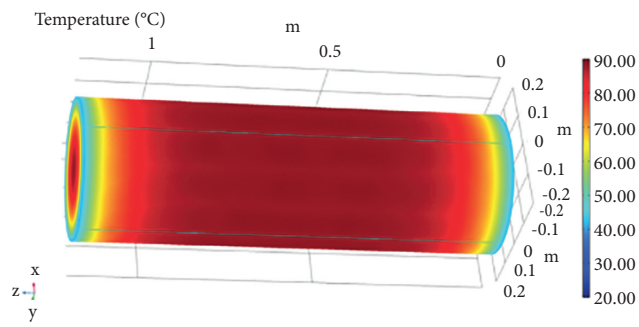

Figure 8: The surface temperature distribution of cylinder model with the loading electric power of 1100 W/m^2.

4.2. OH Curing of Nonmass CFs/CNFs-CS Sample Slab under Ultra-Low Temperature. In the above discussion, the influence of different factors on the temperature distribution of OH cured CFs/CNFs-CS samples has been analyzed by COMSOL program. In order to further confirm the accuracy of simulation analysis, experiments were carried out to investigate the temperature development of CFs/CNFs-CS. The curing temperature of the samples can reach up to 80~90°C with the loading power density of 1000 W/m^2~1200 W/m^2, which has been proved in the previous section. In this section, the loading power density has been determined to be 1100 W/m^2 to promise the proper curing temperature; based on this, the applied electrical power has been set to be 30W. Moreover, the arrangement of the thermocouples in the experiment is shown in Figure 4.

The distributions of temperature field have been recorded numerically and experimentally, and the results are respectively shown in Figures 9 and 10. Figure 9 exhibits the temperature distribution at the measured points of OH cured CFs/CNFs-CS sample at −20°C at the first 500 min curing duration. It can be seen that the temperature development regularity of each point is almost same with the applied electrical power of 30 W, indicating the uniform distribution of conductive paths constructed by CFs/CNFs. To be more specific, the curing temperature of CFs/CNFs-CS

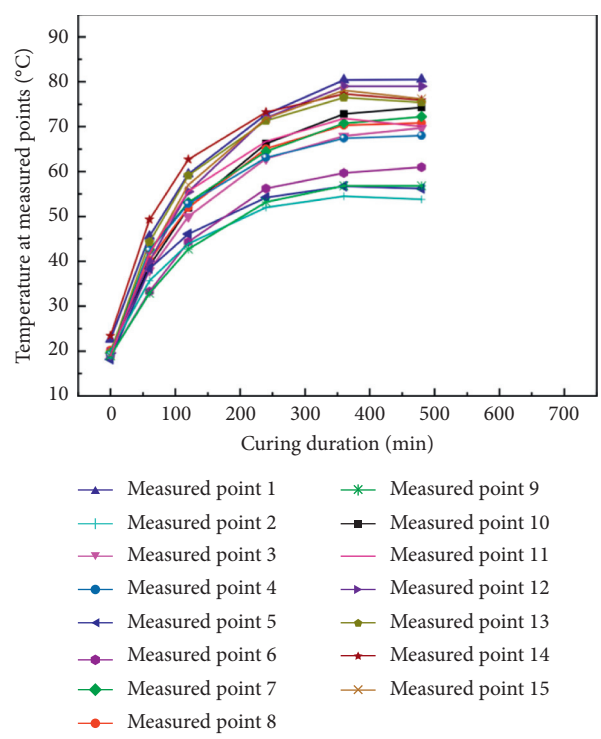

Figure 9: The actual temperature of CM-CF/CNFs slab.

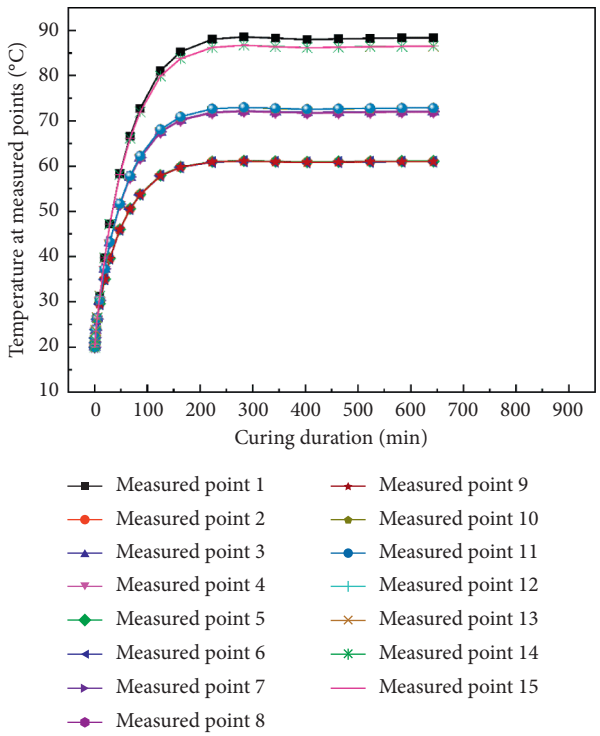

Figure 10: The simulated temperature of CM-CF/CNFs slab.

sample cured by OH curing increases obviously and reaches up to the peak temperature at 400 min. However, the peak temperatures at different measured points seem to have little difference. The peak temperature at the center point of the sample is about 75–80°C, while the peak temperature from the edge area exhibits lower value of 52–60°C. In conclusion, the temperature at the center of the sample is generally higher than that around the sample. The reason for this difference is that the heat transfer path of the edge area is shorter than that of the central area. This causes that the heat dissipation speed is faster at the edge area of the sample compared with that at the central area of the sample [33, 34].

Figure 10 shows the temperature distribution of CFs/CNFs-CS sample simulated by COMSOL program. The peak temperature at the central area of the sample is about 85–88°C, while the peak temperature at the edge area is 60–70°C with the loading power density of 1100 W/m^2. Moreover, it takes 100 minutes with the heating rate of 0.68°C/min for the peak temperature at the central area of the sample to raise from 20°C to 88°C by numerical simulation, while it takes 400 minutes with the heating rate of 0.15 °C/min for the actual center temperature to rise from 20°C to 80°C by experimental measurement. It can be concluded that the temperature and heating rates simulated by COMSOL program are a little higher and faster than the measured temperature and heating rate during OH curing, and this is considered to be the reason that the actual curing condition of OH cured sample is much more complicated than the simulated environment. For example, the resistivity of the sample changed all the time during the curing process, leading to the actual applied power being always lower than the simulated power.

To further compare the curing temperatures of the samples, the peak temperature distribution of CFs/CNFs-CS sample measured numerically and experimentally is listed in Table 5. It can be seen from Table 5 that the whole temperature field simulated by COMSOL program is symmetrical distribution. The peak temperature at the center area is the highest, and the peak temperature gradually decreases with the increase of the distance from the center point. Moreover, it can be seen that the temperature prediction at the center of the sample is close to that of the actual OH cured sample, indicating the accuracy of the program. However, the peak temperature distribution of the sample cured by OH curing at 20°C is not as uniform as that obtained by the simulation analysis, but it still conforms to the temperature distribution regularity. This is considered to be that although CFs and CNFs could construct conductive paths inside the sample, the distribution of CFs/CNFs is not completely uniform, and there is still a certain gap of heating uniformity between the simulation analysis and actual experiment. However, the peak temperature of CFs/CNFs-CS sample cured by OH curing can reach up to 55–80°C at −20°C. This curing temperature is sufficient to promise the proper curing condition of the sample under ultra-low temperature by promoting the hydration reaction of cementitious materials to a great extent. Therefore, the developed simulation program is promising to guide the winter construction of nonmass cementitious materials cured by OH curing under ultra-low temperature.

4.3. Mechanical Properties. As shown in Figure 11, the compressive and flexural strengths of the samples cured with different curing conditions were measured. It can be seen from Figure 11(a) that the compressive strength of the samples cured by 1 day OH curing at −20°C reaches up to 34.3 MPa, which is much greater than the critical frost resistance strength of 3.5 MPa. Moreover, it is also much higher than that of the sample cured by 1 day RT curing (19.7 MPa). Further, the compressive strength of 2 days OH cured CFs/CNFs-CS sample also increases obviously with the value of 48.2 MPa compared with that of the sample cured by 2 days RT curing (38.1 MPa). This shows that the compressive strength of the sample can be significantly improved by OH curing with the electrical power of 30W at −20°C.

Figure 11(b) represents the flexural strengths of CFs/CNFs-CS samples cured with different conditions. The results indicate the flexural strengths of the samples developed in the same regularity as the compressive strengths. As shown in Figure 11(b), the flexural strength of 1 day OH cured sample is 10.5 MPa, which is much higher than that of the sample cured with 1 day RT curing (6.7 MPa). Moreover, the flexural strength of the sample subjected to 2 days OH curing reaches up to 11.5 MPa, which is 22.3% higher than that of the samples with 2 days RT curing.

4.4. SEM Analysis. SEM analysis of CFs/CNFs-CS samples subjected to different curing conditions was conducted and the results are shown in Figure 12. It can be seen from

Table 5: Peak temperatures of the samples measured numerically and experimentally.

Simulated temperature (°C) at different points	1	2	3	4	5	6	7	8
	88.35	61.05	71.97	71.95	61.09	60.09	72.09	71.97
	9	10	11	12	13	14	15	
	61	72.82	72.82	86.49	86.49	86.5	86.48	
Measured temperature (°C) at different points	1	2	3	4	5	6	7	8
	80.5	56.2	63.5	68.1	57.6	54.1	69.7	70.9
	9	10	11	12	13	14	15	
	61.1	74.3	72.2	75.9	76.4	75.4	79	

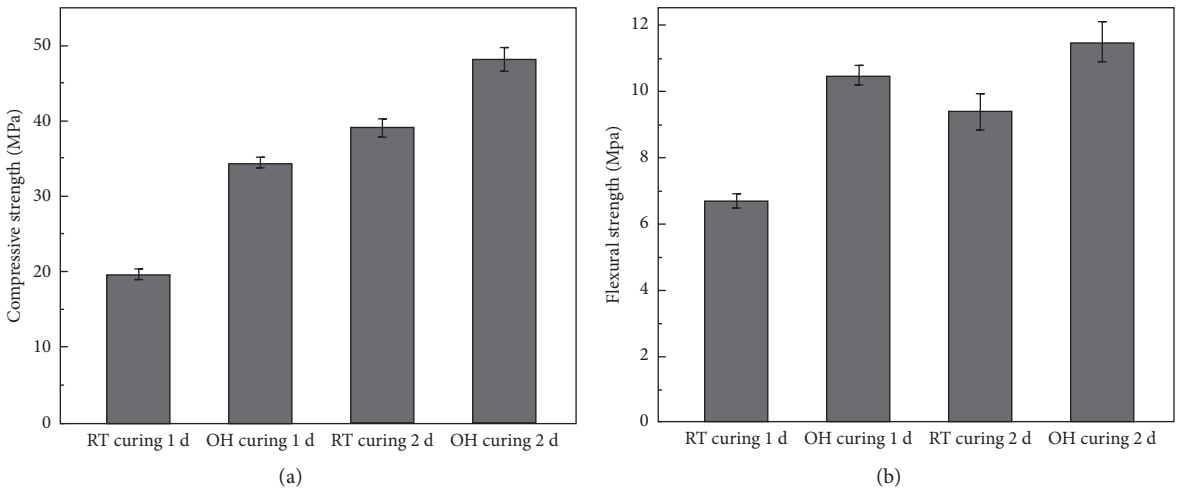

Figure 11: Mechanical properties of CF/CNF-CS samples. (a) Compressive strength and (b) flexural strength.

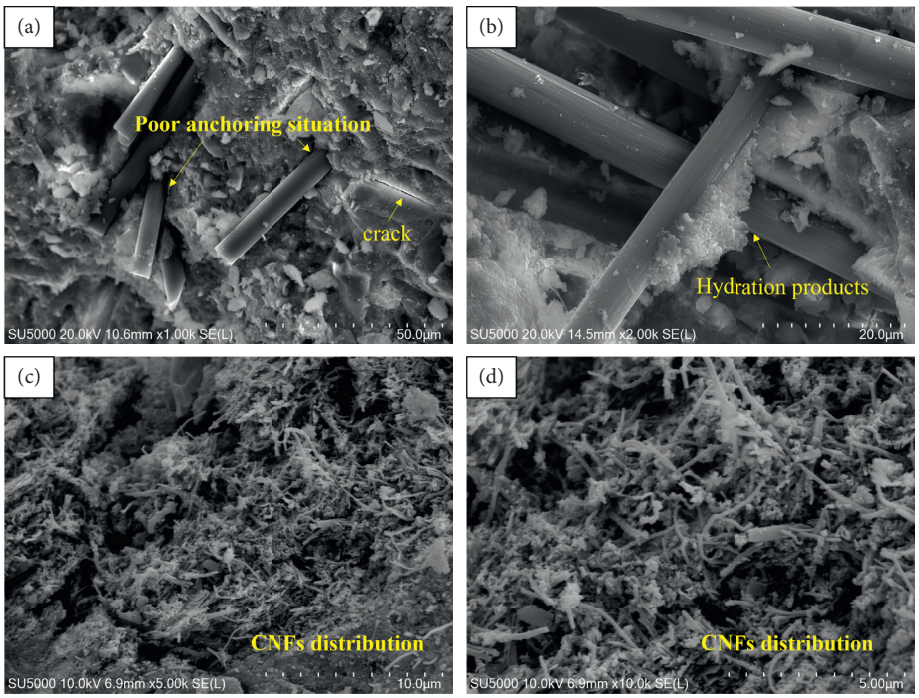

Figure 12: (a) SEM morphology of samples cured by 2 days RT curing with a magnification of 2000x, and the samples cured by 2 days OH curing with the magnifications of (b) 2000x, (c) 5000x, and (d) 10,000x.

Figure 12(a) that the sample cured by 2 days RT curing exhibits relatively loose microstructure, and the surface of CFs are fairly smooth. However, the implementation of 2 days OH curing is beneficial for the microstructure of the samples. To be specific, a much denser microstructure can be found in 2 days OH cured samples, as shown in Figure 12(b). Moreover, hydration products inside the sample exhibit a trend to attach onto the surface of CFs, which can refine the ITZ between CFs and the matrix, and this is beneficial for mechanical properties of the samples. Figures 12(a) and 12(b) respectively display the distribution situation of CFs and CNFs in the samples. A uniformly distributed situation of CNFs can be observed from Figures 12(a) and 12(b). This is beneficial to the stability of OH curing of the samples. In addition, the distribution situation of CNFs has been displayed in Figures 12(c) and 12(d); it is shown that CNFs can uniformly distribute in the sample to construct conductive network from the microscopic point of view. Based on the above microstructure evidences, it can be concluded that 2 days OH curing with 30 W electrical power is beneficial to the strength development of the CFs/CNFs-CS samples compared with 2 days RT curing.

5. Conclusion

This work numerically establishes the relationship between loading power and the curing temperature of the samples cured by OH curing, leading to the accurate guideline of applied power. This lays a solid foundation for concrete construction at cold region with high efficiency and low energy consumption. Detailed conclusions have been shown as follows:

(1) The numerical simulation results of COMSOL program show that the loading power and environmental temperature have a close influence on the curing temperature of nonmass CFs/CNFs-CS. Higher loading power and environmental temperature can lead to higher curing temperature. Moreover, the optimal loading power density of the sample calculated by COMSOL program is determined to be 1000 W/m^2~1200 W/m^2 at −20°C, and this loading power density can help the temperature at the central region of CFs/CNFs-CS sample reach up to 86–88°C in theory.

(2) The peak temperature of CFs/CNFs-CS sample reaches to 80.5°C at −20°C with the loading electrical power of 30 W in the experimental measurement, which is very close to the numerical results. This proves the good prediction effect of COMSOL numerical program. Moreover, the simulated temperature field is symmetrical, and the temperature decreases from the center to the corner of the sample. The temperature field measured by the experiment basically conforms to this regularity.

(3) The compressive strengths of OH cured CFs/CNFs-CS samples for 1 day and 2 days are increased by 74.11% and 26.5%, respectively, compared with those of the samples cured by 1 day and 2 days RT curing. Moreover, the flexural strengths of the samples cured by OH curing for 1 day and 2 days reach up to 10.5 MPa and 11.5 MPa, respectively. In addition, the results of SEM analysis show that the CFs/CNFs-CS samples cured by OH curing exhibit denser microstructure and better anchor situation between fibers and the matrix.

Data Availability

The raw data used to support the findings of this study are available from the corresponding author upon request.

Conflicts of Interest

The authors declare that they have no conflicts of interest.

References

[1] B. Ciuk, D. J. Haavik, and G. Haddad, "Standard specification for cold weather concreting (306.1-90)," *Concrete*, vol. 10, pp. 408-409, 1990.

[2] R. L. Kozikowski, W. C. Mccall, and B. A. Suprenant, "Cold weather concreting strategies," *Concrete International*, vol. 36, no. 5, pp. 45–49, 2014.

[3] R. Demirboga, F. Karagöl, Ri Polat et al., "The effects of urea on strength gaining of fresh concrete under the cold weather conditions," *Construction and Building Materials*, vol. 64, pp. 114–120, 2014.

[4] Z. Liu, A. Sha, M. Xing, and Z. Li, "Low temperature property and salt releasing characteristics of antifreeze asphalt concrete under static and dynamic conditions," *Cold Regions Science and Technology*, vol. 114, pp. 9–14, 2015.

[5] B. Xu, Z. Yang, L. Zhao, D. Cao, H. Zhang, and X. Shi, "Study on the antifreeze performance of porous cement stabilized macadam," *Construction and Building Materials*, vol. 208, no. 8, pp. 13–22, 2019.

[6] M. Ziolkowski and M. Kovtun, "Confined-Direct Electric Curing of NaOH-activated fly ash based brick mixtures under free drainage conditions: Part 2. Confined-DEC versus oven curing," *Construction and Building Materials*, vol. 176, pp. 452–461, 2018.

[7] M. Ziolkowski and M. Kovtun, "Confined-Direct Electric Curing of NaOH-activated fly ash based brick mixtures under free drainage conditions: Part 1. Factorial experimental design," *Construction and Building Materials*, vol. 155, pp. 1050–1062, 2017.

[8] Y. Liu, W. Tian, M. Wang, B. Qi, and W. Wang, "Rapid strength formation of on-site carbon fiber reinforced high-performance concrete cured by ohmic heating," *Construction and Building Materials*, vol. 244, Article ID 118344, 2020.

[9] Y. Liu, M. Wang, and W. Wang, "Ohmic heating curing of electrically conductive carbon nanofiber/cement-based composites to avoid frost damage under severely low temperature," *Composites Part A: Applied Science and Manufacturing*, vol. 115, pp. 236–246, 2018.

[10] Y. Liu, M. Wang, W. Tian, B. Qi, Z. Lei, and W. Wang, "Ohmic heating curing of carbon fiber/carbon nanofiber synergistically strengthening cement-based composites as repair/reinforcement materials used in ultra-low temperature environment," *Composites Part A: Applied Science and Manufacturing*, vol. 125, Article ID 105570, 2019.

[11] W. Lei, Z. Xiao, Y. Hua, and X. Lv, "Investigation and application of fractal theory in cement-based materials: a review," *Fractal and Fractinal*, vol. 5, no. 4, p. 247, 2021.

[12] Z. Mi, Y. Hu, Q. Li, and H. Zhu, "Elevated temperature inversion phenomenon in fracture properties of concrete and its application to maturity model," *Engineering Fracture Mechanics*, vol. 199, pp. 294–307, 2018.

[13] N. J. Jin, I. Seung, Y. S. Choi, and J. Yeon, "Prediction of early-age compressive strength of epoxy resin concrete using the maturity method," *Construction and Building Materials*, vol. 152, pp. 990–998, 2017.

[14] W. Li, Z. Huang, G. Hu, W. D. Hui, and S. P. Shah, "Early-age shrinkage development of ultra-high-performance concrete under heat curing treatment," *Construction and Building Materials*, vol. 131, pp. 767–774, 2017.

[15] K. F. Tan and J. Z. Zhu, "Influences of steam and autoclave curing on the strength and chloride permeability of high strength concrete," *Materials and Structures*, vol. 50, no. 1, pp. 1–9, 2017.

[16] L. Wang, X. Lu, X. Li et al., "Influence of reactivity and dosage of MgO expansive agent on shrinkage and crack resistance of face slab concrete," *Cement and Concrete Composites*, vol. 125, In press, Article ID 104333, 2022.

[17] S. Zandi, P. Saxena, and N. E. Gorji, "Numerical simulation of heat distribution in RGO-contacted perovskite solar cells using COMSOL," *Solar Energy*, vol. 197, pp. 105–110, 2020.

[18] T. Li, X. Yu, O. B. Habibzadeh, G. Lei, and A. J. Puppala, "Heating performance of a novel externally-heated geothermal bridge de-icing system: field tests and numerical simulations," *Sustainable Energy Technologies and Assessments*, vol. 46, Article ID 101280, 2021.

[19] B. Larwa, S. Cesari, M. Bottarelli, D. Boldor, G. M. Aita et al., "Study on thermal performance of a PCM enhanced hydronic radiant floor heating system," *Energy*, vol. 225, Article ID 120245, 2021.

[20] L. B. Leinson and A. Pérez, "Vector current conservation and neutrino emission from singlet-paired baryons in neutron stars," *Physics Letters, Section B: Nuclear, Elementary Particle and High-Energy Physics*, vol. 638, no. 2–3, pp. 114–118, 2006.

[21] R. J. Singh and T. B. Gohil, "The numerical analysis on the variation of electric potential, electric current and Lorentz force with its influence on buoyancy-driven conjugate heat transfer and fluid flow using OpenFOAM," *Fusion Engineering and Design*, vol. 148, Article ID 111300, 2019.

[22] A. Raicu, M. Barhalescu, and F. Memet, "Heat transfer original studies-Theory and applications [J]," *IOP Conference Series: Materials Science and Engineering*, vol. 591, no. 1, 2019.

[23] M. Kim, A. Sergis, S. J. Kim, and Y. Hardalupas, "Assessing the accuracy of the heat flux measurement for the study of boiling phenomena," *International Journal of Heat and Mass Transfer*, vol. 148, Article ID 119019, 2020.

[24] J. C. Cuevas and F. J. V. García, "Radiative heat transfer," *ACS Photonics*, vol. 5, no. 10, pp. 3896–3915, 2018.

[25] H. S. Roh, "Heat transfer theory for thermal non-equilibrium, quasi-equilibrium, and equilibrium," *International Journal of Heat and Mass Transfer*, vol. 64, pp. 661–670, 2013.

[26] V. Rozov, V. Belyakov, V. Kukhtin, E. Lamzin, I. Mazul, and S. Sytchevsky, "Strategy for solving a coupled problem of the electromagnetic load analysis and design optimization for local conducting structures to support the ITER blanket development," *Fusion Engineering and Design*, vol. 89, no. 11, pp. 2691–2708, 2014.

[27] Z. Li, D. J. Corr, B. Han, and S. P. Shah, "Investigating the effect of carbon nanotube on early age hydration of cementitious composites with isothermal calorimetry and Fourier transform infrared spectroscopy," *Cement and Concrete Composites*, vol. 107, Article ID 103513, 2020.

[28] W. Lei, R. Luo, W. Zhang, and M. Jin, "Effects of fineness and content of phosphorus slag on cement hydration, permeability, pore structure and fractal dimension of concrete," *Fractals*, vol. 29, no. 2, Article ID 2140004, 2021.

[29] S. L. Yang, S. G. Millard, M. N. Soutsos, S. J. Barnett, and T. T. Le, "Influence of aggregate and curing regime on the mechanical properties of ultra-high performance fibre reinforced concrete (UHPFRC)," *Construction and Building Materials*, vol. 23, no. 6, pp. 2291–2298, 2009.

[30] C. Kahanji, F. Ali, A. Nadjai, and N. Alam, "Effect of curing temperature on the behaviour of UHPFRC at elevated temperatures," *Construction and Building Materials*, vol. 182, pp. 670–681, 2018.

[31] P. Hu, D. J. Lu, X. Y. Fan, X. Zhou, and Z. S. Chen, "Phase change performance of sodium acetate trihydrate with AlN nanoparticles and CMC," *Solar Energy Materials and Solar Cells*, vol. 95, no. 9, pp. 2645–2649, 2011.

[32] Z. Pavlík, A. Trník, T. Kulovaná et al., "DSC and TG analysis of a blended binder based on waste ceramic powder and portland cement," *International Journal of Thermophysics*, vol. 37, no. 3, pp. 1–14, 2016.

[33] M. I. Stewart, "Heat transfer theory," *Surface Production Operations*, Elsevier, Amsterdam, Nertherlands, pp. 39–97, 2014.

[34] G. T. Polley, "Heat transfer and fluid flow," *Physics in Technology*, vol. 7, no. 3, pp. 132-133, 1976.

Hindawi
Advances in Civil Engineering
Volume 2021, Article ID 2977428, 13 pages
https://doi.org/10.1155/2021/2977428

Research Article

Mechanical Properties of Concrete Incorporating Rice Husk Ash and Wheat Straw Ash as Ternary Cementitious Material

Naraindas Bheel,[1] Paul Awoyera,[2] Irfan Ali Shar,[3] Samiullah Sohu,[4] Suhail Ahmed Abbasi,[4] and A. Krishna Prakash[5]

[1]*Department of Civil and Environmental Engineering, Universiti Teknologi PETRONAS, Bandar Seri Iskandar, Tronoh, Perak, 31750, Malaysia*
[2]*Department of Civil Engineering, Covenant University, Ota, Nigeria*
[3]*Department of Civil Engineering, ISRA University Hyderabad, Hyderabad, Sindh, Pakistan*
[4]*Department of Civil Engineering, Quaid-e-Awam University of Engineering, Science and Technology Campus Larkan, Nawabshah, Sindh, Pakistan*
[5]*Department of Civil Engineering, Anna University, Chennai 600025, India*

Correspondence should be addressed to Naraindas Bheel; naraindas_20001014@utp.edu.my

Received 6 July 2021; Revised 9 November 2021; Accepted 15 November 2021; Published 29 November 2021

Academic Editor: Yushi Liu

Over the last decade, there has been a surge in research into possible cement substitute materials in concrete that are environmentally friendly, cost-effective, and socially beneficial. The alternatives include industrial and agricultural wastes, and their potential advantages can be achieved through recycling, repurposing, and renewing processes. With the use of these wastes as additional and replacement materials, significant energy savings and a reduction in cement use can be achieved, which helps to reduce carbon dioxide (CO_2) emissions in the environment. Therefore, the use of rice husk ash (RHA) and wheat straw ash (WSA) as ternary cementitious material (TCM) in concrete can help reduce the impact on the environment and minimize the use of Portland cement (PC) in the concrete mixture. This research work is performed on the concrete blended with 0%, 5%, 10%, 15%, and 20% of RHA and WSA as TCM in the mixture. However, the purpose of this experimental work is to investigate the influence of RHA and WSA as TCM on the fresh (slump), physical (water absorption and density), and hardened properties (compressive strength, splitting tensile strength, and flexural strength) and drying shrinkage of concrete. In this regard, a total of 240 concrete samples (cylinders, cubes, and beams) were prepared with 1 : 2 : 4 mix proportions at 0.50 water-cement ratio and cured at 7 and 28 days, respectively. Moreover, the workability of green concrete is getting reduced as the quantity of TCM increases in the mixture. Besides, the compressive strength, splitting tensile strength, and flexural strength are enhanced by 12.65%, 9.40%, and 9.46% at 10% of TCM (5% RHA and 5% WSA) on 28 days consistently. Furthermore, the density and water absorption of concrete are reduced with the increase in the dosages of TCM on 28 days, respectively. In addition, the drying shrinkage is reduced with the increase in the quantity of TCM in concrete.

1. Introduction

The use of concrete has been admired for decades throughout the world [1]. Concrete is man-made material prepared by mixing cement paste with fine and coarse aggregates in designed proportions. The construction industry is highly dependent on this incredible material, and for the time being, there is limited availability of resources that include the binding material, i.e., cement, and aggregates, i.e., coarse and fine. Hence, it is necessary to lessen degradation of natural materials and resources [2] by introducing inexpensive and leftover materials possessing pozzolanic properties with the prospect to substitute conventional materials of concrete [3]. Cement is a costly concrete constituent, and its manufacturing discharges huge quantity of carbon dioxide in the atmosphere [4–6]; one ton of carbon dioxide is released

while manufacturing one ton of cement [7]. To lessen cost of manufacturing and amount of carbon dioxide, researchers are investigating to replace cement partially with agricultural or industrial discards, i.e., blast furnace slags, wheat straw ash, rice husk ash, fly ash, glass powder, and others [7, 8]. Moreover, concrete production is also liable to be the source of discharge for greenhouse gases in the atmosphere as yearly concrete production is about 1.6 billion tons, which causes the release of greenhouse gases which account for approximately 7% of total gas emissions [9].

Consequently, effective consumption of solid waste materials in concrete aids in mitigating common problems of environmental pollution, scarcity of raw materials, energy crises, and overhead costs of constructions [10]. Additionally, there could be a major improvement in concrete performance in strength as well as in durability with effective consumption of waste pozzolanic materials, and hence extensive research is being carried out on pozzolans like ashes of sawdust, rice husk, wheat husk, sewage dust, and metakaolin [11], ashes of coconut shell, bottom coal, corn cob [12, 13], and so on. Rice husk ash is a solid waste utilized as cementitious material, and bottom coal ash is utilized in replacement of fine aggregate during this research work. RHA, an agricultural by-product [14–16] generally burned in open space, is regarded as the source of air pollution [17, 18],because it is regarded as a waste product and proper disposal of such kind of waste is a serious concern as 120 million tons of rice husk is thrown away or burned annually [19–21]. RHA contains about 85% of amorphous silica which can be employed as cement substituting material [22–25] because of its pozzolanic property, and thus environmental pollution can be minimized to some extent [26–29]. Various research investigations were carried out on concrete blended with 0%–20% of RHA as cementitious material 10%–15% of RHA provides the highest compressive strength of concrete [30]. As size of RHA particle is finer than cement particle, it can improve concrete performance, and it is used as binding material along with cement; therefore, it plays a major role to increase the intertransition zone of concrete [31, 32]. It also makes concrete dense by working as filler material [33].

According to facts and figures given in 2015 by the Food and Agricultural Organization of the United Nations, wheat production per annum was determined as 734.5 million tons [34]. Wheat straw is acquired after harvesting the wheat crop on removal of stubbles, and with production of each kg of grain, about 1.3 to 1.5 kg of wheat straw is acquired on average [35]. Worldwide, the annual production of wheat is around 534 million tons, and hence a large quantity of wheat straw is dumped or burned in open space generating environmental pollution. To accommodate such situations, various strategies have been recommended over the burning of wheat straw such as being utilized as fuel for energy production [36], being feed for livestock [37], transforming it as fertilizer, and then utilizing it into the soil for crop productions [38]. But every alternative has few drawbacks [39]. This research recommends incineration as an alternative to disposing wheat straw, while incineration is a process of waste burning in the controlled atmosphere which has the most important advantage that this process lessens the amount of waste by 90% and landfill sites required for dumping waste [40, 41]. Therefore, this process is much feasible in urbanized countries like Japan where land available for dumping wastes is too expensive and there is exceptional demand for land. With the incineration process, many developed countries are generating energy [42] which is utilized to further generate electricity [40]. The resulting wheat straw ash possesses pozzolanic property, and thus it is consumed as cement substituting material in construction activities; besides, it releases trivial amount of carbon dioxide in the atmosphere [43]. Moreover, researchers observed that concrete strength increased with the introduction of pozzolanic materials, but due to the low hydration activity of pozzolanic materials such as WSA, strength development in concrete is very slow.

Furthermore, most of the investigations were carried out on concrete blended with WSA and RHA as cementitious material individually, but there is no research work that explored the workability, water absorption, density, compressive strength, splitting tensile strength, flexural strength, and drying shrinkage of concrete incorporating RHA and WSA as ternary cementitious material (TCM) in the mixture. In addition, both RHA and WSA were combined owing to their complementary chemical composition. For instance, RHA has silica as dominant oxide, while WSA has good filling effect in cementitious mixture, but it is not too strong in silica. Thus, combining these TCMs helps in providing pozzolanic effect and filling effect in the developed mixtures. Moreover, this research addresses sustainability issue, and its main focus is to explore the use of RHA and WHA as alternative materials for concrete production, since they are dominant materials in our region. Thus, the research is focused on the beneficial utilization of the materials for construction application.

Therefore, this article summarizes the effect of RHA and WSA as TCM on the fresh property, physical properties, mechanical properties, and drying shrinkage of concrete.

2. Material and Experimental Program

2.1. Material. The rice husk was obtained from an agricultural field near Hyderabad, Sindh, and then it was burnt under an uncontrolled temperature arrangement for five hours to convert into rice husk ash (RHA). After obtaining ash, it was passed from sieve #300 for excluding outsized particles; after that, sieved ash was used in place of cement within mixture. Then, the wheat straw was obtained, and it was burnt under an uncontrolled temperature arrangement for five hours to convert it into wheat straw ash (WSA). After obtaining ash, it was passed from the #300 sieve for eliminating unwanted materials and then the sieved ash was used as cementitious materials in the mixture. Moreover, the Portland cement (PC) was collected from the local market, and it was employed as binder in mixture. Composition of oxides of PC, WSA, and RHA is presented in Table 1. Furthermore, stones used were crushed for this research work as coarse aggregates (CAs) which possess a size of 20 mm, hill sand was used for experimental study, and fine aggregates used were passed by #4 sieve. According to ASTM

Table 1: Oxide's percentages and physical properties of PC, WSA, and RHA.

Materials	Oxide components (%)							Particles size (μm) [44]	Specific surface area (cm^2/gm) [44]	Specific gravity
	SiO_2	Al_2O_3	Fe_2O_3	CaO	Na_2O	SO_3	LOI			
RHA	86.94	0.20	0.10	2.20	0.80	0.86	4.80	8.86	5980	2.23
WSA	67.34	6.44	4.36	10.60	0.47	1.85	4.20	9.13	5540	2.21
PC	20.78	5.11	3.17	60.22	0.18	2.86	2.45	18.61	3250	3.13

C136 [45], aggregate sieve analysis is calculated. The specific gravity of coarse aggregates (CAs) and fine aggregates (FAs) is calculated according to ASTM C127-93 [46] and ASTM C128-93 [47] correspondingly. The ASTM C29-97 [48] code of conduct is used to determine aggregates' bulk density, while the ASTM C127-93 [46] and ASTM C128-93 [47] codes of practice are used to determine water absorption of coarse and fine aggregates, respectively. These aggregates were obtained from Hyderabad, Sindh, and their properties are shown in Table 2, and the sieve analysis curve for coarse and fine aggregates is summarized in Figures 1 and 2. Moreover, water suitable for drinking was used for mixing as well as curing of concrete.

2.2. Mix Proportions. The mixing process in this investigation followed the standard practices used in conventional concrete mixing, and all of the mixing was done manually. For raw material preparation, PC, aggregates, RHA, WSA, and water were all weighed. The dry mix was first completed by manually mixing PC, aggregates, WSA, and RHA in a mixer until they were uniformly mixed. After that, water was added to the dry mix. The mix was mixed until the wet mixture was changed to a homogenous mixture, and then the workability of fresh concrete was checked immediately. After checking the workability, the fresh mixture of concrete was poured into moulds and left for 24 hours for achieving desired shape and was kept in curing until testing. These concrete specimens were used for physical (water absorption and density) and hardened properties (compressive strength, splitting tensile strength, flexural strength, and drying shrinkage) of concrete blended with TCM0 (0% WSA+ 0% RHA), TCM5 (2.5%WSA+ 2.5%RHA), TCM10 (5% WSA+ 5% RHA), TCM15 (7.5% WSA+ 7.5% RHA), and TCM20 (10% WSA+ 10% RHA) in the mixture. In this regard, a total of 240 concrete samples (cylinders, cubes, and beams) were equipped with 1 : 2 : 4 mix proportions at 0.50 water-cement ratio and cured at 7 and 28 days, respectively. The mix proportions are mentioned in Table 3.

2.3. Testing Procedures

2.3.1. Workability (Slump Test). This test had been performed on overall fresh concrete mixes with different proportions of RHA and WSA as TCM by observing code BS EN 12350-2 [49] in concrete.

2.3.2. Mechanical Properties of Concrete. Water absorption and density of hardened concrete were checked over the specimens made of concrete blended with several proportions of RHA and WSA as TCM in concrete as verified by BS 1881 [50] and BS EN 12390-7 [51] techniques on 28 days, correspondingly. However, the compressive strength test was conducted on the cubical specimen with 100 mm × 100 mm × 100 mm dimensions, and the splitting tensile strength test was conducted on cylindrical specimen with 200 mm × 100 mm dimensions, blended with various levels of replacement of PC with RHA and WSA as TCM in the mixture by using the BS EN 12390-3 [52] and BS EN 12390-6 [53] code practice consistently. Besides, the flexural strength was tested on beam specimen with dimensions 500 mm × 100 mm × 100 mm, with replacement of PC with RHA and WSA as TCM in mixture under the BS EN 12390-5 [54] code practice. These concrete samples were cured and tested at 7 and 28 curing days. Furthermore, the drying shrinkage test was performed on concrete cylindrical samples with the addition of RHA and WSA as TCM in concrete mixture by using the BS ISO 1920-8 [55] code technique at 5, 10, 15, 20, 30, 60, and 90 days, correspondingly. The experimental setup of concrete testing is presented in Figure 3.

Table 2: Aggregate properties.

Property	Fine aggregate	Coarse aggregate
Fineness modulus (FM)	2.21	—
Specific gravity (SG)	2.64	2.70
Water absorption (%)	1.72	1.30
Bulk density (kg/m^3)	1890	1569

3. Results and Discussion

3.1. Slump Test. The test performed to measure fresh concrete consistency by addition of WSA and RHA as ternary cementitious material (TCM) is indicated in Figure 4. The optimum value of slump recorded on control mix was 62 mm, and the minimum slump value noted was 24 mm at 10% WSA along with 10% of RHA as TCM in the mixture. It can be perceived that the slump of green concrete is dropped with the addition of WSA and RHA together in a mixture. This drop in slump is due to the high specific surface area of RHA and WSA particles than that of PC as shown in Table 1 which absorb more water as compared to PC while the percentages of RHA and WSA increase in the concrete mixture. Moreover, the 20–24 mm slump is small for practical application. Therefore, the study suggests the use of plasticizer for improving the workability of the mixture. This research work is linked with Al-Akhras and Abu-Alfoul [56] where slump declined with the increase in dosages of WSA

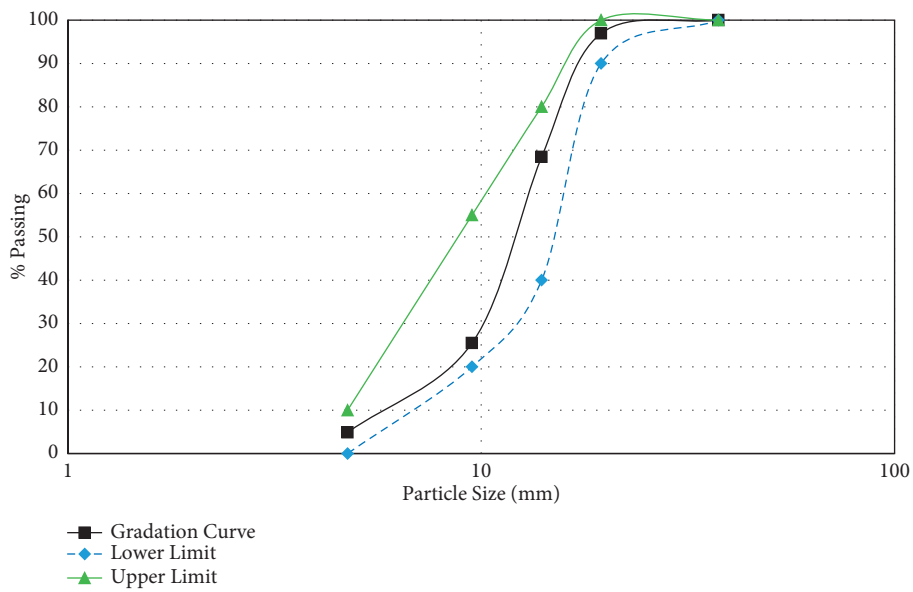

Figure 1: Grading curve of coarse aggregates (CAs).

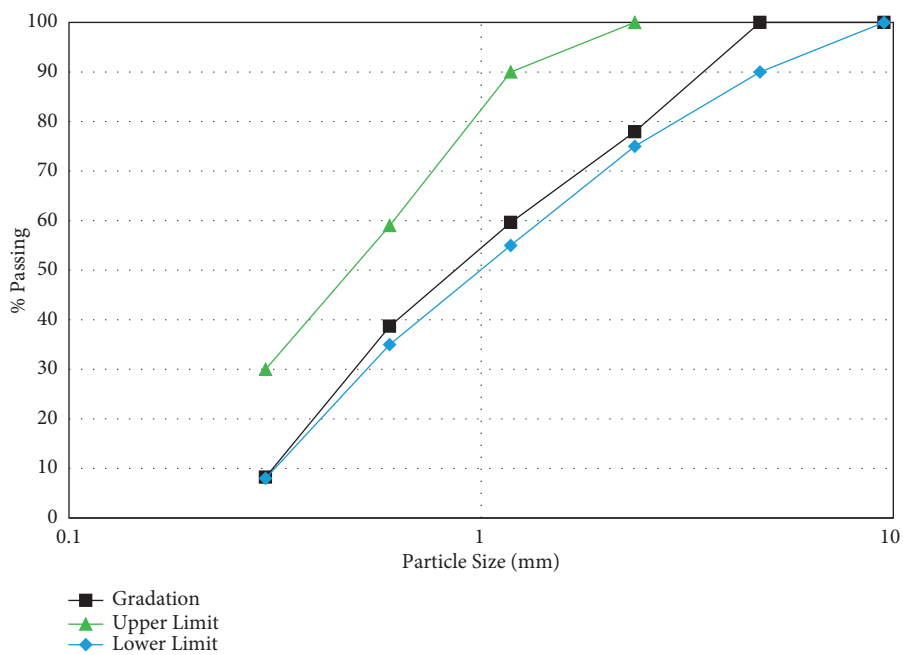

Figure 2: Grading curve of fine aggregates (FAs).

in the concrete. A related research study was carried out by Kurama and Kaya [57] and Adesanya and Raheem [58].

3.2. Density of Concrete. Concrete density using different percentages of WSA and RHA as TCM determined after 28 curing days is presented in Figure 5. However, density of concrete recorded by 2374, 2342, 2300, and 2288 kg per m^3 at 5% (2.5% WSA+2.5%RHA), 10% (5% WSA+5%RHA), 15% (7.5% WSA+7.5%RHA), and 20% (10% WSA+10%RHA) is lower when compared with control mix. It can be seen that the density of concrete has plummeted as the dosages of WSA and RHA rise in the mixture. This reduction in density is due to the fact that the specific gravity of WSA (2.21) and RHA (2.23) is lower than that of cement (3.13). This statement was specified in [59] where the density of concrete declined with the increase of dosages of millet husk ash in the mixture at 28 curing days. This comparable investigation has been performed by Raza et al. [60].

3.3. Water Absorption of Concrete. The test performed on hardened concrete mixture by incorporating WSA and RHA as ternary cementitious material at 28 curing days is

Table 3: Mix proportion of mixture.

Mix ID	Mix ratio	Binder (%)			Aggregates (%)		Water/cement ratio (%)
		PC	WSA	RHA	FA	CA	
TCM0	1 : 2 : 4	100	0	0	100	100	0.50
TCM5	1 : 2 : 4	95	2.5	2.5	100	100	0.50
TCM10	1 : 2 : 4	90	5	5	100	100	0.50
TCM15	1 : 2 : 4	85	7.5	7.5	100	100	0.50
TCM20	1 : 2 : 4	80	10	10	100	100	0.50

(a) (b) (c) (d)

Figure 3: Continued.

(e) (f)

Figure 3: Experimental setup of concrete testing. (a) Slump test. (b) Water absorption test setup. (c) Water curing tank. (d) Compressive strength test. (e) Flexural strength test. (f) Splitting tensile strength test.

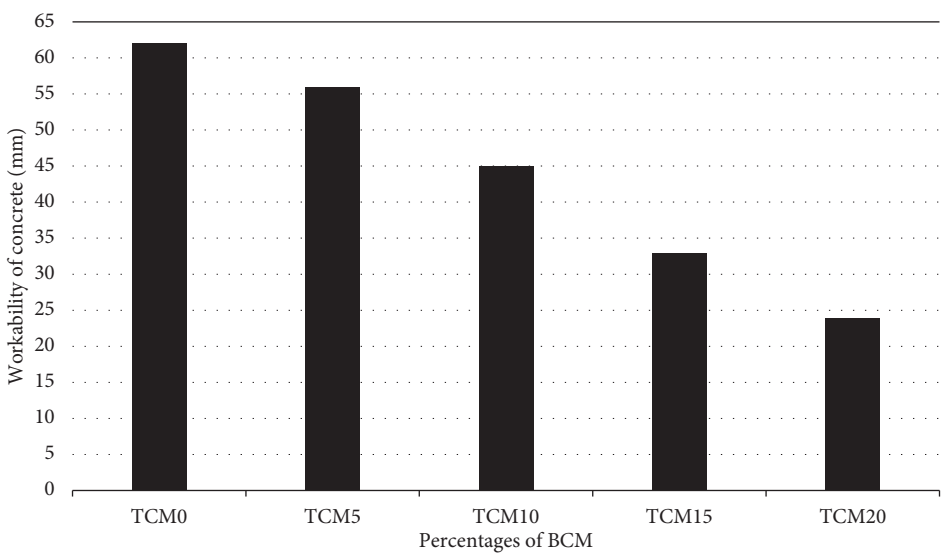

Figure 4: Slump test of green concrete.

indicated in Figure 6. The maximum water absorption is noted as 3.75% at control mix, and the minimum value is noted as 1.88% at 10% WSA and 10% RHA as TCM in concrete mix at 28 days. The outcome is that the water absorption of hardened concrete is reduced with the addition of WSA and RHA together in the concrete mixture. This decline in water absorption is due to the size or finest particles of RHA and WSA compared to PC as shown in Table 1 which seals the remaining micropores left by other constituents of concrete while the percentages of RHA and WSA increase in the concrete mixture. This investigation work is related to Auta et al.'s study [61] where water absorption declined with the increase in incorporation of millet husk ash in concrete. This comparable investigation has been performed by Dharani et al. [62] and Raza et al. [60].

3.4. Compressive Strength of Concrete. The test performed on cubical specimen made with concrete by addition of WSA and RHA as TCM is indicated in Figure 7. The highest compressive strength calculated is 25 MPa and 30.42 MPa at 5% of WSA along with 5% of RHA, and the smallest strength is recorded as 19.2 MPa and 23.3 MPa while utilizing 10% of

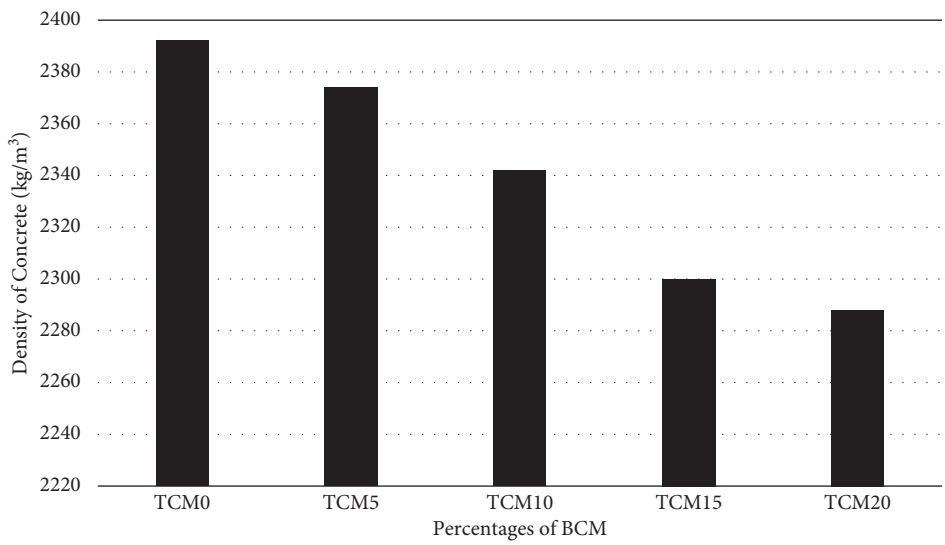

Figure 5: Density of concrete.

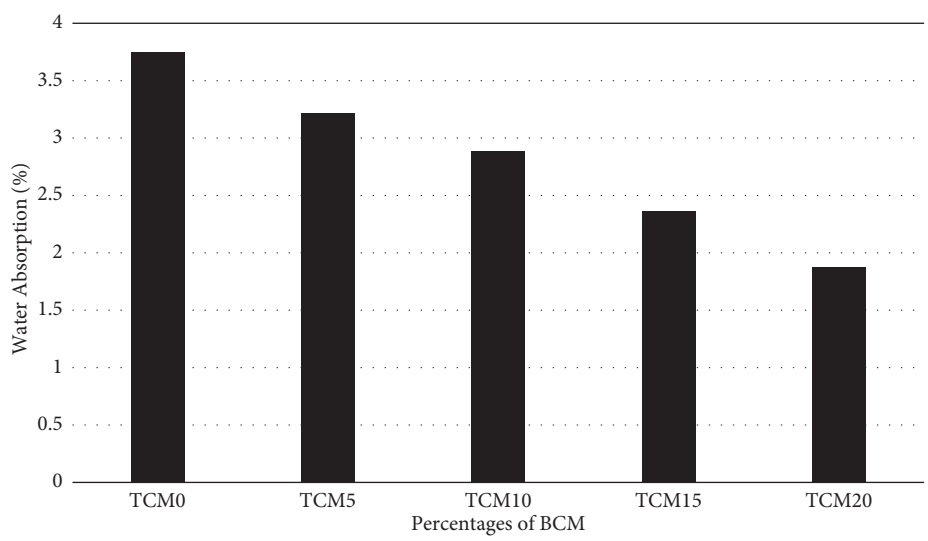

Figure 6: Water absorption of concrete.

WSA along with 10% of RHA as BCM in concrete after 7 and 28 days consistently. The test results pointed out increment in hardened concrete strength while using up to 5% of WSA and 5% of RHA together because of fineness of RHA and WSA particles that occupied micropores left by other concrete ingredients while using concrete up to 5% of WSA and 5% of RHA together. Anwar et al. [63] corroborated this report following their assessment of the effect of ternary binder blends on the concrete microstructure. This starts declining owing to dilution influence of WSA and RHA on cement which reduces the pozzolanic reactions among the concrete ingredients. The result showed that a ternary blend of cementitious materials exhibits superior performance of concrete. In related study, the use of a combination of high calcium fly ash (HCFA), palm oil fuel ash (POFA), and rice husk ash (RHA) proved highly effective for cementitious application in soil [64]. Also, a similar result was obtained in [65] where strength improved by using 7.5% of fly ash along with 7.5% of silica fume in the mixture after 7 and 28 days, respectively. In [66], the strength of concrete is improved while using 5% RHA and 5% of SCBA in the mix after 7, 28, 56, and 90 days, respectively.

3.5. Splitting Tensile Strength. The test performed on cylinder specimen made of concrete with the addition of WSA and RHA as TCM is indicated in Figure 8. The highest splitting tensile strength calculated is 2.74 MPa and 3.52 MPa at 5% of WSA along with 5% of RHA, and the smallest strength is recorded as 2.05 MPa and 2.92 MPa while utilizing 10% of WSA along with 10% of RHA as TCM in concrete after 7 and 28 days consistently. The test results pointed out increment in hardened concrete strength by using up to 5% of WSA and 5% of RHA together because of their larger specific surface areas

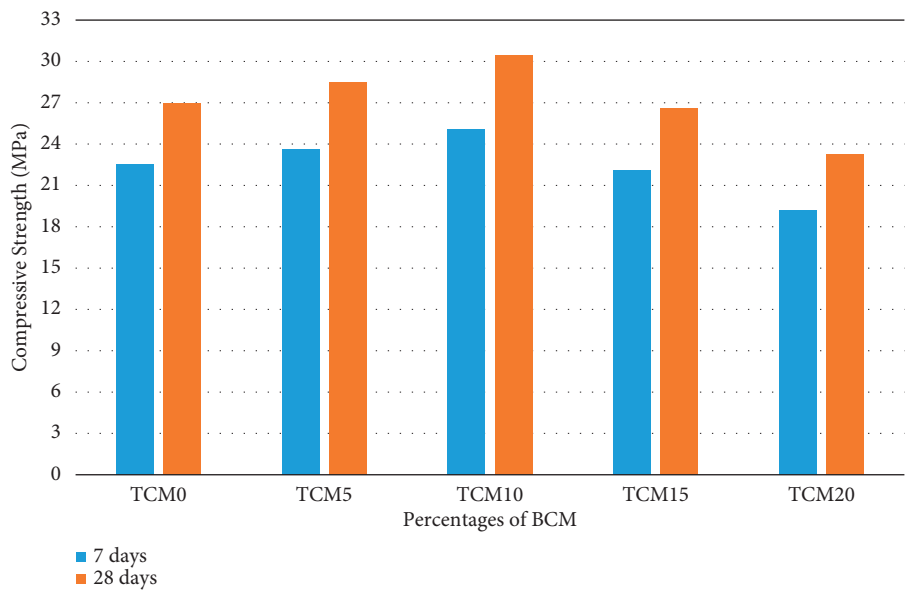

Figure 7: Compressive strength of concrete.

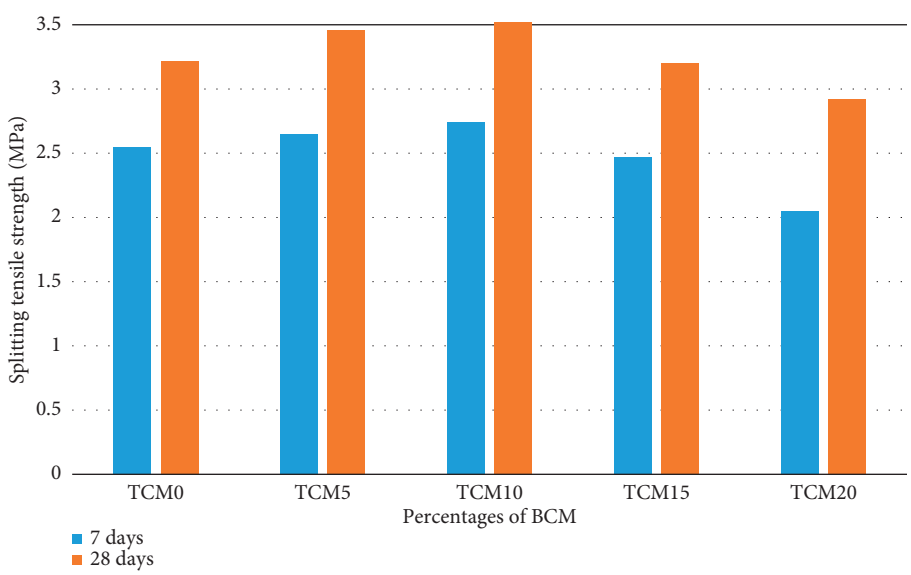

Figure 8: Splitting tensile strength of concrete.

as compared to cement, and with the further addition of WSA and RHA in the mixture, it starts declining which may be associated with low calcium hydroxide in mixture as dilution impact of WSA and RHA. A similar aspect was attained in [67] where strength improved by using 10–15% of RHA and oil palm shell ash in the mixture after 28 days, respectively. An analogous trend was shown by Kumar et al. [68] and Umamaheswari and Vigneshkumar [69]. A correlation was found between splitting tensile strength and compressive strength, as shown in Figure 9. At all ages, there is a good relationship between splitting tensile strength and compressive strength, as shown in Figure 9. The equations in Figure 9 can be used to estimate compressive strength or splitting tensile strength when one of these properties is known.

3.6. Flexural Strength of Concrete. This test is performed on the beam specimens made of concrete with the addition of WSA and RHA as TCM as indicated in Figure 10. The highest flexural strength calculated is 4.05 MPa and 4.86 MPa at 10% of TCM (5% of WSA along with 5% of RHA), and the smallest strength is recorded as 3.40 MPa and 4.0 MPa while utilizing 20% of TCM (10% of WSA along with 10% of RHA) in concrete after 7 and 28 days consistently. The test results showed increased flexural strength by using up to 10% of TCM (5% of WSA and 5% of RHA), while with the further introduction of TCM in mixture, the strength tends to decrease. This observation may be the effect of TCM dilution on PC, which leads to the fact that the transition zone of the interface is not improved and,

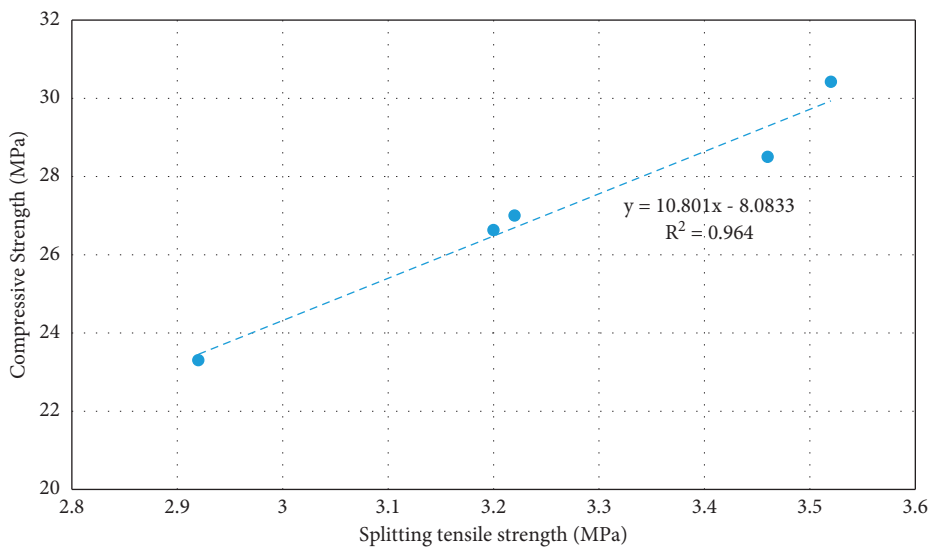

Figure 9: Correlations between compressive strength and splitting tensile strength at 28 days.

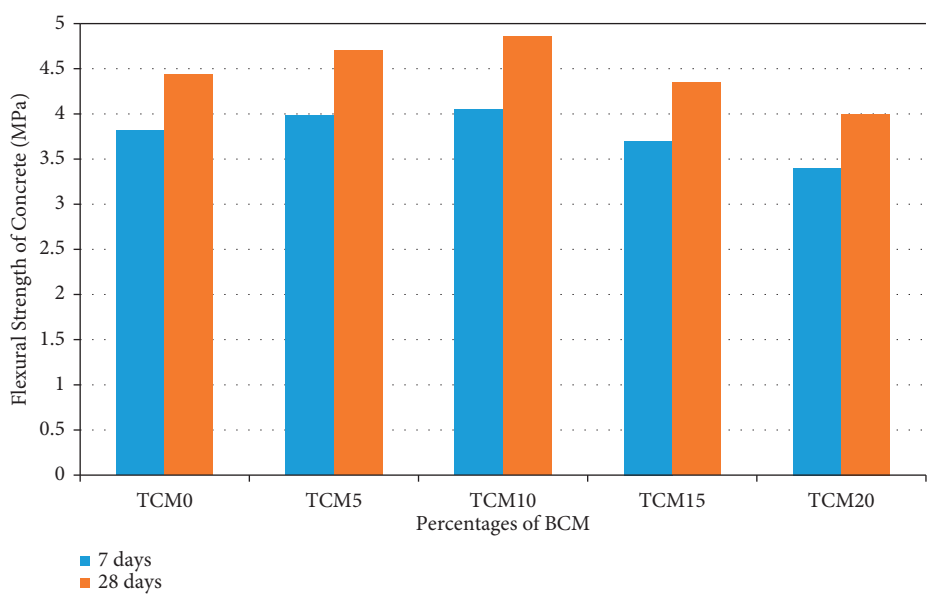

Figure 10: Flexural strength of concrete.

therefore, affects the long-term flexural strength, and with the further addition of WSA and RHA in the mixture, it starts declining which may be associated with low calcium hydroxide in mixture owing to dilution effect of WSA and RHA. A similar trend was presented in [68] where strength improved by using 10% of coconut shell ash and egg shell powder in the mixture after 28 days. A similar type of trend was presented by Umamaheswari and Vigneshkumar [69] and Mo et al. [70]. Figure 11 shows the relationship between flexural strength and compressive strength of concrete mixture. There is a strong linear relationship between these features, as can be seen in the graph. The flexural and compressive strengths, on the other hand, have a more linear relationship. Nonetheless, the two formulations in Figure 11 will be helpful in determining the properties of TCM-containing concrete mixtures at 28 days.

3.7. Drying Shrinkage. In order to control cracks, it is essential to understand the features of concrete shrinkage and its beginning point in the construction of structures. Figure 12 describes outcomes of RHA and WSA as ternary cementitious material on the drying shrinkage of the mixture at 5, 10, 15, 20, 30, 60, and 90 days, respectively. The outcome of the research study is that the drying shrinkage of concrete is decreased with rising content of RHA and WSA as TCM in concrete. This decrement in drying shrinkage of PC pastes may be due to few causes like PC dilution by RHA and WSA, a lesser quantity of PC generating a smaller amount of shrinkage, the pozzolanic reaction of RHA and WSA with calcium hydrates (CH) produced by PC, and increase in capillary tension [70–72]. This observation is in agreement with [73–77] that the drying shrinkage is decreased with PC replacement by RHA with its increase in

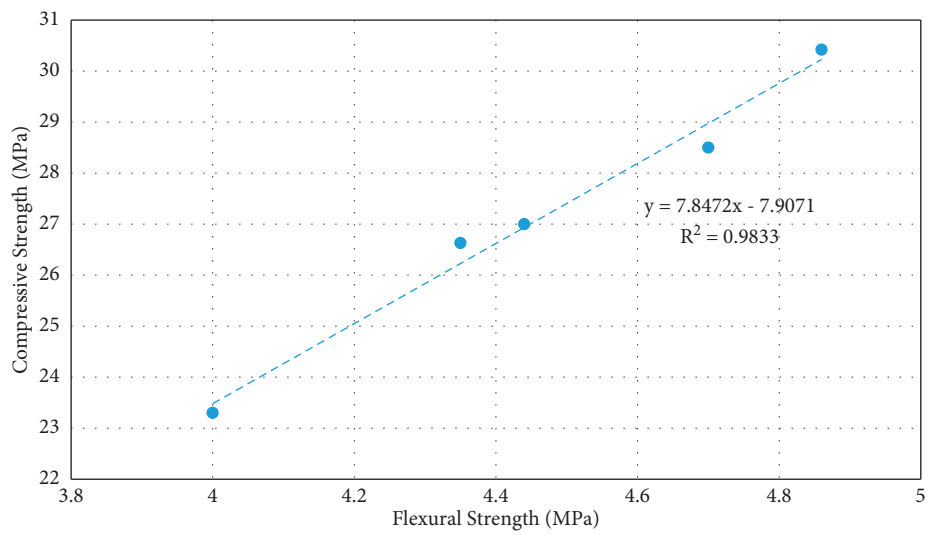

Figure 11: Correlations between compressive strength and flexural strength at 28 days.

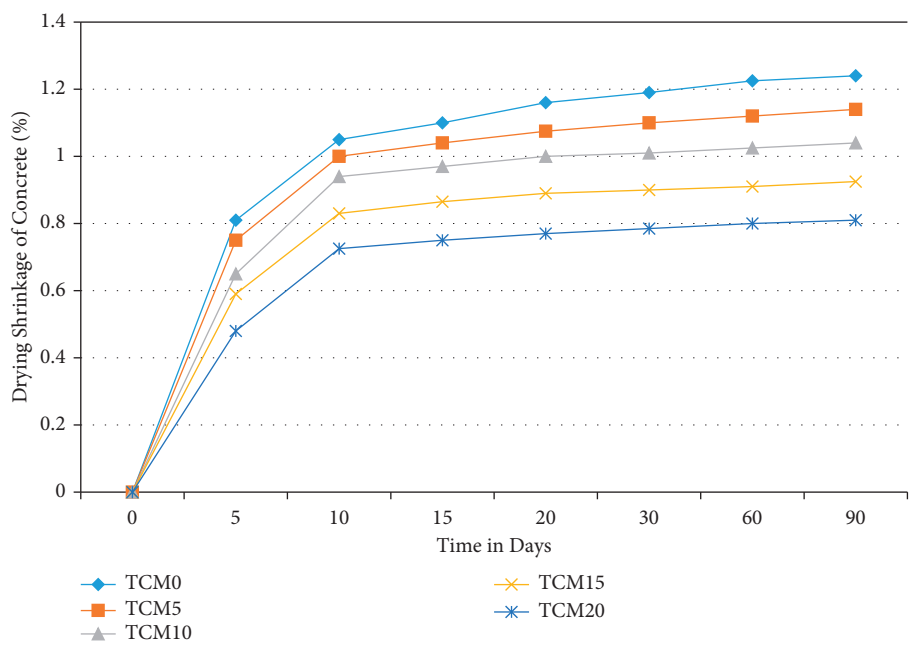

Figure 12: Drying shrinkage of concrete.

concrete. This decrease in drying shrinkage can be due to the RHA and WSA's finer particles, which act as a filler and plug the pores, slowing the rate of shrinkage in the concrete. On the other hand, it may be due to the size of pore and grain size improvement procedures which build up the mechanical interlocking in the transition zone. Therefore, when shrinkage is a concern, the utilization of RHA and WSA can be a part of the strategy to mitigate its effect. According to Lai et al. [78], shrinkage decreases as the amount of cement replacement material (such as ash) increases. The reduction in shrinkage is due to the concrete's wet packing density. A similar kind of research work was conducted in [79] where the drying shrinkage of concrete lowered due to replacement of PC with fly ash, WSA, and maize cob ash as a tertiary cementitious material in concrete.

4. Conclusions

This study determined the mechanical properties of concrete incorporating rice husk ash and wheat straw ash as a ternary cementitious material. The categories of properties explored covered the workability and hardened concrete properties. The following conclusions were drawn from the study:

(i) The slump value for all mixes reduced with increasing content of the added cementitious

materials; thus, the control mix had a slump of 62 mm, and the lowest slump was 24 mm for 10% of WSA and 10% of RHA. Similarly, the density and water absorption measured in the control mix exceeded the modified concrete samples after the 28-day curing regime.

(ii) Generally, for all mixes, the compressive strength, splitting tensile strength, and flexural strength characteristics increased with increasing curing regimes. The study showed that the strength development in the modified concrete exceeded that of the control mix. A mix with 10% supplementary cementitious material yielded the highest strength. However, the strength slightly drops as SCM content goes beyond 10%.

(iii) The drying shrinkage of the concrete samples reduced as the replacement of PC with RHA and WSA increased. Overall, a concrete mix having 5% RHA and 5% WSA contents exhibited the best performance in terms of fresh and hardened state properties.

Data Availability

The datasets generated during the current study are available from the corresponding author upon request.

Conflicts of Interest

The authors declare that they have no conflict of interest.

References

[1] A. Manimaran, M. Somasundaram, and P. T. Ravichandran, "Experimental study on partial replacement of coarse aggregate by bamboo and fine aggregate by quarry dust in concrete," *International Journal of Civil Engineering & Technology*, vol. 8, no. 8, pp. 1019–1027, 2017.

[2] S. Ghorbani, I. Taji, J. De Brito et al., "Mechanical and durability behaviour of concrete with granite waste dust as partial cement replacement under adverse exposure conditions," *Construction and Building Materials*, vol. 194, pp. 143–152, 2019.

[3] P. A. Shirule, A. Rahman, and R. D. Gupta, "Partial replacement of cement with marble dust powder," *International Journal of Advanced Engineering Research and Studies*, vol. 1, no. 3, p. 2249, 2012.

[4] J. Alex, J. Dhanalakshmi, and B. Ambedkar, "Experimental investigation on rice husk ash as cement replacement on concrete production," *Construction and Building Materials*, vol. 127, pp. 353–362, 2016.

[5] E. Aprianti, P. Shafigh, S. Bahri, and J. N. Farahani, "Supplementary cementitious materials origin from agricultural wastes - a review," *Construction and Building Materials*, vol. 74, pp. 176–187, 2015.

[6] R. Khan, A. Jabbar, I. Ahmad, W. Khan, and A Khan, *Repair*, Taylor & Francis, Oxfordshire UK, 2006.

[7] P. Broomfield, "Corrosion of steel in concrete, understanding, investigation, and repair," 2006.

[8] R. R. Hussain and T. Ishida, "Critical carbonation depth for initiation of steel corrosion in fully carbonated concrete and development of electrochemical carbonation induced corrosion model," *International Journal of electrochemical science*, vol. 4, no. 8, pp. 1178–1195, 2009.

[9] C. I. Federation, *CIF Cement Industry Environment Report*, Cement Industry Federation, Forrest, Australia, 2003.

[10] S. Assefa and M. Dessalegn, "Production of lightweight concrete using corncob ash as replacement of cement in concrete," *American Journal of Civil Engineering*, vol. 7, no. 1, pp. 17–20, 2019.

[11] S. A. Mangi, N. Jamaluddin, M. H. Wan Ibrahim, M. Noridah, and S. Sohu, "Utilization of sawdust ash as cement replacement for the concrete production: a review," *Engineering Science and Technology International Research Journal*, vol. 1, no. 3, pp. 11–15, 2017.

[12] S. A. Mangi, M. W. Ibrahim, N. Jamaluddin, M. F. Arshad, and P. J. Ramadhansyah, "Effects of ground coal bottom ash on the properties of concrete," *Journal of Engineering Science & Technology*, vol. 14, no. 1, pp. 338–350, 2019.

[13] A. Mangi, W. Ibrahim, N. Jamaluddin, S. Arshad, and S. Shahidan, "Effects of grinding process on the properties of the coal bottom ash and cement paste," *Journal of Engineering and Technological Sciences*, vol. 51, no. 1, pp. 1–13, 2019.

[14] N. Kad and M. Vinod, "Review research paper on influence of rice husk ash on the properties of concrete," *International Journal of Research*, vol. 2, no. 5, pp. 873–877, 2015.

[15] M. Anwar, T. Miyagawa, and M. Gaweesh, "Using rice husk ash as a cement replacement material in concrete," in *Waste Management Series*vol. 1, , pp. 671–684, Elsevier, 2000.

[16] S. D. Nagrale, H. Hajare, and P. R. Modak, "Utilization of rice husk ash," *Carbon*, vol. 2, no. 6, p. 42, 2012.

[17] Ologunagba, A. S. Daramola, and Daramola, "Feasibility of using rice husk ash as partial replacement for concrete," *International Journal of Engineering Trends and Technology*, vol. 30, no. 5, pp. 267–269, 2015.

[18] A. N. Givi, S. A. Rashid, F. N. A. Aziz, and M. A. M. Salleh, "Contribution of rice husk ash to the properties of mortar and concrete: a review," *Journal of American science*, vol. 6, no. 3, pp. 157–165, 2010.

[19] H. B. Mahmud, N. A. A. Hamid, and K. Y. Chin, "November. Production of high strength concrete incorporating an agricultural waste-rice husk ash," in *Proceedings of the 2010 2nd International Conference on Chemical, Biological and Environmental Engineering*, pp. 106–109, IEEE, Cairo, Egypt, November 2010.

[20] Le, K. Siewert, and Ludwig, "Alkali silica reaction in mortar formulated from self-compacting high performance concrete containing rice husk ash," *Construction and Building Materials*, vol. 88, pp. 10–19, 2015.

[21] M. H. Zhang, R. Lastra, and V. M. Malhotra, "Rice-husk ash paste and concrete: some aspects of hydration and the microstructure of the interfacial zone between the aggregate and paste," *Cement and Concrete Research*, vol. 26, no. 6, pp. 963–977, 1996.

[22] N. P. Hasparyk, P. J. Monteiro, and H. Carasek, "Effect of silica fume and rice husk ash on alkali-silica reaction," *Materials Journal*, vol. 97, no. 4, pp. 486–492, 2000.

[23] K. Sakr, "Effects of silica fume and rice husk ash on the properties of heavy weight concrete," *Journal of Materials in Civil Engineering*, vol. 18, no. 3, pp. 367–376, 2006.

[24] V. Sata, C. Jaturapitakkul, and K. Kiattikomol, "Influence of pozzolan from various by-product materials on mechanical properties of high-strength concrete," *Construction and Building Materials*, vol. 21, no. 7, pp. 1589–1598, 2007.

[25] M. M. Tashima, C. A. Da Silva, J. L. Akasaki, and M. Beniti, "The possibility OF adding rice huskash (RHA)," vol. 2, p. 778, 2004 PRO 40: International RILEM Conference on the Use of Recycled Materials in Buildings and Structures.

[26] A. Antiohos, E. Tapali, M. Zervaki, J. Sousa-Coutinho, S. Tsimas, and V. G. Papadakis, "Low embodied energy cement containing untreated RHA: a strength development and durability study," *Construction and Building Materials*, vol. 49, pp. 455–463, 2013.

[27] L. Prasittisopin and D. Trejo, "Hydration and phase formation of blended cementitious systems incorporating chemically transformed rice husk ash," *Cement and Concrete Composites*, vol. 59, pp. 100–106, 2015.

[28] M. F. M. Zain, M. N. Islam, F. Mahmud, and M. Jamil, "Production of rice husk ash for use in concrete as a supplementary cementitious material," *Construction and Building Materials*, vol. 25, no. 2, pp. 798–805, 2011.

[29] R.-S. Bie, X.-F. Song, Q.-Q. Liu, X.-Y. Ji, and P. Chen, "Studies on effects of burning conditions and rice husk ash (RHA) blending amount on the mechanical behavior of cement," *Cement and Concrete Composites*, vol. 55, pp. 162–168, 2015.

[30] M. Akhter, "Experimental study on effect of wood ash on strength of concrete," *International Research Journal of Engineering and Technology*, vol. 4, no. 7, pp. 1252–1254, 2017.

[31] A. Buregyeya, S. Nwaubani, W. Schmidt, A. G. Kerali, and U. Bagampadde, "Pozzolanic and hydration properties of kamafugites and carbonatitic lavas as supplementary cementitious materials in Portland cement," *African Journal of Science, Technology, Innovation and Development*, vol. 10, no. 7, pp. 845–859, 2018.

[32] A. M. Nevile and J. J. Brooks, *Concrete Technology*, Longman Scientific and Technical, 1990.

[33] S. Rukzon, P. Chindaprasirt, and R. Mahachai, "Effect of grinding on chemical and physical properties of rice husk ash," *International Journal of Minerals, Metallurgy and Materials*, vol. 16, no. 2, pp. 242–247, 2009.

[34] Fao World Food Situation: http://www.fao.org/worldfoodsituation/csdb/en/.

[35] X. Pan and Y. Sano, "Fractionation of wheat straw by atmospheric acetic acid process," *Bioresource Technology*, vol. 96, no. 11, pp. 1256–1263, 2005.

[36] B. Gadde, C. Menke, and R. Wassmann, "Rice straw as a renewable energy source in India, Thailand, and the Philippines: overall potential and limitations for energy contribution and greenhouse gas mitigation," *Biomass and Bioenergy*, vol. 33, no. 11, pp. 1532–1546, 2009.

[37] K. L. Kadam, L. H. Forrest, and W. A. Jacobson, "Rice straw as a lignocellulosic resource: collection, processing, transportation, and environmental aspects," *Biomass and Bioenergy*, vol. 18, no. 5, pp. 369–389, 2000.

[38] H. Kausar, M. Sariah, H. Mohd Saud, M. Zahangir Alam, and M. Razi Ismail, "Development of compatible lignocellulolytic fungal consortium for rapid composting of rice straw," *International Biodeterioration & Biodegradation*, vol. 64, no. 7, pp. 594–600, 2010.

[39] A. John, *Alternatives to Open-Field Burning on Paddy Farms*, Vol. 18, Agricultural and Food Policy Studies Institute: Serdang, , Malaysia, 2013.

[40] W. Bank, "Decision makers' guide to municipal solid waste incineration," 2017, http://web.mit.edu/urbanupgrading/urbanenvironment/resources/references/pdfs/DecisionMakers.pdf.

[41] C. H. K. Lam, A. W. M. Ip, J. P. Barford, and G. McKay, "Use of incineration msw ash: a review," *Sustainability*, vol. 2, no. 7, pp. 1943–1968, 2010.

[42] O. Eriksson, M. Carlsson Reich, B. Frostell et al., "Municipal solid waste management from a systems perspective," *Journal of Cleaner Production*, vol. 13, no. 3, pp. 241–252, 2005.

[43] Y. B. Yang, V. N. Sharifi, and J. Swithenbank, "Effect of air flow rate and fuel moisture on the burning behaviours of biomass and simulated municipal solid wastes in packed beds," *Fuel*, vol. 83, no. 11-12, pp. 1553–1562, 2004.

[44] A. Goyal, H. Kunio, H. Ogata, M. Garg, A. M. Anwar, and M. Ashraf, "Synergic effect of wheat straw ash and rice-husk ash on strength properties of mortar," *Journal of Applied Sciences*, vol. 7, no. 21, pp. 3256–3261, 2007.

[45] C. Astm, *136. Standard Test Method for Sieve Analysis of fine and Coarseaggregates*, American Society for Testing Materials, Pennsylvania, USA, 2005.

[46] Astm C127, *Standard Method of Test for Specific Gravity and Water Absorption of Coarse Aggregate*, American Society for Testing Materials, Pennsylvania, USA, 1993.

[47] Astm C128, *Standard Method of Test for Specific Gravity and Water Absorption of Fine Aggregate*, American Society for Testing Materials, Pennsylvania, USA, 1993.

[48] C. Astm, "29/C 29M,". Standard test," *Method for Bulk Density ("Unit Weight")and Voids in Aggregate*, Vol. 4, Annual Book of ASTM Standards, , Pennsylvania, USA, 1997.

[49] Bs En 12350-2, *Testing Fresh concrete, Part 2: Slump-Test*, BSI, London, UK, 2009.

[50] Bs 1881, *Part 122, "Method, for Determination of Water Absorption"*, British Standards Institution, London UK, 1983.

[51] Bs En 12390–7, *Density of Hardened concrete:2000*, Part 7, p. 389, British Standards Institution, London, UK, British Standards Institution, 2000.

[52] Bs En 12390-3, *Testing Harden concrete. Compressive Strength of Test Specimens*, BSI, London UK, 2009.

[53] Bs En 12390-6, *Testing Hardened concrete. Tensile Splitting Strength of Test Specimens*, BSI, London UK, 2009.

[54] B. S. En 12390-5, *Testing Hardened concrete. Flexural Strength of Test Specimens*, BSI, London UK, 2009.

[55] Bs Iso 1920-8, *Determination of Drying Shrinkage of concrete for Samples Prepared in the Field or in the Laboratory*, ISO, Geneva, Switzerland, 2009.

[56] N. M. Al-Akhras and B. A. Abu-Alfoul, "Effect of wheat straw ash on mechanical properties of autoclaved mortar," *Cement and Concrete Research*, vol. 32, no. 6, pp. 859–863, 2002.

[57] D. A. Adesanya and A. A. Raheem, "A study of the workability and compressive strength characteristics of corn cob ash blended cement concrete," *Construction and Building Materials*, vol. 23, no. 1, pp. 311–317, 2009.

[58] H. Kurama and M. Kaya, "Usage of coal combustion bottom ash in concrete mixture," *Construction and Building Materials*, vol. 22, no. 9, pp. 1922–1928, 2008.

[59] J. R. Ajayi, B. O. Rasheed, and O. F. Mojirade, "Exploratory assessment of strength characteristics of millet husk ash (MHA) blended cement laterized concrete," *Advances in Applied Science Research*, vol. 4, no. 1, pp. 452–457, 2013.

[60] M. S. Raza, R. A. I. Kunal, D. Kumar, and A. L. I. Mutahar, "Experimental study of physical, fresh-state and strength parameters of concrete incorporating wood waste ash as a cementitious material," *Journal of Materials and Engineering Structures «JMES»*, vol. 7, no. 2, pp. 267–276, 2020.

[61] S. M. Auta, A. J. Shiwua, and T. Y. Tsado, "Compressive strength of concrete with millet husk ash (MHA) as a partial

replacement for cement," *Magazine of Civil Engineering*, vol. 59, no. 7, pp. 74–79, 2015.

[62] D. Dharani and V. A. iravida Selvan, "Durability studies on concrete by using groundnut shell ash as mineral admixture," *International Journal for Innovative Research in Science & Technology*, vol. 3, no. 10, pp. 168–172, 2017.

[63] M. Anwar and D. A. Emarah, "Pore structure of concrete containing ternary cementitious blends," *Results in Materials*, vol. 1, Article ID 100019, 2019.

[64] H. M. Jafer, W. Atherton, M. Sadique, F. Ruddock, and E. Loffill, "Development of a new ternary blended cementitious binder produced from waste materials for use in soft soil stabilisation," *Journal of Cleaner Production*, vol. 172, pp. 516–528, 2018.

[65] A. Kumar, N. Bheel, I. Ahmed, S. H. Rizvi, R. Kumar, and A. A. Jhatial, "Effect of silica fume and fly ash as cementitious material on hardened properties and embodied carbon of roller compacted concrete," *Environmental Science and Pollution Research*, pp. 1–13, 2021.

[66] S. H. Channa, S. A. Mangi, N. Bheel, F. A. Soomro, and S. H. Khahro, "Short-term analysis on the combined use of sugarcane bagasse ash and rice husk ash as supplementary cementitious material in concrete production," *Environmental Science and Pollution Research*, pp. 1–10, 2021.

[67] S. Foong, R. Alengaram, W. Jumaat, and G. Mo, "Enhancement of the mechanical properties of lightweight oil palm shell concrete using rice husk ash and manufactured sand," *Journal of Zhejiang University - Science*, vol. 16, no. 1, pp. 59–69, 2015.

[68] R. R. Kumar, R. Mahendran, S. G. Nathan, D. Sathya, and K. Thamaraikannan, "An experimental study on concrete using coconut shell ash and egg shell powder," *South Asian Journal of Engineering and Technology*, vol. 3, no. 7, pp. 151–161, 2017.

[69] R. Umamaheswari and M. Vigneshkumar, "Experimental study on partial replacement of cement with coconut shell ash and silica fume in concrete," *Int Res J Eng Technol*, vol. 5, no. 7, pp. 2175–2179, 2018.

[70] K. H. Mo, F. A. Mohd Anor, U. J. Alengaram, M. Z. Jumaat, and K. J. Rao, "Properties of metakaolin-blended oil palm shell lightweight concrete," *European Journal of Environmental and Civil Engineering*, vol. 22, no. 7, pp. 852–868, 2018.

[71] J. J. Brooks and M. A. Megat Johari, "Effect of metakaolin on creep and shrinkage of concrete," *Cement and Concrete Composites*, vol. 23, no. 6, pp. 495–502, 2001.

[72] S. Wild, J. M. Khatib, and L. J. Roose, "Chemical shrinkage and autogenous shrinkage of Portland cement-metakaolin pastes," *Advances in Cement Research*, vol. 10, no. 3, pp. 109–119, 1998.

[73] J. M. Kinuthia, S. Wild, B. B. Sabir, and J. Bai, "Self-compensating autogenous shrinkage in Portland cement-metakaolin-fly ash pastes," *Advances in Cement Research*, vol. 12, no. 1, pp. 35–43, 2000.

[74] B. Chatveera and P. Lertwattanaruk, "Durability of conventional concretes containing black rice husk ash," *Journal of Environmental Management*, vol. 92, no. 1, pp. 59–66, 2011.

[75] G. A. Habeeb and M. M. Fayyadh, "Rice husk ash concrete: the effect of RHA average particle size on mechanical properties and drying shrinkage," *Australian Journal of Basic and Applied Sciences*, vol. 3, no. 3, pp. 1616–1622, 2009.

[76] S. I. Khassaf, A. T. Jasim, and F. K. Mahdi, "Investigation the properties of concrete containing rice husk ash to reduction the seepage in canals," *International Journal of Scientific Technology Research*, vol. 3, no. 4, pp. 348–354, 2014.

[77] Q. Mahmud, A. Malik, R. Kahar, E. Zain, and W. Raman, "Mechanical properties and durability of normal and water reduced high strength grade 60 concrete containing rice husk ash," *Journal of Advanced concrete Technology*, vol. 7, no. 1, pp. 21–30, 2009.

[78] M. H. Lai, S. A. M. Binhowimal, A. M. Griffith et al., "Shrinkage, cementitious paste volume, and wet packing density of concrete," *Structural Concrete*, 2020.

[79] N. Bheel, A. Awoyera, and D. Olalusi, "Engineering properties of concrete with a ternary blend of fly ash, wheat straw ash, and maize cob ash," *International Journal of Engineering Research in Africa*, vol. 54, pp. 43–55, 2021.

Hindawi
Advances in Civil Engineering
Volume 2021, Article ID 4976169, 22 pages
https://doi.org/10.1155/2021/4976169

Review Article

High-Volume Fly Ash-Based Cementitious Composites as Sustainable Materials: An Overview of Recent Advances

Sen Du,[1,2,3] **Qingxin Zhao**,[1,4] **and Xianming Shi**[3]

[1]*State Key Laboratory of Metastable Materials Science and Technology, Yanshan University, Qinhuangdao 066004, China*
[2]*Key Laboratory of Green Construction and Intelligent Maintenance for Civil Engineering of Hebei Province, Yanshan University, Qinhuangdao 066004, China*
[3]*Department of Civil & Environmental Engineering, Washington State University, Pullman, WA 99164-2910, USA*
[4]*Hebei Province Low-Carbon and Clean Building Heating Technology Innovation Center, Yanshan University, Qinhuangdao 066004, China*

Correspondence should be addressed to Xianming Shi; xianming.shi@wsu.edu

Received 21 July 2021; Revised 20 September 2021; Accepted 22 September 2021; Published 11 October 2021

Academic Editor: Adewumi Babafemi

High-volume fly ash (HVFA) cementitious composites (paste, grout, mortar, and concrete) have been widely investigated as a class of sustainable materials due to their lower carbon footprint and often better life cycle performance than conventional Portland cement mixtures. Recent years have seen increased research in HVFA-based materials, and the potential of this type of mixtures in engineering applications has significantly improved. In this context, this work reviews the renewed knowledge of HVFA mixtures, focusing on the relevant papers published over the last decade. The effects of replacing cement with a HVFA binder on the fresh properties, mechanical properties, durability performance, and environmental impact of HVFA cementitious composites are explored. Measures that can compensate for the main drawbacks that limit the wider application of HVFA mixtures are discussed in detail. At last, we summarize the research needs and remaining challenges of HVFA cementitious composites.

1. Introduction

Fly ash, the main by-product of coal combustion in thermal power plants, is one of the most commonly used supplementary cementitious materials (SCMs) in concrete. The global annual generation of coal combustion products is approximately 1.1 billion metric tonnes, more than 85% of which is fly ash, resulting in about 935 metric tonnes of fly ash produced every year [1]. The estimated worldwide production of fly ash will rise over 50% by 2030 [2]; however, only about 35% of fly ash can be recycled or reutilized [3]. The considerable production and low utilization rate of fly ash could result in the material ending up in a landfill polluting soil and water due to the heavy metal elements it leaches [4]. Using fly ash in cementitious composites to partially replace cement is an effective way to solidify the potential hazardous elements in cementitious composites. It is also an economical approach to improving the engineering properties of the cementitious composite.

The history of the use of fly ash in concrete spans more than half a century. Fly ash was used in the late 1940s as a mineral admixture in mass concrete to reduce hydration heat and early-age cracking [5]. Since then, acting as a SCM, fly ash has been used widely in cementitious composites, including paste, grout, mortar, and concrete. Traditionally, the cement replacement ratio by fly ash in cementitious composites is typically limited to about 20% to 25% by the mass of binder. Reasons for this limitation include the variability of fly ash sources, negative effects on air entrainment, and reduced early-age strength of the mixtures [6]. At such a replacement level, fly ash could not only improve the workability and cost economy of cementitious composites but could also improve the resistance to sulfate attack, alkali-aggregate reactions, and thermal cracking [7].

Although fly ash is a valuable mineral admixture for concrete, its low utilization rate raises the interest to replace cement with a high volume of fly ash in cement-based materials [8]. In the 1980s, Malhotra proposed a novel use of fly ash in cement-based materials, i.e., further increasing the cement replacement level to more than 50%, through which high-volume fly ash (HVFA) mixtures can be generated [9]. This type of mixture is fabricated to contain more fly ash than cement by mass, usually with a water-to-cementitious material ratio (w/cm) less than 0.35 and an adjustable amount of high-range water reducing admixture (HRWRA) to obtain the desired workability. Since HVFA mixtures contain substantial quantities of industrial by-product, they feature both low production cost and reduced environmental carbon footprint [10, 11].

In the span of more than three decades, a growing number of studies have been devoted to investigate the fresh properties, mechanical properties, durability performance, and environmental impact of HVFA-based materials, including paste, grout, mortar, and concrete [12]. In addition, HVFA-based materials have been successfully applied in some conventional construction domains such as beams, pavements, and dams. Recently, increased research on the potential of these types of mixtures in emerging engineering applications has significantly improved. For example, HVFA mortar can be modified by admixing nanomaterials or other pozzolanic materials to improve the rheological behavior and structural build-up for successful implementation in 3-D printing [13, 14]. Some techniques in the field of novel concrete materials, such as self-healing concrete and ultra-high performance concrete, have also seen increasing application of HVFA binder in concrete. In this context, there is a need to synthesize the renewed knowledge with the latest information of HVFA mixtures as sustainable construction materials, especially regarding the fresh and hardened properties and environmental impact.

To develop a comprehensive overview of recent advances in HVFA mixtures, a thorough literature search was conducted with a focus on relevant publications over the last decade. The topics for keywords searched in the Google Scholar, Springer, ASCE, ICE, Taylor & Francis, and SAGE databases included fresh properties, mechanical properties, durability performance, life cycle assessment, and measures or treatments used to improve the application potential of HVFA-based materials. Through this approach, a total of about 147 publications were identified and included in this review by using the following criteria: relevance to the review topics, quality and credibility, observation of issues related to the application, and indication of future trends of HVFA mixtures.

This work firstly summarizes the fresh properties of HVFA cementitious composites. Then, we proceed to provide an overview of the mechanical properties, durability performance, and environmental impact of HVFA cementitious composites. Given that low early-age strengths are a main concern of HVFA mixtures, this review also discusses measures that can address this concern. Finally, the knowledge gaps related to the HVFA mixtures (based on the examined references) are identified to promote the proper use of this sustainable material in industry.

2. Fresh Properties

While HVFA cementitious composites exhibit very good potential in engineering applications, some practical issues related to construction processes remain. The main challenges are related to the workability and setting time of HVFA mixtures, as detailed in this section.

2.1. Workability. Generally, the slump value of concrete increases with the replacement level of cement by fly ash at low volume [15], as the spherical-shaped fly ash particles serve to reduce interparticle friction. The vast majority of fly ash particles feature a smooth surface and spherical shape, working as "ball-bearings" in mixtures, which can overcome the internal friction between grains and mitigate the agglomeration of flocs and fragmentation to release the trapped water [16]. The shear force between the fine aggregates can also be reduced by the ball-bearing effect of fly ash [17], as shown in Figure 1. As shown, cementitious mixtures with a low-volume fly ash replacement of cement feature reduced water demand and improved workability.

However, with a further increase of fly ash replacement of cement, a decrease of slump value may occur in HVFA mixtures [11, 15, 18–23]. Figure 2 summarizes the effect of the fly ash replacement ratio on the slump value of HVFA mixtures from relevant references. In general, replacing cement with fly ash in the range of 40% to 60% by mass provides the best workability of FA-based cementitious composites. In this range, the slump value of mixtures is usually increased by about 20–40 mm compared with ordinary Portland cement (OPC) mixtures that contain no fly ash. Beyond the optimum range, the slump will fall due to the higher surface area of fly ash [15]. Normally, cement particles feature a specific surface area of about 303–636 m^2/kg [19, 20, 22, 24], while most fly ash particles feature a higher specific surface area of 320–1521 m^2/kg [19, 22, 24]. An even lower workability of HVFA mixtures can be expected when ultrafine fly ash (with specific surface areas as high as 2510 m^2/kg) is incorporated [25], making less water available for mixing due to the higher water demand of fly ash particles [15].

2.2. Setting Time. It is well known that the setting time of concrete can be retarded by replacing cement with fly ash. HVFA mixtures require a longer initial setting time and final setting time relative to the equivalent mixtures containing no fly ash [26–34]. Moreover, higher retardation times are obtained for the concrete with higher fly ash replacement levels [20]. Figure 3 shows the box plot of the initial and final setting times of OPC and HVFA mixtures based on information from relevant studies. Generally, HVFA mixtures exhibit initial and final setting times that are 3 h to over 10 h longer than those of OPC mixtures without fly ash.

Normally, the concrete setting mainly depends on a variety of parameters including cement fineness, cement-to-water ratio (w/c), and dispersion/flocculation of the cement particles [35]. Figure 4 illustrates the concept of cement dilution and deflocculation in a 60% fly ash system. It is

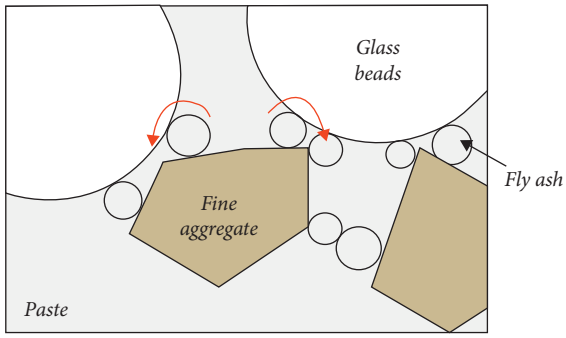

Figure 1: Ball-bearing effect of fly ash on the interaction between fine aggregates, reproduced from [17], with permission from Elsevier, 2021.

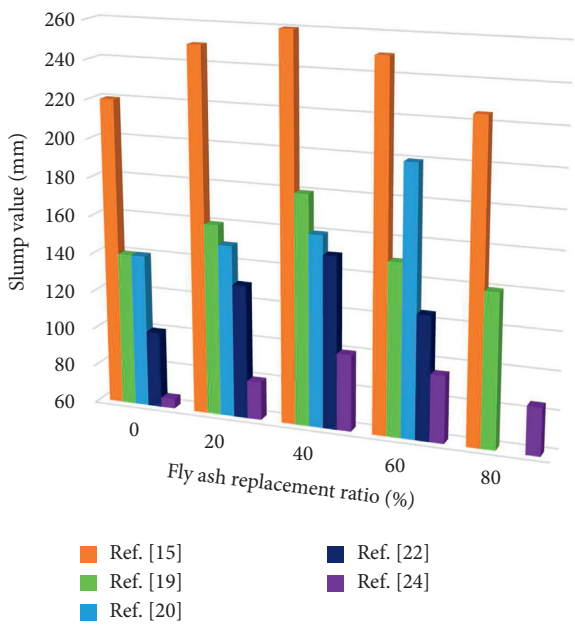

Figure 2: Slump value of FA-based cementitious composites as a function of the fly ash replacement ratio, based on data collected from relevant studies.

obvious that the presence of fly ash particles in HVFA mixture reduces the number of contacts between cement particles. A decrease in the flocculation level of cement particles can be achieved as the fly ash particles break up some of the flocculated cement 3-D network structure [31]. If the fly ash particles are removed (Figure 4(c)), the cement particles' spacing is significantly increased compared with the plain OPC system, resulting in the dilution of cement in a HVFA mixture. As a result, the reduced concentration of cement and the slow pozzolanic reaction in HVFA mixtures account for the observed retardation in the setting times [31].

HVFA mixtures containing Class F fly ash exhibit longer setting times than their counterparts containing Class C fly ash [33]. According to the newly released ASTM C618, Class F fly ash features low CaO content (18% maximum), while Class C fly ash features a higher CaO content (>18%). Class F fly ash generally exhibits pozzolanic properties, whereas Class C fly ash exhibits pozzolanic and cementitious

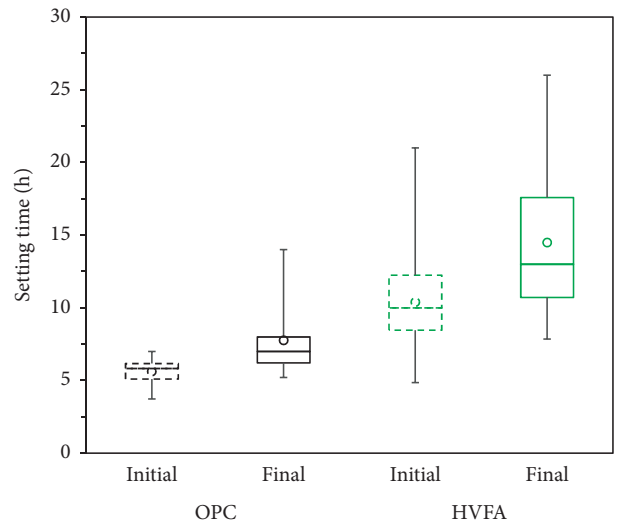

Figure 3: Comparison of setting times between OPC and HVFA mixtures, based on data collected from relevant studies.

properties simultaneously [31]. The pozzolanic reaction of Class F fly ash only occurs in the presence of calcium hydroxide [33]. As a result, Class F fly ash remains relatively inert during the first 24 h. In comparison, Class C fly ash can be quite reactive at early ages, resulting in a shorter retardation time than Class F fly ash [26].

3. Mechanical Properties

3.1. Compressive Strength. Compressive strength is a fundamental property of concrete, making it the most common mechanical property investigated in almost every study of HVFA mixtures. Given the same w/cm and curing regime, a reduction in the compressive strength at various curing ages (mainly ranging from 1 d to 365 d) is generally reported when replacing cement with HVFA [36–44]. The level of strength reduction increases with increasing fly ash content and decreases with increasing curing age.

Figure 5 depicts a typical example that contrasts the compressive strength development between HVFA and OPC concretes. For HVFA concrete, both the early-age and later-age compressive strength development trends can be explained by the delay in calcium-silicate-hydrate (C-S-H) formation because the pozzolanic reaction becomes the major reaction as the curing time increases [45]. At early ages (up to 14 d), the strength of HVFA concrete is mainly contributed by the hydration of cement [38]. As fewer cement particles are available for hydration due to the dilution effect, HVFA concrete has fewer hydration products and thus a lower compressive strength than its OPC counterpart. At later ages (beyond 28 d), the compressive strength gain of HVFA concrete mainly results from the pozzolanic reaction of fly ash [33, 42], because such reaction becomes fast enough to contribute to the strength development of HVFA mixtures [46, 47]. As a result, as the curing age increases, the difference in compressive strength between HVFA and OPC mixtures diminishes [20, 48]. At the curing time of 90 days, the compressive strength of HVFA mixtures may reach

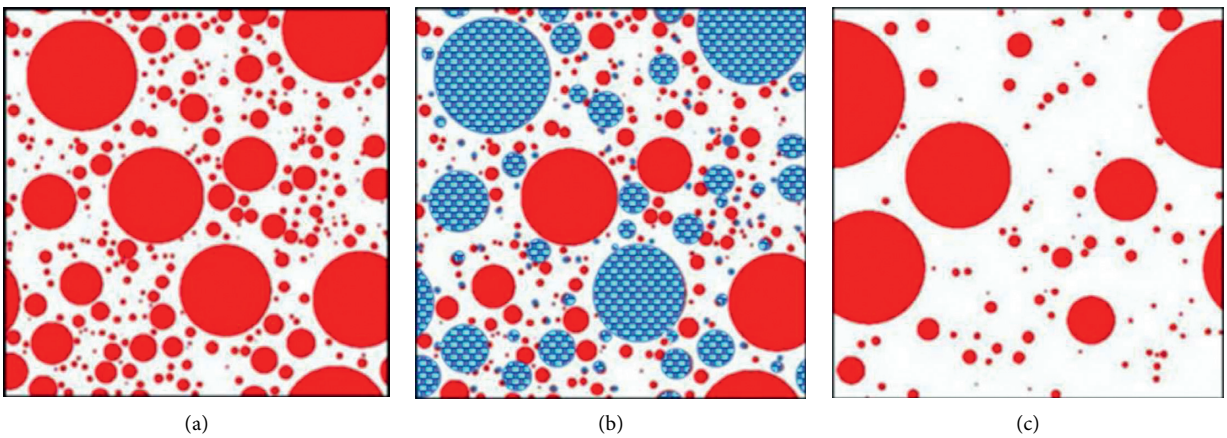

Figure 4: (a) Cement particles in OPC; (b) deflocculation; and (c) dilution of cement particles in HVFA system (red part, cement particles; blue patterned part, fly ash particles), reproduced from [31], with permission from Elsevier, 2021.

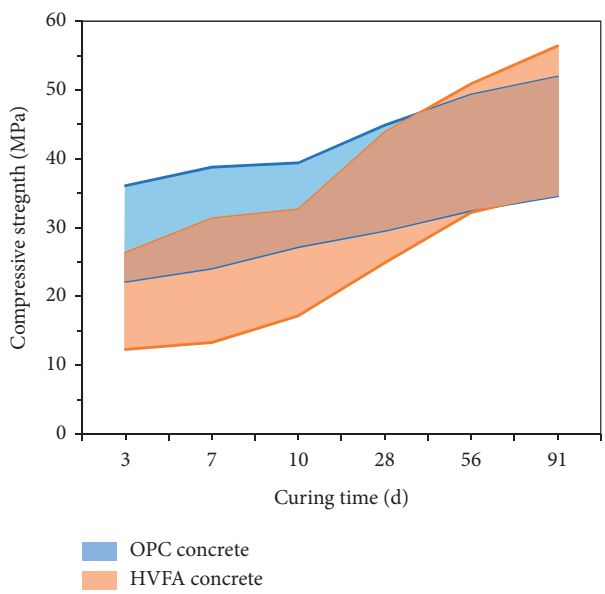

Figure 5: Temporal evolution of compressive strength of OPC and HVFA concretes, based on the data collected from reference [19].

comparable or even higher values than that of their OPC counterparts, as illustrated in Figure 5.

The enhanced compressive strength of HVFA mixtures observed at later ages is influenced by several factors, including the amorphous SiO_2 and Al_2O_3 contents, alkalinity of the amorphous phase, and the specific surface area of fly ash [33]. The physical, chemical, and mineralogical properties of fly ash tend to fluctuate from one source to another and sometimes within the same source. These changes in fly ash properties could have a profound impact on the mechanical properties of HVFA mixtures [49].

To date, there have been some limited studies aimed at correlating the properties or performance of HVFA mixtures with the characteristics of fly ash. For instance, isothermal calorimetry and rheological measurements have been used as screening tools to assess the early-age behavior of HVFA mixtures and as a means of quality control to evaluate and qualify fly ashes [49]. With the aid of soft computing techniques, the artificial neural network model [50] or support vector machine model [51] can be developed to predict the compressive strength of HVFA mixtures using relevant parameters such as the content and type of fly ash as model inputs. Mohammed et al. [52] demonstrated the use of neuro-swarm and neuro-imperialism models for predicting the compressive strength of fly ash concretes, using 9 mix design parameters as model inputs and 379 data points from published literature. They also demonstrated the use of soft computing techniques [53] to accurately predict the compressive strength of HVFA concrete based on curing time and several key mix design parameters, using experimental data of 450 tested HVFA concrete mixes.

A recent study proposed that the efficiency factor (k value) of fly ash is a function of its chemical composition and density based on the database of 440 HVFA mixtures obtained from the last 31 years. This factor was capable of reasonable prediction of the compressive strength of HVFA concretes made with 40–75% Class F fly ash and normal-weight aggregate [12]. The proposed k mainly considers the ratio of CaO to the sum of SiO_2 and Al_2O_3, abbreviated as $C/(S+A)$ ratio, and the fly ash fineness indirectly characterized by the fly ash density, as expressed in the following equation:

$$k = a \cdot \gamma_{FA} \cdot \frac{C}{S+A}, \tag{1}$$

where a is the coefficient of correction and γ_{FA} is the density of fly ash. The incorporation of density as a measure of fineness in the calculation of k value of fly ash led to a decrease in the results scattering of compressive strength of HVFA concretes [12, 54]. The predicted improvement was based on the fact that the density of fly ash can be determined more reliably than the Blaine specific surface area [12].

3.2. Flexural Strength. Flexural strength, a.k.a. modulus of rupture, is another important mechanical property to consider in studies of HVFA mixtures, especially for the fabrication of beams and concrete slabs. Similar to the

compressive strength, the flexural strength of HVFA mixtures is lower than that of OPC mixtures with the same w/cm at ages up to 1 year [20, 32, 48, 55–57]. Moreover, the flexural strength of HVFA mixtures increases with age and decreases with fly ash content. With sufficiently low w/cm, HVFA mixtures can achieve a 28 d flexural strength greater than the lower limit for pavement design, which is considered to be in the range of 4.0 to 4.5 MPa [57]. Furthermore, in later ages, HVFA mixtures may develop superior flexural strength to OPC mixtures, attributing to the pozzolanic reaction between fly ash and calcium hydroxide (CH) and resulting in the formation of additional hydration products. This process can decrease the porosity of the composite matrix and the transition zone [32].

Similar to OPC mixtures, there is a close relationship between flexural strength and compressive strength of HVFA mixtures, and various studies reported either a power fit [32] or a linear fit [20, 48]. This discrepancy may be ascribed to the fact that the w/cm and fly ash contents used differ from study to study. Figure 6 presents the overall trend between the compressive strength and flexural strength of HVFA mixtures from relevant references, which follows a power relationship. In other words, the flexural strength of HVFA mixtures increases as the compressive strength increases, but the slope of the increment gradually declines with the strength increase. The likely explanation is as follows. The compressive strength of HVFA mixtures is defined by both the pozzolanic reaction and the pore-filling effect of fly ash; however, the flexural strength of HVFA mixtures is primarily defined by the pozzolanic reaction [58].

3.3. Splitting Tensile Strength. In practice, splitting tensile strength is generally used to characterize the tensile strength of concrete since it is easily conducted as a conventional and conservative test [59]. For HVFA mixtures, many studies have reported a reduction in the splitting tensile strength with the inclusion of 50–70% fly ash as cement replacement [20, 48, 57, 59, 60]. Usually, the splitting tensile strength of HVFA concrete is slightly lower than the flexural strength as they correspond to 7–10% and 10–11% of the compressive strength, respectively [48].

The lower splitting tensile strength of HVFA mixtures likely results from the weaker bond between the cementitious matrix and the aggregates. The addition of fibers can increase the splitting tensile strength of HVFA concrete that contains 50% fly ash [57]. Particularly, longer fibers that have hooked ends are more effective in increasing the tensile strength than short and straight fibers [57].

The vibration method utilized during the production of HVFA mixtures is also reported to affect their splitting tensile strength. For instance, self-compacting HVFA concretes usually feature a higher splitting tensile strength than normally vibrated concretes or roller compacted concretes, even if with a lower compressive strength [36]. This might be attributed to the higher deformability and better homogeneity of self-compacting concrete, which result in an improved bond in the interfacial transition zone (ITZ) and thus an increased splitting tensile strength.

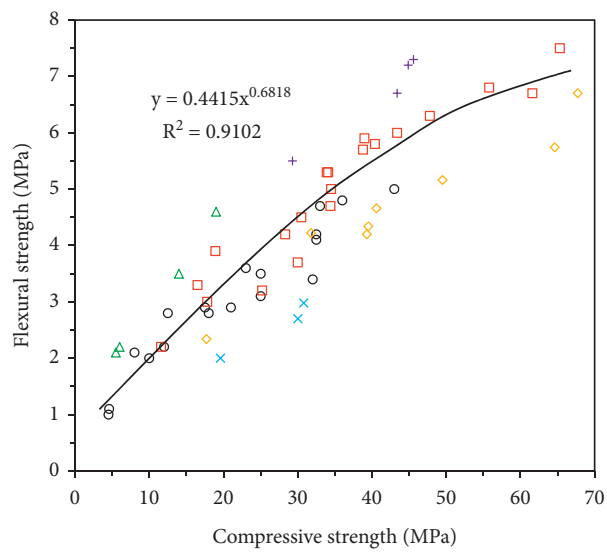

Figure 6: Relationship between compressive strength and flexural strength of HVFA mixtures, based on the data collected from relevant studies.

3.4. Modulus of Elasticity. Modulus of elasticity is used to characterize the stiffness of hardened concrete. Each component of concrete and its intrinsic modulus have a determinative effect on the elastic modulus of the concrete as a composite material. As such, HVFA mixtures that partially replace Portland cement with fly ash exhibit a different elastic modulus than their OPC counterparts [23]. In general, the modulus of elasticity of HVFA mixtures is lower than that of OPC mixtures with equivalent w/cm [20, 23, 32, 59, 61]. A further reduced modulus of elasticity can be expected with the increase of fly ash content in HVFA mixtures; however, at mature ages, HVFA mixtures can develop a comparable modulus of elasticity to their OPC counterparts [59]. It should be noted that the tensile modulus of HVFA mixtures usually exceeds the compressive modulus, and it is more rational to evaluate the tensile stress by using tensile modulus [59].

4. Durability Performance

In cement-based materials, the incorporation of HVFA binder reduces the cost of production and makes the composites more sustainable in terms of lower footprint and, in many cases, more durable. This section focuses on the durability performance of HVFA mixtures, including abrasion resistance, carbonation resistance, freezing-thawing resistance, deicing salt scaling resistance, shrinkage, transport properties, resistance to alkali-aggregate reactions, and resistance to chemical attack.

4.1. Abrasion Resistance. Abrasion resistance is an important property of concrete to consider, especially for applications such as pavement. Generally, the abrasion resistance of HVFA mixtures is lower than their OPC counterparts [18, 46, 62, 63]. During the abrasion test, the depth of wear or mass loss increases by increasing the fly ash content and

decreases by increasing the curing age of HVFA mixtures. The change in the abrasion resistance is mainly attributed to the change in compressive strength of HVFA mixtures [46, 62, 63]. Generally, the abrasion resistance of HVFA mixtures increases when increasing the compressive strength [18], and this is similar to OPC mixtures.

In addition to compressive strength, surface finishing and curing conditions have been reported to strongly influence the surface abrasion resistance of HVFA mixtures [62]. For instance, improper surface finishing could result in an unusually high content of fine-grained material (including pastes of cement and SCMs) in the surface layer of HVFA concretes, causing lower abrasion resistance than that prepared with proper finishing [64]. Surface finishing also leads to distinct pore structures and hardness in the surface zone, contributing to the change in the abrasion resistance of HVFA mixtures [65]. If not cured properly, the surface quality of HVFA concretes is negatively affected, thus reducing their abrasion resistance [46]. Our recent study found that the incorporation of trace amounts of a novel nanomaterial, graphene oxide, improved the microhardness, scratch surface roughness, scratch hardness, and friction coefficient of 60% fly ash-contained HVFA concretes resulting in their increased abrasion resistance [66].

4.2. Carbonation Resistance. As mentioned earlier, HVFA concrete with 50% fly ash in the binder generally exhibits a lower level of strength, which translates to higher permeability, thus facilitating the carbonation of concrete by allowing a higher rate of CO_2 ingress into the concrete. One study reported that the negative correlation between compressive strength and carbonation depth of HVFA mixtures was strong and linear [67]. Many studies have concluded that HVFA mixtures are more susceptible to carbonation than their OPC counterparts of equivalent w/cm, with the depth of carbonation increasing with the fly ash content [19, 67–70].

In addition to the lower strength, the reduction of CH content (due to the pozzolanic reaction of fly ash) also explains the reduced carbonation resistance of HVFA concrete [67]. Moreover, the existence of excessive ettringite, which results from the noncompletion of pozzolanic reactions, further deteriorates the carbonation resistance of HVFA concrete [69]. Figure 7 shows the split sections after the phenolphthalein spray of a HVFA concrete vs. OPC concrete after 7 days in the accelerated carbonation test, respectively [71]. Phenolphthalein is naturally colorless but turns pink in the presence of high alkalinity. In the case of concrete, the carbonated area features lower alkalinity, thus failing to turn pink. Figure 7 illustrates that the 50% fly ash HVFA concrete experienced severe carbonation, while its OPC counterpart exhibited a clear carbonation front and much less carbonation.

4.3. Freezing-Thawing Resistance. The freezing-thawing (F-T) resistance of HVFA mixtures is generally lower than their OPC counterparts of equivalent w/cm [72–75]. Moreover, the F-T damage in HVFA mixtures tends to increase with the fly ash content. Interestingly, the air-void characteristic (e.g., spacing factor) is a more significant factor affecting the F-T performance of HVFA mixtures than the fly ash content or w/cm [75]. Therefore, the most commonly used strategy for improving the F-T durability of HVFA mixtures is air entrainment. The F-T resistance of the air-entrained HVFA mixtures can be excellent, with the durability factor being higher than 95% at the end of the rapid F-T cycling test [73, 75, 76]. However, the free carbon in fly ash particles could absorb the air-entraining admixture, compromising the F-T durability of HVFA mixtures [75]. Besides air entrainment, improving the quality of the ITZ is another approach to enhance the F-T resistance of HVFA mixtures [72]. Improved ITZ can slow down the liquid transport in the HVFA mixture, resulting in less water available in the cementitious composite and thus less F-T damage caused by ice crystallization pressure [72], hydraulic pressure, or osmotic pressure.

Adequate air-void parameters can provide HVFA mixtures with sufficient resistance against repeated F-T cycles but may fail to prevent salt scaling. In general, HVFA mixtures perform poorly in the F-T cycling test, even though they feature improved F-T resistance when air entrained [75, 77]. The performance of nonair-entrained HVFA concretes in a salt scaling test would be even more worse [75]. One reasonable explanation for the failure of HVFA mixtures in a salt scaling test may be the reduction in their surface strength due to the carbonation [75]. In addition, the ITZ is easily deteriorated and the integrity of ITZ's microstructure is compromised when HVFA concretes are subjected to salt scaling damage [76], as shown in Figure 8. At the beginning of the test, the gaps and air voids in the ITZ around the aggregate are full of salt solution, leading to the separation of ITZ by ice expansion force, shrinkage of cementitious paste [78], etc. Therefore, improving the ITZ could result in an increased salt scaling resistance of HVFA mixtures, by slowing down the ingress of water and reducing the concentration of ions in the pore solution [78].

4.4. Shrinkage. In HVFA mixtures, cracking occurs when the tensile stress induced by shrinkage strain exceeds the local tensile strength of the composite material. Generally, the amount of cement paste accounts for the shrinkage in concrete. HVFA mixtures usually exhibit lower shrinkage than their OPC counterparts when a large amount of cement in the mixture is replaced with fly ash [32, 79–82]. Furthermore, the unhydrated fly ash particles in HVFA mixtures may act as microaggregates and thus restrain shrinkage [81]. This microaggregate characteristic of fly ash is attributed to the good dispersibility of its particles in the HVFA mixture as well as the high strength (over 700 MPa) of the glass microbeads in the fly ash [83]. Therefore, it is reasonable to state that the use of Class F (instead of Class C) fly ash in HVFA mixtures could further reduce the shrinkage strain [80], considering the higher amount of Class F fly ash that remains unhydrated.

4.5. Alkali-Aggregate Reactions. The resistance of HVFA mixtures to alkali-aggregate reactions (AARs) benefits from the high-level replacement of cement by fly ash. This is attributed to the fact that the replacement of cement by fly

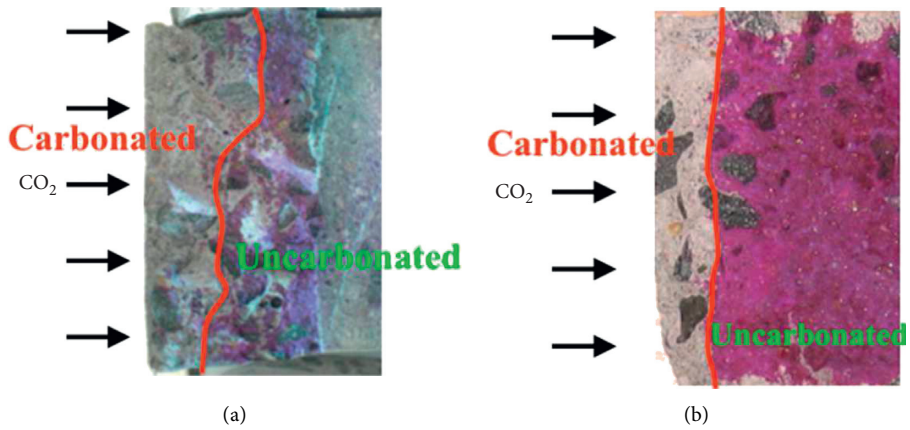

Figure 7: Split section after the phenolphthalein spray of (a) 50% fly ash HVFA concrete and (b) OPC concrete, reproduced from [71], with permission from Elsevier, 2021.

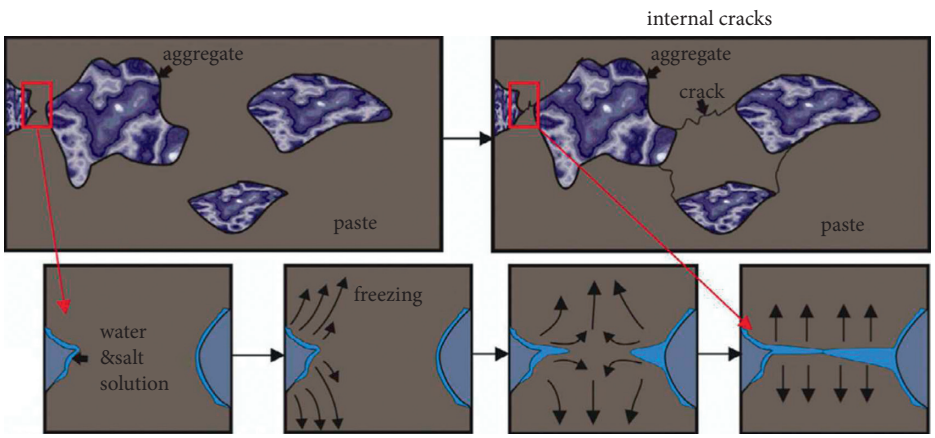

Figure 8: Propagation of internal cracks of HVFA concretes during F-T cycles in the presence of salt, reproduced from [78], with permission from Elsevier, 2021.

ash could reduce the amount of dissolvable alkali released from the binder [84]. For instance, one study reported that concretes containing HVFA binder exhibited no adverse expansion when highly reactive aggregates were used [85]. Another study reported that even with added alkali activator, the use of HVFA binder in concrete still effectively inhibited the expansion due to AARs [84]. The inhibited expansion could also be ascribed to the densification of the concrete microstructure, thereby lowering the release rate of alkalis from the cementitious binder.

Ca- and S-rich phases in fly ash particles are released more rapidly than the alkalis [84, 86], as illustrated in Figure 9. Specifically, Figure 9 shows that calcium and sulfur exhibit higher elemental concentration in the hydration products than in the fly ash particles; in contrast, potassium and sodium exhibit higher values in the fly ash particles. This indicates a slower depletion of alkali (Na and K) from the fly ash particles [86], contributing to the increased AAR resistance of HVFA mixtures. Furthermore, some larger fly ash particles in the 28 d HVFA mortar did not fully participate in the cementitious phase because their pozzolanic reaction only occurred on the surface layer of a few microns. In other words, much of the "core" of these fly ash particles remained intact and actually served as a fine aggregate phase. This highlights the need to activate the fly ash and some activation treatments are discussed in a later section.

In addition, the alkali's binding effect of calcium-aluminate-silicate-hydrates (C-A-S-H) that formed in HVFA mixtures can reduce the alkalinity of the pore solution [87]. Another possible mechanism is that the aluminate sourced from fly ash could slow down the dissolution kinetics and reduce the extent of dissolved silica from the aggregate, contributing to the low AAR expansion [88]. A recent study confirmed that the presence of unbound aluminum discharged from fly ash is effective in limiting the dissolution of amorphous reactive aggregates, which is beneficial for the AAR mitigation of concrete [89].

4.6. Transport Properties. The use of HVFA binder in cement-based materials can cause pore and grain refinement, which leads to the improved transport properties of HVFA mixtures, including reductions in water permeability, water sorptivity, gas permeability, and chloride ion penetration [61, 74, 77, 80, 90–96]. The presence of HVFA binder can also increase the capillary network tortuosity, decrease pore interconnectivity, and generate additional C-S-H by the pozzolanic reaction. HVFA binder also reduces the susceptibility to the

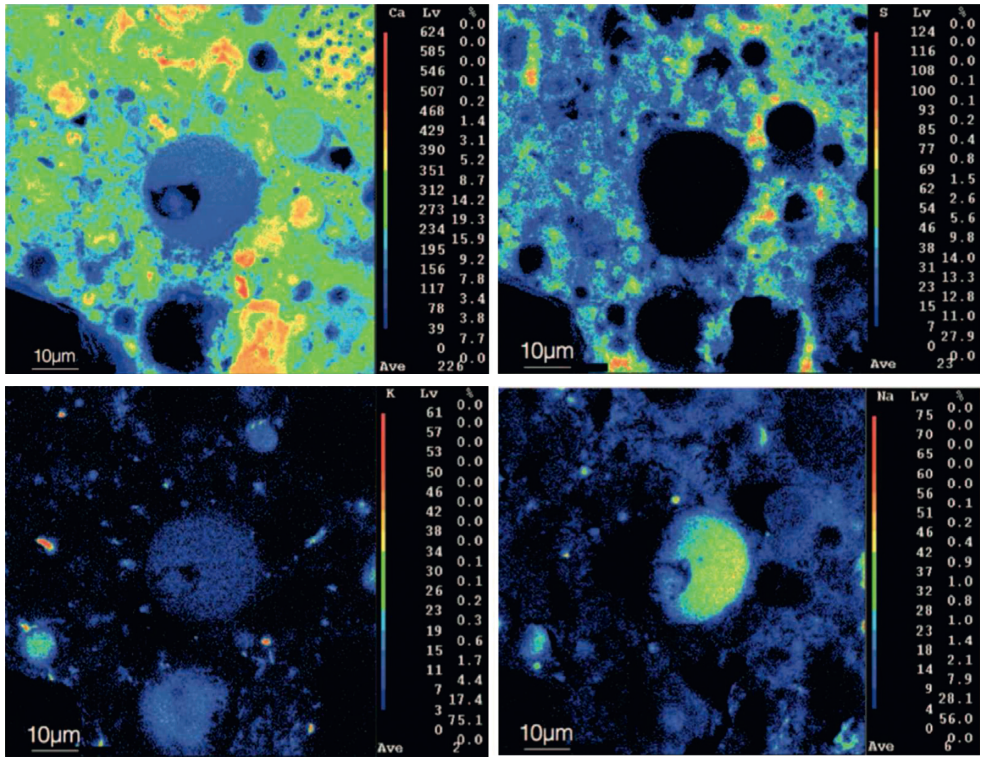

Figure 9: Element mapping of Ca, S, K, and Na in the same area in HVFA mortar at the curing age of 37 d, reproduced from [86], with permission from American Society of Civil Engineers, 2021.

penetration of gas and migration of free water or chloride ions [92, 94]. Moreover, HVFA mixtures usually feature a reduced number of capillary pores, thus lower capillary absorption and lower water sorptivity [97]. Some studies suggested the reduction of microcracking in the ITZ in HVFA mixtures as another reason for the improved transport properties [80, 92].

For chloride ion penetration, the alumina in fly ash can react with chlorides to form stable chloro complexes [72]. Therefore, HVFA mixtures usually feature a significantly reduced chloride ion penetration and their chloride binding capacity tends to increase with the fly ash content [70, 72, 77, 95]. Figure 10 shows an example of the colorimetric test of a HVFA concrete, where the area with color change to white corresponds to the chloride penetration depth [92]. The chloride penetration depth in HVFA mixtures could be reduced to one-third of the original value in OPC mixtures with the addition of HVFA binder [72, 92]. Meanwhile, the electrical resistivity of HVFA mixtures is increased due to the incorporation of HVFA binder [86, 98]. The electrical resistivity of cement-based materials is an indirect indicator that provides a rapid evaluation of their chloride permeability [99]. The higher electrical resistivity could translate to lower chloride permeability of HVFA mixtures, even though there are ions other than Cl^- in the pore solution that also affect the electrical resistivity of the concrete.

4.7. Chemical Attack. The deterioration of cementitious composites by chemicals is mainly due to the paste erosion and expansion caused by the reactions of chemical ions with Portlandite and other hydration products. Relative to their OPC counterparts, the resistances of HVFA mixtures to

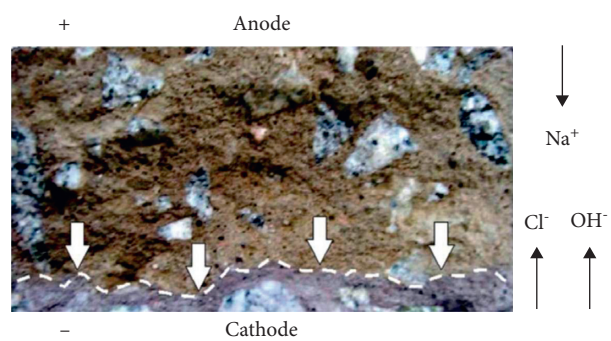

Figure 10: Colorimetric test of concrete with 50% fly ash (wide arrows indicate the precipitated chloride reaction front), reproduced from [92], with permission from American Society of Civil Engineers, 2021.

sulfate, lactic acid, acetic acid, and hydrochloric acid are improved [90, 100]. This can be explained by the reduction in CH content in the hydrated HVFA binder and the dense and discontinuous pore structure of HVFA mixtures (due to the pozzolanic reaction of fly ash). In a 75-day test where concretes were exposed to 2% hydrochloric acid, the HVFA concretes only exhibited minor surface erosion, whereas the OPC concretes already experienced edge loss [90].

HVFA concretes also feature less susceptibility to external or internal forms of sulfate attack, relative to their OPC counterparts. This is due to the pozzolanic behavior of fly ash that leads to increased consumption of CH [100]. Figure 11 depicts a comparison (by visual observation) between OPC and HVFA concretes after exposure to 10 wt% sodium sulfate

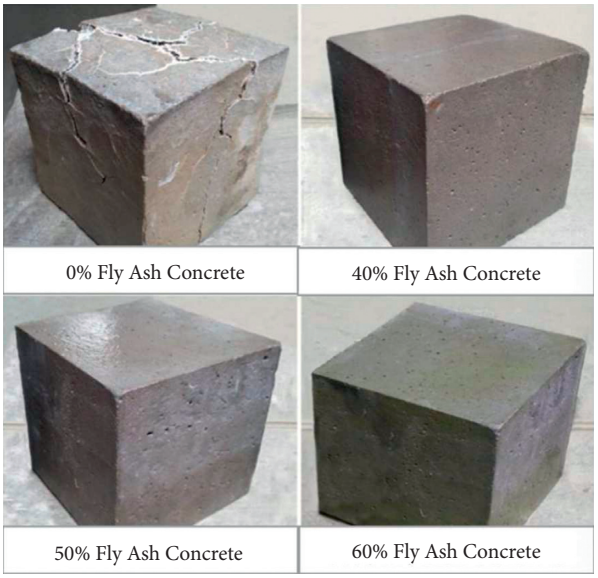

Figure 11: Concrete cubes after exposure to 10 wt.% sodium sulfate solution, reproduced from [90], a paper published in an open access journal.

solution for 550 days in an alternating drying and wetting scheme [90]. It is obvious that the OPC concrete is seriously deformed, whereas the HVFA concrete stays intact (no significant change to the physical appearance).

5. Environmental Assessment

As mentioned above, HVFA mixtures generally feature superior long-term durability performance compared with conventional OPC mixtures, except for the resistances to carbonation and deicing salt scaling. Therefore, from a life cycle perspective, it is likely that HVFA mixtures could offer greater cost savings, as well as reduced CO_2 emissions generated in the production of a unit volume of the mixture [101]. Normally, a life cycle assessment (LCA) methodology is recommended to evaluate the environmental impact of cement-based materials. In this methodology, a full description of the product from the extraction of raw materials to the waste treatment, i.e., cradle-to-grave approach, is required to quantify its impact on the environment [102]. However, for HVFA-based materials, a cradle-to-gate approach is usually used to exclude the influence of the end-of-life scenarios, thus emphasizing on the production process. Generally, the cradle-to-gate approach includes extraction of cement raw materials, manufacturing of cement, extraction and processing of aggregates, manufacturing of superplasticizers, preparation and collection of fly ash, transportation of raw materials, and concrete batching; the analysis ends at the concrete plant with the final product ready to be used in the construction field [103, 104], as illustrated in Figure 12. In evaluating the environmental impact of HVFA mixtures, all emissions during the cradle-to-gate approach are converted into CO_2 equivalent (CO_2-eq) to calculate the global warming potential (GWP) [105, 106]. These emissions may include greenhouse gas (mainly CO_2) and air pollutants associated with the use of electricity, fuel, transportation, and production, such as CO, NO_x, PM_{10}, and SO_2 [103].

A function unit of 1 m^3 HVFA concrete with a service life of 50 years was adopted to conduct the LCA analysis, and the results revealed that the CO_2-eq footprint of HVFA concrete was about 25%–40% less than the reference OPC concrete exposed to different deterioration processes [102, 105]. Using the concept of the CO_2-eq intensity, which represents the CO_2-eq per unit volume of concrete per compressive strength, one study concluded that a lower CO_2-eq intensity was achieved by Portland cement being replaced with HVFA binder in concrete [103]. Although the HVFA mixtures possessed high compressive strength, in that case, the reduced GWP associated with the HVFA mixtures was more notable [39, 107]. This is mainly because that the environmental impact of manufacturing fly ash is considered as zero since it is treated as waste [108], while about 70% of the total greenhouse gas emission in concrete production is related to the production of clinker in cement [104, 109]. Figure 13 depicts the information related to the total consumption of fuel and electricity for fly ash. It is obvious that the majority greenhouse gas emission related to fly ash occurs in the transportation stage [108].

When using different allocations (to none, by mass or by economic value) associated with fly ash, economic allocation is preferable since the mass allocation results in an environmental impact that is an order of magnitude higher [110]. A similar conclusion was drawn from another study [111], in which the environmental impact of concrete was strongly dependent on the allocation scenario applied. Yet, the environmental impact of HVFA mixtures decreased with increasing fly ash content in all allocation scenarios [111]. The incorporation of a HVFA binder reduces the environmental impact of concrete by about 50% [112, 113], regardless of the locations of the coal power plant (fly ash supplier) and the concrete plant [109, 114–116]. However, if the impacts from allocation or transportation are large enough to reduce the benefits associated with the use of the HVFA binder in mitigating GWP, increasing fly ash replacement may become less favorable in concrete production [117].

6. Measures to Improve the Strengths of HVFA Mixtures

As discussed earlier, HVFA cementitious composites have relatively low early-age strengths, which is a main hurdle that limits the implementation of HVFA mixtures [30]. Some of the relatively poor durability performance, which correlate closely with mechanical properties (especially compressive strength), are also concerns for HVFA mixtures in various service environments. Fabricating HVFA mixtures with lower w/cm can compensate for the delayed strength development. Yet, the pozzolanic reaction of fly ash only occurs in the presence of sufficient moisture [118]. In addition, the content of CH produced from the hydration of cement is usually less than that required for the pozzolanic reaction of the whole mass of fly ash present in the concrete [119]. Therefore, a critical combination of the fly ash replacement level and w/cm would exist in the HVFA mixtures. In this case, the amount of

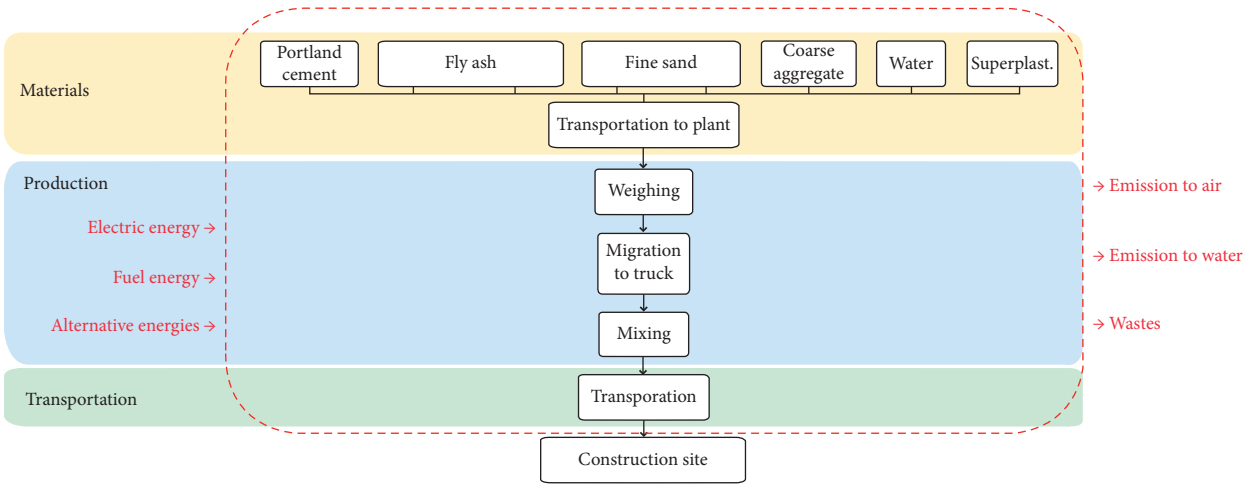

Figure 12: Schematic diagram of the cradle-to-gate approach LCA of HVFA concrete, reproduced from [39], with permission from Elsevier, 2021.

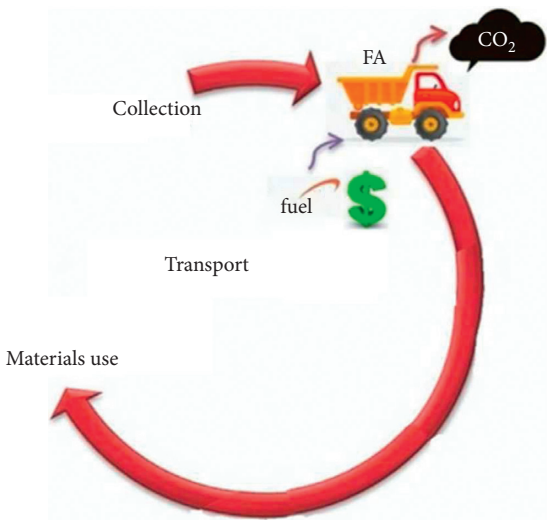

Figure 13: Various stages of the life cycle of fly ash, reproduced from [108], with permission from Elsevier, 2021.

CH or moisture is exactly enough for participating in the pozzolanic reaction of fly ash [23]. As the physicochemical characteristics of fly ash used vary from study to study, the optimum substitution rates of fly ash and w/cm lie in the range of 50%–60% and 0.3–0.4, respectively [23, 120]. Besides, there exists the risk of significant shrinkage if low w/cm are employed [30].

Other than lowering the w/cm, the limitations of HVFA mixtures in practice can be addressed using different curing conditions, activation treatments, finer SCMs, nanomaterials addition, and fiber inclusion, as detailed in this section.

6.1. Special Curing Conditions. Special curing conditions, including elevated-temperature curing and internal curing, have been employed to induce an increase in the strength development rate of HVFA mixtures [30, 80, 98, 121]. Warm-air curing can increase the compressive strength at the early age of HVFA concretes by expediting the hydration process of cement and the pozzolanic reaction of fly ash [80]. In contrast, HVFA concretes cured in warm water feature both increased early-age and long-term compressive strengths, compared with those cured at room temperature [98]. Internal curing is a method employed to provide additional moisture from the presaturated porous aggregate to support the pozzolanic reaction of fly ash [30], as illustrated in Figure 14. The water used for curing can be delivered internally to the concrete as "packets or inclusions" rather than just being placed on the surface of the mixtures. The internal curing reportedly enhanced the compressive strength by 61%, 32%, and 49% in a 60% fly ash HVFA mortar at 1 d, 28 d, and 365 d, respectively [30]. These strength improvements mainly resulted from higher degrees of hydration of cement and the pozzolanic reaction of fly ash.

6.2. Activation Treatments. In addition to specific curing conditions, some activation treatments have been employed in HVFA mixtures to improve their mechanical properties. Generally, the activation treatments include mechanical activation and chemical activation. Mechanical activation, such as the grinding of fly ash, endows HVFA concretes with higher compressive strength than those without activation applied [122], by improving the reactivity of the fly ash. As mentioned earlier, the specific surface area (particle size) of fly ash is a significant factor that affects the compressive strength of HVFA mixtures [33]. It should be noted that there exists an optimum grinding duration for the fly ash (about 2 hours), beyond which the size of the fly ash particles cannot be further reduced and the strength of HVFA mixtures cannot be further improved. This is because of the agglomeration of the particles or the overgrinding of the softer material with the harder material, resulting in noneffectiveness of further grinding [122]. A similar conclusion was drawn in other studies [123, 124], in which the median particle size of fly ash could be reduced from 19.70 μm to 2.67 μm by 2 hours of wet grinding. Through this process, both the pozzolanic activity and dissolution of fly ash are significantly promoted, contributing to the formation of hydration products and thus the strength development [123].

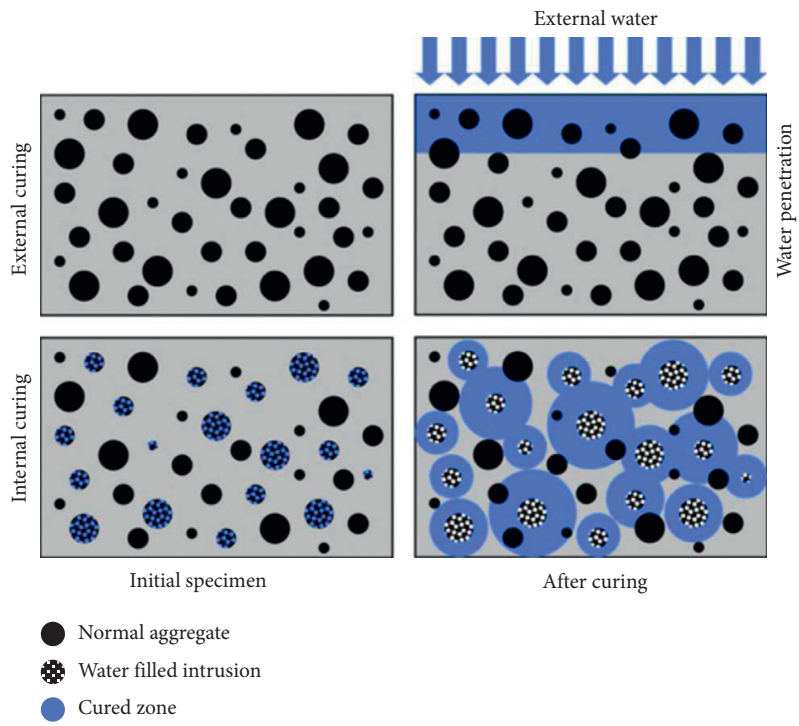

Figure 14: Conceptual illustration of the differences between external and internal curing, reproduced from [30], with permission from Elsevier, 2021.

Sodium sulfate, a neutral pH chemical activator, is found effective in improving the compressive strength of HVFA mortars at both the early and later ages [82, 100]. The improved compressive strength correlates with the process of increased ettringite formation and CH consumption, suggesting an accelerated pozzolanic reaction and improved hydration degree of fly ash. Moreover, with the addition of 3%–5% Na_2SO_4 by mass, the HVFA mixtures showcased the stability of free sulfate ions present within the samples during the expansion test, which demonstrates the applicability of this activator in practice [100]. With both 3 wt% Na_2SO_4 (SS) and 2 wt% nanosilica (NS) added, the HVFA mortars exhibited a sharper increase in their compressive strength, relative to the increases seen in the single system. Figure 15 depicts the presence of a synergistic effect between SS and NS in promoting the strength development of HVFA mortars [125], with the strength enhancement notably stronger than that of the sum of these single systems at the same dosage.

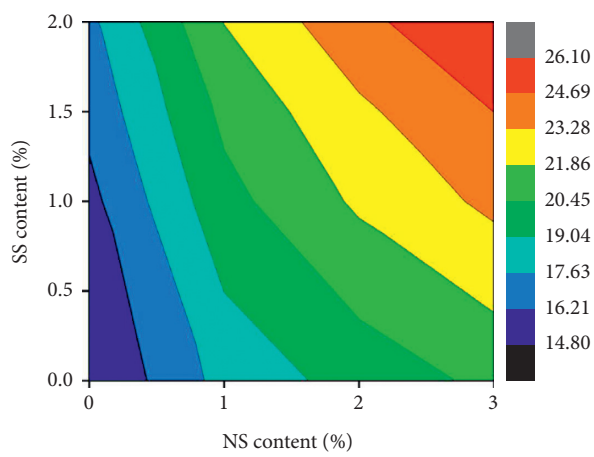

Figure 15: Effect of NS and SS on the compressive strength of HVFA mortars, reproduced from [125], with permission from Elsevier, 2021.

With high alkali and sulfate contents, cement kiln dust (CKD) has been shown to enhance the early-age strength of HVFA mixtures through the activation of fly ash [122, 126]. Figure 16 presents the contour plot illustrating the effect of the three binder constituents on the 2 d compressive strength of a HVFA paste. With the contents of fly ash, cement, and CKD set as 60%, 30%, and 10% by mass, respectively, the 2 d compressive strength can be maximized to 184% higher than that of the control paste without CKD [126].

Different from the chemical activation of fly ash used during the fresh mixture stage, electro-mutagenesis is an interesting technique that activates HVFA cementitious composites during the hardened stage. Conceptually, this technique uses sodium hydroxide and sodium silicate as the source of alkaline ions and applies an electric field across the composite matrix [127]. As illustrated in Figure 17, this treatment forces external alkaline ions into the capillary pores in HVFA concretes, where they react with unhydrated fly ash particles and contribute to the formation of hydration products and thus a denser microstructure. Depending on the detailed process parameters used, this electrochemical treatment may induce risks such as AARs, undesirable alternation of the microstructure, and hydrogen embrittlement of the embedded metal. These risks are similar to some cases of electrochemical chloride extraction and

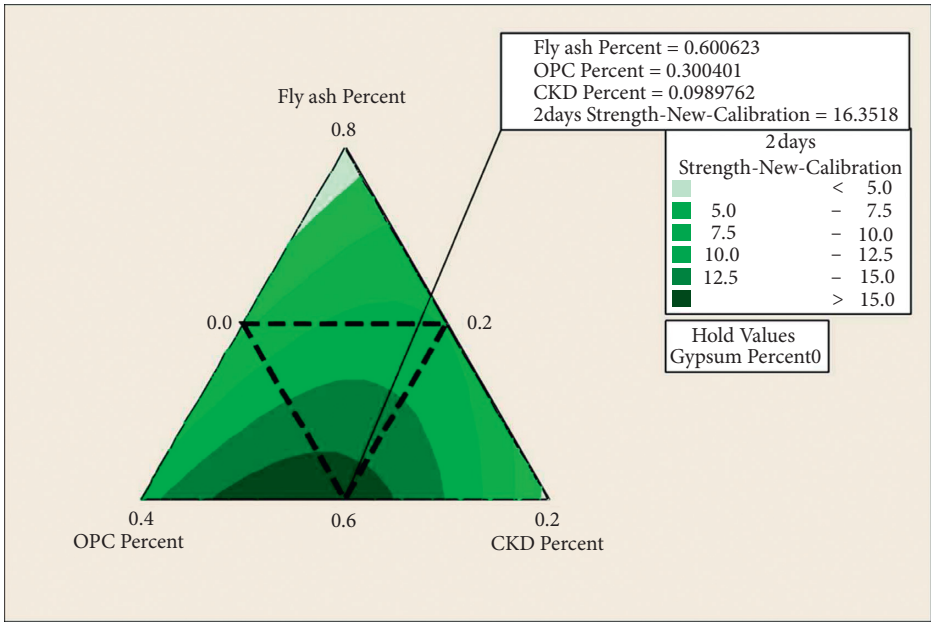

Figure 16: Proportion optimization of a HVFA paste based on 2 d compressive strength, reproduced from [126], with permission from Elsevier, 2021.

electrochemical injection of corrosion inhibitors [115]. Accordingly, it is crucial to design the electrochemical treatment process with appropriate levels of current density, external electrolyte, electrode configuration, and treatment duration in light of the condition of the existing HVFA cementitious composite.

6.3. Replacement by Finer SCMs. Supplementary cementitious materials with finer sized fly ash, such as ultrafine fly ash, fine limestone powder, glass powder, and silica fume, show an ability to improve the mechanical properties of HVFA mixtures at both early and later stages when replacing normal fly ash at a low dosage (i.e., 10%–15% by mass). An ultrafine fly ash, which features the mean size of 3.4 μm and the amorphous content of about 81%, consumes CH faster than normal fly ash (mean size of 10 μm and amorphous content of 63%) and hence generates more amorphous C-S-H in HVFA mixtures [25].

The incorporation of limestone powder with a median size of 0.7 μm in diameter could recover a portion of the loss in compressive strength of HVFA mixtures [128]. The fine limestone powder is able to compact the structure of HVFA mixtures through the pore-filling effect, resulting in the improved compressive strength at early ages (first 3 days) [129]. At more than 56 days, limestone powder in HVFA mixtures facilitates the pozzolanic reaction of fly ash by providing additional surfaces for the nucleation and growth of reaction products and participates in the production of carboaluminate hydrates via reaction with aluminate phases [128, 129]. Admixed limestone can also stabilize ettringite, lower the CH content, and increase the amount of C-S-H and C-A-S-H gels in concrete incorporating other SCMs [118].

With a mean size of 20 μm and a significant amorphous content of about 90%, a glass powder has been reported to positively influence the mechanical properties of a HVFA mixture, through the nucleation effect at an early age and pozzolanic reaction at later age [130].

When silica fume is added to concrete to replace fly ash at levels from 2% to 20% by mass, it significantly increases the compressive strength of HVFA concrete [24, 80, 131–133]. Replacing fly ash with silica fume at levels of 10% and 20% could reportedly result in an enhancement of 140% and 191% in the compressive strength of HVFA concrete, respectively [131]. As the finest SCM (other than nanomaterials) usually admixed in cement-based materials, silica fume features a specific surface area as high as 20200 m^2/kg [132], as shown in Figure 18. Therefore, silica fume significantly benefits the compressive strength of HVFA mixture through multiple effects, by filling the pores (i.e., "packing"), serving as nucleation sites, improving the pore size distribution, and being a high-reactive pozzolan [131].

6.4. Addition of Nanomaterials. Recently, nanomaterials have become increasingly popular in cement-based materials, showing great potential in improving their resistance to physical and chemical deterioration [134]. There are cumulative studies on HVFA cementitious composites dedicated to enhancing the mechanical properties of HVFA mixtures by admixing nanomaterials. At the optimum dosage of 1-2 wt%, nano-$CaCO_3$ contributes to the improvement of compressive strength of HVFA concretes because its reaction with the silicate and aluminate contents in fly ash, resulting in the generation of additional hydration products (e.g., carboaluminates) and the densification of the microstructure [43, 58, 93, 135, 136]. The increased consumption of CH and the presence of ettringite (AFt) in HVFA mixtures both indicate that $CaCO_3$ nanoparticles facilitate the pozzolanic reaction of fly ash and the hydration of cement, which also contribute to the strength

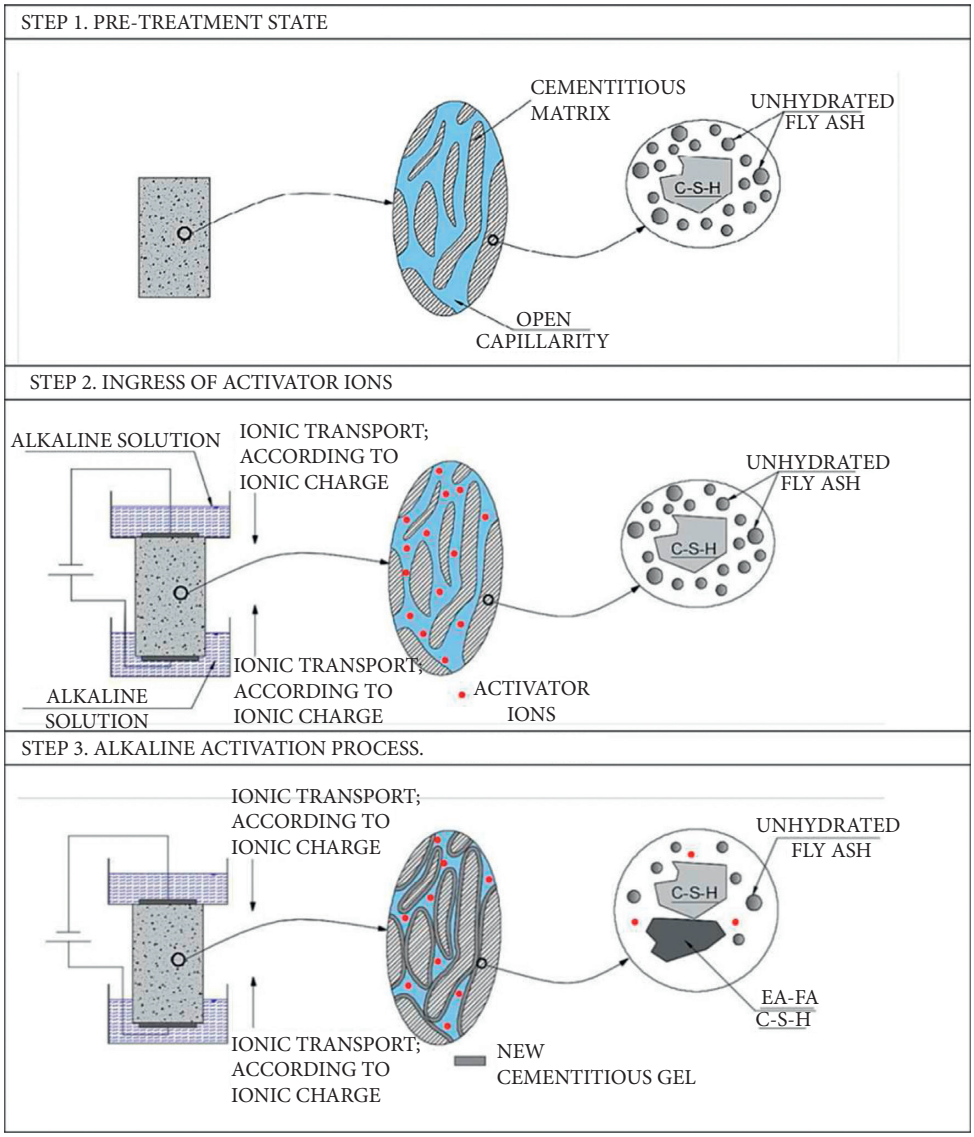

Figure 17: Preliminary conceptual model of the electrochemical activation process, reproduced from [127], with permission from Elsevier, 2021.

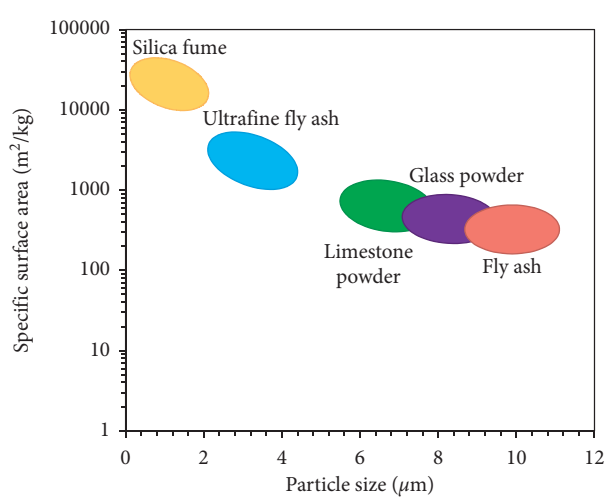

Figure 18: Particle size and specific surface area related to SCMs, based on data collected from relevant studies.

development of HVFA mixtures [93]. As shown in Figure 19 [97], the $CaCO_3$ nanoparticles-modified HVFA paste (FA59NC1) showed reductions in the intensity of CH peaks and calcium silicate peaks, as well as the presence of AFt peaks, relative to the pure HVFA paste (FA60). In the case of HVFA mortar containing 60% fly ash, the addition of 1% nano-$CaCO_3$ increased the 7 d and 28 d compressive strengths by about 100% and 111%, respectively [136]. Another study confirmed that the strength loss of HVFA concretes due to the partial replacement of cement with fly ash can be recovered by the incorporation of 1% nano-$CaCO_3$ [58], especially at 28 d [135].

Nanosilica is a highly reactive pozzolanic nanomaterial that can react with CH at an early age and increase the pozzolanic activity of fly ash at a later age, both of which contribute to better mechanical properties of HVFA mixtures [133]. Nanosilica enables better particle packing (due to its extremely small particle size), which also benefits the compressive strength development [137]. The addition of 1–5 wt% powdery or colloidal nanosilica in HVFA mixtures could compensate for the decrease in the early-age strength of HVFA mixtures [25, 36, 38, 40, 44, 133, 138]. Specifically, the addition of 2 wt% nanosilica increased the compressive strength of a 60% fly ash HVFA concrete by 95%, 7%, and 48% at 3, 7, and 28 d, respectively [21]. The ITZ of HVFA concrete can also be compacted by the admixed nanosilica [36, 38]. Figure 20 shows the microstructure of ITZ in a HVFA concrete, in which the reduction of CH and generation of C-S-H in the ITZ due to nanosilica can be observed, resulting in a densified ITZ and consequently an increased strength.

It should be noted that an adverse effect was observed in the later-age strength of HVFA mixtures when admixing colloidal nanosilica. This adverse effect was due to the lower hydration degree of fly ash that resulted from the lack of CH as well as the hindered hydration of cement by colloidal nanosilica [139]. Moreover, although HVFA mixtures could feature smaller pores with a high amount of nanosilica (such as 7.5%) admixed, the growth of AFt crystals in them exerts expansive pressure on the pore walls, inducing the development of microcracks [138].

6.5. Inclusion of Fibers. The admixed fibers either have no significant effect on the compressive strength of HVFA mixtures or the common increase is limited to about 10%. In contrast, they can increase the flexural strength and splitting tensile strength by about 20%, given the same dosage of fiber [44, 57]. The inclusion of 0.03–1 vol% fiber, especially straight steel fiber and polyester fiber, can slightly improve the compressive strength of HVFA mixtures [37, 46, 57, 137, 140, 141]. This improvement is attributed to the ability of the small fibers to delay the microcracks formation and arrest their propagation [142]. As a result, the admixed fibers can delay the cracking in concrete upon loading and thus compensate for the strength loss due to the fly ash substitution for cement [57]. The fact that the fibers act as crack arresters contributes more to enhancing the tensile and ductility properties of HVFA mixtures relative to compressive strength [46].

The fiber strands are usually discretely distributed throughout the HVFA mixtures [37]. If the fiber is admixed at high dosage (above 3 vol%), a decrease in the compressive strength of HVFA mixtures can be observed; in other words, there is an optimum dosage of fiber, beyond which the agglomeration of fibers would occur [140].

The fibers and nanomaterials can be used synergistically to benefit the mechanical properties of HVFA mixtures [44, 143, 144]. Figure 21 depicts the positive effect of nanosilica (NS) on the microstructure of HVFA mortars incorporating polyvinyl acetate (PVA) microfibers. It is clearly shown that due to the 1 wt% admixed NS, the surface of the PVA microfibers is covered by hydration products (mainly additional C-S-H). This mechanism improved the bonding between fibers and HVFA matrix, resulting in an efficient load transfer by fiber bridging and thus increased mechanical properties [44]. Another study similarly revealed the synergistic effects of montmorillonite nanoclay and polyethylene microfiber in a 70% fly ash HVFA foamed cementitious paste [145].

7. Research Needs and Remaining Challenges of HVFA Mixtures

Cumulative studies have investigated multiple aspects of HVFA cementitious composites and most of them demonstrated that HVFA mixtures can be successfully applied in construction if implemented appropriately. Figure 22 presents the overview of this review, including the superior aspects (workability, later-age strength, shrinkage, alkali-aggregate reaction, transport properties, chemical attack, and environmental impact) and inferior aspects (setting time, early-age strength, abrasion, carbonation, freezing-thawing, and salt scaling) of HVFA mixtures relative to OPC counterparts, as well as the measures that can be taken to improve their main hurdle (early-age strength) for wider acceptance. However, the following gaps (in the current knowledge base) and/or challenges need to be addressed, likely through multidisciplinary innovations and collaboration, before the construction industry can efficiently move forward with the optimal use of this promising type of material and introduce it into mainstream use.

There is a very limited understanding to enable quantitative and reliable prediction of the mechanical properties and durability performance of HVFA mixtures, based on a selection of physical and chemical characteristics of fly ash, such as chemical composition, fineness, crystallinity, and loss-on-ignition. Depending on the supply source and upstream process, fly ash is an industrial by-product with great variability in its physicochemical characteristics, making its quality assurance difficult yet critical. Although there are studies aiming to correlate the performance of HVFA mixtures with the characteristics of fly ash, the obtained correlations are unique for the fly ash used in each study and vary from one study to another.

Furthermore, in some areas, the supply of conventional fly ash is dwindling because of the rapid construction using up the supply or the changes of fuel sources at the electric power plants (e.g., from coal to natural gas). In this context,

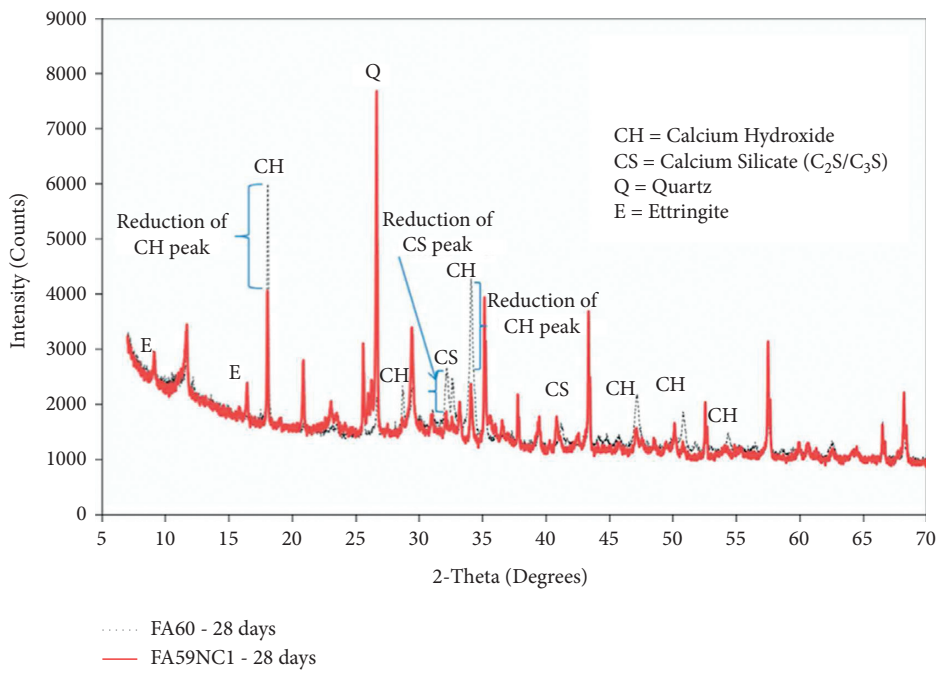

Figure 19: XRD analysis of HVFA pastes with and without nano-$CaCO_3$ at 28 d, reproduced from [93], with permission from Elsevier, 2021.

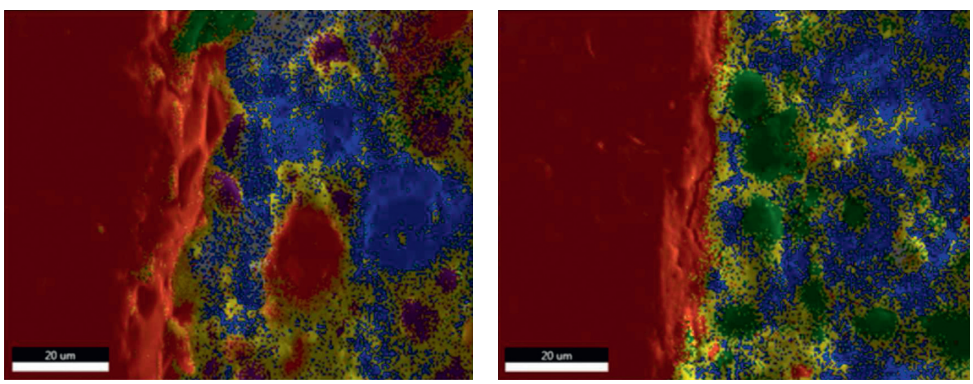

(a) (b)

Figure 20: SEM-EDS analysis of the ITZ in HVFA concrete: (a) no addition of nanosilica; (b) admixing 1 wt% nanosilica (Red part, Si-rich phase such as aggregate; blue and yellow parts, Ca-rich phase such as CH; green part, C-S-H), reproduced from [38], with permission from Elsevier, 2021. SEM, scanning electron microscopy; EDS, energy-dispersive X-ray spectroscopy.

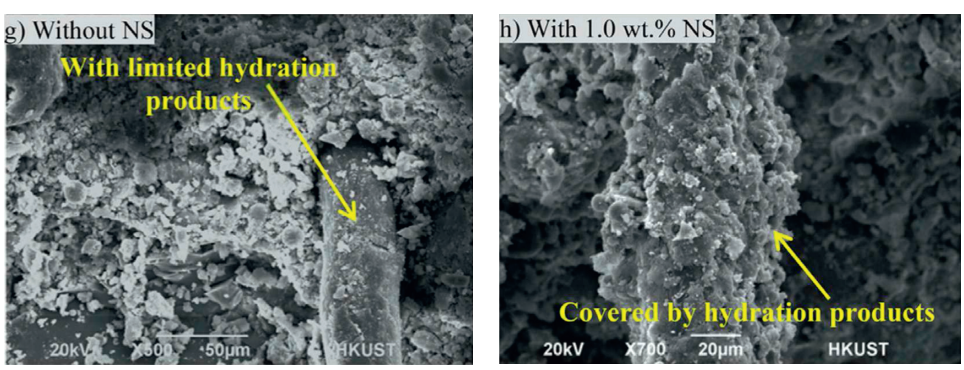

(a) (b)

Figure 21: SEM images of a microfiber-modified HVFA mortar with and without NS, reproduced from [44], with permission from Elsevier, 2021.

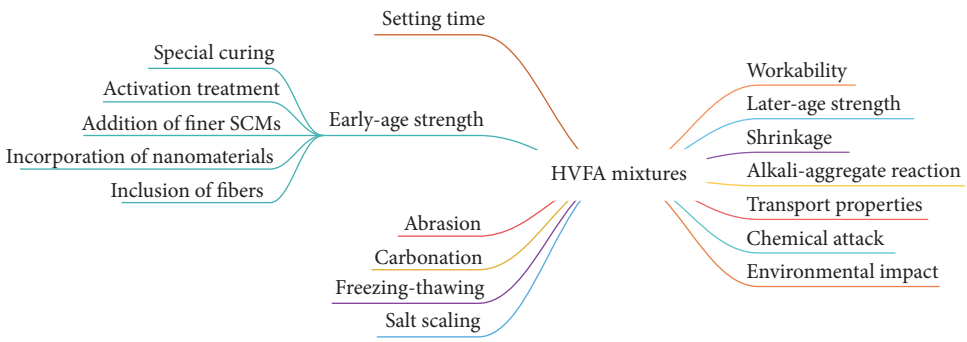

Figure 22: Renewed perspective about the superior and inferior aspects of HVFA mixtures relative to OPC counterparts.

some unconventional sources of fly ash have been considered for use in HVFA mixtures, such as ash disposed of in landfills or impoundments and biomass fly ash. This makes the prediction of the performance of HVFA mixtures based on the physicochemical characteristics of fly ash more complicated yet increasingly necessary.

Nearly every study about the HVFA mixture claims its superiority to OPC mixture in terms of carbon footprint, environmental friendliness, and sustainability. However, to reduce the setting time and increase the early-age strength of HVFA mixtures, some measures are taken to facilitate its application in the field, including the use of special curing regimes, activators, finer SCMs, nanomaterials, or fibers. These measures may induce extra costs and environmental impact for the production of HVFA mixtures. In these cases, it is in an urgent need to conduct the LCA analysis of the modified HVFA mixtures beyond the plain HVFA mixtures [39]. In addition, field implementation of in-place measurement methods for estimating the setting time and compressive strength is crucial for successful application of HVFA mixtures [146, 147].

There is a lack of fundamental understanding of HVFA mixtures as types of multiscale, heterogeneous composite materials, particularly in terms of deterioration under coupled mechanical and environmental loadings and potential chemical and physical synergies between various constituents (cement, fly ash, admixtures, other SCMs, fibers, and nanomaterials). Many of the existing studies are limited to treating concrete as a homogenous material and empirically evaluating its properties and performance in a macroscopic manner. The fundamental understanding of composition-property-performance relationships is crucial to guide best practices in selecting materials, preserving, maintaining, and possibly rehabilitating and recycling HVFA cementitious composites.

8. Concluding Remarks

This work provides an overview regarding recent advances in fresh properties, engineering performance, and environmental impact of HVFA cementitious composites. Some key findings from the review are provided as follows:

(i) The replacement of cement with HVFA binder in cementitious materials could increase the slump with the fly ash content lower than 60% due to the ball-bearing effect of fly ash, beyond which the slump of HVFA mixtures begins to decline because of the high surface area of fly ash. The setting time of HVFA mixtures is retarded, resulting from the dilution of cement and the slow pozzolanic reaction of fly ash.

(ii) There exists a reduction in the mechanical properties of HVFA mixtures compared with OPC mixtures, especially at early ages. This reduction increases with increasing fly ash content and decreases with increasing curing age. The combination of 50%–60% fly ash and w/cm of 0.3–04 is optimal for the pozzolanic reaction of fly ash.

(iii) Relative to their OPC counterparts, HVFA cementitious composites exhibit lower resistances to abrasion and carbonation. Freeze-thaw and salt scaling resistances are also lowered by the replacement of cement by HVFA binder, but proper air entrainment can endow HVFA mixtures with excellent freeze-thaw durability. HVFA mixtures exhibit lower environmental impact and better durability performance in terms of shrinkage, AARs, transport properties, and chemical attack.

(iv) To compensate the loss in mechanical properties due to the introduction of HVFA in cement-based materials, many measures can be taken, including elevated-temperature curing, internal curing, physical or chemical activation treatments, partially replacing normal fly ash by SCM with a finer size, admixing nanomaterials at appropriate dosage, and incorporating fibers.

(v) Both nanoscience and nanoengineering hold great promise in advancing the technology of HVFA cementitious composites.

(vi) Some aspects of HVFA-based materials, such as the application of HVFA binder in emerging concrete technologies (3-D printing concrete, ultra-high performance concrete, self-healing concrete, etc.), beneficial use of marginal fly ashes (biomass fly ash, municipal solid waste incineration fly ash, disposed fly ash, and ponded fly ash), and life cycle assessment considering all possible constituents and footprint, need to be researched and reviewed in future work.

Data Availability

All the relevant data are presented in this review article.

Additional Points

Highlights. (i) HVFA cementitious composites as a class of sustainable materials were reviewed. (ii) The combination of 50%–60% fly ash and w/cm of 0.3–04 is optimal for HVFA mixtures. (iii) Lower environmental impact and better durability in terms of shrinkage, AARs, transport properties, and chemical attack. (iv) Low early-age strength and low resistance to abrasion, carbonation, and salt scaling. (v) Alternative curing, activation, and use of finer SCM, fibers, and nanomaterials can help. (vi) Nanotechnology holds great promise in advancing HVFA concrete technology. (vii) Beneficial uses of marginal fly ashes, LCA of HVFA mixtures containing all possible constituents, etc., need to be further explored.

Conflicts of Interest

The authors declare that they have no conflicts of interest.

Acknowledgments

The funding support provided by the USDOT Center for Environmentally Sustainable Transportation in Cold Climates (CESTiCC) and the National Center for Transportation Infrastructure Durability & Life-Extension (TriDurLE) for Dr. Sen Du's dissertation work is greatly acknowledged. Dr. Sen Du sincerely appreciates the funding support by the 2018 John Faber Scholarship provided by American Coal Ash Association Educational Foundation (ACAAEF) and the 2018 and 2019 Richard Perteet Graduate Fellowship in Civil Engineering provided by Washington State University. Financial support from the Natural Science Foundation of Hebei Province of China under Grant no. E2021203214 is also gratefully acknowledged.

References

[1] D. Harris, C. Heidrich, and J. Feuerborn, "Global aspects on coal COmbustion products," in *Proceedings of the World of Coal Ash (WOCA) Confernece*, St. Louis, Missouri, 2019.

[2] S. Naganathan, A. Y. O. Mohamed, and K. N. Mustapha, "Performance of bricks made using fly ash and bottom ash," *Construction and Building Materials*, vol. 96, pp. 576–580, 2015.

[3] D. Adak and S. Mandal, "Strength and durability performance of fly ash-based process-modified geopolymer concrete," *Journal of Materials in Civil Engineering*, vol. 31, no. 9, Article ID 04019174, 2019.

[4] Z. T. Yao, X. S. Ji, P. K. Sarker et al., "A comprehensive review on the applications of coal fly ash," *Earth-Science Reviews*, vol. 141, pp. 105–121, 2015.

[5] T. R. Naik, S. S. Singh, and M. M. Hossain, "Abrasion resistance of high-strength concrete made with class C fly ash," *M and O*, vol. 92, pp. 649–659, 1995.

[6] H. Lavasani and A. Werner, "Practicality and sustainability of using HVFA for concrete sidewalks," in *Construction Research Congress 2012*, pp. 1931–1940, American Society of Civil Engineers, West Lafayette, IND, US, 2012.

[7] P. K. Mehta, "High-performance, high-volume fly ash concrete for sustainable development," in *Proceedings of the International Workshop on Sustainable Development and Concrete Technology*, pp. 3–14, May 2004, http://core.ac.uk/download/pdf/11346106.pdf#page=14.

[8] A. M. Rashad, "A brief on high-volume Class F fly ash as cement replacement - a guide for Civil Engineer," *International Journal of Sustainable Built Environment*, vol. 4, no. 2, pp. 278–306, 2015.

[9] V. M. Malhotra, "High-performance high-volume fly ash concrete," *Concrete International*, vol. 24, pp. 30–34, 2002.

[10] E. Mohamed, B. Hakan, and K. Ali, "Green concrete with high-volume fly ash and slag with recycled aggregate and recycled water to build future sustainable cities," *Journal of Materials in Civil Engineering*, vol. 29, Article ID 04016219, 2017.

[11] X.-Y. Wang, "Simulation for optimal mixture design of low-CO2 high-volume fly ash concrete considering climate change and CO2 uptake," *Cement and Concrete Composites*, vol. 104, Article ID 103408, 2019.

[12] J. Dragaš, S. Marinković, and V. Radonjanin, "Prediction models for high-volume fly ash concrete practical application: mechanical properties and experimental database," *Building Materials and Structures*, vol. 64, pp. 19–43, 2021.

[13] B. Panda, S. Ruan, C. Unluer, and M. J. Tan, "Improving the 3D printability of high volume fly ash mixtures via the use of nano attapulgite clay," *Composites Part B: Engineering*, vol. 165, pp. 75–83, 2019.

[14] B. Panda and M. J. Tan, "Rheological behavior of high volume fly ash mixtures containing micro silica for digital construction application," *Materials Letters*, vol. 237, pp. 348–351, 2019.

[15] S. Mukherjee, S. Mandal, and U. B. Adhikari, "Comparative study on physical and mechanical properties of high slump and zero lump high volume fly ash concrete (HVFAC)," *Global NEST Journal*, vol. 15, no. 4, pp. 578–584, 2013.

[16] T. Yang, H. Zhu, Z. Zhang, X. Gao, C. Zhang, and Q. Wu, "Effect of fly ash microsphere on the rheology and microstructure of alkali-activated fly ash/slag pastes," *Cement and Concrete Research*, vol. 109, pp. 198–207, 2018.

[17] N. Puthipad, M. Ouchi, S. Rath, and A. Attachaiyawuth, "Enhancement in self-compactability and stability in volume of entrained air in self-compacting concrete with high volume fly ash," *Construction and Building Materials*, vol. 128, pp. 349–360, 2016.

[18] H. A. Alaka and L. O. Oyedele, "High volume fly ash concrete: the practical impact of using superabundant dose of high range water reducer," *Journal of Building Engineering*, vol. 8, pp. 81–90, 2016.

[19] N. Bouzoubaâ, A. Bilodeau, B. Tamtsia, and S. Foo, "Carbonation of fly ash concrete: laboratory and field data," *Canadian Journal of Civil Engineering*, vol. 37, no. 12, pp. 1535–1549, 2010.

[20] A. Durán-Herrera, C. A. Juárez, P. Valdez, and D. P. Bentz, "Evaluation of sustainable high-volume fly ash concretes," *Cement and Concrete Composites*, vol. 33, no. 1, pp. 39–45, 2011.

[21] F. U. A. Shaikh, S. W. M. Supit, and P. K. Sarker, "A study on the effect of nano silica on compressive strength of high

volume fly ash mortars and concretes," *Materials & Design*, vol. 60, pp. 433–442, 2014.

[22] G. Sua-iam and N. Makul, "Incorporation of high-volume fly ash waste and high-volume recycled alumina waste in the production of self-consolidating concrete," *Journal of Cleaner Production*, vol. 159, pp. 194–206, 2017.

[23] S. Yoon, P. J. M. Monteiro, D. E. Macphee, F. P. Glasser, and M. S.-E. Imbabi, "Statistical evaluation of the mechanical properties of high-volume class F fly ash concretes," *Construction and Building Materials*, vol. 54, pp. 432–442, 2014.

[24] J. Yu, C. Lu, C. K. Y. Leung, and G. Li, "Mechanical properties of green structural concrete with ultrahigh-volume fly ash," *Construction and Building Materials*, vol. 147, pp. 510–518, 2017.

[25] S. W. M. Supit, F. U. A. Shaikh, and P. K. Sarker, "Effect of ultrafine fly ash on mechanical properties of high volume fly ash mortar," *Construction and Building Materials*, vol. 51, pp. 278–286, 2014.

[26] D. P. Bentz, "Activation energies of high-volume fly ash ternary blends: hydration and setting," *Cement and Concrete Composites*, vol. 53, pp. 214–223, 2014.

[27] D. P. Bentz, T. Sato, I. de la Varga, and W. J. Weiss, "Fine limestone additions to regulate setting in high volume fly ash mixtures," *Cement and Concrete Composites*, vol. 34, no. 1, pp. 11–17, 2012.

[28] D. P. Bentz, J. Tanesi, and A. Ardani, "Ternary blends for controlling cost and carbon content," *Concrete International*, vol. 35, pp. 51–59, 2013.

[29] D. P. Bentz, S. Z. Jones, and K. A. Snyder, "Design and performance of ternary blend high-volume fly ash concretes of moderate slump," *Construction and Building Materials*, vol. 84, pp. 409–415, 2015.

[30] I. De la Varga, J. Castro, D. Bentz, and J. Weiss, "Application of internal curing for mixtures containing high volumes of fly ash," *Cement and Concrete Composites*, vol. 34, no. 9, pp. 1001–1008, 2012.

[31] I. De la Varga, J. Castro, D. P. Bentz, F. Zunino, and J. Weiss, "Evaluating the hydration of high volume fly ash mixtures using chemically inert fillers," *Construction and Building Materials*, vol. 161, pp. 221–228, 2018.

[32] C.-H. Huang, S.-K. Lin, C.-S. Chang, and H.-J. Chen, "Mix proportions and mechanical properties of concrete containing very high-volume of Class F fly ash," *Construction and Building Materials*, vol. 46, pp. 71–78, 2013.

[33] G. D. Moon, S. Oh, and Y. C. Choi, "Effects of the physicochemical properties of fly ash on the compressive strength of high-volume fly ash mortar," *Construction and Building Materials*, vol. 124, pp. 1072–1080, 2016.

[34] X.-Y. Wang and K.-B. Park, "Analysis of compressive strength development of concrete containing high volume fly ash," *Construction and Building Materials*, vol. 98, pp. 810–819, 2015.

[35] D. P. Bentz and C. F. Ferraris, "Rheology and setting of high volume fly ash mixtures," *Cement and Concrete Composites*, vol. 32, no. 4, pp. 265–270, 2010.

[36] M. Adamu, B. S. Mohammed, and M. Shahir Liew, "Mechanical properties and performance of high volume fly ash roller compacted concrete containing crumb rubber and nano silica," *Construction and Building Materials*, vol. 171, pp. 521–538, 2018.

[37] M. Afroz, S. Venkatesan, and I. Patnaikuni, "Effects of hybrid fibers on the development of high volume fly ash cement composite," *Construction and Building Materials*, vol. 215, pp. 984–997, 2019.

[38] M. Liu, H. Tan, and X. He, "Effects of nano-SiO2 on early strength and microstructure of steam-cured high volume fly ash cement system," *Construction and Building Materials*, vol. 194, pp. 350–359, 2019.

[39] P. R. d. Matos, M. Foiato, and L. R. Prudêncio, "Ecological, fresh state and long-term mechanical properties of high-volume fly ash high-performance self-compacting concrete," *Construction and Building Materials*, vol. 203, pp. 282–293, 2019.

[40] J. Sun, X. Shen, G. Tan, and J. E. Tanner, "Modification effects of nano-SiO2 on early compressive strength and hydration characteristics of high-volume fly ash concrete," *Journal of Materials in Civil Engineering*, vol. 31, no. 6, Article ID 04019057, 2019.

[41] S. W. M. Supit and F. Makalew, "Effects of micro- and ultrafine metakaolin on compressive strength and water sorptivity of high volume fly ash concrete," in *Proceedings of the AICCE'19*, F. Mohamed Nazri, Ed., pp. 415–427, Springer International Publishing, Penang, Malaysia, 2020.

[42] N. Tošić, S. Marinković, N. Pecić, I. Ignjatović, and J. Dragaš, "Long-term behaviour of reinforced beams made with natural or recycled aggregate concrete and high-volume fly ash concrete," *Construction and Building Materials*, vol. 176, pp. 344–358, 2018.

[43] H. Yang, Y. Che, and F. Leng, "High volume fly ash mortar containing nano-calcium carbonate as a sustainable cementitious material: microstructure and strength development," *Scientific Reports*, vol. 8, pp. 1–11, 2018.

[44] J. Yu, M. Zhang, G. Li, J. Meng, and C. K. Y. Leung, "Using nano-silica to improve mechanical and fracture properties of fiber-reinforced high-volume fly ash cement mortar," *Construction and Building Materials*, vol. 239, Article ID 117853, 2020.

[45] G. Hannesson, K. Kuder, R. Shogren, and D. Lehman, "The influence of high volume of fly ash and slag on the compressive strength of self-consolidating concrete," *Construction and Building Materials*, vol. 30, pp. 161–168, 2012.

[46] R. Siddique, K. Kapoor, E.-H. Kadri, and R. Bennacer, "Effect of polyester fibres on the compressive strength and abrasion resistance of HVFA concrete," *Construction and Building Materials*, vol. 29, pp. 270–278, 2012.

[47] R. Thangaraj and R. Thenmozhi, "Industrial and environmental application of high volume fly ash in concrete production," *Nature Environment and Pollution Technology*, vol. 12, p. 7, 2013.

[48] A. Mardani-Aghabaglou and K. Ramyar, "Mechanical properties of high-volume fly ash roller compacted concrete designed by maximum density method," *Construction and Building Materials*, vol. 38, pp. 356–364, 2013.

[49] J. Tanesi, A. Ardani, R. Meininger, and M. Nicolaescu, "Evaluation of high-volume fly ash (HVFA) mixtures (paste and mortar components) using a dynamic shear rheometer (DSR) and an isothermal calorimeter (interim results)," in *International Conference on Long-Life Concrete Pavement*p. 28, Seattle, WA, USA, 2012.

[50] R. Rajeshwari and S. Mandal, "Prediction of compressive strength of high-volume fly ash concrete using artificial neural network," *Lecture Notes in Civil Engineering*, vol. 25, pp. 471–483, 2018.

[51] M. Azimi-Pour, H. Eskandari-Naddaf, and A. Pakzad, "Linear and non-linear SVM prediction for fresh properties and compressive strength of high volume fly ash self-compacting concrete," *Construction and Building Materials*, vol. 230, Article ID 117021, 2020.

[52] A. Mohammed, R. Kurda, D. J. Armaghani, and M. Hasanipanah, "Prediction of compressive strength of concrete modified with fly ash: applications of neuro-swarm and neuro-imperialism models," *Computers and Concrete*, vol. 27, pp. 489–512, 2021.

[53] A. Mohammed, S. Rafiq, P. Sihag, R. Kurda, and W. Mahmood, "Soft computing techniques: systematic multiscale models to predict the compressive strength of HVFA concrete based on mix proportions and curing times," *Journal of Building Engineering*, vol. 33, Article ID 101851, 2020.

[54] K. Kuder, D. Lehman, J. Berman, G. Hannesson, and R. Shogren, "Mechanical properties of self consolidating concrete blended with high volumes of fly ash and slag," *Construction and Building Materials*, vol. 34, pp. 285–295, 2012.

[55] M. Rohit, I. Patel, and C. D. Modhera, "Comparative study on flexural strength of plain and fibre reinforced," *HVFA Concrete by Destructive and Non Destructive Techniques*, vol. 1, pp. 42–48, 2012.

[56] A. Sofi, K. Swathy, and G. Srija, "Toughness study on fly ash based fiber reinforced concrete," *International Journal of Advanced Structural Engineering*, vol. 5, no. 1, p. 17, 2013.

[57] V. M. Sounthararajan and A. Sivakumar, "Performance evaluation of metallic fibres on the low and high volume class F flyash based cement concrete," *International Journal of Engineering and Technology*, vol. 5, p. 14, 2013.

[58] T. Hemalatha, M. Mapa, N. George, and S. Sasmal, "Physico-chemical and mechanical characterization of high volume fly ash incorporated and engineered cement system towards developing greener cement," *Journal of Cleaner Production*, vol. 125, pp. 268–281, 2016.

[59] B. I. Yoshitake, H. Wong, T. Ishida, and A. Y. Nassif, "Thermal stress of high volume fly-ash (HVFA) concrete made with limestone aggregate," *Construction and Building Materials*, vol. 71, pp. 216–225, 2014.

[60] P. Saravanakumar and G. Dhinakaran, "Strength characteristics of high-volume fly ash-based recycled aggregate concrete," *Journal of Materials in Civil Engineering*, vol. 25, no. 8, pp. 1127–1133, 2013.

[61] O. Kayali and M. Sharfuddin Ahmed, "Assessment of high volume replacement fly ash concrete–concept of performance index," *Construction and Building Materials*, vol. 39, pp. 71–76, 2013.

[62] A. M. Rashad, H. E.-D. H. Seleem, and A. F. Shaheen, "Effect of silica fume and slag on compressive strength and abrasion resistance of HVFA concrete," *International Journal of Concrete Structures and Materials*, vol. 8, no. 1, pp. 69–81, 2014.

[63] R. Siddique, "Wear resistance of high-volume fly ash concrete," *Leonardo Journal of Sciences*, vol. 17, pp. 21–36, 2010.

[64] A. A. Shirzadi Javid and M. A. Arjmandi Nejad, "Packing density and surface finishing condition effects on the mechanical properties of various concrete pavements containing cement replacement admixtures," *Construction and Building Materials*, vol. 141, pp. 307–314, 2017.

[65] M. Rosenqvist, L.-W. Pham, A. Terzic, K. Fridh, and M. Hassanzadeh, "Effects of interactions between leaching, frost action and abrasion on the surface deterioration of concrete," *Construction and Building Materials*, vol. 149, pp. 849–860, 2017.

[66] S. Du, Y. Jiang, J. Zhong, Y. Ge, and X. Shi, "Surface abrasion resistance of high-volume fly ash concrete modified by graphene oxide: macro- and micro-perspectives," *Construction and Building Materials*, vol. 237, Article ID 117686, 2020.

[67] Y. Jia, B. Aruhan, and P. Yan, "Natural and accelerated carbonation of concrete containing fly ash and GGBS after different initial curing period," *Magazine of Concrete Research*, vol. 64, no. 2, pp. 143–150, 2012.

[68] C. Gunasekara, Z. Zhou, D. W. Law, M. Sofi, S. Setunge, and P. Mendis, "Microstructure and strength development of quaternary blend high-volume fly ash concrete," *Journal of Materials Science*, vol. 55, no. 15, pp. 6441–6456, 2020.

[69] N. Singh and S. P. Singh, "Carbonation resistance and microstructural analysis of low and high volume fly ash self compacting concrete containing recycled concrete aggregates," *Construction and Building Materials*, vol. 127, pp. 828–842, 2016.

[70] D. F. Velandia, C. J. Lynsdale, J. L. Provis, and F. Ramirez, "Effect of mix design inputs, curing and compressive strength on the durability of Na2SO4-activated high volume fly ash concretes," *Cement and Concrete Composites*, vol. 91, pp. 11–20, 2018.

[71] A. Younsi, P. Turcry, E. Rozière, A. Aït-Mokhtar, and A. Loukili, "Performance-based design and carbonation of concrete with high fly ash content," *Cement and Concrete Composites*, vol. 33, no. 10, pp. 993–1000, 2011.

[72] S. Du, Y. Ge, and X. Shi, "A targeted approach of employing nano-materials in high-volume fly ash concrete," *Cement and Concrete Composites*, vol. 104, Article ID 103390, 2019.

[73] Z. Liu and W. Hansen, "Freezing characteristics of air-entrained concrete in the presence of deicing salt," *Cement and Concrete Research*, vol. 74, pp. 10–18, 2015.

[74] A. Mardani-Aghabaglou, Ö. Andiç-Çakir, and K. Ramyar, "Freeze-thaw resistance and transport properties of high-volume fly ash roller compacted concrete designed by maximum density method," *Cement and Concrete Composites*, vol. 37, pp. 259–266, 2013.

[75] P. Van den Heede, J. Furniere, and N. De Belie, "Influence of air entraining agents on deicing salt scaling resistance and transport properties of high-volume fly ash concrete," *Cement and Concrete Composites*, vol. 37, pp. 293–303, 2013.

[76] Y. Li, R. Wang, S. Li, Y. Zhao, and Y. Qin, "Resistance of recycled aggregate concrete containing low- and high-volume fly ash against the combined action of freeze-thaw cycles and sulfate attack," *Construction and Building Materials*, vol. 166, pp. 23–34, 2018.

[77] E. G. Moffatt, M. D. A. Thomas, and A. Fahim, "Performance of high-volume fly ash concrete in marine environment," *Cement and Concrete Research*, vol. 102, pp. 127–135, 2017.

[78] B. Pang, Z. Zhou, X. Cheng, P. Du, and H. Xu, "ITZ properties of concrete with carbonated steel slag aggregate in salty freeze-thaw environment," *Construction and Building Materials*, vol. 114, pp. 162–171, 2016.

[79] H.-J. Chen, N.-H. Shih, C.-H. Wu, and S.-K. Lin, "Effects of the loss on ignition of fly ash on the properties of high-volume fly ash concrete," *Sustainability*, vol. 11, no. 9, Article ID 2704, 2019.

[80] H. El-Chabib and A. Ibrahim, "The performance of high-strength flowable concrete made with binary, ternary, or quaternary binder in hot climate," *Construction and Building Materials*, vol. 47, pp. 245–253, 2013.

[81] M. Şahmaran, Ö. Yaman, and M. Tokyay, "Development of high-volume low-lime and high-lime fly-ash-incorporated self-consolidating concrete," *Magazine of Concrete Research*, vol. 59, 2015.

[82] D. F. Velandia, C. J. Lynsdale, J. L. Provis, F. Ramirez, and A. C. Gomez, "Evaluation of activated high volume fly ash systems using Na 2 SO 4 , lime and quicklime in mortars with high loss on ignition fly ashes," *Construction and Building Materials*, vol. 128, pp. 248–255, 2016.

[83] J. Yu, G. Li, and C. K. Y. Leung, "Hydration and physical characteristics of ultrahigh-volume fly ash-cement systems with low water/binder ratio," *Construction and Building Materials*, vol. 161, pp. 509–518, 2018.

[84] W. Müllauer, R. E. Beddoe, and D. Heinz, "Leaching behaviour of major and trace elements from concrete: effect of fly ash and GGBS," *Cement and Concrete Composites*, vol. 58, pp. 129–139, 2015.

[85] H. Ye and Z. Chen, "Mechanisms of alkali-silica reaction in alkali-activated high-volume fly ash mortars," *Journal of Advanced Concrete Technology*, vol. 17, no. 6, pp. 269–281, 2019.

[86] S. Du, X. Shi, and Y. Ge, "Electron probe microanalysis investigation into high-volume fly ash mortars," *Journal of Materials in Civil Engineering*, vol. 29, no. 7, Article ID 04017043, 2017.

[87] Y. Kawabata and K. Yamada, "Evaluation of alkalinity of pore solution based on the phase composition of cement hydrates with supplementary cementitious materials and its relation to suppressing ASR expansion," *Journal of Advanced Concrete Technology*, vol. 13, no. 11, pp. 538–553, 2015.

[88] T. Chappex and K. Scrivener, "Alkali fixation of C-S-H in blended cement pastes and its relation to alkali silica reaction," *Cement and Concrete Research*, vol. 42, no. 8, pp. 1049–1054, 2012.

[89] R. Hay and C. P. Ostertag, "New insights into the role of fly ash in mitigating alkali-silica reaction (ASR) in concrete," *Cement and Concrete Research*, vol. 144, Article ID 106440, 2021.

[90] B. Balakrishnan and A. S. M. A. Awal, "Durability properties of concrete containing high volume MALAYSIAN fly ash," *International Journal of Renewable Energy Technology*, vol. 3, no. 4, pp. 529–533, 2014.

[91] S. Du, H. Zhao, Y. Ge, Z. Yang, and X. Shi, "Laboratory investigation into the modification of transport properties of high-volume fly ash mortar by chemical admixtures," *Journal of Materials in Civil Engineering*, vol. 29, no. 10, Article ID 04017184, 2017.

[92] J. H. Filho, M. H. F. Medeiros, E. Pereira, P. Helene, and G. C. Isaia, "High-volume fly ash concrete with and without hydrated lime: chloride diffusion coefficient from accelerated test," *Journal of Materials in Civil Engineering*, vol. 25, no. 3, pp. 411–418, 2013.

[93] F. U. A. Shaikh and S. W. M. Supit, "Mechanical and durability properties of high volume fly ash (HVFA) concrete containing calcium carbonate (CaCO3) nanoparticles," *Construction and Building Materials*, vol. 70, pp. 309–321, 2014.

[94] P. Van den Heede, E. Gruyaert, and N. De Belie, "Transport properties of high-volume fly ash concrete: capillary water sorption, water sorption under vacuum and gas permeability," *Cement and Concrete Composites*, vol. 32, no. 10, pp. 749–756, 2010.

[95] A. Yerramala and K. Ganesh Babu, "Transport properties of high volume fly ash roller compacted concrete," *Cement and Concrete Composites*, vol. 33, no. 10, pp. 1057–1062, 2011.

[96] Z. Zhang, S. Qian, and H. Ma, "Investigating mechanical properties and self-healing behavior of micro-cracked ECC with different volume of fly ash," *Construction and Building Materials*, vol. 52, pp. 17–23, 2014.

[97] M. Gesoğlu, E. Güneyisi, and E. Özbay, "Properties of self-compacting concretes made with binary, ternary, and quaternary cementitious blends of fly ash, blast furnace slag, and silica fume," *Construction and Building Materials*, vol. 23, pp. 1847–1854, 2009.

[98] Y. Liu and F. Presuel-Moreno, "Effect of elevated temperature curing on compressive strength and electrical resistivity of concrete with fly ash and ground-granulated blast-furnace slag," *ACI Materials Journal*, vol. 111, pp. 531–541, 2014.

[99] P. Ghosh and Q. Tran, "Influence of parameters on surface resistivity of concrete," *Cement and Concrete Composites*, vol. 62, pp. 134–145, 2015.

[100] A. Dakhane, S. Tweedley, S. Kailas, R. Marzke, and N. Neithalath, "Mechanical and microstructural characterization of alkali sulfate activated high volume fly ash binders," *Materials & Design*, vol. 122, pp. 236–246, 2017.

[101] D. P. Bentz and C. F. Ferraris, "Mixture proportioning options for improving high volume fly ash concretes," *International Journal of Pavement Research and Technology*, vol. 33, p. 7, 2010.

[102] P. Van den Heede and N. De Belie, "Durability related functional units for life cycle assessment of high-volume fly ash concrete," in *Proceedings of the Second International Conference on Sustainable Construction Materials and Technologies*, Ancona, Italy, 2010.

[103] K. Celik, C. Meral, A. Petek Gursel, P. K. Mehta, A. Horvath, and P. J. M. Monteiro, "Mechanical properties, durability, and life-cycle assessment of self-consolidating concrete mixtures made with blended portland cements containing fly ash and limestone powder," *Cement and Concrete Composites*, vol. 56, pp. 59–72, 2015.

[104] E. R. Teixeira, R. Mateus, A. Camões, and F. G. Branco, "Quality and durability properties and life-cycle assessment of high volume biomass fly ash mortar," *Construction and Building Materials*, vol. 197, pp. 195–207, 2019.

[105] P. Van den Heede, E. Gruyaert, N. Robeyst, and N. De Belie, "Life cycle assessment of a column supported isostatic beam in high-volume fly ash concrete (HVFA concrete)," in *Proceedings of the 2nd International Symposium on Service Life Design for Infrastructure*, pp. 437–444, RILEM Publications. Delft, The Netherlands, 2010.

[106] P. Van den Heede and N. De Belie, "A service life based global warming potential for high-volume fly ash concrete exposed to carbonation," *Construction and Building Materials*, vol. 55, pp. 183–193, 2014.

[107] S. A. Miller, P. J. M. Monteiro, C. P. Ostertag, and A. Horvath, "Concrete mixture proportioning for desired strength and reduced global warming potential," *Construction and Building Materials*, vol. 128, pp. 410–421, 2016.

[108] G. F. Huseien and K. W. Shah, "Durability and life cycle evaluation of self-compacting concrete containing fly ash as GBFS replacement with alkali activation," *Construction and Building Materials*, vol. 235, Article ID 117458, 2020.

[109] R. Kurda, J. D. Silvestre, J. de Brito, and H. Ahmed, "Optimizing recycled concrete containing high volume of fly ash in terms of the embodied energy and chloride ion resistance," *Journal of Cleaner Production*, vol. 194, pp. 735–750, 2018.

[110] P. Van den Heede and N. De Belie, "Environmental impact and life cycle assessment (LCA) of traditional and 'green' concretes: literature review and theoretical calculations,"

Cement and Concrete Composites, vol. 34, no. 4, pp. 431–442, 2012.

[111] K. E. Seto, C. J. Churchill, and D. K. Panesar, "Influence of fly ash allocation approaches on the life cycle assessment of cement-based materials," *Journal of Cleaner Production*, vol. 157, pp. 65–75, 2017.

[112] C. Gunasekara, M. Sandanayake, Z. Zhou, D. W. Law, and S. Setunge, "Effect of nano-silica addition into high volume fly ash–hydrated lime blended concrete," *Construction and Building Materials*, vol. 253, Article ID 119205, 2020.

[113] J. Li, W. Zhang, C. Li, and P. J. M. Monteiro, "Eco-friendly mortar with high-volume diatomite and fly ash: performance and life-cycle assessment with regional variability," *Journal of Cleaner Production*, vol. 261, Article ID 121224, 2020.

[114] R. Kurda, J. D. Silvestre, and J. de Brito, "Life cycle assessment of concrete made with high volume of recycled concrete aggregates and fly ash," *Resources, Conservation and Recycling*, vol. 139, pp. 407–417, 2018.

[115] D. K. Panesar, D. Kanraj, and Y. Abualrous, "Effect of transportation of fly ash: life cycle assessment and life cycle cost analysis of concrete," *Cement and Concrete Composites*, vol. 99, pp. 214–224, 2019.

[116] R. Kurda, J. de Brito, and J. D. Silvestre, "A comparative study of the mechanical and life cycle assessment of high-content fly ash and recycled aggregates concrete," *Journal of Building Engineering*, vol. 29, Article ID 101173, 2020.

[117] S. A. Miller, "Supplementary cementitious materials to mitigate greenhouse gas emissions from concrete: can there be too much of a good thing?," *Journal of Cleaner Production*, vol. 178, pp. 587–598, 2018.

[118] J. H. Wu, X. C. Pu, F. Liu, and C. Wang, "High performance concrete with high volume fly ash," *Key Engineering Materials*, vol. 302-303, pp. 470–478, 2006.

[119] H. Myadraboina, S. Setunge, and I. Patnaikuni, "Pozzolanic Index and lime requirement of low calcium fly ashes in high volume fly ash mortar," *Construction and Building Materials*, vol. 131, pp. 690–695, 2017.

[120] H. Zhao, X. Qin, J. Liu, L. Zhou, Q. Tian, and P. Wang, "Pore structure characterization of early-age cement pastes blended with high-volume fly ash," *Construction and Building Materials*, vol. 189, pp. 934–946, 2018.

[121] T. J. Barrett, I. D. la Varge, J. Schlitter, and W. J. Weiss, "Reducing the risk of cracking in high volume fly ash concrete by using internal curing," in *Proceedings of the World of Coal Ash (WOCA) Confernece*, p. 14, Denver, CO, USA, 2011.

[122] D. Bondar and E. Coakley, "Effect of grinding on early age performance of high volume fly ash ternary blended pastes with CKD & OPC," *Construction and Building Materials*, vol. 136, pp. 153–163, 2017.

[123] H. Tan, K. Nie, X. He et al., "Compressive strength and hydration of high-volume wet-grinded coal fly ash cementitious materials," *Construction and Building Materials*, vol. 206, pp. 248–260, 2019.

[124] J. Yang, L. Zeng, X. He et al., "Improving durability of heat-cured high volume fly ash cement mortar by wet-grinding activation," *Construction and Building Materials*, vol. 289, Article ID 123157, 2021.

[125] J. Mei, H. Tan, H. Li et al., "Effect of sodium sulfate and nano-SiO_2 on hydration and microstructure of cementitious materials containing high volume fly ash under steam curing," *Construction and Building Materials*, vol. 163, pp. 812–825, 2018.

[126] D. Bondar and E. Coakley, "Use of gypsum and CKD to enhance early age strength of High Volume Fly Ash (HVFA) pastes," *Construction and Building Materials*, vol. 71, pp. 93–108, 2014.

[127] J. Lizarazo-Marriaga, F. García, and C. Higuera, "Preliminary electrochemical cementation of high volume fly ash mortars," *Construction and Building Materials*, vol. 122, pp. 54–62, 2016.

[128] J. Tanesi, D. Bentz, and A. Ardani, *Enhancing High Volume Fly Ash Concretes Using Fine Limestone Powder*American Concrete Institute Spring Meeting, Minneapolis, MN, USA, 2013.

[129] P. Shafigh, M. A. Nomeli, U. J. Alengaram, H. B. Mahmud, and M. Z. Jumaat, "Engineering properties of lightweight aggregate concrete containing limestone powder and high volume fly ash," *Journal of Cleaner Production*, vol. 135, pp. 148–157, 2016.

[130] H. Siad, M. Lachemi, M. Sahmaran, H. A. Mesbah, and K. M. A. Hossain, "Use of recycled glass powder to improve the performance properties of high volume fly ash-engineered cementitious composites," *Construction and Building Materials*, vol. 163, pp. 53–62, 2018.

[131] A. M. Rashad, "An exploratory study on high-volume fly ash concrete incorporating silica fume subjected to thermal loads," *Journal of Cleaner Production*, vol. 87, pp. 735–744, 2015.

[132] A. M. Rashad, "Potential use of silica fume coupled with slag in HVFA concrete exposed to elevated temperatures," *Journal of Materials in Civil Engineering*, vol. 27, no. 11, Article ID 04015019, 2015.

[133] M.-H. Zhang and J. Islam, "Use of nano-silica to reduce setting time and increase early strength of concretes with high volumes of fly ash or slag," *Construction and Building Materials*, vol. 29, pp. 573–580, 2012.

[134] S. Du, J. Wu, O. AlShareedah, and X. Shi, "Nanotechnology in cement-based materials: a review of durability, modeling, and advanced characterization," *Nanomaterials*, vol. 9, Article ID 1213, 2019.

[135] R. Roychand, S. D. Silva, S. Setunge, and D. Law, "A quantitative study on the effect of nano SiO2, nano Al2O3 and nano CaCO3 on the physicochemical properties of very high volume fly ash cement composite," *European Journal of Environmental and Civil Engineering*, vol. 0, pp. 1–16, 2017.

[136] S. W. M. Supit and F. U. A. Shaikh, "Effect of nano-CaCO3 on compressive strength development of high volume fly ash mortars and concretes," *Journal of Advanced Concrete Technology*, vol. 12, no. 6, pp. 178–186, 2014.

[137] F. U. A. Shaikh, Y. Shafaei, and P. K. Sarker, "Effect of nano and micro-silica on bond behaviour of steel and polypropylene fibres in high volume fly ash mortar," *Construction and Building Materials*, vol. 115, pp. 690–698, 2016.

[138] R. Roychand, S. De Silva, D. Law, and S. Setunge, "High volume fly ash cement composite modified with nano silica, hydrated lime and set accelerator," *Materials and Structures*, vol. 49, no. 5, pp. 1997–2008, 2016.

[139] P.-k. Hou, S. Kawashima, K.-j. Wang, D. J. Corr, J.-s. Qian, and S. P. Shah, "Effects of colloidal nanosilica on rheological and mechanical properties of fly ash-cement mortar," *Cement and Concrete Composites*, vol. 35, no. 1, pp. 12–22, 2013.

[140] E. Aydin, "Staple wire-reinforced high-volume fly-ash cement paste composites," *Construction and Building Materials*, vol. 153, pp. 393–401, 2017.

[141] I. Patel and D. C. D. Modhera, "Study basic properties OF fiber reinforced high volume," *Fly Ash Concrete*, vol. 1, pp. 60–70, 2010.

[142] G. K. Kate, C. B. Nayak, and S. B. Thakare, "Optimization of sustainable high-strength-high-volume fly ash concrete with and without steel fiber using Taguchi method and multi-regression analysis," *Innovative Infrastructure Solutions*, vol. 6, no. 2, p. 102, 2021.

[143] R. Gopalakrishnan and R. Kaveri, "Using graphene oxide to improve the mechanical and electrical properties of fiber-reinforced high-volume sugarcane bagasse ash cement mortar," *The European Physical Journal Plus*, vol. 136, no. 2, p. 202, 2021.

[144] H.-D. Li, Q.-M. Zhang, G. Feng, L. Mei, Y. Wang, and W.-J. Long, "Multi-scale improved damping of high-volume fly ash cementitious composite: combined effects of polyvinyl alcohol fiber and graphene oxide," *Construction and Building Materials*, vol. 260, Article ID 119901, 2020.

[145] J. Gong, Z. Li, R. Zhang, J. Li, and X. Shi, "Synergistic effects of nano-montmorillonite and polyethylene microfiber in foamed paste with high volume fly ash binder," *Journal of Nanoscience and Nanotechnology*, vol. 19, pp. 4465–4473, 2019.

[146] A. Baral, J. Roesler, and J. Fu, *Early-age Properties of High-volume Fly Ash Concrete Mixes for Pavement: Volume 2*, Illinois Center for Transportation, Rantoul, IL, USA, 2021.

[147] A. Baral, J. Roesler, M. Ley et al., *High-volume Fly Ash Concrete for Pavements Findings: Volume 1*, Illinois Center for Transportation, Rantoul, IL, USA, 2021.

Hindawi
Advances in Civil Engineering
Volume 2021, Article ID 3427451, 7 pages
https://doi.org/10.1155/2021/3427451

Research Article

Effect of Low Temperatures on the Mechanical Performance of GFRC Modified by Low Carbon Cement

Meimei Song [1] **and Chuanlin Wang** [2]

[1] *Department of Mechanical Engineering, Xi'an Shiyou University, Xi'an, China*
[2] *College of Engineering, Shantou University, Shantou, China*

Correspondence should be addressed to Chuanlin Wang; clwang@stu.edu.cn

Received 14 July 2021; Revised 27 September 2021; Accepted 28 September 2021; Published 8 October 2021

Academic Editor: Xianming Shi

Glass fibre reinforced cement (GFRC) is a composite material with great ductility but it undergoes severe strength and ductility degradation with ageing. Calcium sulfoaluminate (CSA) cement is low carbon cement, and more importantly, it exhibits great potential to produce more ductile and durable GFRC. This study focuses on mechanical performance, e.g., compressive strength, stress-strain curve, and freeze-thaw resistance of CSA/GFRC as well as its microstructural characteristics under low temperatures. XRD was applied to investigate the hydration mechanism of CSA cement under −5°C, 0°C, and 5°C. It was found out that low-temperature environments have very little effect on the type of hydration products, and the main hydration product of hydrated CSA cement cured under low temperatures is ettringite. Moreover, low-curing temperatures have an adverse effect on the compressive strength developments of CSA/GFRC but the strength difference compared with that under 20°C reduces gradually with increasing curing ages. In terms of bending performance, both ultimate tensile strength and ultimate strain value indicate considerable degradation with ageing under low temperatures after 14 d. The ultimate strain value reduces to 0.34% at −5°C, 0.39% at 0°C, and 0.44% at 5°C compared with 0.51% for that cured at 20°C for 28 d. The tensile strength of samples cured at −5°C for 28 d is only 15.2 MPa, taking up only 40% of that under 20°C. CSA/GFRC also demonstrated great capability in the antifreeze-thaw performance, and the corresponding strength remains 95.9%, 94.7%, 94.2%, and 94.3%, respectively, for that cured under 20°C, 5°C, 0°C, and −5°C after 50 freeze-thaw cycles. Microstructural studies reveal that densification of the interfilamentary space with intermixtures of C-A-S-H and ettringite is the main reason that causes the degradation of CSA/GFRC, which may result in loss on flexibility when forces are applied, therefore reducing the post-peak toughness to some extent.

1. Introduction

Glass fibre reinforced cement (GFRC) is widely applied in practical engineering, e.g., façade panel and pavement over the past two decades; this can be attributed to its superior ductility resulted from the bridging effect of glass fibre [1–3]. However, it was reported that severe reductions in compressive strength and ductility may occur in GFRC with ageing [4, 5], which has become a common concern for the service life of engineering members made of GFRC. The intrinsic microstructural reasons corresponding to this degradation are normally associated with chemical corrosion of fibre by the alkalinity in pore solution [6] and severe CH densification between and around fibres that results in loss of flexibility [7]. At the same time, in the global background of low carbon emission, cement industry is faced with great challenge as it contributed about 6% to total global anthropogenic CO_2 emission every year [8, 9]. Therefore, in order to produce more environmental friendly, ductile, and durable GFRC, efforts should be made to study the modified cement matrix with lower carbon emission, lower CH formation, and reduced alkalinity in the pore solution.

Calcium sulfoaluminate (CSA) cement is characterized as a kind of low carbon cementitious material due to lower calcium content in the raw materials and a lower burning temperature at 1250°C, which is about 200°C lower than that for the production of Portland cement. More importantly,

CSA cement has superior antifreeze property, high compressive strength, and durability [10–12]. In addition, extremely low alkalinity can also be discovered in the pore solution of CSA cement due to the absence of CH during hydration process [13], which can provide a less aggressive environment for the durability of embedded glass fibre. Therefore, CSA cement possesses great potential to produce more environmental friendly, ductile, and durable GFRC.

GFRC modified by CSA cement (CSA/GFRC) has aroused great attention among researchers, and many studies have been undertaken to investigate its mechanical properties and microstructural characteristics under different curing regimes [14–16]. Research by Peŕra and Ambroise [17] showed that CSA/GFRC exhibited rapid development of modulus of rupture, which reaches 8 MPa at 3 h, 9.3 MPa at 24 h, and 20.5 MPa at 28 d. Song et al. [15] demonstrated that CSA/GFRC still retained a large proportion of toughness after ageing for 10 years at 25°C. There were insignificant changes in the composite strength compared with the unaged sample, and the fibres still showed great ability to absorb energy and may control crack growth by bridging effect. Corresponding ultimate strain reduced to about 0.5% compared with a value of 0.8% for the unaged sample. Microstructural studies revealed that the space between and around the glass fibres was considerably vacant and porous. Research by Purnell and Beddows [5] reported that under accelerated ageing at 50°C for 140 d, tensile strength and ultimate strain of CSA/GFRC remained almost unchanged. However, at a longer age of 316 d under the same regime, corresponding ultimate tensile strength exhibited a medium reduction from 30 MPa to 22 MPa but the bridging effect provided by glass fibres was still obvious.

In cold environments, when the hydraulic pressure caused by freezing water exceeds the tensile strength of GFRC, local cracking may initiate which significantly threatens the safety and service life of GFRC structures. More importantly, freeze-thaw cycles generated under cold environment may cause multiphase damage media of water, ice, cement, and aggregate, and the uneven frost heaving force and deformation may subsequently lead to cracking propagation. It was reported that CSA cement has favorable antifreeze property due to the high compactness within the matrix which is beneficial to resist the freezing pressure and expansion pressure to some extent [12]. Research by Li et al. [18] indicated that flexural strength of CSA cement mortar was maintained 95% after 56 cycles of freeze-thaw were conducted. Janotka and Krajei [19] demonstrated that the dynamic modulus of elasticity of CSA cement mortar was maintained 95% after 34 cycles of freeze-thaw, and crack propagation was also observed on the surface of CSA cement mortar.

In conclusion, CSA cement has favorable antifreeze property and indicates great potential to produce durable GFRC under low temperatures. However, previous studies on CSA/GFRC mainly concentrated on its mechanical properties and microstructure characteristics under standard curing or hot water accelerated ageing while the performance of CSA/GFRC under cold temperatures remains not fully understood; this is of great significance before wider application of CSA/GFRC under low temperatures can be made. The present study aims to investigate the effect of low temperatures on the hydration mechanism, stress-strain performance, and freeze-thaw cycle property of CSA/GFRC, and the underlying microstructure changes are also investigated to correlate to the changes in macroproperties.

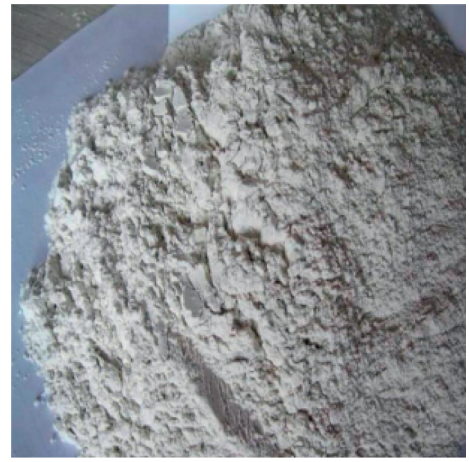

Figure 1: Commercial CSA cement used in the present study.

2. Materials and Methods

2.1. Materials. To produce CSA/GFRC, commercial CSA cement produced by Dengdian Cement Group in China was used in the present study, as shown in Figure 1. CSA cement and OPC were mixed with a ratio of 3 : 7, and quartz sand was added with a sand to cement ratio of 1 : 1. A water to cement ratio of 0.3 was applied in this study. Chemical compositions of CSA cement and ordinary Portland cement (OPC) used in this study are listed in Table 1. In order to improve the brittleness of cementitious materials, 0.5 wt. % glass fibre was added in the dry mix to produce CSA/GFRC composites. Glass fibre was chopped and randomly orientated in the form of bundles. The detailed mixing design is listed in Table 2.

2.2. Experimental Work

2.2.1. XRD Analysis. Corresponding cement pastes were prepared for XRD analysis to investigate the hydration products of CSA-based cement under low temperatures. XRD was carried out by Bruker D8 using CuKα1 radiation, and XRD data of the powder samples were collected in a 2θ range of 5° to 60° with a step size of 0.02°. After casting for 24 h, the specimens were cured in a water bath set at a temperature of 20 ± 1°C. At a curing age of 7 d, the samples were ground into fine powder and then applied in the XRD equipment for testing.

2.2.2. Mechanical Testing. CSA/GFRC was cast in two different sizes, i.e., a thin slab size (250 mm × 50 mm × 10 mm) for stress-strain performance testing and a cubic size

Table 1: Chemical compositions of CSA and OPC cement.

Composition (%)	SiO_2	Al_2O_3	Fe_2O_3	CaO	MgO	SO_3	TiO_2	Loss
CSA	8.92	32.15	1.32	44.68	1.71	8.92	1.85	0.54
OPC	19.38	4.99	1.96	63.69	2.33	4.95	0.47	2.23

Table 2: Mixing design of CSA/GFRC.

OPC (kg/m^3)	CSA (kg/m^3)	Water (kg/m^3)	Sand (kg/m^3)	Retarder (kg/m^3)	Glass fibre (wt. %)
666.7	285.7	285.7	952.4	4.8	0.5

(100 mm × 100 mm × 100 mm) for both compressive strength and antifreeze testing. After casting for 24 h, they were demolded and continued to be cured under different temperatures (−5°C, 0°C, 5°C, and 20°C) for 1, 3, 7, 14, and 28 d.

Four-point bending test was undertaken by Tinius Olsen H25KS with a major span of 200 mm and a load rate at 1.8 mm/min; relative experimental setup is shown in Figure 2. In this study, stress-strain performance of CSA/GFRC under −5°C, 0°C, 5°C, and 20°C for 1, 3, 7, 14, and 28 d was tested, respectively. In order to investigate the durability of CSA/GFRC under cold climates, antifreeze testing was also undertaken according to Chinese Standard GB/T50082-2009 (the standard for test method of long-term performance and durability of ordinary concrete). Before testing, the reference samples were still kept under the standard curing condition, but the specimens for antifreeze testing were taken out and then restored in water at 20 ± 1°C for 4 d. Then, CSA/GFRC samples were weighed and then put in the freeze-thaw testing chamber (set at −5°C, 0°C, and 5°C) for 6 h.

2.2.3. Microstructure Analysis. SEM was undertaken by JEOL JSM-5800LV equipped with EDX. Backscattered electron imaging mode was selected to characterize the morphologies on polished surfaces of CSA/GFRC. Elemental mapping was applied to investigate the arrangement of chemical elements within the matrix. In order to investigate the chemical compositions at the interfilamentary space, three representative points at the interfilamentary space were selected to give overall information on the hydrated phases between fibres.

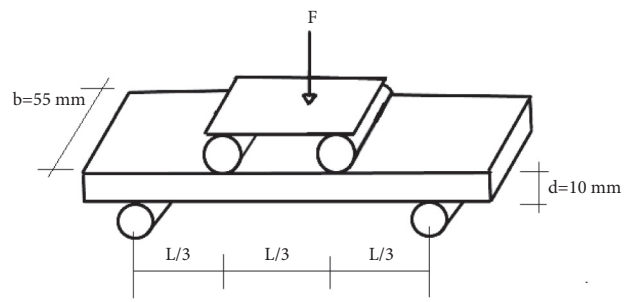

Figure 2: Experimental setup of the four-point bending test.

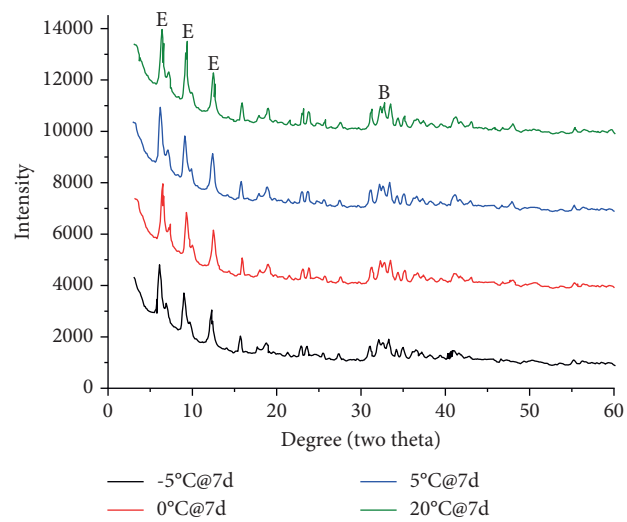

Figure 3: XRD pattern of CSA pastes cured at −5°C, 0, 5°C, and 20°C at 7 d.

3. Results and Discussion

3.1. XRD Analysis. XRD results of corresponding CSA cement pastes cured at −5, 0, 5, and 20°C for 7 d are shown in Figure 3. It can be found out that low-temperature environments have very little effect on the type of hydration products of CSA modified cement. Crystalline CH is still absent, and large amounts of ettringite can be traced in all the specimens of CSA modified cement under low-curing temperatures, which is in agreement with the previous research [14, 16]. The sharp peak of ettringite in the CSA paste cured at −5°C suggests that hydration of CSA cement still continues at lower temperature, which is beneficial for the development of both strength and densified microstructure. It was reported that formation of ettringite was extremely sensitive to curing temperatures and decreased levels of ettringite are generated under low temperatures [12]. This is because lower curing temperature is not conducive to the breaking of chemical bond and thus may lead to a slower nucleation rate of ettringite, especially for those below 0°C [16]. In addition, a broad peak at about 32° indicates remnants of unhydrated belite clinker in all the specimens. This can be explained that hydration of calcium sulfoaluminate initiates rapidly once in contact with water, and it continues readily in the first 1-2 days; therefore, insufficient water will be remained for the hydration of belite at early ages [20]. In particular, the broad peak of belite remnants in

the CSA paste cured at −5°C suggests that hydration degree of CSA cement is limited to some extent under lower temperatures [21].

3.2. Compressive Strength. Compressive strength of CSA/GFRC cured under −5, 0, 5, and 20°C for 1 d, 3 d, 7 d, and 28 d is shown in Figure 4. It can be found out that low-curing temperatures, especially those below 0°C, have an adverse effect on the compressive strength development of CSA/GFRC. At an early age of 1 d, CSA/GFRC under lower temperatures exhibited an extremely low compressive strength compared with that cured at 20°C. The corresponding compressive strength is only 8.2 MPa, 10.5 MPa, and 16.7 MPa under −5°C, 0°C, and 5°C, which is 35.8%, 45.8%, and 72.9% of that cured at 20°C. This is because ettringite is the main contributions to the early strength of CSA cement and reduced ettringite is generated at lower curing temperatures owning to a reduced nucleation rate [12]. With increasing curing ages, CSA/GFRC obtained quick strength development under lower temperatures, and strength difference with that under 20°C is reduced gradually. In detail, compressive strength reaches 40.3 MPa, 47.2 MPa, and 50.2 MPa under −5°C, 0°C, and 5°C for 28 d, which occupies 67.7%, 79.3%, and 84.4% of that under 20°C. The relatively rapid strength development of CSA/GFRC under low-curing temperatures suggests that it can ensure the basic construction requirement in winter, and further mechanical performance needs to be investigated before wider application can be made.

3.3. Stress-Strain Performance. Stress-strain performances of CSA/GFRC cured under low temperatures for 1 d, 7 d, 14 d, and 28 d are illustrated in Figure 5. It can be observed that there is insignificant changes in the ultimate strain value at low temperatures at 1 d, which is 0.67% for −5°C, 0.78% for 0°C, and 0.87% for 5°C, respectively, compared with 0.82% for 20°C. However, low-curing temperatures have an adverse effect on the ultimate tensile strength of CSA/GFRC at early ages. It reduces to ~25 MPa at 5°C, 23 MPa at 0°C, and 18 MPa at −5°C, which is 83.3%, 76.7%, and 60.0% compared with that at 20°C.

With a progressive curing age until 14 d, CSA/GFRC demonstrates slight degradation in stress but it still exhibits great ductility properties. At a longer curing age of 28 d, there are obvious reductions in both ultimate strain value and ultimate tensile strength. For example, the ultimate strain value reduces to 0.34% at −5°C, 0.39% at 0°C, and 0.44% at 5°C compared with 0.51% for that cured at 20°C. The tensile strength of samples cured at −5°C for 28 d is only 15.2 MPa, taking up only 40% of that under 20°C.

It can be concluded that there is less influence of low-curing temperatures on the ductility properties of CSA/GFRC at early ages; however, both ultimate tensile strength and ultimate strain value indicate medium degradation after 14 d. This degradation process is similar to the previous results on CSA/GFRC [5, 16], in which CSA/GFRC indicates gradual and medium reduction on both strength and ductility under accelerated ageing.

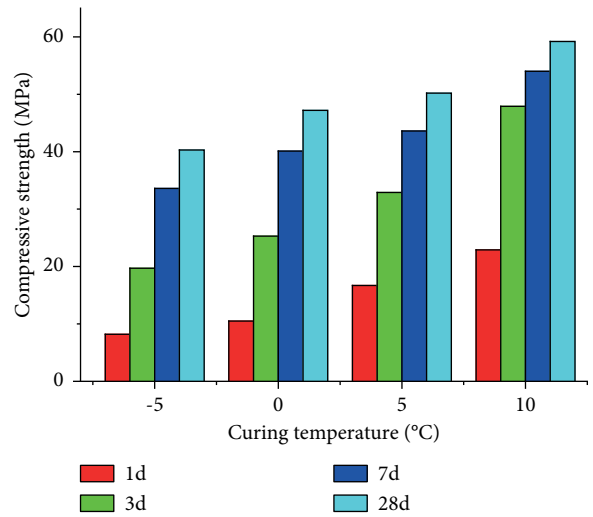

Figure 4: Compressive strength of CSA/GFRC at −5, 0, 5, and 20°C.

3.4. Freeze-Thaw Performance. The compressive strength of CSA/GFRC under freeze-thaw attack is present in Figure 6. It can be found out that with increasing freeze-thaw cycles, compressive strength of CSA/GFRC indicates gradual reduction and this strength reduction is more evident with lower curing temperatures. Beneficial freeze-thaw resistance property can be observed in CSA/GFRC, and the corresponding strength remains 95.9%, 94.7%, 94.2%, and 94.3%, respectively, for that cured under 20°C, 5°C, 0°C, and −5°C after 50 freeze-thaw cycles. This is in consistence with the previous research [18, 19], suggesting that reduction in both flexural strength and dynamic modulus of elasticity of CSA cement mortar is less than 5% after more than 30 cycles of freeze-thaw. The favorable freeze-thaw resistance of CSA/GFRC provides great confidence in its application under low temperatures.

3.5. Microstructure at Interfilamental Space. Microstructure of CSA/GFRC cured at −5°C for 28 d is present in Figure 7. It can be seen from Figure 7(a) that the interfilamentary spaces are partly occupied by hydration products, with some empty voids between fibres occasionally. This densification at the interfilamentary space may result in loss on flexibility when forces are applied [22, 23], which subsequently reduce the post-peak toughness of CSA/GFRC to some extent. This is in agreement with the previous studies concluding that partial densification of the space between fibres by hydrated products may become a deciding microstructural factor in the degradation of GFRC [3, 13, 14]. Elemental mappings were also obtained in this study to investigate the spatial distributions of Ca, S, and Al as shown in Figure 7(b). It can be concluded that elements of Ca, Si, and S are accumulated in the interfilamentary spaces.

In order to investigate the chemical compositions of the hydration phases, spot analysis on three representative points located between fibres is listed in Figure 7(c). The spot analysis results on Point 1 showed a medium accumulation of Ca and S at the interfilamentary zone, involving 26.1 wt. % Ca and 10.0

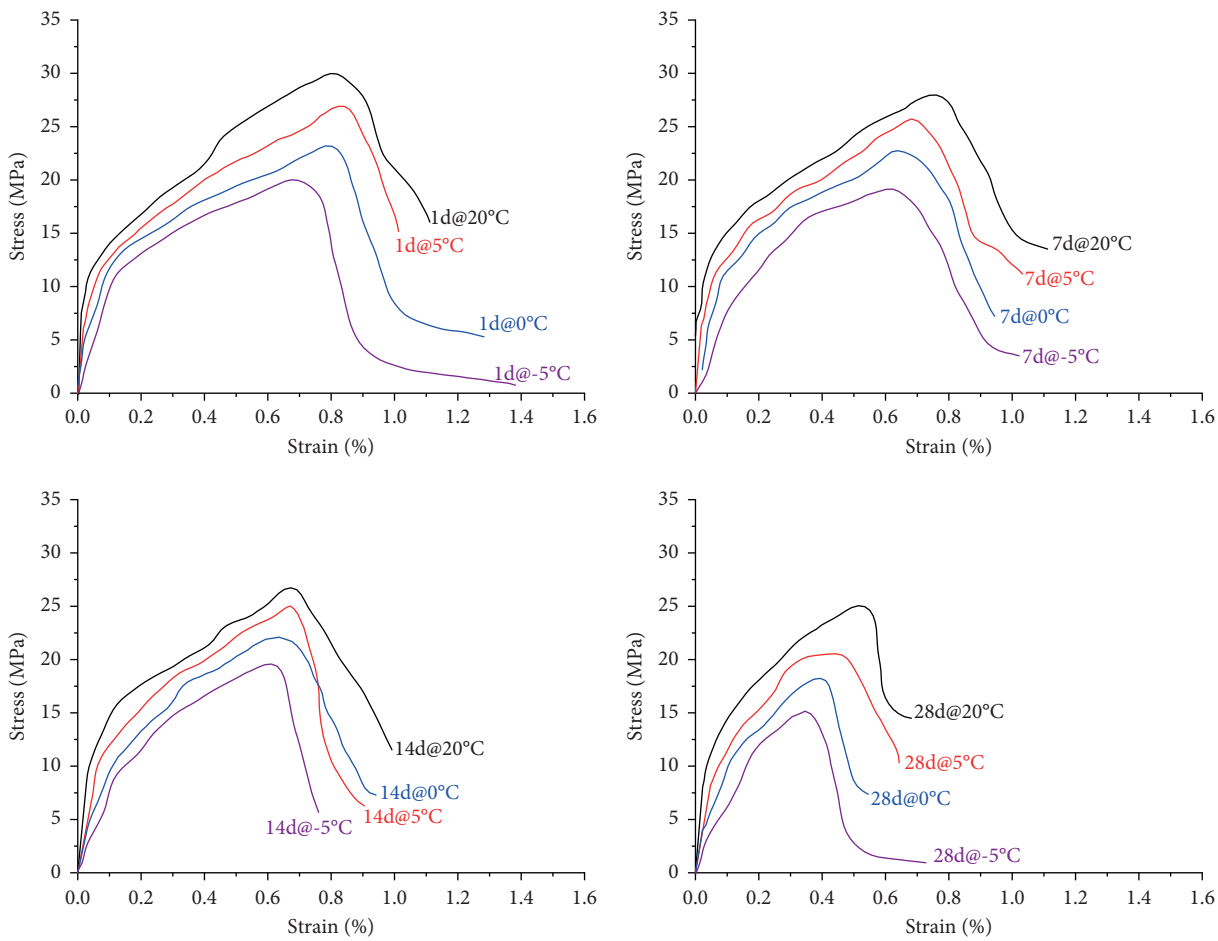

Figure 5: Stress-strain curves of CSA/GFRC at −5, 0, 5, and 20°C at different ages.

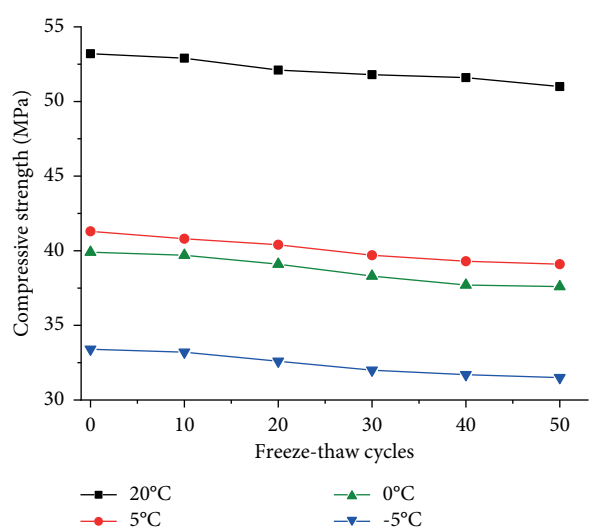

Figure 6: Compressive strength after freeze-thaw cycles.

wt. % S, with small amounts of Al and Si included as well. The corresponding Al/Ca was 0.36 and S/Ca ratio was 0.48 at Point 1, which is considered as ettringite-type phases (Al/Ca = 0.33, S/Ca = 0.5) with small inclusions of C-A-S-H gel. The Al/Ca of Point 2 and 3 reaches 0.54 and 0.55, respectively, with corresponding S/Ca of 0.17 and 0.14. This suggests an increased level of Al inclusion and reduced level of S compared with Point 1. It can be presumed that the main hydration phases at the two points are ettringite intermixed with larger amount of C-A-S-H. Therefore, it can be concluded that hydrated phases

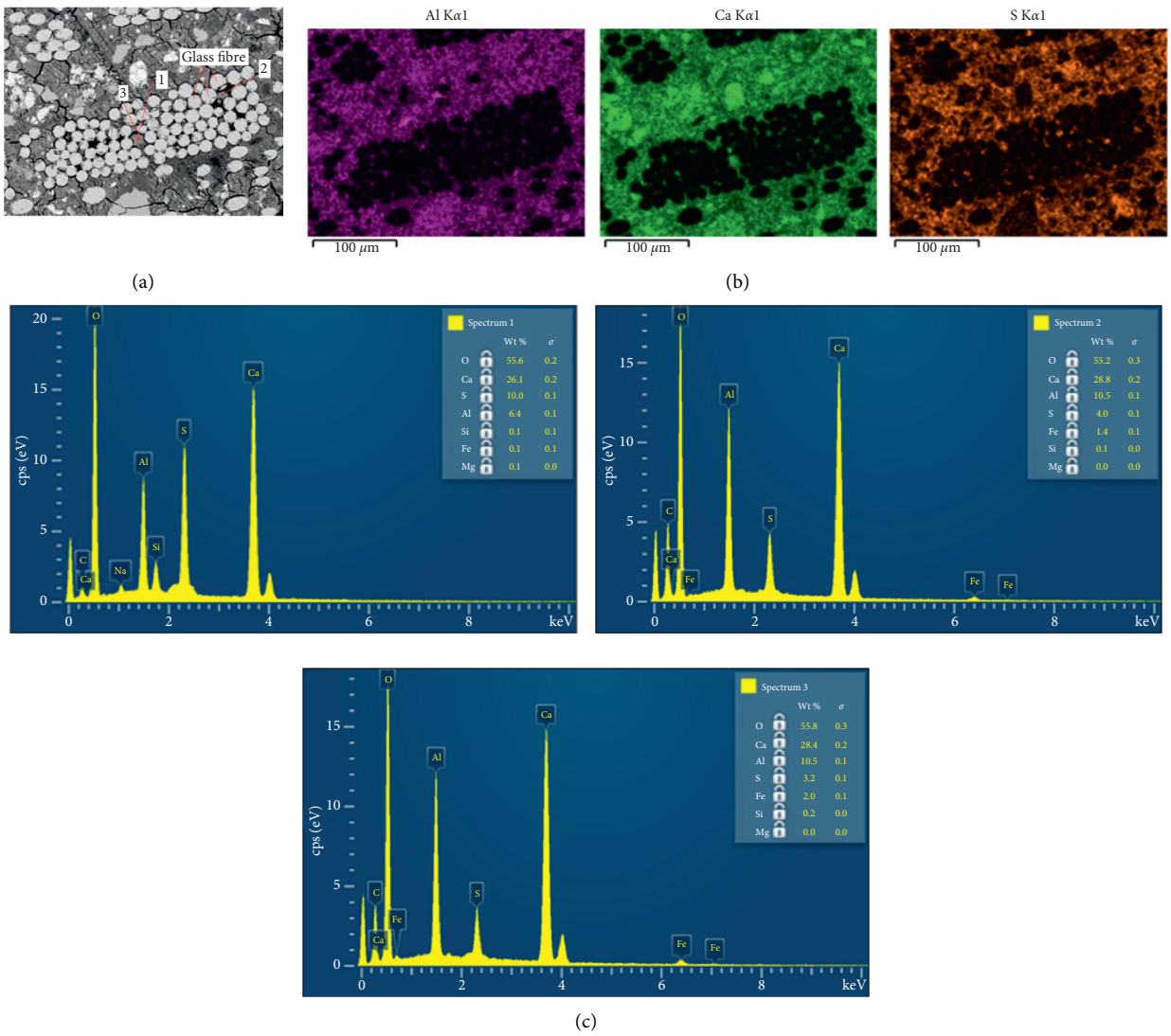

Figure 7: Microstructure of CSA/GFRC cured at −5°C for 28 d: (a) microstructure at interfilamentary spaces; (b) elemental mappings of Ca, Al, and S in CSA/GFRC; (c) EDX result on Point 1, 2, and 3 at the interfilamentary space.

at the interfilamentary space of CSA/GFRC cured under low temperature are mainly ettringite phases finely intermixed with C-A-S-H gels at varying proportions.

4. Conclusions

It can be concluded that low-temperature environment has very little effect on the type of hydration products in hydrated CSA cement. The main hydration product of hydrated CSA cement cured under low temperatures is ettringite which suggests that hydration of CSA cement still continues under lower temperatures.

It can also be found out that low-curing temperatures have an adverse effect on the strength development of CSA/GFRC, but the strength difference compared with that under 20°C reduces gradually with increasing curing ages. Corresponding compressive strength is 40.3 MPa, 47.2 MPa, and 50.2 MPa under −5°C, 0°C, and 5°C for 28 d, which occupies 67.7%, 79.3%, and 84.4% of that under 20°C.

In terms of bending performance, there are insignificant changes in ultimate strain value at low temperatures at early ages, however, but both ultimate tensile strength and ultimate strain value indicate considerable degradation with ageing under low temperatures after 14 d. The ultimate strain value reduces to 0.34% at −5°C, 0.39% at 0°C, and 0.44% at 5°C compared with 0.51% for that cured at 20°C for 28 d. The tensile strength of samples cured at −5°C for 28°d is only 15.2 MPa, taking up only 40% of that under 20°C.

CSA/GFRC also demonstrated great capability in the antifreeze-thaw performance. The corresponding strength remains 95.9%, 94.7%, 94.2%, and 94.3%, respectively, for that cured under 20°C, 5°C, 0°C, and −5°C after 50 freeze-thaw cycles.

Microstructural studies suggest that the interfilamentary spaces are partly occupied by hydration products, with some empty voids between fibres occasionally. Spot analysis on three representative points at the interfilamentary space demonstrates that hydrated phases at the interfilamentary

space of CSA/GFRC cured under low temperature are mainly ettringite phases finely intermixed with C-A-S-H gels at varying proportions. This densification may result in loss on flexibility when forces are applied, therefore reducing the post-peak toughness to some extent. Therefore, studies on how to optimize the interfilamentary spaces with more flexibility are necessary before durable CSA/GFRC can be created and applied in field under low temperatures.

Data Availability

The data used to support the findings of this study are available from the corresponding author upon request.

Conflicts of Interest

The authors declare that there are no conflicts of interest.

Acknowledgments

This project was funded by the National Natural Science Foundation of China (No. 51674199), Key Laboratory of Structure and Wind Tunnel of Guangdong Higher Education Institutes Open Fund (No. 202002), and Natural Science Basic Research Program of Shaanxi Province (No. 2021JQ-605).

References

[1] J. G. Ferreira and F. A. Branco, "Structural application of GRC in telecommunication towers," *Construction and Building Materials*, vol. 21, no. 1, pp. 19–28, 2007.

[2] A. Enfedaque, L. S. Paradela, and V. Sánchez-Gálvez, "An alternative methodology to predict aging effects on the mechanical properties of glass fiber reinforced cements (GRC)," *Construction and Building Materials*, vol. 27, no. 1, pp. 425–431, 2012.

[3] M. Butler, V. Mechtcherine, and S. Hempel, "Durability of textile reinforced concrete made with AR glass fibre: effect of the matrix composition," *Materials and Structures*, vol. 43, no. 10, pp. 1351–1368, 2010.

[4] A. Enfedaque, D. Cendón, F. Gálvez, and V. Sánchez-Gálvez, "Failure and impact behavior of facade panels made of glass fiber reinforced cement (GRC)," *Engineering Failure Analysis*, vol. 18, no. 7, pp. 1652–1663, 2011.

[5] P. Purnell and J. Beddows, "Durability and simulated ageing of new matrix glass fibre reinforced concrete," *Cement and Concrete Composites*, vol. 27, no. 9-10, pp. 875–884, 2005.

[6] A. Nourredine, "Influence of curing conditions on durability of alkali-resistant glass fibres in cement matrix," *Bulletin of Materials Science*, vol. 34, no. 4, pp. 775–783, 2011.

[7] M. A. Boumehraz, M. Mellas, K. Goudjil, and F. Boucetta, "Study of the aging of a concrete reinforced by alkali resistant glass fiber in the wet environment," *Annales de Chimie Science des Matériaux*, vol. 44, no. 2, pp. 85–90, 2020.

[8] J. S. Damtoft, J. Lukasik, D. Herfort, D. Sorrentino, and E. M. Gartner, "Sustainable development and climate change initiatives," *Cement and Concrete Research*, vol. 38, no. 2, pp. 115–127, 2008.

[9] F. P. Glasser and L. Zhang, "High-performance cement matrices based on calcium sulfoaluminate–belite compositions," *Cement and Concrete Research*, vol. 31, no. 12, pp. 1881–1886, 2001.

[10] C. Hu, D. Hou, and Z. Li, "Micro-mechanical properties of calcium sulfoaluminate cement and the correlation with microstructures," *Cement and Concrete Composites*, vol. 80, pp. 10–16, 2017.

[11] L. H. J. Martin, F. Winnefeld, E. Tschopp, C. J. Müller, and B. Lothenbach, "Influence of fly ash on the hydration of calcium sulfoaluminate cement," *Cement and Concrete Research*, vol. 95, pp. 152–163, 2017.

[12] T. Lee, J. Lee, and H. Choi, "Effects of accelerators and retarders in early strength development of concrete based on low-temperature-cured ordinary Portland and calcium sulfoaluminate cement blends," *Journal of Materials*, vol. 13, no. 7, p. 1505, 2020.

[13] R. Trauchessec, J. M. Mechling, A. Lecomte, A. Roux, and L. Rolland, "Hydration of ordinary Portland cement and calcium sulfoaluminate cement blends," *Cement and Concrete Composites*, vol. 56, pp. 106–114, 2015.

[14] M. Borstnar, N. Daneu, and S. Dolenec, "Phase development and hydration kinetics of belite-calcium sulfoaluminate cements at different curing temperatures," *Ceramics International*, vol. 46, no. 18, pp. 29421–29428, 2020.

[15] M. Song, P. Purnell, and I. Richardson, "Microstructure of interface between fibre and matrix in 10-year aged GRC modified by calcium sulfoaluminate cement," *Cement and Concrete Research*, vol. 76, pp. 20–26, 2015.

[16] M. Song, K. Wu, and Y. Dou, "Durability of GFRC modified by calcium sulfoaluminate cement under elevated curing temperatures," *Advances in Materials Science and Engineering*, vol. 2019, Article ID 2915684, 6 pages, 2019.

[17] J. Péra and J. Ambroise, "New applications of calcium sulfoaluminate cement," *Cement and Concrete Research*, vol. 34, no. 4, pp. 671–676, 2004.

[18] L. Li, R. Wang, and Q. Lu, "Influence of polymer latex on the setting time, mechanical properties and durability of calcium sulfoaluminate cement mortar," *Construction and Building Materials*, vol. 169, pp. 911–922, 2018.

[19] I. Janotka and L. È Krajèi, "Resistance to freezing and thawing of mortar specimens made from sulphoaluminate-belite cement," *Bulletin of Materials Science*, vol. 23, no. 6, pp. 521–527, 2000.

[20] Q. Huang, X. Zhu, D. Liu, L. Zhao, and M. Zhao, "Modification of water absorption and pore structure of high-volume fly ash cement pastes by incorporating nanosilica," *Journal of Building Engineering*, vol. 33, no. 3, Article ID 101638, 2020.

[21] X. Zhu, M. Zhang, Y. Yang, K. Yang, and F. Wu, Q. Li, L. Yu, C. Yang, and M. Basheer, "Understanding the aqueous phase of alkali-activated slag paste under bath-curing," *Advances in Cement Research*, vol. 33, no. 2, pp. 1–33, 2019.

[22] J. Gong, Z. Li, R. Zhang, J. Li, and X. Shi, "Synergistic effects of nano-montmorillonite and polyethylene microfiber in foamed paste with high volume fly ash binder," *Journal of Nanoscience and Nanotechnology*, vol. 19, pp. 4465–4473, 2019.

[23] Z. Li, J. Gong, S. Du et al., "Nano-montmorillonite modified foamed paste with a high volume fly ash binder," *RSC Advances*, vol. 7, p. 9803, 2017.

Hindawi
Advances in Civil Engineering
Volume 2021, Article ID 9134889, 11 pages
https://doi.org/10.1155/2021/9134889

Research Article

Experimental Research on Thermomechanical Properties of Thermal Energy Storage Cement Mortar Incorporated with Phase-Change Material

Kunyang Yu,[1,2] **Yong Huang**,[1] **Bo Jin**,[1] **and Yushi Liu**[1,2]

[1]*Key Laboratory of Earthquake Engineering and Engineering Vibration, Institute of Engineering Mechanics, China Earthquake Administration, Harbin, China*
[2]*School of Civil Engineering, Harbin Institute of Technology, Harbin 150090, China*

Correspondence should be addressed to Bo Jin; jinbo@iem.ac.cn and Yushi Liu; liuyushi@hit.edu.cn

Received 13 April 2021; Revised 8 July 2021; Accepted 3 August 2021; Published 11 August 2021

Academic Editor: Filippo Ubertini

In the current work, the thermal energy storage cement mortars were prepared by physical mixing between cement mortar and form-stable hydrated salt based on disodium hydrogen phosphate dodecahydrate/carbon nanofiber-expanded graphite (DSP/CNF-EG). The DSP/CNF-EG was incorporated into cement mortar through replacing standard sand of 5 wt%, 10 wt%, and 15 wt%. The pore structure results obtained from the mercury intrusion porosimeter (MIP) demonstrated that the incorporation of DSP/CNF-EG form-stable hydrated salt PCM can cause the increased porosity of the cement mortar. The mechanical strengths of the thermal energy storage cement mortars were decreased with increasing DSP/CNF-EG incorporation amount, and they still meet the strengths of the building envelope. Moreover, dynamic mechanical analysis (DMA) results suggested that the damping properties of the thermal energy storage cement mortar were enhanced by incorporating DSP/CNF-EG, which were related to the porosity and the internal friction action. In addition, the thermal conductivity and the specific heat capacity results confirmed that the introduction of DSP/CNF-EG can endow cement mortar with excellent thermal energy storage capacity. The thermal performance test further indicated that the thermal energy storage cement mortar showed good endothermic and exothermic characteristics, and it played a prominent role in weakening the indoor temperature peak.

1. Introduction

With the continuous consumption of fossil fuels, the issue of energy shortage is becoming increasingly serious. In particular, energy applied in buildings accounts for more than 30% of the global total energy consumption [1]. Therein, the energy consumption of thermal form is dominant. For this reason, thermal energy storage building materials have been developed by incorporating phase-change materials (PCMs) into building materials. [2, 3]. The building materials incorporating PCMs can realize the building energy saving relied on the feature of PCMs absorbing and releasing heat during the phase transition. Moreover, building thermal fluctuation can be mitigated based on the latent heat storage capacity of PCMs as well [4, 5]. Therefore, building energy saving and indoor thermal comfort are achieved by the incorporation of PCMs into building materials [6, 7].

The typical building materials include concrete [8–13], cement mortars [14, 15], and gypsum [16, 17]. Among various building materials, cement mortars have been widely used in walls and are highly suitable for the incorporation of PCMs due to the larger area occupied in doors. The incorporation approaches of PCMs into the cement mortar mainly include three kinds: one is that PCMs are directly immersed into the cement mortar [18], the second is that PCMs are encapsulated and then incorporated into cement mortar [19], and the third is that macroencapsulated PCMs [20] or composite PCMs [21] are integrated into the cement mortar in the form of layered panels. Although the direct immersion method is simple and of low cost, PCMs are easy

to seep from cement mortar undergoing several heating-cooling cycles. This is unacceptable due to the large loss of heat storage capacity. As for layered panels containing PCMs, the layered structure leads to the increase in wall thickness, inevitably occupying a lot of building space. The encapsulated PCMs (also known as form-stable PCMs) can effectively avoid the leakage of PCMs. In recent years, a large number of thermal energy cement mortars containing form-stable PCM (FSPCM) were developed. For example, Sang et al. [22] prepared a kind of thermal energy storage cement-based mortar with good thermal performance by incorporating 25.9 wt% form-stable organic PCM. He et al. [23] synthetized a fatty acid/expanded perlite FSPCM, and then the FSPCM was added into the cement mortar to form the phase-change mortar composite. The results indicated that the air temperature of the simulated indoor box was well controlled using this composite. Sun and Wang [24] adopted epoxy resin to coat the FSPCM with paraffin core material and expanded perlite support and then explored the influence of the FSPCM incorporation amount on the mechanical properties of the prepared phase-change mortar. It turned out that the compressive and flexural strengths of the phase-change mortar were decreased by increasing the FSPCM content. Ramakrishnan et al. [25] used paraffin/hydrophobic expanded perlite FSPCM to replace 80 vol.% quartz sand to prepare the thermal energy storage mortar. It was found that the compressive strength of the mortar cured by 28 days was decreased by 66.7% compared with that of the control mortar. Zhang et al. [26] investigated the evolution of compressive strength of cement mortar containing octadecane/expanded graphite FSPCM. The result suggested that the compressive strength of the mortar showed a significant deterioration from 23.7 MPa to 10.5 MPa when octadecane/expanded graphite FSPCM reached to 2.5% incorporating amount. Xu et al. [27] developed a lightweight mortar with thermal energy storage capacity using paraffin/expanded vermiculite FSPCM to completely replace the river sand. The 28-day compressive strength of the lightweight mortar was 18.1 MPa, which was decreased by 56.5% compared with that of the mortar with river sand.

Based on the above research situation, most of research studies only adopted form-stable organic PCMs to fabricate the thermal energy storage mortar. However, the features of higher cost and lower latent heat of organic PCMs severely limit their applications in buildings. In addition, the universal flammability of organic PCMs also rises building fire risk [28]. Inorganic hydrated salt PCMs have been attracting increasing attention for thermal energy storage due to the advantages of low cost, high latent heat, nonflammability, etc. [29, 30]. Moreover, the phase-change temperature of most inorganic hydrated salt PCMs is closer to the temperature range of indoor thermal comfort compared to the organic PCMs [29]. Hence, form-stable inorganic PCMs have a promising application in terms of preparing thermal energy storage mortar.

In addition, the mechanical properties of cement mortar containing form-stable PCMs should be inspected as well since its good mechanical properties can ensure the favorable workability and serviceability. Nevertheless, the current research studies have been only focused on the static mechanical properties such as compressive strength and flexural strength of the cement mortar incorporating form-stable PCM. The results from the reported works indicated that the static mechanical properties of the cement mortar incorporating form-stable PCM were significantly deteriorated. Moreover, the degradation level of static mechanics increases with the increase of the percentage of form-stable phase-change materials [31]. The reasons could be explained by the poor compatibility between the form-stable PCM and cement matrix and the soft matter nature of form-stable PCMs [32]. These two reasons lead to the increase of porosity and the decrease of local elastic modulus of cement mortar. Although some efforts have been made to study the incorporation of form-stable PCMs on the static mechanical properties of cement mortar, to date, the research on the dynamic mechanical properties for cement mortar incorporating form-stable PCMs is hardly found in the literature studies.

Notably, the introduction of form-stable PCMs into mortar usually results in the increased porosity and the decreased elastic modulus of mortar. However, the dynamic mechanical properties of mortar are greatly affected by the changes in the porosity and the elastic modulus. In particular, the energy dissipation for cement mortar under dynamic load will be enhanced through the increase of porosity and the decrease of elastic modulus [33]. Therefore, it can be expected that the ability of cement mortar to resist some dynamic actions may be enhanced by the incorporation of form-stable PCMs.

In our group's previous work, a novel disodium hydrogen phosphate dodecahydrate/carbon nanofiber-expanded graphite (DSP/CNF-EG) hybrid composite with a melting temperature of 33.7°C and latent heat of 208.9 J/g was developed as a form-stable hydrated salt PCM for building energy saving. In this work, we used DSP/CNF-EG to prepare a novel thermal energy storage cement mortar based on the mechanical blending between cement mortar and DSP/CNF-EG. The compressive strength, flexural strength, pore structure, thermal conductivity, specific heat capacity, and thermal energy storage performance of the cement mortar containing DSP/CNF-EG were investigated. In addition, the damping property of the prepared thermal energy storage cement mortar was tested to evaluate its dynamic mechanical performance.

2. Materials and Methods

2.1. Raw Materials. The PO 42.5 ordinary Portland cement was supplied by Yatai Co., Ltd., and the physical properties are shown in Table 1. The standard sand was obtained from Sinoma Co., Ltd. Based on the synthetic method described by our previous work [34], the disodium hydrogen phosphate dodecahydrate/carbon nanofiber-expanded graphite (DSP/CNF-EG) form-stable hydrated salt phase-change material was prepared, and the average particle size of DSP/CNF-EG used in this work was consistent with that of standard sand (≤2 mm). The specific preparation process of DSP/CNF-EG was as follows: first, 50 g disodium hydrogen

Table 1: Physical properties of the PO 42.5 ordinary Portland cement.

Setting time (min)		Compressive strength (MPa)		Flexural strength (MPa)	
Initial setting	Final setting	3 d	28 d	3 d	28 d
185	239	16.9	46.6	4.8	7.5

phosphate dodecahydrate (DSP) was poured into a beaker kept in the thermostatic water bath at 65°C and melted to form the clear and transparent solution; afterwards, 0.75 g carbon nanofiber (CNF) was added into the DSP solution, followed by stirring it for 2 hours at 1600 rpm; then, 1 g expanded graphite (EG) was further added into the DSP/CNF suspension, and the mixture was continued to stir for 6 hours at 65°C; lastly, DSP/CNF-EG was obtained via the suction filtration method.

2.2. Preparation and Characterization of Thermal Energy Storage Cement Mortar Containing Form-Stable Hydrated Salt PCM

2.2.1. Mix Proportion. The mix proportion of control cement mortar (CM) is shown in Table 2. Three thermal energy storage cement mortar (TESCM) samples were fabricated by incorporating DSP/CNF-EG into the cement mortar using physical mixing. The specific process is as follows: firstly, a certain amount of DSP/CNF-EG and sand were fully mixed in an agitator for 3 min at 125 rpm; afterwards, cement and water were poured into the agitator and further stirred for 3 min; finally, the thermal energy storage mortar samples were casted in mould. Figure 1 presents the schematic illustration of fabricating thermal energy storage cement mortar containing DSP/CNF-EG by physical blending. DSP/CNF-EG was introduced into CM through partially replacing standard sand. The replacement levels of DSP/CNF-EG were 0, 5 wt%, 10 wt%, and 15 wt%, respectively. The CMs with different replacement levels of DSP/CNF-EG were named as DSP/CNF-EG/CM-3.3, DSP/CNF-EG/CM-6.7, and DSP/CNF-EG/CM-10 based on the mass ratio of DSP/CNF-EG to DSP/CNF-EG/CM.

2.2.2. Compressive Strength and Flexural Strength Test. The CM and DSP/CNF-EG/CM were casted into 40 mm × 40 mm × 160 mm moulds followed by curing in the condition of 20 ± 2°C and relative humidity (RH) ≥ 99% for 28 days. 28-day compressive strengths and 28-day flexural strengths of CM and DSP/CNF-EG/CM samples were tested based on ISO 679:1989 and GB/T 17671-1999. For each sample, the tests were repeated 3 times, and the strength value of each data point was represented as mean ± standard deviation.

2.2.3. Pore Structure Analysis. The pore structure distribution of CM and DSP/CNF-EG/CM samples was measured by an IV 9510 mercury intrusion porosimeter (MIP), and the pressure was set within the range of 0–60,000 psi. The samples were cut into about 4-5 mm particles.

2.2.4. Thermal Conductivity and Specific Heat Capacity Measurement. The thermal conductivity and specific heat capacity of CM and DSP/CNF-EG/CM samples were measured by using a laser thermal conductivity measuring instrument (NETZSCH, Newsletter-LFA467). The size of the samples was $9.5 \times 9.5 \times 2.0\,\text{mm}^3$.

2.2.5. Thermal Performance Test. The self-designed heating setup (Figure 2) was carried out for evaluating the thermal performance of CM and DSP/CNF-EG/CM samples. As shown in Figure 2, the self-designed heating setup mainly contained a 100 W infrared lamp mounted on the top bracket, a polystyrene test box, and the multichannel temperature measuring system. A rectangular opening was cut at the upper surface center of the test box to place CM and DSP/CNF-EG/CM samples with the size of $200 \times 150 \times 20\,\text{mm}^3$. Two thermocouples were, respectively, fixed on the lower surface of the samples and the center of the test box to record the temperature change. The temperature data were recorded every 5 min. The infrared lamp was used as the heating source to heat the samples for 80 min. Subsequently, the infrared lamp was turned off, and the sample was naturally cooled for 120 min.

2.2.6. Damping Properties' Test. The damping properties' test procedure of the samples was provided by Yu et al. [35]. Dynamic mechanical analysis (DMA Q800, TA Instruments) was used to measure the damping properties of CM and DSP/CNF-EG/CM samples with the size of 40 mm × 10 mm × 2 mm. The samples were tested in the three-point bending mode with a span of 50 mm at 20°C. The sine waves with a frequency of 0.2 Hz were collected, and the displacement amplitude was 10 μm. Three parameters of loss tangent (η), storage modulus (E'), and loss modulus (E'') relating to the damping properties were obtained.

3. Results and Discussion

3.1. Pore Structure Analysis of DSP/CNF-EG/CM. The pore structure analysis results of CM and DSP/CNF-EG/CM samples cured for 28 days are shown in Figure 3. Figure 3(a) presents the pore diameter distribution of CM, DSP/CNF-EG/CM-3.3, DSP/CNF-EG/CM-6.7, and DSP/CNF-EG/CM-10. It can be found that the pores of DSP/CNF-EG/CM in the range of 100 nm–100 μm significantly increased with the increase of the replacement amount of DSP/CNF-EG form-stable hydrated salt PCM. Figure 3(b) shows the relationship between cumulative mercury pore volume and pore diameter of CM, DSP/CNF-EG/CM-3.3, DSP/CNF-EG/CM-6.7, and DSP/CNF-EG/CM-10. It can be seen that the curves of DSP/CNF-EG/CM samples deviated the direction of larger pore size. Moreover, the deviation became more obvious as the incorporation of DSP/CNF-EG increased. In order to present the detailed difference in the

Table 2: Mix proportion of cement mortar.

Water/cement	Cement/standard sand	DSP/CNF-EG replacing sand amount	Mass ratio of DSP/CNF-EG to DSP/CNF-EG/CM
1 : 2	1 : 3	0	0
		5 wt%	3.3 wt%
		10 wt%	6.7 wt%
		15 wt%	10.0 wt%

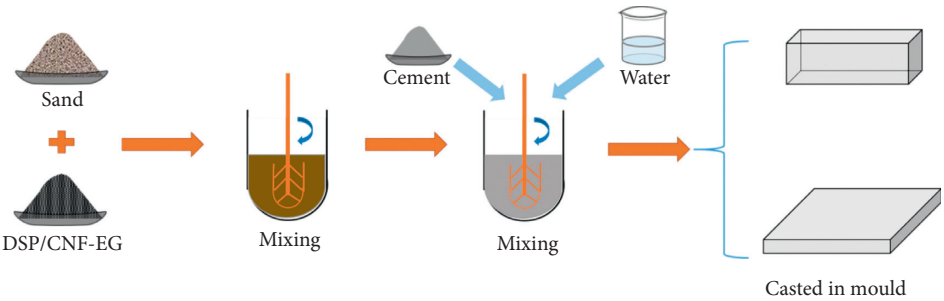

Figure 1: Schematic illustration of fabricating thermal energy storage cement mortar containing DSP/CNF-EG by physical blending.

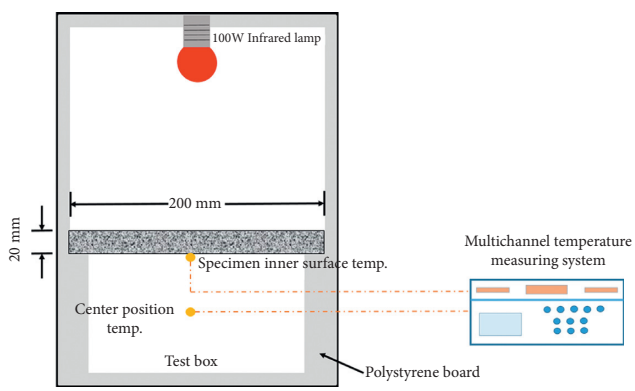

Figure 2: Schematic illustration of the self-designed heating setup.

pore structure of CM and DSP/CNF-EG/CM samples, the total porosity and the proportion of pores greater than 100 nm in the total pore are reorganized in Figures 3(c) and 3(d), respectively. As shown in Figure 3(c), the total porosities of DSP/CNF-EG/CM samples were much higher than those of CM (12.18%). Moreover, with the increase of DSP/CNF-EG incorporation amount, the total porosities of DSP/CNF-EG/CM samples also increased gradually. Therein, DSP/CNF-EG/CM-10 showed the highest total porosity of 14.74%. The pores with the size of larger than 100 nm need to be emphatically investigated because they had adverse effects on compressive and flexural strengths of mortars [36, 37]. It was notable from Figure 3(d) that the percentages of pores with the size of larger than 100 nm were gradually increased from CM of 51.1% to DSP/CNF-EG/CM-10 of 63.7% by the elevation of DSP/CNF-EG incorporation amount.

The increases of total porosity and pores with the size of larger than 100 nm can be attributed to the inferior compatibility between the cement matrix and DSP/CNF-EG form-stable hydrated salt PCM. To be specific, the main support of DSP/CNF-EG was expanded graphite (EG), and its surface property was hydrophobic. This made it difficult to retain water around DSP/CNF-EG. It was well known that the hardened cement was formed by the hydration reaction between cement clinker and water. Therefore, less hardened cement was formed around DSP/CNF-EG particles compared with that of control CM, resulting in the increase of porosity and formation of larger size pores.

3.2. Compressive Strength and Flexural Strength of DSP/CNF-EG/CM. The compressive strengths and flexural strengths of CM and DSP/CNF-EG/CM samples cured for 7 days and 28 days are displayed in Figure 4. As shown in Figure 4(a), the compressive strengths and flexural strengths of DSP/CNF-EG/CM samples cured for 7 days gradually decreased with increasing DSP/CNF-EG form-stable hydrated salt PCM. The 7-day compressive strengths were 29.3 ± 0.7 MPa, 20.2 ± 0.5 MPa, 14.7 ± 0.9 MPa, and 8.3 ± 0.4 MPa for CM, DSP/CNF-EG/CM-3.3, DSP/CNF-EG/CM-6.7, and DSP/CNF-EG/CM-10 samples. As for the 7-day flexural strengths, the values of CM, DSP/CNF-EG/CM-3.3, DSP/CNF-EG/CM-6.7, and DSP/CNF-EG/CM-10 samples were 7.1 ± 0.4 MPa, 4.5 ± 0.3 MPa, 3.9 ± 0.3 MPa, and 3.1 ± 0.5 MPa. Figures 4(c) and 4(d) show the compressive strengths and flexural strengths of CM and DSP/CNF-EG/CM samples cured for 28 days. With the prolongation of curing time, it can be seen that 28-day compressive and flexural strengths of each sample were increased compared with the 7-day compressive and flexural strengths of the samples. However, the downward trend of 28-day strengths of DSP/CNF-EG/CM samples was still unchanged with the incorporation of DSP/CNF-EG. To be specific, the 28-day compressive strengths of CM, DSP/CNF-EG/CM-3.3, DSP/CNF-EG/CM-6.7, and DSP/CNF-EG/CM-10 were 40.9 ± 1.3 MPa, 31.9 ± 0.8 MPa, 19.7 ± 1.6 MPa, and 12.5 ± 0.7 MPa, respectively. As for 28-day flexural strengths,

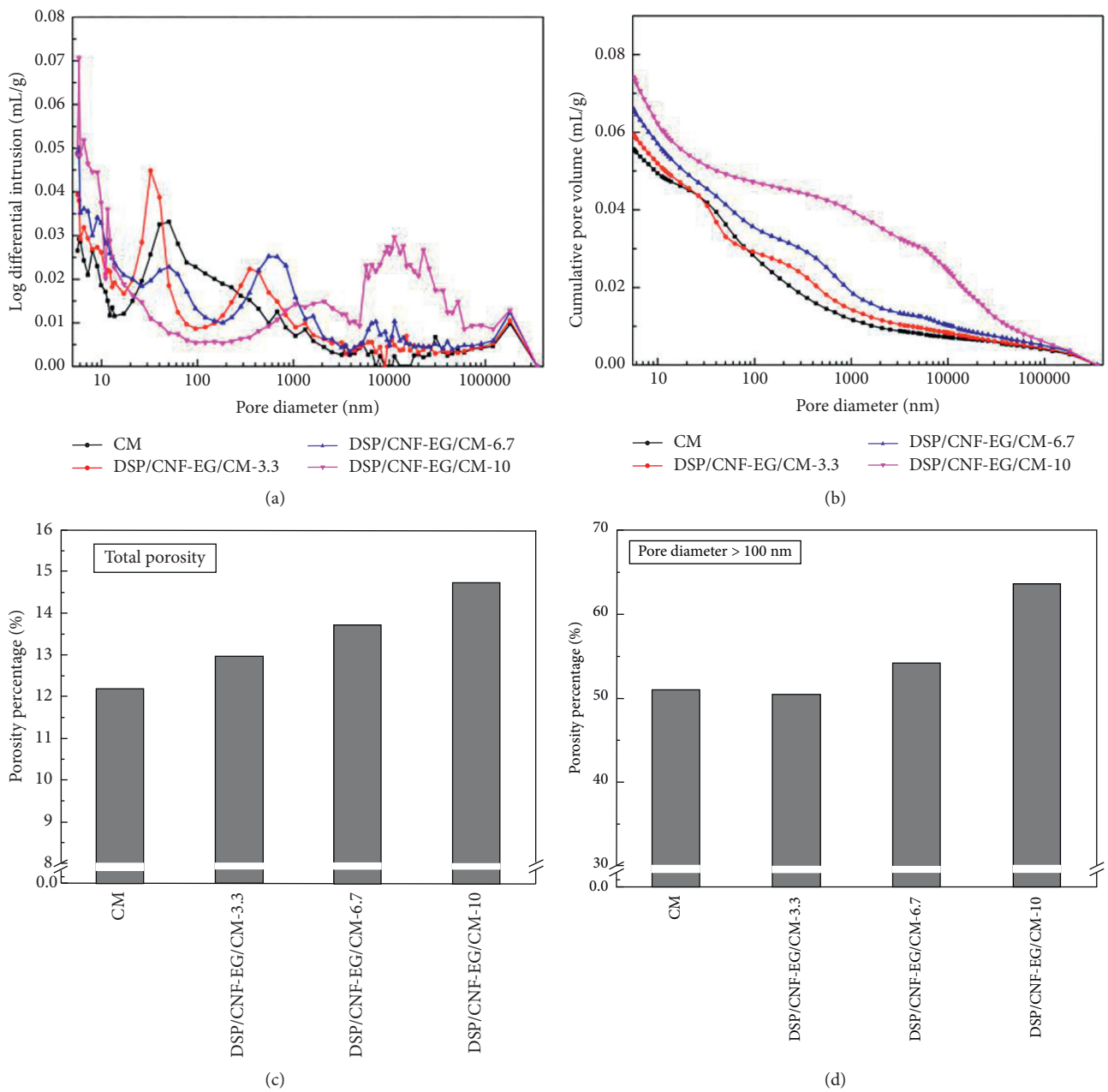

Figure 3: Pore structure analysis of CM, DSP/CNF-EG/CM-3.3, DSP/CNF-EG/CM-6.7, and DSP/CNF-EG/CM-10: (a) pore diameter distribution, (b) cumulative pore volume, (c) total porosity, and (d) the proportion of pores greater than 100 nm in the total pore.

the values were 7.4 ± 0.4 MPa, 5.3 ± 0.5 MPa, 4.5 ± 0.2 MPa, and 3.3 ± 0.1 MPa, respectively.

From the above results, the compressive strengths and flexural strengths of DSP/CNF-EG/CM decreased with increasing DSP/CNF-EG form-stable hydrated salt PCM incorporation. This was similar to most of thermal energy storage mortars containing form-stable PCMs reported in literature studies [14, 38]. The degradation of mechanical properties of DSP/CNF-EG/CM samples may be ascribed to the two reasons. On the one hand, the hydrophobicity of supporting materials EG and CNF of DSP/CNF-EG resulted in the formation of the loose interfacial transition zone between DSP/CNF-EG and cement matrix. This led to the increase of total porosity within DSP/CNF-EG/CM, which had been confirmed by the results of the pore structure as described in Section 3.1. Moreover, the pores with the size of larger than 100 nm were also increased. This had a great negative impact on the mechanical properties of mortars [36, 37]. On the other hand, sand played a skeleton role in mortar, which contributed to the mechanical properties of mortar. The composition of standard sand used in this study was natural quartz. The natural quartz had excellent strength performance. However, the CNF-EG hybrid structure in DSP/CNF-EG was porous and loose; thus, the strength of DSP/CNF-EG mainly came from DSP. Apparently, the mechanical strength of both crystalline DSP and molten DSP

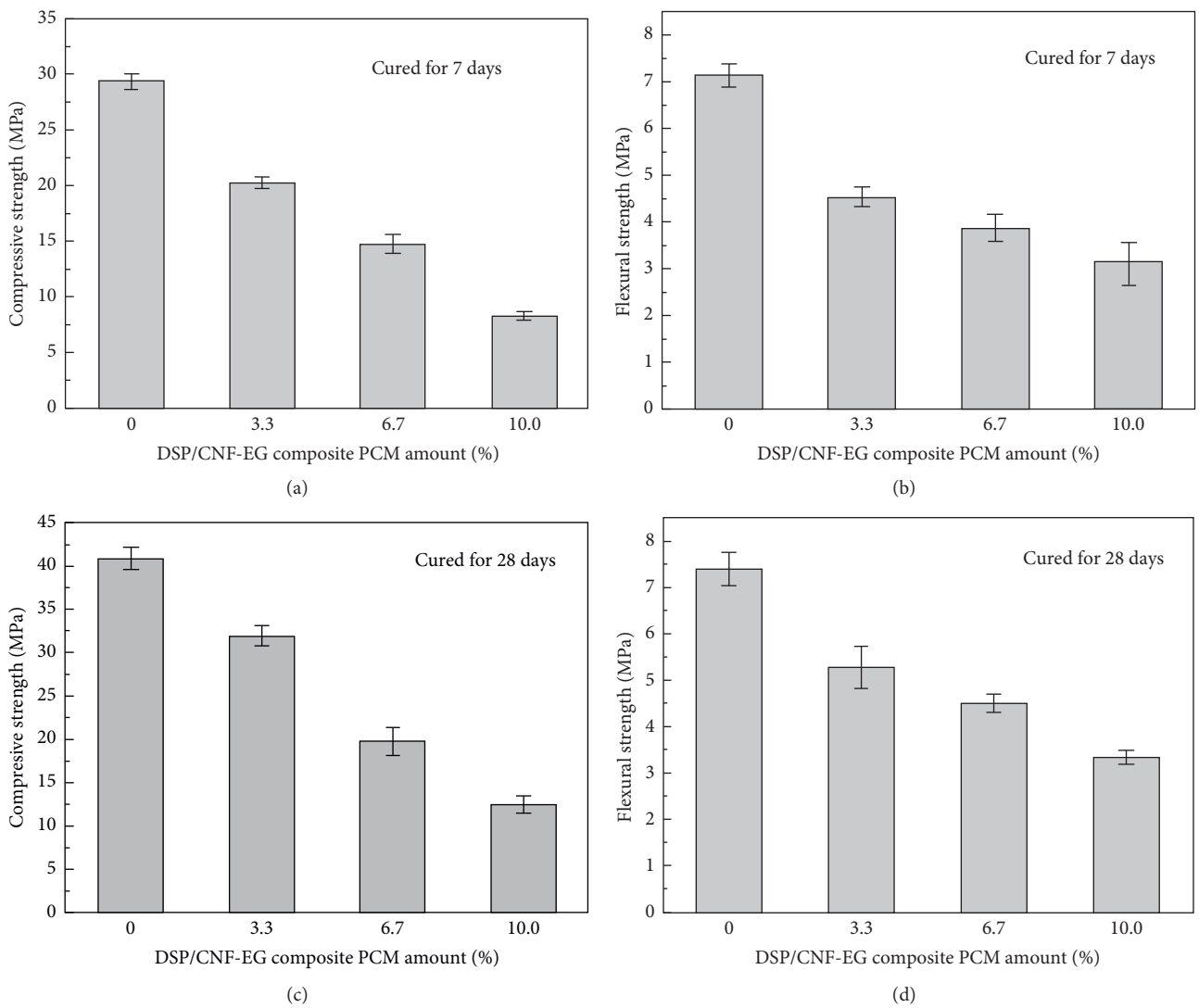

Figure 4: Compressive strength and flexural strength of CM and DSP/CNF-EG/CM samples with different curing periods: compressive strength cured for (a) 7 days and (c) 28 days and flexural strength cured for (b) 7 days and (d) 28 days.

was far less than that of natural quartz. Hence, the skeleton supporting function of DSP/CNF-EG form-stable PCM in the mortar was significantly weaker than that of sand. Although the mechanical properties of DSP/CNF-EG/CM decreased significantly, DSP/CNF-EG/CM-10 with the lowest compressive strength of 12.5 MPa still met the strength grade requirements for masonry mortar and plastering mortar based on the Chinese National Standard GB50574-2010. Hence, the prepared thermal energy storage cement mortar can be applied in the building envelope.

3.3. Damping Properties of DSP/CNF-EG/CM. The parameters reflecting damping properties of CM and DSP/CNF-EG/CM samples cured for 28 days are displayed in Figure 5. As shown in Figure 5(a), it can be seen that the storage modulus of DSP/CNF-EG/CM samples presented a downward trend with the increasing content of DSP/CNF-EG because of the weakening of bearing capacity. The maximum decrease range was from the control CM of 22.4 GPa to DSP/CNF-EG/CM-10 of 16.5 GPa. However, the loss modulus of the samples was increased with the gradual incorporation of DSP/CNF-EG. This phenomenon can be due to the fact that the enriched porosity of cement mortar led to the increase of energy dissipation [33]. In addition, the loose contact between DSP/CNF-EG and cement matrix could cause the interface friction action, also dissipating a lot of energy under the vibration load [39]. Based on the obtained storage modulus and loss modulus, the loss tangent of the samples can be calculated by using the following equation [40]:

$$\eta = \frac{E''}{E'} = 2\zeta, \tag{1}$$

where η is the loss tangent, E'' is the storage modulus, E' is the loss modulus, and ζ is the damping ratio of the samples. Therein, the parameter η can be used as the index to evaluate the damping of CM and DSP/CNF-EG/CM samples. Larger

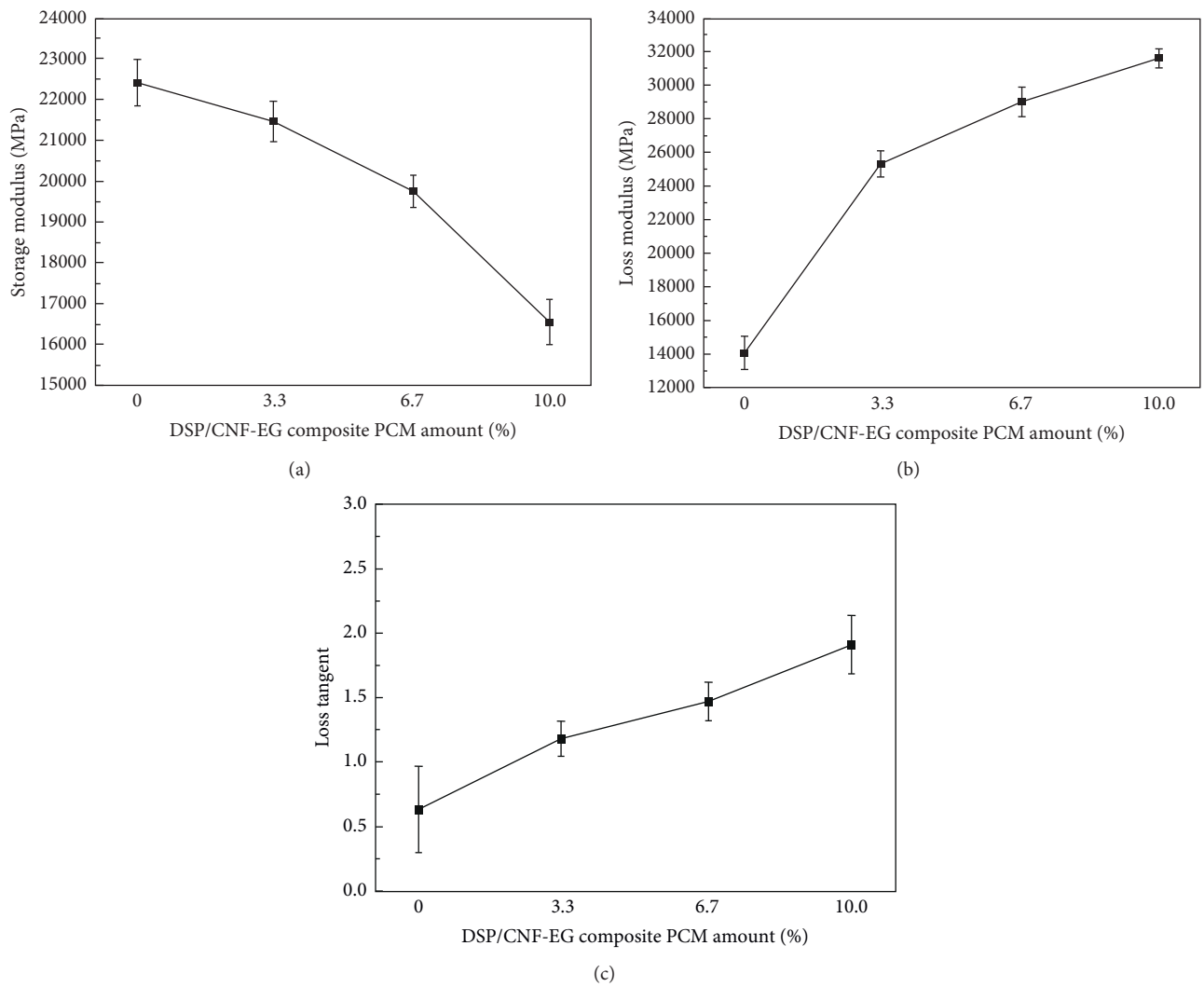

Figure 5: Damping properties of CM and DSP/CNF-EG/CM samples: (a) storage modulus, (b) loss modulus, and (c) loss tangent.

η means that the samples can weaken more vibration and dissipate more energy under the action of dynamic load, and vice versa [40].

As shown in Figure 5(c), the loss tangent values of CM, DSP/CNF-EG/CM-3.3, DSP/CNF-EG/CM-6.7, and DSP/CNF-EG/CM-10 were 0.63 ± 0.34, 1.18 ± 0.13, 1.47 ± 0.15, and 1.91 ± 0.23, respectively. Obviously, the addition of DSP/CNF-EG played a great positive role in enhancing the damping performance for DSP/CNF-EG/CM samples. This was profound because it enriches the functionality of thermal energy storage cement mortar containing form-stable PCM. This provided a novel insight into achieving the dual purpose of resisting dynamic load and improving heat storage capacity for cement mortar by the introduction of form-stable PCMs.

3.4. Thermal Conductivity and Specific Heat Capacity of DSP/CNF-EG/CM. Thermal conductivity and specific heat capacity of CM and DSP/CNF-EG/CM samples are shown in Figure 6. For each sample, the experiments were repeated 5 times, and the value of each data point was presented as the mean value ± standard deviation. As shown in Figure 6(a), the thermal conductivities of CM, DSP/CNF-EG/CM-3.3, DSP/CNF-EG/CM-6.7, and DSP/CNF-EG/CM-10 were 1.173 W/m·K, 0.934 W/m·K, 0.852 W/m·K, and 0.726 W/m·K, respectively. It can be found that the incorporation of DSP/CNF-EG form-stable hydrated salt caused the decreased thermal conductivity for cement mortar. DSP/CNF-EG/CM-10 had the lowest thermal conductivity, which is 38.1% lower than that of control CM. As for specific heat capacity, the results exhibited a contrary trend to the thermal conductivity. The specific heat capacity values of CM and DSP/CNF-EG/CM samples were 1.263 kJ/kg·K, 1.398 kJ/kg·K, 1.472 kJ/kg·K, and 1.621 kJ/kg·K, respectively. The highest specific heat capacity of DSP/CNF-EG/CM-10 was 28.3% higher than that of control CM. In many reported works [18, 26], the cement mortars containing form-stable PCMs showed reduced thermal conductivity and elevated specific heat capacity. This was due to the enhanced thermal energy storage capacity of the mortar samples by incorporation of DSP/CNF-EG. Therefore, the obtained results

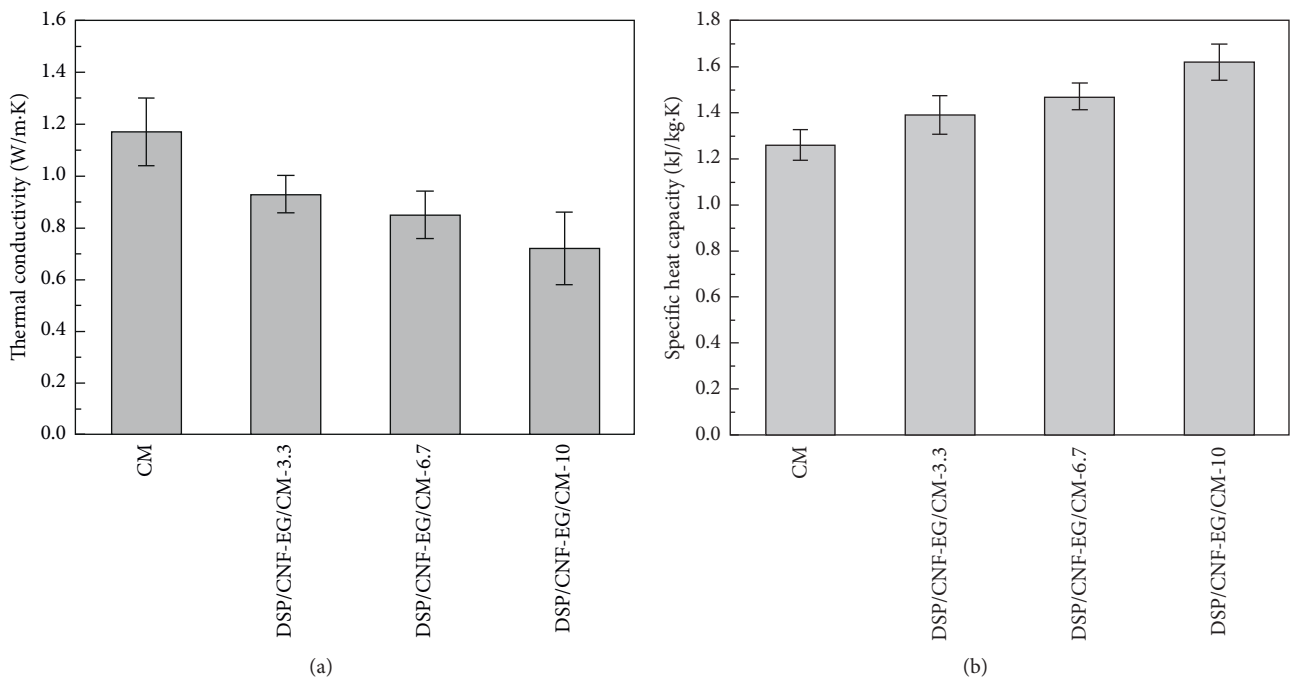

Figure 6: Thermal conductivity (a) and specific heat capacity (b) of CM and DSP/CNF-EG/CM samples.

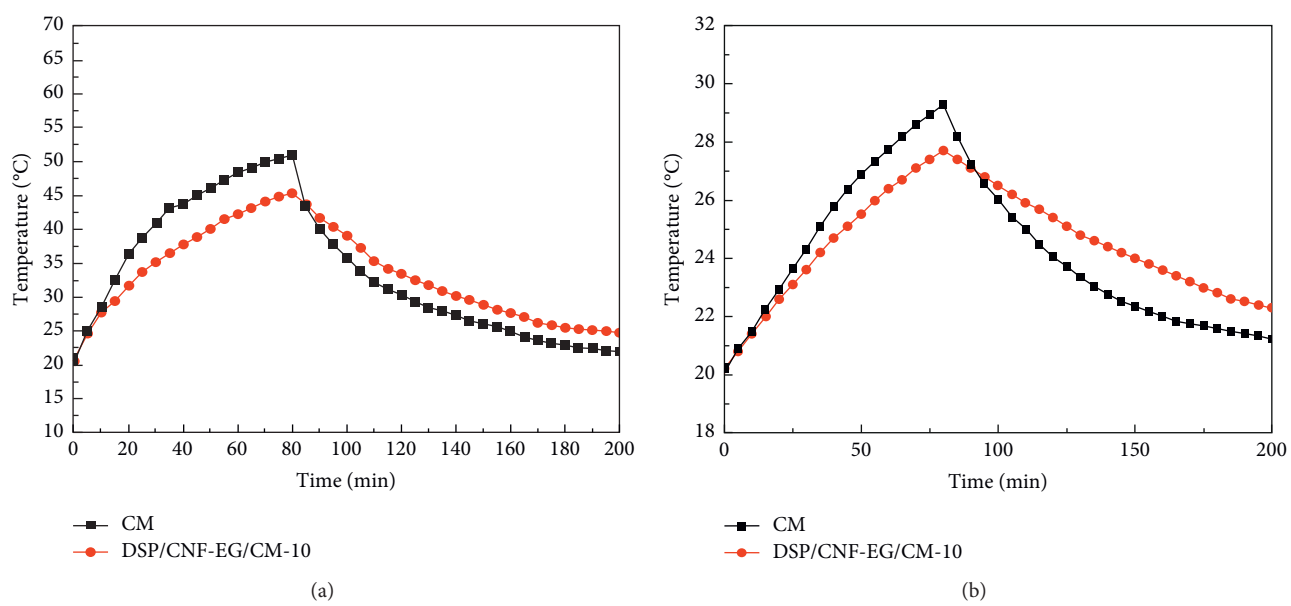

Figure 7: Thermal performance comparison between CM and DSP/CNF-EG/CM-10: (a) the temperature-time curves at the lower central surface of CM and DSP/CNF-EG/CM-10 specimens and (b) the temperature-time curves in the center position in the test box.

confirmed that the introduction of DSP/CNF-EG can endow cement mortar with excellent thermal energy storage capacity.

3.5. Thermal Performance Evaluation of DSP/CNF-EG/CM. The thermal performance comparison between CM and DSP/CNF-EG/CM-10 specimens is depicted in Figure 7. As shown in Figure 7(a), the temperature peak value of DSP/CNF-EG/CM-10 was much lower than that of the control CM. To be specific, the temperature peak values of CM and DSP/CNF-EG/CM-10 specimens were 51.1°C and 45.3°C, respectively, showing a temperature peak weakening of 5.8°C. This confirmed endothermic and exothermic features of DSP/CNF-EG/CM-10 during the heating and cooling process. Figure 7(b) shows the temperature-time curves at

the center position in the test box with, respectively, covering control CM and DSP/CNF-EG/CM-10 specimens. It can be found that their temperature curves were highly similar to those displayed in Figure 7(a). The temperature-time curve in the center position in the test box covering the DSP/CNF-EG/CM-10 specimen was gentle compared to that of control CM, showing an excellent temperature control performance. Moreover, the temperature peak for covering the DSP/CNF-EG/CM-10 specimen was significantly reduced by 1.6°C compared with that of control CM.

In the previous reports from literature studies, some researchers also fabricated the test box with one side replaced by the thermal energy storage building material specimen plate to evaluate the thermal energy storage performance. These reports indicated that the specimen plate with the thermal energy storage property can weaken the indoor temperature fluctuation. For example, Xu et al. [27] prepared a kind of lightweight thermal energy storage cement-based composite (LW-TESCC) by incorporating paraffin/expanded vermiculite form-stable PCM. The obtained result indicated that the temperature peak inside the test box equipped with the LW-TESCC plate was weakened by 2°C compared with that of the control specimen. Li et al. [41] measured the thermal energy storage cement mortar (TESCM) containing paraffin/expanded graphite form-stable PCM. The results indicated that the temperature peak in the test box fitted with the TESCM plate could be significantly reduced by 2.2°C, compared with that of the control CM plate. Fang et al. [42] found that the gypsum plate incorporating 20 wt% RT20/MMT phase-change composite could reduce the internal temperature peak of the test box by 5°C. In this study, although different test boxes are used, the prepared DSP/CNF-EG/CM-10 also showed the ability to weaken the temperature peak, reflecting the excellent indoor temperature control performance.

4. Conclusions

In summary, DSP/CNF-EG form-stable hydrated salt PCM was incorporated into cement mortar by physical mixing to fabricate thermal energy storage cement mortar. Based on the experiment results and the profound discussion, the following conclusions can be obtained:

(1) As the level of DSP/CNF-EG replacing sand increased, the pore size distributions of DSP/CNF-EG/CM samples were gradually shifted to the larger pore size, and the total porosity and the pores with the size of larger than 100 nm were also increased due to the inferior interface compatibility between DSP/CNF-EG and cement matrix.

(2) The compressive strength of DSP/CNF-EG/CM gradually decreased with the increasing content of DSP/CNF-EG. As the incorporation amount of DSP/CNF-EG reached to 10 wt%, DSP/CNF-EG/CM-10 presented the 28-day compressive strength of 12.5 MPa. The compressive strength could well meet the strength requirement applied in the building envelope.

(3) The introduction of DSP/CNF-EG played a positive role in enhancing the damping properties of DSP/CNF-EG/CM because enriched porosity and interface friction action of DSP/CNF-EG/CM significantly increased the energy dissipation under dynamic load. The loss tangent of DSP/CNF-EG/CM-10 was 1.91, showing 203.2% increase compared with that of control CM.

(4) The incorporation of DSP/CNF-EG resulted in the reduced thermal conductivity and elevated specific heat capacity of DSP/CNF-EG/CM. DSP/CNF-EG/CM-10 had the lowest thermal conductivity of 0.726 W/m·K and the highest specific heat capacity of 1.621 kJ/kg·K.

(5) The DSP/CNF-EG/CM-10 specimen plate was integrated into the upper side of the test box of the self-design heating setup to evaluate the thermal performance. The results illustrated that the thermal energy storage capacity of cement mortar was improved by the incorporation of DSP/CNF-EG form-stable hydrated salt PCM.

Overall, the introduction of DSP/CNF-EG form-stable hydrated salt PCM endowed cement mortar with good heat storage capacity. The formed thermal energy storage cement mortar can be used in building envelopes and to improve the relationship between supply and demand in terms of building thermal energy, thus achieving building energy saving.

Data Availability

The data used to support the findings of this study are available from the corresponding author upon request.

Conflicts of Interest

The authors declare that they have no conflicts of interest.

Acknowledgments

The financial support from the Scientific Research Fund of Institute of Engineering Mechanics, China Earthquake Administration (Grant no. 2020D09) for the current research is gratefully acknowledged.

References

[1] P. Sukontasukkul, P. Uthaichotirat, T. Sangpet et al., "Thermal properties of lightweight concrete incorporating high contents of phase change materials," *Construction and Building Materials*, vol. 207, pp. 431–439, 2019.

[2] Y. Liu, E. Xu, M. Xie, X. Gao, Y. Yang, and H. Deng, "Use of calcium silicate-coated paraffin/expanded perlite materials to improve the thermal performance of cement mortar," *Construction and Building Materials*, vol. 189, pp. 218–226, 2018.

[3] Y. Liu, M. Xie, E. Xu, X. Gao, Y. Yang, and H. Deng, "Development of calcium silicate-coated expanded clay based form-stable phase change materials for enhancing thermal and mechanical properties of cement-based composite," *Solar Energy*, vol. 174, pp. 24–34, 2018.

[4] Y. Liu, K. Yu, X. Gao, M. Ren, M. Jia, and Y. Yang, "Enhanced thermal properties of hydrate salt/poly (acrylate sodium) copolymer hydrogel as form-stable phase change material via incorporation of hydroxyl carbon nanotubes," *Solar Energy Materials and Solar Cells*, vol. 208, Article ID 110387, 2020.

[5] K. Yu, Y. Liu, F. Sun, M. Jia, and Y. Yang, "Graphene-modified hydrate salt/UV-curable resin form-stable phase change materials: continuously adjustable phase change temperature and ultrafast solar-to-thermal conversion," *Energy & Fuels*, vol. 33, no. 8, pp. 7634–7644, 2019.

[6] B. Lamrani, K. Johannes, and F. Kuznik, "Phase change materials integrated into building walls: an updated review," *Renewable and Sustainable Energy Reviews*, vol. 140, Article ID 110751, 2021.

[7] S. G. Yoon, Y. K. Yang, T. W. Kim, M. H. Chung, and J. C. Park, "Thermal performance test of a phase-change-material cool roof system by a scaled model," *Advances in Civil Engineering*, vol. 2018, Article ID 2646103, 2018.

[8] C. Fabiani, A. L. Pisello, A. D'Alessandro, F. Ubertini, L. F. Cabeza, and F. Cotana, "Effect of PCM on the hydration process of cement-based mixtures: a novel thermo-mechanical investigation," *Materials*, vol. 11, p. 871, 2018.

[9] A. Eddhahak-Ouni, S. Drissi, J. Colin, J. Neji, and S. Care, "Experimental and multi-scale analysis of the thermal properties of Portland cement concretes embedded with microencapsulated phase change materials (PCMs)," *Applied Thermal Engineering*, vol. 64, no. 1-2, pp. 32–39, 2014.

[10] A. L. Pisello, A. D'Alessandro, C. Fabiani et al., "Multi-functional analysis of innovative PCM-filled concretes," in *Proceedings of the 8th International Conference on Sustainability in Energy and Buildings*, R. Howlett, A. Capozzoli, and V. Serra, Eds., Seb-16, Turin, Italy, pp. 81–90, March 2017.

[11] D. P. Bentz and R. Turpin, "Potential applications of phase change materials in concrete technology," *Cement and Concrete Composites*, vol. 29, no. 7, pp. 527–532, 2007.

[12] H. Huang, X. Gao, K. H. Khayat, and A. Su, "Influence of fiber alignment and length on flexural properties of UHPC," *Construction and Building Materials*, vol. 290, Article ID 122863, 2021.

[13] H. Huang, X. Gao, and L. Teng, "Fiber alignment and its effect on mechanical properties of UHPC: an overview," *Construction and Building Materials*, vol. 296, Article ID 123741, 2021.

[14] H. Abbasi Hattan, M. Madhkhan, and A. Marani, "Thermal and mechanical properties of building external walls plastered with cement mortar incorporating shape-stabilized phase change materials (SSPCMs)," *Construction and Building Materials*, vol. 270, Article ID 121385, 2021.

[15] C. Guardia, G. Barluenga, I. Palomar, and G. Diarce, "Thermal enhanced cement-lime mortars with phase change materials (PCM), lightweight aggregate and cellulose fibers," *Construction and Building Materials*, vol. 221, pp. 586–594, 2019.

[16] T. Shi, W. Sun, and Y. Yang, "Preparation and heat storage/release behavior of latent heat storage gypsum-based building materials," *Materials and Structures*, vol. 47, no. 3, pp. 533–539, 2014.

[17] L.-C. Pop, M. Baibarac, I. Anghel, and L. Baia, "Gypsum composite boards incorporating phase change materials: a review," *Journal of Nanoscience and Nanotechnology*, vol. 21, no. 4, pp. 2269–2277, 2021.

[18] S. A. Memon, "Phase change materials integrated in building walls: a state of the art review," *Renewable and Sustainable Energy Reviews*, vol. 31, pp. 870–906, 2014.

[19] Y. Liu, M. Xie, X. Gao, Y. Yang, and Y. Sang, "Experimental exploration of incorporating form-stable hydrate salt phase change materials into cement mortar for thermal energy storage," *Applied Thermal Engineering*, vol. 140, pp. 112–119, 2018.

[20] X. Bao, H. Yang, X. Xu et al., "Development of a stable inorganic phase change material for thermal energy storage in buildings," *Solar Energy Materials and Solar Cells*, vol. 208, Article ID 110420, 2020.

[21] R. Ye, W. Lin, X. Fang, and Z. Zhang, "A numerical study of building integrated with CaCl2·6H2O/expanded graphite composite phase change material," *Applied Thermal Engineering*, vol. 126, pp. 480–488, 2017.

[22] G. Sang, Y. Zhang, M. Fan et al., "Thermo-mechanical properties of compaction molded cement-based composite containing a high mass fraction of phase change material for thermal energy storage," *Composites Part A: Applied Science and Manufacturing*, vol. 128, Article ID 105657, 2020.

[23] Y. He, X. Zhang, and Y. Zhang, "Preparation technology of phase change perlite and performance research of phase change and temperature control mortar," *Energy and Buildings*, vol. 85, pp. 506–514, 2014.

[24] D. Sun and L. Wang, "Utilization of paraffin/expanded perlite materials to improve mechanical and thermal properties of cement mortar," *Construction and Building Materials*, vol. 101, pp. 791–796, 2015.

[25] S. Ramakrishnan, X. Wang, J. Sanjayan, and J. Wilson, "Thermal performance assessment of phase change material integrated cementitious composites in buildings: experimental and numerical approach," *Applied Energy*, vol. 207, pp. 654–664, 2017.

[26] Z. Zhang, G. Shi, S. Wang, X. Fang, and X. Liu, "Thermal energy storage cement mortar containing n-octadecane/expanded graphite composite phase change material," *Renewable Energy*, vol. 50, pp. 670–675, 2013.

[27] B. Xu, H. Ma, Z. Lu, and Z. Li, "Paraffin/expanded vermiculite composite phase change material as aggregate for developing lightweight thermal energy storage cement-based composites," *Applied Energy*, vol. 160, pp. 358–367, 2015.

[28] A. Sharma, V. V. Tyagi, C. R. Chen, and D. Buddhi, "Review on thermal energy storage with phase change materials and applications," *Renewable and Sustainable Energy Reviews*, vol. 13, no. 2, pp. 318–345, 2009.

[29] K. Yu, Y. Liu, and Y. Yang, "Review on form-stable inorganic hydrated salt phase change materials: preparation, characterization and effect on the thermophysical properties," *Applied Energy*, vol. 292, Article ID 116845, 2021.

[30] Y. Liu, F. Sun, K. Yu, and Y. Yang, "Experimental and numerical research on development of synthetic heat storage form incorporating phase change materials to protect concrete in cold weather," *Renewable Energy*, vol. 149, pp. 1424–1433, 2020.

[31] A. D'Alessandro, A. L. Pisello, C. Fabiani, F. Ubertini, L. F. Cabeza, and F. Cotana, "Multifunctional smart concretes with novel phase change materials: mechanical and thermo-energy investigation," *Applied Energy*, vol. 212, pp. 1448–1461, 2018.

[32] H. Zhang, F. Xing, H.-Z. Cui et al., "A novel phase-change cement composite for thermal energy storage: fabrication, thermal and mechanical properties," *Applied Energy*, vol. 170, pp. 130–139, 2016.

[33] P.-H. Chen and D. D. L. Chung, "Mechanical energy dissipation using cement-based materials with admixtures," *ACI Materials Journal*, vol. 110, pp. 279–289, 2013.

[34] K. Yu, B. Jin, Y. Liu, and L. Li, "Enhanced thermal conductivity of form-stable phase change materials using carbon nanofiber-expanded graphite hybrid structure," *Materials Research Express*, vol. 6, no. 2, 2019.

[35] P. Yu, Z. Wang, P. Lai, P. Zhang, and J. Wang, "Evaluation of mechanic damping properties of montmorillonite/organo-modified montmorillonite-reinforced cement paste," *Construction and Building Materials*, vol. 203, pp. 356–365, 2019.

[36] B. Li, B. Huo, R. Cao, S. Wang, and Y. Zhang, "Sulfate resistance of steam cured ferronickel slag blended cement mortar," *Cement and Concrete Composites*, vol. 96, pp. 204–211, 2019.

[37] H. Zhao, Q. Xiao, D. Huang, and S. Zhang, "Influence of pore structure on compressive strength of cement mortar," *Science World Journal*, vol. 2014, Article ID 247058, 2014.

[38] M. Li and J. Shi, "Review on micropore grade inorganic porous medium based form stable composite phase change materials: preparation, performance improvement and effects on the properties of cement mortar," *Construction and Building Materials*, vol. 194, pp. 287–310, 2019.

[39] L. Liu and M. Eriten, "Frictional energy dissipation in wavy surfaces," *Journal of Applied Mechanics-Transactions of the Asme*, vol. 83, 2016.

[40] L. Chi, S. Lu, and Y. Yao, "Damping additives used in cement-matrix composites: a review," *Composites Part B: Engineering*, vol. 164, pp. 26–36, 2019.

[41] M. Li, Z. Wu, and J. Tan, "Heat storage properties of the cement mortar incorporated with composite phase change material," *Applied Energy*, vol. 103, pp. 393–399, 2013.

[42] X. Fang, Z. Zhang, and Z. Chen, "Study on preparation of montmorillonite-based composite phase change materials and their applications in thermal storage building materials," *Energy Conversion and Management*, vol. 49, no. 4, pp. 718–723, 2008.

Hindawi
Advances in Civil Engineering
Volume 2021, Article ID 5557040, 10 pages
https://doi.org/10.1155/2021/5557040

Research Article

Laboratory Investigations into the Bearing Capacity of Straw Bales for Low-Rise Building Applications

Baozhu Cao, Jun Hu, Yuansong Sun, and Hongxin Nie

School of Civil Engineering and Architecture, Hainan University, Haikou 570228, China

Correspondence should be addressed to Jun Hu; hj7140477@hainanu.edu.cn

Received 20 January 2021; Revised 22 March 2021; Accepted 26 June 2021; Published 6 July 2021

Academic Editor: Yingzi Yang

Investigations were carried out to study the mechanical performance under uniaxial load of unplastered and plastered straw bales. Results from tests on 30 rice straw bales indicated nonlinear load-bearing properties with large deformations and anisotropy. Since the deformations observed did not conform to the current building code requirements, the evaluation of ultimate bearing capacity through the maximum axial vertical load was not possible. To obtain the design strength of rice straw bales in composite walls, further 21 specimens of plastered straw bales were also tested in compression. The permissible deformation of the straw bales was evaluated. It is noteworthy that the large deformability of straw bales can reduce the damage to structures after an earthquake. Consequently, the straw bale use can widely enhance the seismic performance of low-rise buildings.

1. Introduction

The rapid development of economy and industry in China poses a derogatory effect on the environment around us continuously. The government emphatically promotes the use of sustainable materials to construct green houses, especially in rural areas. As of today, there are more than 600 single-story straw bale houses built in North East China. Several two-story dwelling houses with light-weight steel structures and straw bales have been built as examples of modern green buildings. Human beings have a long history of utilizing straw in forms for construction of their dwelling places. Historically, they have not excluded the use of grass or reed in various forms for building construction. These materials were used because they were both readily available and reliable. European houses built of straw or reeds are now over two hundred years old. In the United States, people turned to straw houses in the 1890s with the advent of the hay/straw baler. The oldest straw bale house (built in 1903) is single-storied and still standing in Nebraska today [1]. Some books [2–4] describe the design and construction methods adopted, considering the bearing capacity and thermal properties of straw bales. They cover details of different types of straw buildings that comply with building regulation requirements. In Europe and North America, tens of thousands of people have chosen straw bales to build their homes as straw bale building is certainly becoming popular by its unique features and alternative styles.

For straw buildings to be accepted widely, more research on mechanical properties of straw bales needs to be carried out to confirm the suitability of them being adopted in dwelling houses. Over decades, many researchers have made significant effort to research on environmentally friendly materials. The cropped straw was used as fibers mixed in Earth plaster or as compressed in straw bales. Yetgin et al. [5] reported compression and tensile tests that were conducted on five different adobe mixtures. The important part of their study consisted of uniaxial compressive tests done on natural fiber mixtures. Their mechanical test results were presented in the form of stress-strain graphs and showed that compressive and tensile strength decreased with increasing fiber content. Taha et al. [6] measured the thermal conductivity of some natural plaster materials compatible for use in straw bale buildings. Such plaster materials consisted of soil, sand, and straw, with the straw being a reinforcing fiber in the plaster. In some developing countries, mud houses are still used as dwelling places. Chel and Tiwari [7] reported the potential of the annual heating and

cooling energy saving with mud house through a case study of a vault roof mud house in India. Thus, thermal performance and embodied energy of a passive house can be evaluated. In fact, cereal straw, including wheat, barley, and rice, offers a renewable and sustainable resource stream for a variety of construction products, including compressed board panels, thatched roofing, and bales [8]. Although the use of straw bales as thermal insulation within the external envelope of building has been adequately demonstrated around the world, straw building projects are often still not regarded as straightforward in competitive solutions. This can be attributed to concerns relating to the long-term durability of the straw. Results from experimental investigations have indicated that keeping a steady humidity on equilibrium moisture content can improve its durability. The roofs of single-story straw bale buildings are supported on the straw walls, which make the strength of straw bale walls seemingly more important. A series of experiments were conducted by O'Dogherty [9] to measure the physical properties, tensile and shear strengths, and elastic moduli of the stems between nodes of wheat straw. His results showed that tensile strength was in the range of 21.2 to 31.2 MPa, and the shear strength was in the range of 4.91 to 7.26 MPa. The strength of straw bale or straw bale walls is very different from that of the straw stem, because there exist too many void spaces in large volumes. Vardy's PhD thesis [10] presented new models for predicting the compressive strength of plastered straw bale assemblies that are subjected to concentric and eccentric loading [11]. A constitutive model for lime-cement plaster was adapted from a stress–strain model for concrete available in the literature. Twenty-two cylinder tests on plasters typically used for straw bale construction were used to verify the constitutive model. In 2014, Palermo et al. [12] provided a more refined compression field theory for plastered straw bale walls by considering walls consisting of straw and plaster as a single entity. In another publication of Taha et al. [13], an experiment conducted with straw bale subjected to uniaxial load was described. Though the relationship of stress and strain was obtained, the stress-strain curves were described without giving the design strength for straw bales.

The research on straw bales as building materials have been mainly developed in Europe and the United States. California construction law stipulates that straw bales must be compressed to twice their initial density to be deemed to have reached failure. Simonsen from Oregon State University in the United States and Liu Kun from Northeast Forestry University in China considered the density as a control index for the bearing capacity in the straw bale performance [14, 15] and obtained the relationship between stress and strain under unidirectional loading to show that straw bales were materials that can sustain large deformation. On the basis of straw bales being heavily deformable materials, taking the displacement/deformation was considered as the control index. The authors, alternately, advocate that the point of failure occurs when the flat straw bales are compressed to one third of its initial height. However, since sidelong and upright straw bales exhibit a large deformation, they would be deemed to have reached failure when they have been compressed by 100 mm. The bearing capacity at the point of failure was deemed as the ultimate compressive strength. Kim et al. [16] in their research on straw bale and plastered bale structural members conducted tests on a series of seven specimens to study the behavior of reinforced plastered straw bale composite sandwich walls. The composite system significantly improved the load-bearing capacity of straw bale and was particularly noticeable when coarse mesh and GFRP bars were used.

The aforementioned research achievements can provide better supportive references for design and construction of straw bale structures, although their application is still empirical as currently available information is limited. Undoubtedly, there may be wide differences in the properties of straw obtained from different areas or climates. This paper presents a laboratory study on the behavior of 30 straw bales and 21 plastered straw bales measuring their stiffness moduli from their respective stress-strain curves. The permissible deformation of straw bales was observed together with the contribution from the cement plaster was evaluated. The specimens for testing used rice straw harvested from Jilin province in China, and the straw bales were manufactured using a hydraulic machine.

2. Materials and Methods

2.1. Materials. The rice straw was first packed into bales and kept in a dry environment. The moisture content of the rice straws need to be determined and noted when the rice straw specimens were fabricated and prepared for testing. Moisture content of 20% was considered as a safe maximum for a building bale (this was the same figure for lumber) [17]. Some literatures recommend 14% as the ideal moisture content of a straw bale wall [18]. The experiments were carried out at Changchun city in Jilin province located in Northeast of China, which is characterized by a dry, but cold climate in winter. The moisture content of rice straw used in the testing was 6.1%, very much lower than the permitted value. The nominal block size of common straw bales is in the range of 300~1200 mm × 460 mm × 360 mm (length, width, and height), and the density of the bales remains constant for straw bales fabricated by the same baling machine. The dimensions of specimens fabricated for the testing were 500 mm × 400 mm × 200 mm and 500 mm × 400 mm × 300 mm. However, a wide variation of densities was observed, and they were 100 kg/m^3, 200 kg/m^3, 300 kg/m^3, and 400 kg/m^3. It was therefore necessary to put the rice straw first into a mould as illustrated in Figure 1 and compressed using a servocontrolled hydraulic testing machine. After the straw bales were compressed to the design size, 3.4 mm diameter steel wire was used for baling (Figure 2). The size and density of specimens fabricated did not always conform exactly with the design. Table 1, which lists the exact details of the specimens, presents the deviation from the original plan. There were 10 groups with three specimens in each group, thereby totaling 30 straw bale specimens prepared for testing. While specimens in groups 1, 2, and 4~10 were laid flat and tested in a horizontal

Figure 1: The wood mould of rice straw bale.

Figure 2: The rice straw specimens.

orientations, specimens in group 3 were laid on an edge and tested in a vertical orientation.

As there are cement plaster layers on both surfaces of straw bale walls in conventional construction practices, 21 specimens of straw bales were fabricated with such cement plaster layers. To represent loading conditions in practice, the straw bales were subjected to uniaxial loading. 16 specimens in group 11~16 were plastered straw bales, as shown in Figure 3(a), and three specimens in group 17 were plastered straw bales as shown in Figure 3(b). In addition, thin steel meshes were placed on specimens in group 16. There were also three specimens in each group. While the design strengths anticipated for the three types of plaster were 5 MPa, 7.5 MPa, and 10 MPa, the measured in situ strengths of the three plasters were 6.4 MPa, 8.0 MPa, and 10.2 MPa. The dimensions and densities of the plastered straw bales were designed to be the same as unplastered straw bale specimens. All specimens were placed flat in horizontal orientations for testing. The detailed parameters of the straw bales and plastered straw bales are shown in Table 2.

2.2. Methods. Since the surface of rice straws was not smooth and with the anticipation that test blocks will generate large horizontal (lateral) deformations under vertical (axial) loads, a unique method was adopted to observe the displacements (deformations) in the horizontal and vertical directions. A total of eight displacement sensors linked to a data logging computer were used to measure the horizontal and vertical displacements of straw bales. The four vertical displacement sensors responded to the vertical movement of the hydraulic testing machine's steel loading platen. Tips of the other four sensors measuring the test block's horizontal displacement were touching the stiff planar wooden laminate cards placed on the side surfaces of straw bales (Figure 4). The displacement values corresponding to the different axial loads were used to calculate the strength, rigidity modulus, and Poisson's ratio of the bale being tested. With increasing vertical uniaxial load, the test bale became denser with the consequent rapidly changing horizontal and vertical displacements. The continuous vertical uniaxial loading was stopped when the vertical displacement corresponded to 1/3 of the initial dimension of the block height. The mechanical performances of the plastered straw bale specimens were probably affected by the cement plaster, particularly the ultimate strength being reached even after the cement plaster was destroyed.

3. Experimental Program

3.1. Test Setup. The test setup for unplastered straw bales is shown in Figure 5. This setup consisted of three 10 mm thick wooden plates, three 20 mm thick steel plates, three 120 mm long square-sectioned wooden beams, and 150 mm long square-sectioned wooden beam. The axial compressing load was provided by a hydraulic servotesting machine, whose maximum force was 60 tons. The same setup was used for plastered straw bales, except that the 150 mm square wooden beam was substituted by an "I" section steel beam (Figure 6).

3.2. Test Protocol. The quality and dimensions of the rice straw bales were observed, measured, and recorded prior to the application of the vertical load from the microcomputer-controlled electrohydraulic servotesting machine. The loading was applied with the loading platen movement as a control index and a rate of relative movement of 0.2 mm/s being adopted. Concurrent with the application of the vertical load, the vertical (axial) and lateral displacement sensors were accurately monitored. The data acquisition from all sensors was timed to sample and log the data at intervals of every two seconds.

During the testing of unplastered straw bale blocks laid flat, the blocks became denser with increasing vertical load as expected. When the height of the straw bale blocks was

Table 1: The parameters of straw bale specimens.

Designation	Length (mm)	Width (mm)	Height (mm)	Weight (kg)	Density (kgm^{-3})	Ultimate strength (MPa)	Elastic modulus (MPa)	Poisson's ratio
1A	510	397	161	7.76	237	0.31	0.282	0.13
1B	485	391	180	7.86	230	0.34	0.257	0.14
1C	500	397	178	7.90	222	0.24	0.179	0.11
2A	492	227	382	7.88	184	0.07	0.531	0.20
2B	495	224	396	7.94	181	0.06	0.293	0.17
2C	498	243	362	7.88	180	0.06	0.237	0.23
3A	372	235	371	7.92	243	0.09	0.617	0.31
3B	385	217	474	7.90	199	0.05	0.149	0.29
3C	386	219	474	277.94	198	0.05	0.183	0.26
4A	501	401	124	3.80	151	0.22	0.195	0.11
4B	507	407	120	3.80	152	0.09	0.107	0.35
4C	515	440	121	3.80	139	0.04	0.044	0.17
5A	472	372	251	11.86	268	0.75	0.621	0.15
5B	500	392	238	11.62	249	0.56	0.404	0.13
5C	493	381	247	11.56	249	0.61	0.281	0.26
6A	520	425	234	15.88	307	0.60	0.445	0.17
6B	500	406	263	15.90	298	0.54	0.366	0.14
6C	500	395	263	15.92	306	0.65	0.353	0.29
7A	535	397	194	5.71	138	0.05	0.068	0.17
7B	485	380	207	5.84	153	0.10	0.122	0.12
7C	527	398	203	5.86	138	0.05	0.070	0.11
8A	527	450	288	11.40	166	0.16	0.059	0.20
8B	492	380	294	12.14	221	0.37	0.182	0.35
8C	470	377	275	11.90	244	0.48	0.369	0.16
9A	495	390	319	18.08	294	0.85	0.496	0.33
9B	522	402	305	17.52	273	0.60	0.433	0.32
9C	510	403	295	17.74	292	0.69	0.697	0.33
10A	520	407	340	23.96	333	1.19	0.565	0.38
10B	537	443	335	23.92	299	0.63	0.452	0.29
10C	522	408	329	23.68	338	1.20	0.615	0.34

(a) (b)

Figure 3: Plastered straw bales. (a) Straw bales with incomplete plaster (no plaster on the corners). (b) Straw bales with complete plaster.

reducing, the horizontal dimensions of the block were expanding laterally. When the vertical deformation of straw bale blocks exceeded 1/3 of block's initial height, any further vertical loading was stopped.

In the case of plastered straw bales, the strength of specimens probably relied more on that of the plaster layers; therefore, the stage of the plaster failing was the criterion to stop any further loading.

Table 2: The parameters of plastered straw bale specimens.

Designation	Straw bales					Plaster				Composite bales	
	Length (mm)	Width (mm)	Height (mm)	Weight (kg)	Density (kgm^{-3})	Length (mm)	Width (mm)	Thickness (mm)	Strength (MPa)	Ultimate strength (MPa)	Vertical displacement (mm)
11A	490	390	200	8.10	212	250	230	5	8.0	46.5	3.012
11B	490	390	200	8.12	212	250	230	5	8.0	56.0	3.366
11C	500	390	200	8.10	208	250	230	5	8.0	38.5	4.748
12A	490	400	210	8.04	195	250	230	9	8.0	78.5	3.485
12B	490	400	210	7.94	193	250	230	9	8.0	45.8	3.063
12C	490	400	200	8.04	205	250	230	9	8.0	40.3	3.079
13A	500	400	200	8.00	200	250	230	13	8.0	83.1	3.588
13B	490	400	200	8.04	205	250	230	13	8.0	85.5	3.503
13C	500	390	200	8.06	207	250	230	13	8.0	104.7	3.861
14A	490	390	200	7.94	208	250	230	9	6.4	50.2	3.538
14B	490	390	210	8.06	201	250	230	9	6.4	57.7	4.516
14C	500	390	210	8.02	196	250	230	9	6.4	27.9	3.311
15A	490	390	210	8.10	202	250	230	9	10.2	68.0	2.211
15B	500	390	200	8.00	205	250	230	9	10.2	101.0	3.073
15C	490	390	200	8.10	212	250	230	9	10.2	73.9	2.073
16A	500	400	190	8.06	212	250	230	9	8.0	77.0	3.351
16B	500	410	200	8.06	197	250	230	9	8.0	64.2	3.128
16C	490	400	210	8.02	195	250	230	9	8.0	64.4	3.222
17A	500	400	200	8.02	201	518	418	9	8.0	107.9	3.338
17B	500	400	200	8.02	201	518	418	9	8.0	80.2	3.282
17C	500	400	200	8.08	202	518	418	9	8.0	109.2	3.052

Figure 4: Setup and displacement sensors.

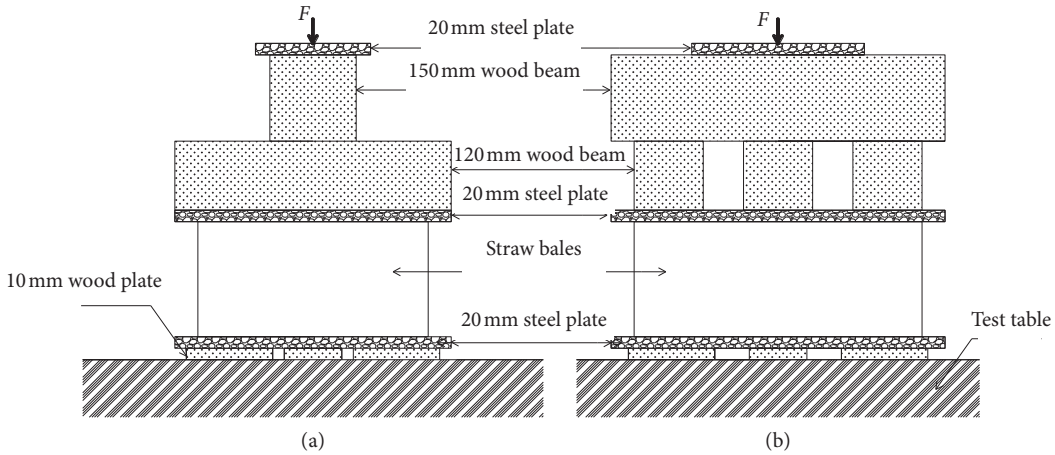

Figure 5: The experimental setup of unplastered straw bales. (a) Front elevation. (b) Side elevation.

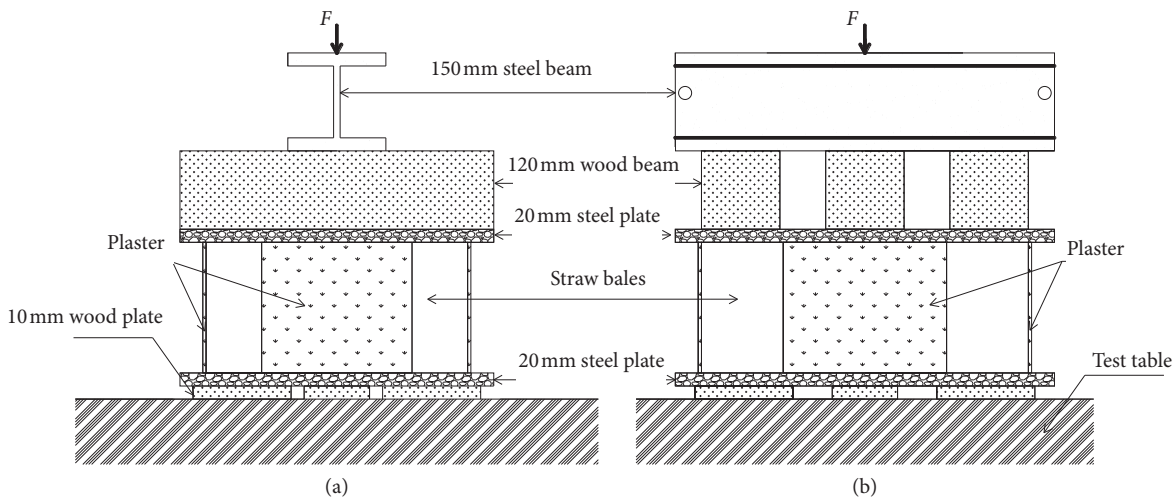

Figure 6: The experimental setup of plastered straw bales. (a) Front elevation. (b) Side elevation.

3.3. Test Sequence and Phenomena. Cement stucco was used for plaster construction, and cubes of plaster were tested after natural open air curing for four weeks. Cube strengths of the plaster cubes are listed in Table 2. The thickness of plaster layers on the side surfaces of straw bales were not the same. Therefore, the mean thickness of plaster on each side was adopted for analyzing.

The deformed unplastered straw bales after testing are shown in Figure 7. At this stage, the bearing load could have been increased further, but the tests were terminated as the vertical deformation had reached the controlled limit criterion. The lateral elongation in a direction along the straw stems was very small, and the deformation in other orthogonal directions was more significant. The straw bale specimens tested when the blocks were laid in a horizontal orientation gave the usually expected deformation under a vertical uniaxial load of 10 kN, but the specimens tested when the blocks were laid in a vertical orientation resulted in a larger axial deformation under a vertical load of 5 kN. The lateral deformation of straw bales laid in a vertical orientation during testing was much more significant than that observed when the blocks were laid in a horizontal orientation.

With plastered straw bale specimens, it was found that the deformation was not as expected. The vertical displacement was about 3~4 mm when signs of failure phenomena occurred in the plastered layers. Some such failure phenomena that were observed in the plastered specimens are shown in Figure 8. The three different examples in Figure 8 are meant to show (a) the failure observed in straw bales plastered inadequately with no mesh, (b) the failure in straw bales plastered incompletely but with fine steel mesh, and (c) the failure observed in completely plastered straw bales. From the failure types in (a) and (b), it can be deduced that the failure was caused by the fracture of plaster layers. However, similarly induced crack patterns were apparent in the failure of completely plastered straw bale specimens. Comparing the bearing capacity of the three types of plastered specimens, the bearing capacity of the completely plastered straw bales was approximately 20% greater than that with incomplete plaster. It was also noted that when a thin steel mesh was used in the straw bales with incomplete plaster, its bearing capacity improved by approximately 10%.

4. Results and Discussion

4.1. Unplastered Straw Bales. There were 30 specimens of unplastered straw bales tested in the experimental program. Three bales (3A, 3B, and 3C) were tested when laid on an on-edge orientation, and the other bales on an on-edge orientation were laid horizontal in a flat orientation. The testing results, including density, ultimate strength, elastic modulus, and Poisson's ratio, are listed in Table 1. All specimens displayed regular similarity in the relationship of load with vertical displacement. Eight representative load-displacement curves of bales with different densities are presented in Figure 9. Figure 9(a) shows that, in the case of bales with an approximate initial volume of 0.04 m^3, the rate of load increase with displacement increases with increasing straw bale density. A similar observation can be deduced from Figure 9(b), where the initial volume of the straw bale was larger and approximately 0.06 m^3. During this research, the unplastered straw bales displayed a nonlinear mechanical performance, making it unfeasible to establish either a bearing capacity or an elastic modulus reliably. The bearing capacity of straw bales was determined using the load sustained at a vertical displacement of 1/3 of initial block height. The elastic modulus was calculated using the stress-strain curves observed for straw bales. Stress–strain curves were evaluated from the load-displacement data. Figure 10 illustrates the relationship between ultimate strength and straw bale density. The deduction was that as expected the ultimate strength increases with increasing density. Similarly, Figure 11 shows that the elastic modulus also increases with the density of the unplastered straw bales. Although the data collected from tests for these two figures were on different and separate specimens, they confirm the trends that were expected. Since the straw bale specimens were manually fabricated, it inherently embodies some deviations

Figure 7: The large deformation of straw bale.

(a) (b) (c)

Figure 8: The phenomena of plastered straw bales. (a) Incompletely plastered straw bale. (b) Incompletely plastered straw bale with mesh. (c) Completely plastered straw bales.

from the design of experiment. Table 1 shows that elastic moduli of flat straw bales were extremely low and highly variable, ranging from 0.044 MPa to 0.697 MPa. Poisson's ratio for flat bales was found to be ranging from 0.11 to 0.38. For on-edge specimens, the straw bale modulus was found to be ranging from 0.149 MPa to 0.617 MPa, and Poisson's ratio ranged from 0.26 to 0.31. The authors believe that more consistent values of elastic modulus and Poisson's ratio for unplastered straw bales can be determined for building design, if the straw bales fabrication is standardized.

4.2. Plastered Straw Bales. Large displacements were observed in the tests of unplastered straw bales, but these will not occur if and when the straw bales are plastered with a

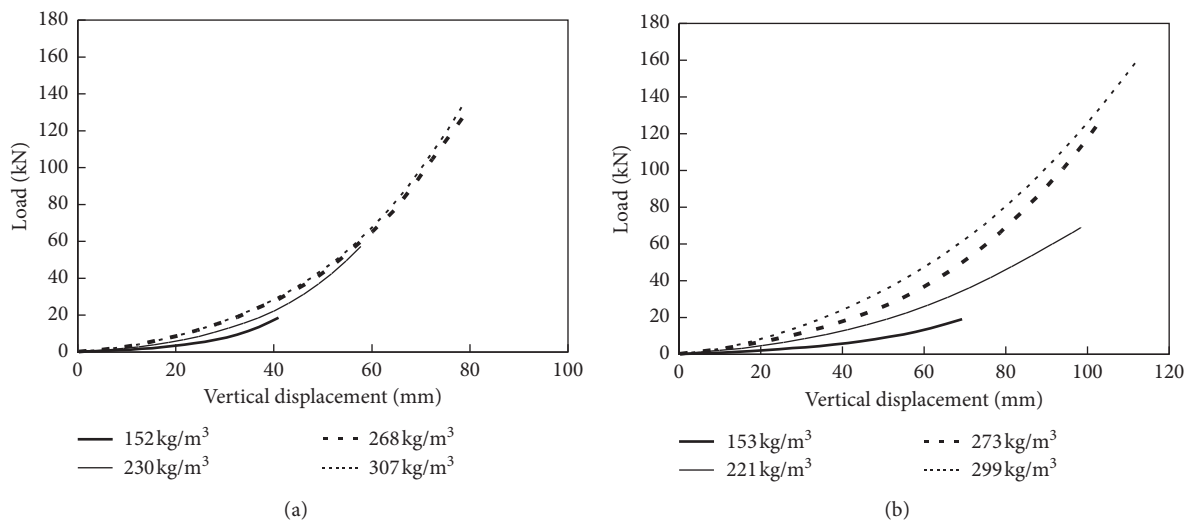

Figure 9: Load–displacement curves for the unplastering straw bales laid flat. (a) Initial volume of 0.04 m^3. (b) Initial volume of 0.06 m^3.

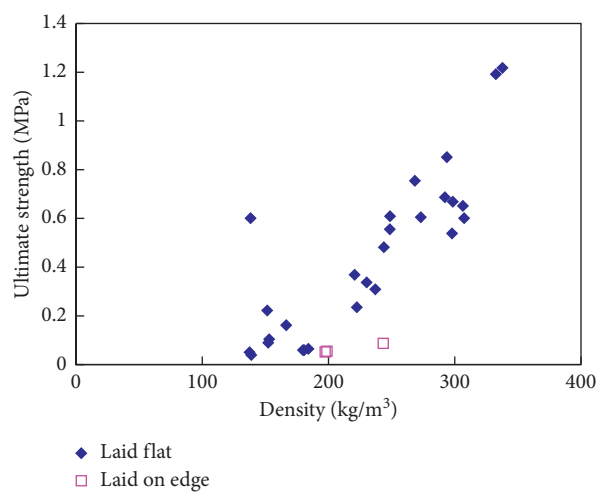

Figure 10: The relationship between the ultimate strength and density of unplastered straw bales.

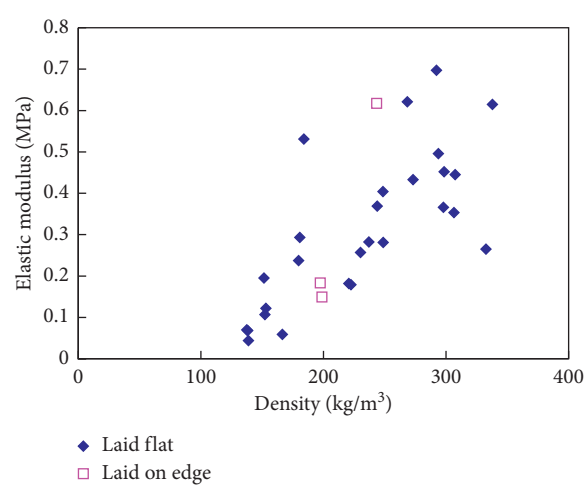

Figure 11: The relationship between the elastic modulus and density of unplastered straw bales.

cement layer on the side surfaces. In fact, it is a norm that all straw bale walls of houses are covered with plaster layers, creating the effect of a composite structure. Hence, the contributory beneficial effects from plaster should be harnessed and considered in the evaluation of bearing capacity of straw bale walls. Twenty-one specimens of plastered straw bales were tested to evaluate the ultimate bearing capacity through observations of the vertical displacement and load-displacement relationship. The ultimate strengths of composite specimens and maximum vertical displacements are listed in Table 2, and a plot of load-displacement curves for the plastered straw bales is as shown in Figure 12. According to the curves in this figure, the mechanical characteristics show that its slope at the start of the loading is flat. After the vertical displacement exceeded 2 mm, the slope of the curves rose gradually to become steep. The peak of the curves gives the ultimate load and corresponding displacement. Subsequently, the curves dropped with displacement. Specimen 11B was an incompletely plastered straw bale (Figure 8(a)), specimen 16B was an incompletely plastered straw bale with a steel mesh (Figure 8(b)), and specimen 17B was a completely plastered straw bale (Figure 8(c)). Notably, the three completely plastered specimens gave a similar strength of 8.0 MPa. Hence, it can also be inferred that placing a steel wire mesh in the plaster can further improve the ultimate strength of specimen. A straw bale completely enclosed with plaster will improve the strength even more.

Equation (1) presents the sharing mechanism of the contributions by the straw bales and the plaster to account for the ultimate strength of the composite specimens. The ultimate bearing capacity could be expressed as

$$F_u = f_c' \cdot A_c + f_s \cdot A_s + E_{str} \cdot \varepsilon_0 \cdot A_{str}, \quad (1)$$

where F_u is the ultimate bearing load of composite specimens, f_c' and A_c are the strength and bearing area of plaster, f_s and A_s are the strength and corresponding area of steel wire mesh section, E_{str} and A_{str} are the elastic modulus and bearing area of straw bales when laid flat, and ε_0 is the strain corresponding to the ultimate strength of the plaster.

4.3. Discussion and Advices. Similar mechanical compression curves were obtained for the straw bales when plotted separately based on each physical parameter (density, dimensions, and bale orientation) through the analysis of the load–displacement curve. As one would expect, on comparing the tests on plastered bales with unplastered bales, it was shown that using plaster improved the load-bearing capacity of the straw bales. The maximum vertical displacement observed for straw bales in the tests was beyond 40 mm, whereas the cement plaster layer was destroyed at displacements no more than 5 mm. Therefore, the bearing capacity of straw bales could be insufficient, if and when the plaster is compressed to failure. According to literature [10], the maximum strain in plaster at failure is in the order of 0.00253. If uniform deformation of plastered straw bale is achieved, the strain in the straw (ε_0) will also be approximately 0.00253 at failure. The method adopted to determine the elastic modulus of straw bales is very important as it can affect the calculated bearing capacity considerably. The moduli of straw bales vary with different densities. Elastic modulus can be defined in at least two ways: tangent modulus or secant modulus. Here, the secant modulus at the point of plaster's yielding strain is recommended when determining the elastic modulus of the straw bales. Thus, the corresponding stress in the straw bale needs to be considered as the design bearing strength.

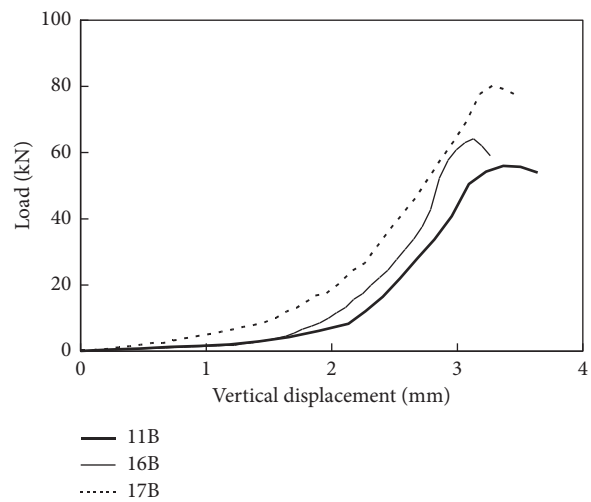

Figure 12: Load–displacement curves for the plastered straw bales laid flat.

The material and mechanical properties of straw bales can be different and vary characteristically depending on the type and source of the straw. Testing of straw materials should be carried out before a straw structure is designed. Though straw bales can be used to construct a single-story house, it is advisable to limit its use to internal enclosure walls because of its property of being overly compressible. Alternately, if they were to be used as load-bearing walls and before plastering, the stock pile of straw bale assemblies can be exhausted by the mere load of roof. Prestressing technique can be adapted to minimize the occurrence of excessive postconstruction deformation. The characteristic large deformability of straw bales can be appropriately accommodated to improve the building performance against seismic damage during an earthquake. Straw bales therefore can be ideally placed as antiseismic structural members to act as latent defense to protect dwellings and occupants.

5. Conclusions

Instead of being classed and discarded as unwanted and difficult to dispose of, rice straw could become a viable commodity to be harvested. This paper summarizes work from ongoing study on the bearing capacity of straw bales. The test results demonstrate that straw bales are anisotropic, nonlinear, and highly deformable building material. Modulus of elasticity and bearing capacity of straw bale increased with increasing density. When straw bale blocks have a density being greater than 300 kg/m^3, the bearing capacity of straw bale blocks will be reliably desirable. When the density of straw bales is 337.80 kg/m^3, the bearing capacity of straw

bales is 1.20 MPa. Existing baling machines can easily make the straw bale blocks to achieve the desired density, so that can be easily fabricated promoting the use of straw bales as building materials.

Data Availability

All the data used to support the findings of this study are included within the article.

Conflicts of Interest

The authors declare no conflicts of interest.

Acknowledgments

This research was supported by the Hainan Major Science and Technology Project (ZDKJ201803), National Natural Science Foundation of China (51968019 and 51368016), High-Level Talent Project of Hainan Basic and Applied Basic Research Plan (2019RC148 and 2019RC351), and "Nanhai Series" Yucai Program (no. 21 Document of Hainan Talent Office, 2019).

References

[1] C. Atkinson, "Building with straw bales-home grown home lecture notes," 2011, https://www.homegrownhome.co.uk/homegrown homelecturenote.html.

[2] B. Hodge, *Building Your Straw Bale home*, Landlinks Press, Colling Wood, Australia, 2006.

[3] N. Corum, *Building a Straw Bale House: The Red Feather Construction Handbook*, Princeton Architectural Press, New York, NY, USA, 2005.

[4] C. Magwood, P. Mack, and T. Therrien, *More Straw Bale Building—A Complete Guide to Designing and Building with Straw*, New Society Publishers, Gabriola, Canada, 2005.

[5] S. Yetgin, Ö. Cavdar, and A. Cavdar, "The affects of the fiber contents on the mechanic properties of the adobes," *Construction and Building Materials*, vol. 22, pp. 222–227, 2008.

[6] A. Taha, W. Hansjorg, G. Heiko, B. Franz Josef, and W. Wei, "The influence of natural reinforcement fibres on insulation values of earth plaster for straw bale buildings," *Materials and Design*, vol. 31, pp. 4676–4685, 2010.

[7] A. Chel and G. N. Tiwari, "Thermal performance and embodied energy analysia of a passive house-case study of vault roof mud-house in India," *Applied Energy*, vol. 86, pp. 1956–1969, 2009.

[8] A. Thomson and P. Walker, "Durability characteristics of straw bales in building envelopes," *Construction and Building Materials*, vol. 68, pp. 135–141, 2014.

[9] M. J. O'Dogherty, J. A. Huber, J. Dyson, and C. J. Marshall, "A study of the physical and mechanical properties of wheat straw," *Journal of Agricultural Engineering Research*, vol. 62, pp. 133–142, 1995.

[10] S. P. Vardy, "Structural behavior of plastered straw bale assembles under concentric and eccentric loading," Ph.D. thesis, Queen's University, Kingston, Canada, 2009.

[11] S. Vardy and C. MacDougall, "Concentric and eccentric compression experiments of plastered straw bale assemblies," *Journal of Structural Engineering*, vol. 139, pp. 448–461, 2013.

[12] M. Palermo, L. M. Gil-Martin, E. Hernandez-Montes, and M. Aschheim, "Refined compression field theory for plastered straw bale walls," *Construction and Building Materials*, vol. 58, pp. 101–110, 2014.

[13] A. Taha, H. Georg, and W. Wu, "Performance of straw bale wall: a case of study," *Energy and Buildings*, vol. 43, pp. 1960–1967, 2011.

[14] B.-A. Ghailene, "Straw bales and straw bale wall systems," Master's thesis, University of Arizona, Tucson, Arizona, 1993.

[15] Liukun, E. Jiang, and J. Duan, *Research on Bearing Capacity of Straw Bale*, Chinese Society of Agricultural Engineering, Beijing, China, 2005.

[16] Y. J. Kim, A. Reberg, and M. Hossain, "Bio-building materials for load-bearing applications: conceptual development of reinforced plastered straw bale composite sandwich walls," *Journal of Performance of Constructed Facilities*, vol. 26, pp. 38–45, 2012.

[17] C. Magwood, P. Mack, and T. Therrien, *More Straw Bale Building*, New Society Publishers, Gabriola Island, Canada, 2005.

[18] S. Goodhew, R. Griffiths, and W. Tom, "An investigation of the moisture content in the wall of a straw-bale building," *Building and Environment*, vol. 39, pp. 1443–1451, 2004.

Hindawi
Advances in Civil Engineering
Volume 2021, Article ID 5547744, 15 pages
https://doi.org/10.1155/2021/5547744

Research Article

Investigation on the Role of Steel Slag Powder in Blended Cement Based on Quartz Powder as Reference

Wei He,[1] **Jihui Zhao**,[2,3] **and Gangqiang Yang**[2]

[1]*School of Civil and Transportation Engineering, Beijing University of Civil Engineering and Architecture, Beijing 100044, China*
[2]*School of Civil Engineering, Sun Yat-sen University, Guangzhou 510275, China*
[3]*Southern Marine Science and Engineering Guangdong Laboratory, Zhuhai 519082, China*

Correspondence should be addressed to Jihui Zhao; zhaojihui324@163.com

Received 17 February 2021; Revised 21 April 2021; Accepted 12 June 2021; Published 29 June 2021

Academic Editor: Yushi Liu

To clarify the role of steel slag powder in blended cement, steel slag powders with different amounts and particle sizes were mixed into blended cement and the inert quartz powder was selected as the reference. The influences of steel slag powder with different amounts and particle sizes on the hydration and hardening properties of blended cement were studied from hydration heat, nonevaporable water content, porosity, hydration products, and strength. The results show that the influence coefficient of nonevaporable water content (Φ_{Wn}) of blended cement paste is in an exponential relationship with the amount of steel slag powder. Moreover, at a dosage of 30%, Φ_{Wn} of blended cement gradually decreases with the increase of steel slag particle size. Both the early and late compressive strengths of blended cement are in a binomial relationship with the amount of steel slag powder. The influence coefficient of steel slag powder on the compressive strength of blended cement is negative at the age of 3 days, whereas it is positive at the age of 28 days. The chemical filling effect of 30% steel slag powder with different particle sizes in the blended cement paste is very small, only 1.13%–5.06%. The hydration products of blended cement containing steel slag are mainly amorphous C-S-H gels and platy $Ca(OH)_2$, and their density are consistent with the law of their porosity.

1. Introduction

It is well known that cement-based material is a nonhomogeneous and multiphase porous material [1–3]. The pore structure (including porosity and pore size distribution) and hydration reaction characteristics (including hydration degree, hydration product type, and quantity) are two key factors that affect the overall performance of cement-based materials [4–7]. Except for cement clinker, modern cement-based materials usually contain supplementary cementitious materials, such as slag and fly ash [8–10]. According to a lot of scholars' research, the influences of supplementary cementitious materials components on the properties of cement-based composites include two aspects: chemical action (i.e., the hydration reaction role) and the physical action (i.e., the physical filling role) [11–13]. The chemical action is not related to only the intrinsic activity of the supplementary cementitious component itself but also its interaction with cement clinker, while the physical action is mainly related to the filling role of the supplementary cementitious component on the system and effect on the pore structure [14–18]. There is a great distinction between the different supplementary cementitious components due to chemical composition, activity, and hydration reaction mechanism, so the hydration and hardening performance of cement-based composites containing different supplementary cementitious materials also greatly differ [19–21]. Therefore, it is necessary to reveal the chemical and physical effects of different supplementary cementitious components on cement-based composites, especially blended cement.

Steel slag is the main industrial waste produced in smelting steel. In China, the basic oxygen converter steel slag is the major kind of steel slag because the main smelting method is dominated by the converter steelmaking. The basic oxygen converter steel slag (hereafter called steel slag in this paper) is rich in silicate minerals, such as dicalcium silicate (C_2S) and tricalcium silicate (C_3S), similar to the mineral components of cement clinker, and it possesses a

certain hydration activity and cementitious materials after grinding [22–24]. Therefore, it has great potential as supplementary cementitious materials (or called mineral admixture). Meanwhile, the application of steel slag in cement and concrete is also an important way of steel slag resource utilization [25–28]. However, the hydration activity and hydration rate of the steel slag powder are much lower than those of the cement. In the blended cement, the cement clinker firstly starts hydration and hardening reaction, resulting in the formation of the system framework by the hydration products [25, 29, 30]. The effect of steel slag as a supplementary cementitious component on the hydration and hardening of blended cement includes two aspects, i.e., the filling role and the hydration effect. The former leads to the change of pore structure, whereas the latter is reflected in the change of hydration degree of composite cementitious materials. However, most of the current studies in literature focus on the mechanical properties and application effects of steel slag powder in cement and concrete, less paying attention to directly reveal the physical effect (namely, filling role) and chemical effect (namely, hydration role) of steel slag powder with different particle sizes or additional amounts in blend cement. In order to better use the steel slag powder as supplementary cementitious material, it is necessary to reveal the role of the steel slag powder with different amounts or particle sizes in blended cement so as to guide the blended cement containing the steel slag powder to obtain good comprehensive performance.

In this article, steel slag powders with different particle sizes were prepared and mixed into blended cement. The influences of steel slag powder with different amounts or particle sizes on the hydration and hardening properties of blended cement were studied from hydration heat, nonevaporable water content, porosity, hydration products, and strength. Meanwhile, the inert quartz powder, whose particle size distribution is similar to that of the steel slag powder, was also selected as the reference so as to initially reveal the role or contribution of steel slag powder in the hydration and hardening of blended cement. The results of this study also guide how to select or determine the best particle size or addition amounts of steel slag powder in blended cement, which is also meaningful or valuable for the efficient application of steel slag powder building materials.

2. Materials and Methods

2.1. Materials. Steel slag used is the converter steel slag after heat-stewing process treatment, which was provided from Laiwu steel company of Shandong province in China. The quartz used is the natural quartz sand with the content of silicon dioxide not less than 95%. The chemical composition and mineral composition, which were determined by X-ray fluorescence (XRF) and X-ray diffraction (XRD) analysis, respectively, are shown in Table 1 and Figure 1.

Steel slag powder and quartz powder with different particle sizes were prepared using a laboratory ball mill under different grinding times. Then, four types of steel slag powders with median diameter in the range of 10~15 μm (denoted by $R1$), 15~20 μm (denoted by $R2$), 20~30 μm (denoted by $R3$), and 60~70 μm (denoted by $R4$) were selected, respectively. Meanwhile, four kinds of quartz powders, whose particle sizes are similar to those of the steel slag powders, were selected as the reference. The median diameters and particle size distribution of powders selected are shown in Table 2 and Figure 2, respectively.

The cement used was prepared using a laboratory ball mill according to the ratio of 95% clinker with 5% gypsum. The sieving residue of 80 μm is 4.4%, with a specific surface area of 402 m^2/kg and a median diameter of 20.91 μm. The chemical composition of cement is also shown in Table 1.

2.2. Mix Design. The mixture proportions shown in Table 3 were designed for the research of the influence of different percentages of steel slag on the hydration and hardening of blended cement. Meanwhile, the influences of steel slag powder with different particle sizes on the properties of the blended cement were studied using the mixture proportions, as shown in Table 4.

2.3. Testing Methods

(1) The hydration heat of blended cement paste containing steel slag powder was measured using a TAM Air isothermal calorimeter from TA instruments. The testing was performed at 25°C, within 96 h, and the water-to-binder ratio of paste is 0.5.

(2) The blended cement pastes with the water-to-binder ratio of 0.35 were prepared for the determination of nonevaporable water content, morphology, and pore structure of hardened blended cement paste. When the paste specimens were cured at a temperature of about 20 ± 1°C and $>95\%$ relative humidity to testing ages, the middle portions of specimens were obtained, broken, and soaked in absolute ethanol to stop hydration. Then, the sample is dried at 105°C for at least 24 h so that it reaches a constant weight. Next, the test methods of nonevaporated water content and porosity are as follows:

(a) Before testing the nonevaporable water content, the dried specimens need to be ground into a fine powder (less than 80 μm). Then, the nonevaporable water content was determined as the difference in mass between the specimen heated at 105°C and 1000°C normalized by the mass after heating at 105°C and correcting for the loss on ignition of the unhydrated specimen [31]. The calculation formula is as follows:

$$W_n = \frac{W_1 - W_2}{W_1\left(1 - L_{SSC}\right)} - \frac{L_{ssc}}{1 - L_{ssc}}, \quad (1)$$

where W_n is the nonevaporable water content of specimen, (%); W_1 is the mass of specimen at 105°C (i.e., dried mass of specimen), (g); W_2 is the mass of specimen at 1000°C, (g); L_{ssc} is a coefficient taking into account the loss on

Table 1: Chemical compositions of steel slag and cement (%).

Materials	CaO	SiO_2	Al_2O_3	Fe_2O_3	MgO	K_2O	SO_3	P_2O_5	Others
Steel slag powder	46.28	16.75	2.29	22.17	5.49	0.03	0.25	2.54	4.20
Quartz powder	1.93	95.30	0.70	—	0.65	0.21	—	—	1.21
Cement	62.13	20.76	4.58	3.27	3.13	0.75	2.80	0.12	2.46

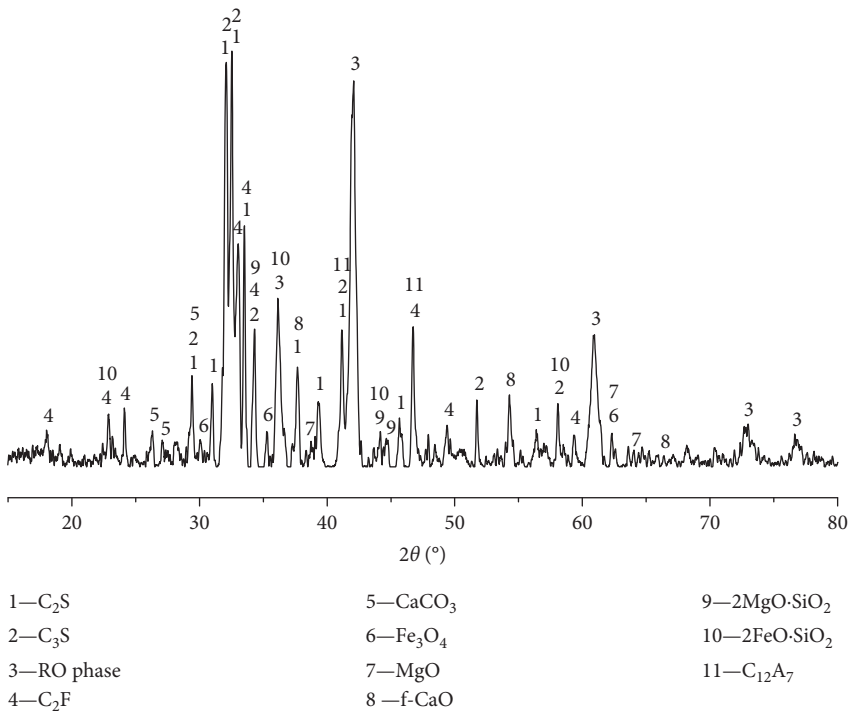

Figure 1: XRD pattern of steel slag used in this study.

Table 2: Median diameters of steel slag and quartz powder (μm).

Materials	10~15 ($R1$)	15~20 ($R2$)	20~30 ($R3$)	60~70 ($R4$)
Steel slag powder	14.52	18.16	29.63	65.36
Quartz powder	13.56	19.01	28.05	63.28

ignition of cement and steel slag used in blend cement. The latter is calculated as follows:

$$L_{ssc} = p_{ss} r_{ss} + p_c r_c, \quad (2)$$

where p_{ss}, and p_c are the weight percentages of steel slag and cement in blended cement, respectively, and r_{ss} and r_c are the loss on ignition of steel slag and cement, respectively.

(b) The morphologies of hydration products of blended cement pastes containing steel slag powder were observed using a FEI Quanta 200F scanning electron microscope (SEM, 15 KV) under high vacuum condition.

(c) The porosities and pore size distribution of hardened cement pastes containing steel slag powder and quartz powder were determined using an Autopore 9500 Mercury intrusion porosimetry (MIP) from Micromeritics Instruments Corporation, whose pore analysis range was 3 to 4500000 nm.

(d) Paste bars ($4 \times 4 \times 16$ cm) were prepared for the determination of the strength of blended cement pastes containing steel slag powder and quartz powders. The compressive strengths of paste specimens after curing for 3 days, 7 days, and 28 days at 20°C were measured according to the Chinese National Standard GB/T17671-1999.

3. Influence of Steel Slag Powder Content on the Properties of Blended Cement

3.1. Hydration Heat of Blended Cement Paste. The hydration heat curves of blended cements containing different amounts of steel slag powder are shown in Figure 3. As can be seen from Figure 3, the incorporation of steel slag powder prolongs the induction period of cement hydration, delays the second exothermic peak, and decreases the peak value. The second exothermic peak becomes broader. The higher the content of steel slag powder, the longer the induction period of blended cement, the later the appearance of the second exothermic peak, the lower the peak, and the broader the peak, showing that the addition of steel slag powder

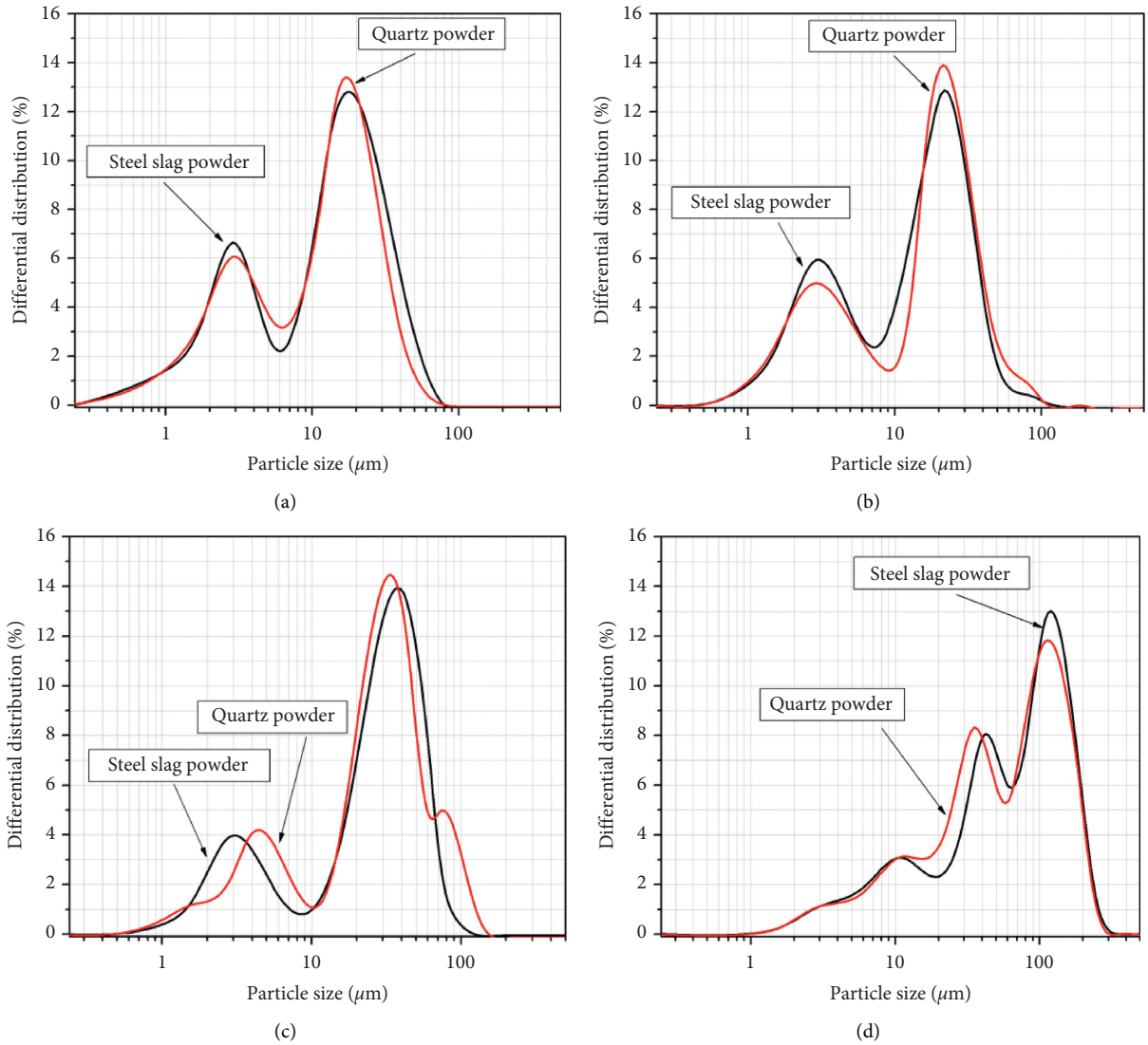

Figure 2: Particle size distributions of steel slag and quartz powder. (a) $R1$. (b) $R2$. (c) $R3$. (d) $R4$.

Table 3: Mixing proportions of blended cements containing different amounts of steel slag powder.

Specimens	Water-to-binder ratio	Mixture proportions (%)		
		Cement	Steel slag powder ($R2$)	Quartz powder ($R2$)
Cement		100	0	0
CSS20		80	20	0
CSS40		60	40	0
CSS60		40	60	0
CSS80	0.35	20	80	0
CQ20		80	0	20
CQ40		60	0	40
CQ60		40	0	60
CQ80		20	0	80

slows down the hydration reaction rate of blended cement. This is mainly due to the low activity of steel slag powder, which slows down the overall hydration process of cement after replacing cement. In addition, the relatively high content of P_2O_5 or phosphate in the steel slag powder used will also delay the hydration process of cement. The heat release of the reference cement and the cement mixed with 20% steel slag powder is mainly concentrated before 30 h, while the heat release of the high content (40% and 50%) of steel slag cement is mainly after 20 h. The second exothermic peaks of steel slag cement mixed with 20%~50% are about 2/3, 2/5, and 1/4 of the reference cement, respectively. For the

Table 4: Mixing proportions of blended cements containing steel slag powder with different particle sizes.

Specimens	Water-to-binder ratio	Mixture proportions (%)								
			Steel slag powder (SS)				Quartz powder (Q)			
		Cement	*R*1	*R*2	*R*3	*R*4	*R*1	*R*2	*R*3	*R*4
Cement		100								
SSR1		70	30							
SSR2		70								
SSR3		70								
SSR4	0.35	70								
QR1		70		30						
QR2		70			30					
QR3		70				30				
QR4		70					30			
								30		
									30	
										30

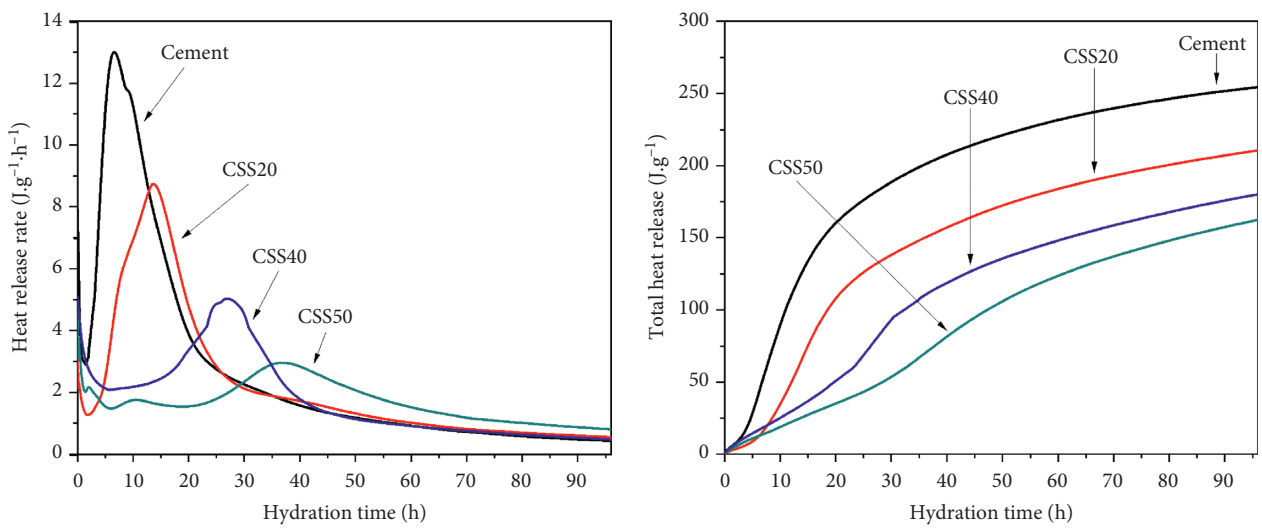

Figure 3: Hydration heat curves of blended cement containing different amounts of steel slag powder. (a) Exothermic rate. (b) Total heat release.

total heat release, as the amount of steel slag powder increases, the blended cement's complete heat release decreases gradually. The blended cement's cumulative heat release mixed with 20% to 50% steel slag powder was 0.83, 0.71, and 0.64 of the reference cement samples, respectively, after 96 h hydration time.

3.2. Nonevaporable Water Content of Blended Cement Paste. The nonevaporable water content of blended cements containing different amounts of steel slag powder at 28 days is shown in Figure 4. It can be seen from Figure 4 that the nonevaporable water content of the blended cement gradually decreases with the increase of steel slag powder content. The addition of a small amount of steel slag powder (such as 20% content) has little effect on the nonevaporable water content of the blended cement. When the steel slag powder content is greater than 40%, the nonevaporable water content of the blended cement is significantly reduced. Moreover, there is a binomial relationship between the nonevaporable water content of blended cement and the amount of steel slag powder.

In order to further reflect the contribution of steel slag powder to the nonevaporable water content of blended cement, the quartz powder (inert material) with similar particle size distribution was selected as a reference. Moreover, it is assumed that the nonevaporable water content of blended cement is generated by the hydration superposition of clinker and steel slag. Furthermore, the influence coefficient of nonevaporable water content, Φ_{Wn}, is used to represent the contribution of steel slag powder to the nonevaporable water content of the blended cement. The calculation formula is as follows:

$$\Phi_{Wn} = \frac{Wn_{(CSS)} - Wn_{(CQ)}}{Wn_{(CSS)}} \times 100\%, \quad (3)$$

where $Wn_{(CSS)}$ is the nonevaporable water content of the blended cement paste containing steel slag powder; and $Wn_{(CQ)}$ is the nonevaporable water content of the blended cement paste containing quartz powder.

As shown in Figure 5, the influence coefficient of nonevaporable water content (Φ_{Wn}) gradually increases with the increase of the amount of steel slag powder, and the two

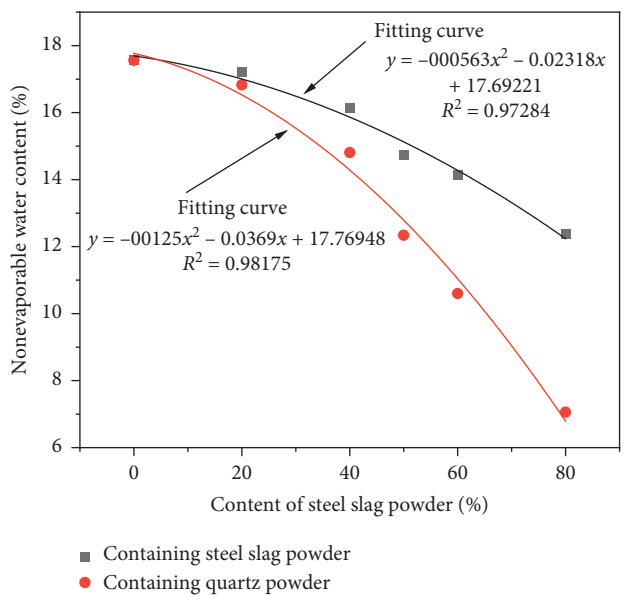

Figure 4: Nonevaporable water content of blended cement containing different amounts of steel slag powder.

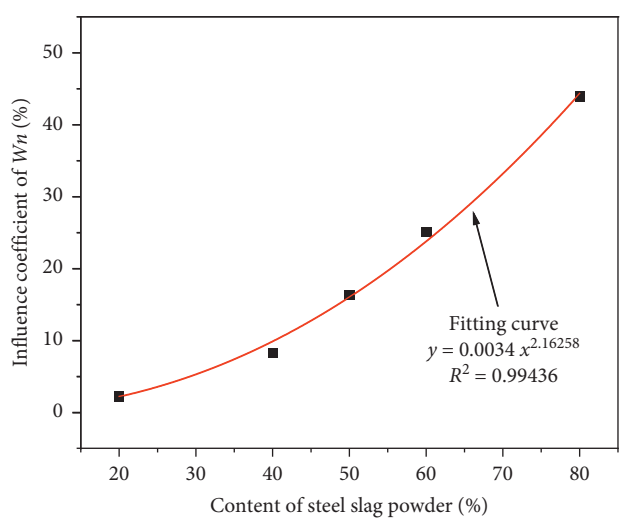

Figure 5: Influence coefficient of steel slag powder content on nonevaporable water content of blended cement.

meet an exponential relationship. When the amount of steel slag powder is less than 40%, Φ_{Wn} of blended cement is less than 10%, which also indicates that the contribution of steel slag powder to the nonevaporable water content of blended cement is much less than that of cement clinker.

3.3. Strength of Blended Cement Paste. The compressive strengths of blended cement paste containing different amounts of steel slag powder are shown in Figure 6. It can be seen from the figure that the amount of steel slag powder has a significant effect on the strength of cement paste. The compressive strengths of blended cement paste at various ages decrease with the increase of steel slag powder content. Steel slag powder has the most obvious effect on the 3 d

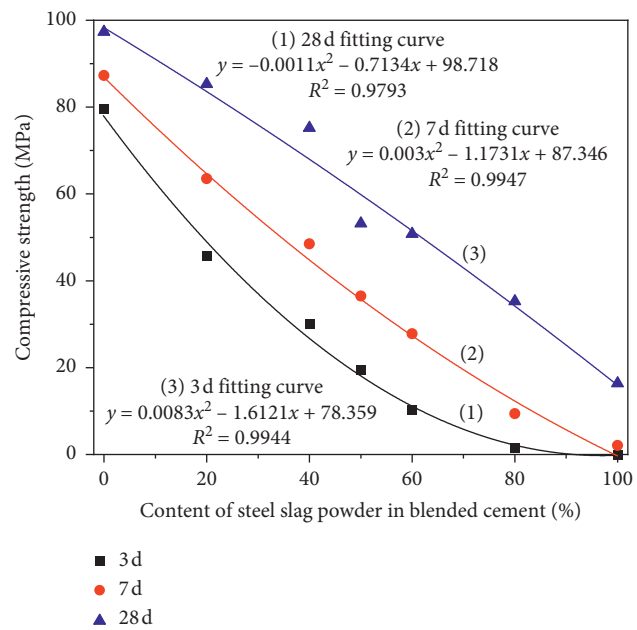

Figure 6: Strength and fitting result of blended cement containing steel slag powder.

strength of blended cement. For example, when 20% steel slag powder is added, the 3d strength of blended cement decreases by 42.6%, while the 28 d strength decreases by only 12.3%. From the fitting results of the strength of blended cement and the amount of steel slag powder, it can be seen that the influence of the amount of steel slag powder on the strength of the blended cement at various ages conforms to the binomial function relationship.

Similarly, the quartz powder, an inert material with a similar particle size distribution, is selected as a reference, and it is assumed that the strength of the blended cement is only produced by the hydration of the clinker and steel slag. Therefore, the strength influence coefficient, Φ_S, is used to represent the contribution of steel slag powder to the strength of blended cement. The calculation formula is as follows (4), and the result is shown in Figure 7:

$$\Phi_S = \frac{S_{CSS} - S_{CQ}}{S_{CSS}} \times 100\%, \tag{4}$$

where S_{CSS} is the compressive strength of the blended cement paste containing steel slag powder and $Wn_{(CQ)}$ is the compressive strength of the blended cement paste containing quartz powder.

The results in Figures 7(a) and 7(b) show that the compressive strength of the blended cement paste containing steel slag powder at the age of 3 days is lower than that of the blended cement containing quartz powder, but the result is the opposite at the age of 28 days. The reason is that the quartz powder is an inert material and does not participate in the hydration reaction. It plays a "dilution" effect on the blended cement system in the early stage, thereby increasing the actual water-to-cement ratio of the clinker minerals involved in hydration reaction and promoting its early hydration reaction degree. By contrast, the

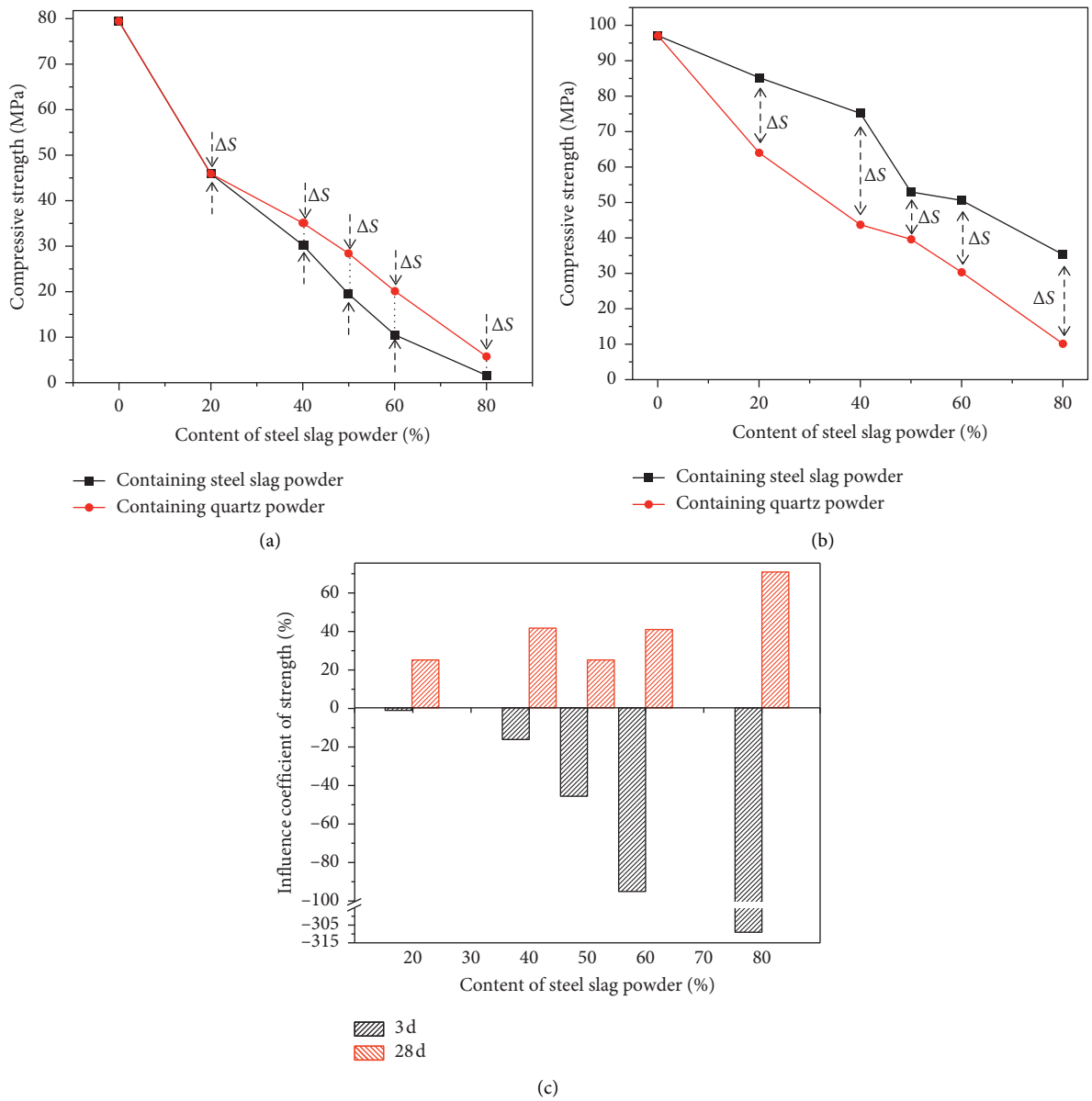

Figure 7: Influence coefficient of steel slag powder on compressive strength of blended cement. (a) 3 d. (b) 28 d. (c) Influence coefficient of strength.

steel slag powder has a low hydration degree at the age of 3 days due to the low early activity, so its contribution to the early strength of blended cement is very small. However, at the same time, it needs to occupy the water in the system to dissolve the mineral ions so that the water involved in the hydration reaction of clinker mineral is relatively reduced, delaying its hydration process, resulting in its strength contribution is also reduced.

However, with the prolongation of the age, the hydration degree of steel slag powder in blended cement gradually increases. By the age of 28 d, the strength of blended cement produced by hydration of clinker and steel slag will exceed that of blended cement containing quartz powder. It can be seen intuitively from Figure 7(c) that the strength influence coefficient of the blended cement paste, Φ_S, is negative at the age of 3 d. The greater the amount of steel slag powder, the greater the negative influence on the compressive strength. However, Φ_S is positive at the age of 28 days and exceeds 25%.

3.4. Morphology of Blended Cement Paste. The morphologies of blended cement containing different amounts of steel slag powder (*R*2) at 3 days and 28 days are shown in Figure 8.

It can be seen from Figure 8(a) that the morphologies of blended cement have changed obviously with the increase of the amount of steel slag powder. Blended cement with a small additional amount (such as 20%) of steel slag powder has more hydration products, such as amorphous C-S-H gels and $Ca(OH)_2$, and compact structure with fewer pores.

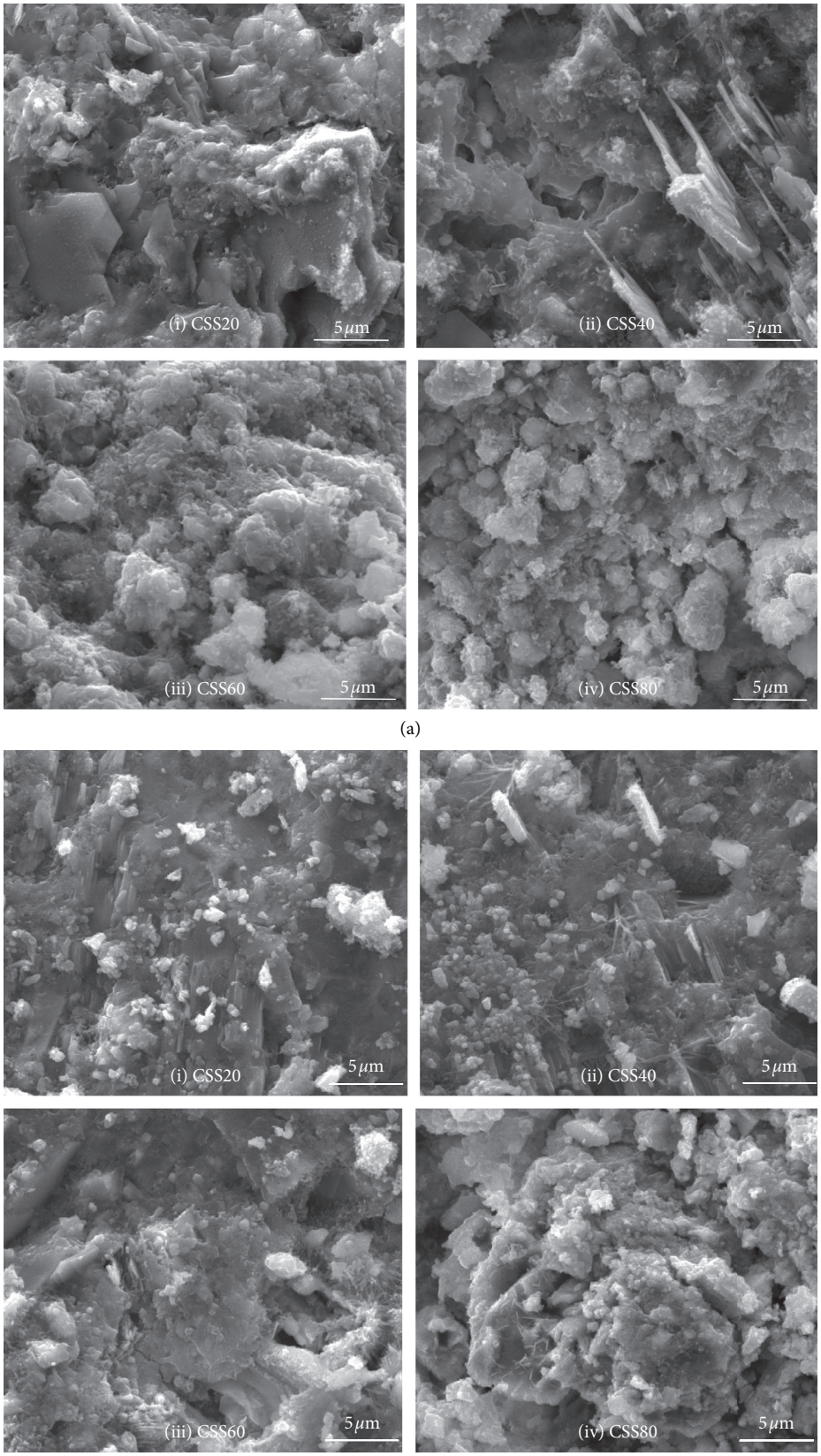

Figure 8: Morphology of blended cement containing different amounts of steel slag powder. (a) 3 d. (b) 28 d.

Moreover, the product system mainly consists of cement hydration products, in which a very small number of hydration products of steel slag are wrapped. On the contrary, when the addition amount of steel slag powder is high (such as 80%), the hydration products of steel slag are the main components in the blended cement, but the hydration products in the system are initially formed with scattered distribution and loose structure with more pores and poor compactness.

Figure 8(b) shows that the hydration products of blended cement increased significantly at 28 days, and the amorphous C-S-H gels accumulated on one another and were basically connected as a whole. Moreover, with the increase of the addition amount of steel slag powder, the change of the morphology and microstructure of blended cement at 28 days is relatively smaller than that at 3 days. This is due to the fact that the hydration of steel slag at 28 days is obviously sufficient compared with that at 3 days, and the hydration products generated continuously fill the pore structure and improve the compactness in the system during 28 days. Thereout, the effect of steel slag powder content on the morphology and microstructure of the hydration products of blended cement is relatively weakened at 28 days, which is consistent with the above-mentioned influence of steel slag powder content on the strength of blended cement.

3.5. Pore Structure of Blended Cement Paste. The pore volume distribution and aperture parameter value of blended cement paste containing steel slag powder at 28 days are shown in Figures 9 and 10, respectively. It can be seen from Figure 9 that the pore size of blended cement paste is mainly distributed in the range of 3–10 nm and 30–100 nm. The higher the content of steel slag powder in blended cement, the higher the cumulative pore volume of the paste. As shown in Table 5, the total pore volume, median pore size, and porosity of the blended cement paste gradually increase with the increase of steel slag powder content. The total pore volume increased from 0.1178 mL/g to 0.1995 mL/g, the median pore size increased from 21.1 nm to 34.4 nm, and the porosity increased from 21.62% to 34.80%. In particular, the pores of blended cement paste with a large amount of steel slag increased significantly.

4. Effect of Particle Size of Steel Slag Powder on the Properties of Blended Cement

4.1. Nonevaporable Water Content of Blended Cement Paste. The nonevaporable water contents of blended cement pastes containing 30% steel slag powder or quartz powder with different particle sizes at 28 days are shown in Figure 10. The results show that the nonevaporable water contents of blended cement paste are gradually decreased with the increase of particles' size of steel slag powder. However, the nonevaporable water contents of blended cement paste containing quartz powder show an opposite law. The reason is that the quartz powder does not participate in the hydration reaction and plays a "dilution" effect on the blended cement system. The larger the particle size of quartz powder, the stronger the "dilution" effect in a blended cement system. Thus, the hydration reaction of the clinker minerals will be promoted, resulting in a relatively high nonevaporable water content.

As shown in Figure 11, Φ_{Wn} gradually decreases with the increase of particles' size of steel slag powder. When the particle size of steel slag powder is $R1$, Φ_{Wn} of blended cement is 18.32%, and when the particle size of steel slag powder increases to $R2$, the influence coefficient decreases to 9.5%. It indicates that 30% steel slag powder has little contribution to the nonevaporable water content of blended cement, and its contribution is also greatly affected by particle size.

4.2. Porosity of Blended Cement Paste. The porosities of blended cement pastes containing 30% steel slag powder or quartz powder with different particle sizes at 28 days are shown in Figure 12. The results show that the porosities of blended cement paste gradually increase with the increase of particle size of steel slag powder or quartz powder. The reason is that the quartz powder is an inert material and only plays a filling role in blended cement. Therefore, quartz powder with a particle size distribution similar to steel slag powder can be used to approximate the physical filling effect of steel slag powder on blended cement.

It can be seen from Figure 12 that the porosity of blended cement paste decreases with the decrease of quartz particle size; that is, the physical filling effect of steel slag powder on blended cement is enhanced with the decrease of particle size. Comparing the porosities of the blended cement paste with steel slag powder and the quartz powder, it can be seen that the smaller the particle size, the greater the gap between the two. This is because the steel slag powder with a small particle size has relatively high hydration activity, which promotes the production of more hydration products and further fills the pores of the paste, thereby reducing the porosity of paste. The filling effect caused by the hydration reaction of steel slag powder can be regarded as the chemical filling role (Φ_F) of steel slag powder on blended cement. The calculation formula is as follows (5), and the result is shown in Figure 13.

$$\Phi_F = \frac{P_{CQ} - P_{CSS}}{100 - P_{CSS}} \times 100\%, \tag{5}$$

where P_{CSS} is the porosity of the blended cement paste containing steel slag powder; S_{CQ} is the porosity of the blended cement paste containing quartz powder.

As shown in Figure 13, the chemical filling role gradually weakens with the increase of the particle size of steel slag powder. Generally, the chemical filling role of steel slag powder on the blended cement is relatively small. The chemical filling role of 30% steel slag powder with different particle sizes in blended cement paste is only in the range of 1.13%–5.06%.

4.3. Strength of Blended Cement Paste. The strengths of blended cement pastes containing 30% steel slag powder or

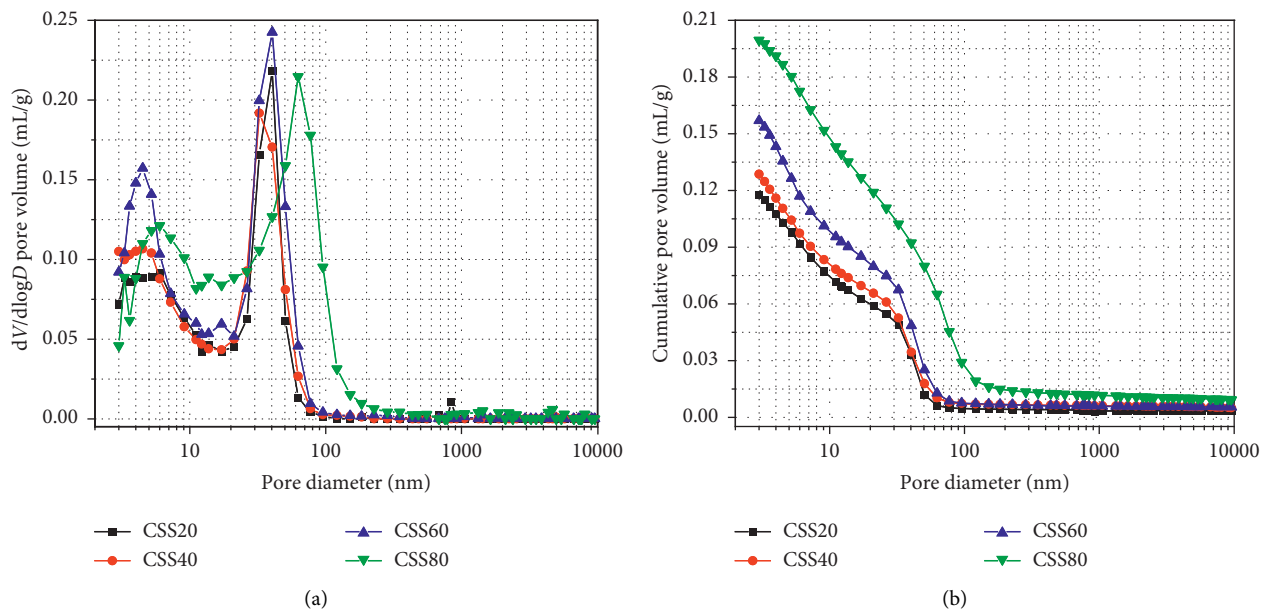

Figure 9: Pore volume distribution of blended cement paste containing steel slag powder. (a) Differential distribution. (b) Cumulative distribution.

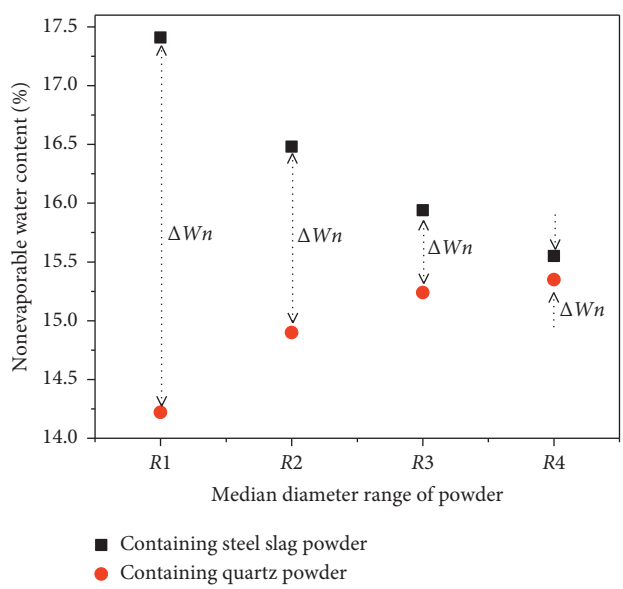

Figure 10: Nonevaporable water content of blended cement containing steel slag powder with different particle sizes.

Table 5: Aperture parameters of blended cement paste containing steel slag powder.

Specimens	Total pore volume (mL/g)	Median pore size (nm)	Porosity (%)
CSS20	0.1178	21.1	21.62
CSS40	0.1286	22.5	23.61
CSS60	0.1569	23.2	28.85
CSS80	0.1995	34.4	34.80

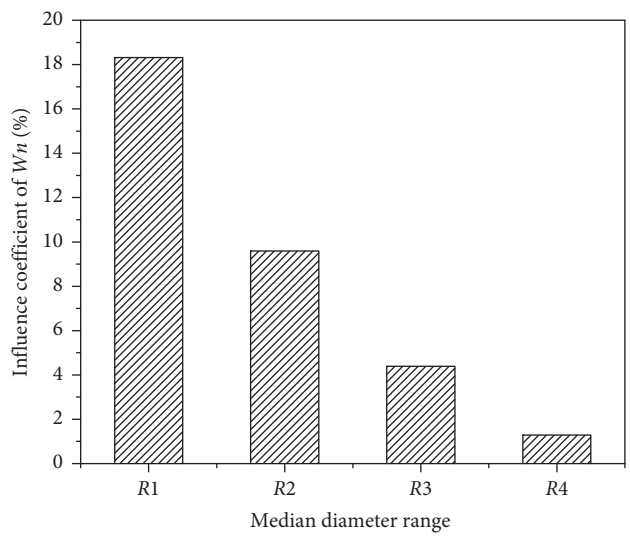

Figure 11: Influence coefficient of steel slag powder with different particle sizes on nonevaporable water content of blended cement.

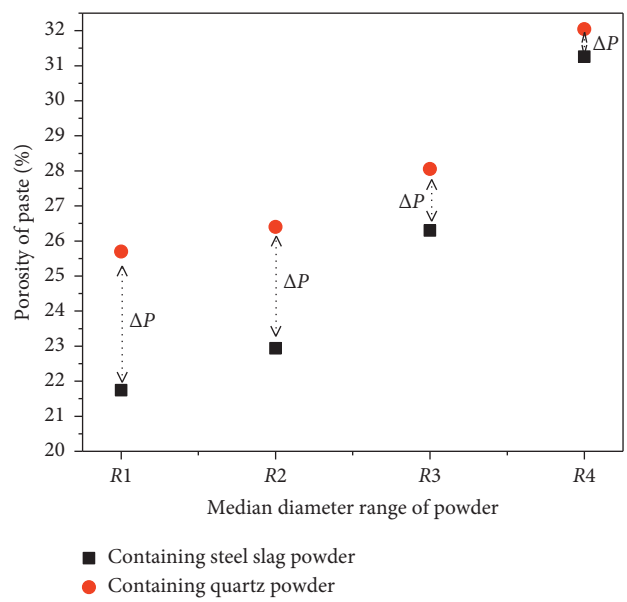

Figure 12: Effects of steel slag and quartz powder on the porosity of blended cement.

quartz powder with different particle sizes at 28 days are shown in Figure 14. The results show that the particle size of steel slag powder has different effects on the 3 d and 28 d strength of the blended cement paste. With the increase of particle size of the steel slag powder, the 3 d strength of the blended cement paste first increases and then decreases, while the 28 d strength gradually decreases. The reason is similar to the explanation in Section 3.3.

As shown in Figure 15, the results show that the influence coefficient of steel slag powder on the compressive strength of the blended cement paste is negative at 3 days, and the smaller the particle size of steel slag powder, the greater the negative impact on compressive strength. At the age of 28 days, the influence coefficient of strength is positive and in the range of 25%–30%. This is also just close to the amount of steel slag powder in the blended cement in this study.

4.4. Morphology of Blended Cement Paste. The morphologies of blended cement containing steel slag powder with different particle size at 3 days and 28 days are shown in Figure 16.

It can be seen from Figure 16(a) that the type and morphology of the hydration products of the four kinds of blended cement basically did not change much, but the compactness of the paste structure gradually increased slightly with the increase of the particle size of steel slag. Figure 16(b) shows an opposite rule; that is, with the increase of the particle size of steel slag, the hydration products of blended cement gradually decrease at 28 days, the structure of paste becomes loose, and the compactness also gradually decreases. This is consistent with the above-mentioned influence of particle size of steel slag powder on the strength of blended cement. The reason is that the early

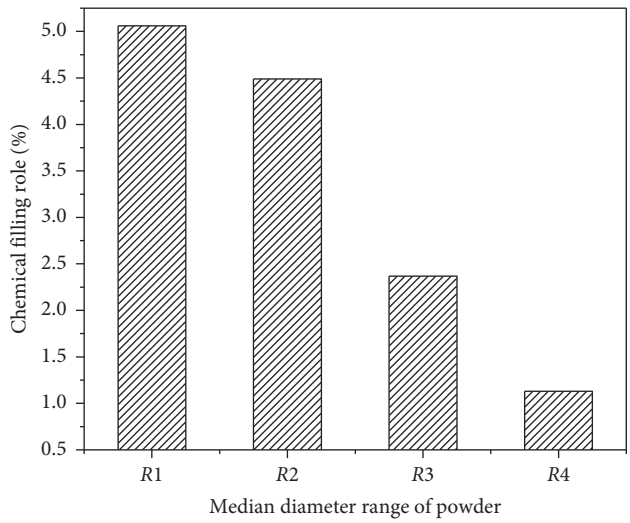

Figure 13: Chemical filling role of steel slag powder with different particle sizes in blended cement paste.

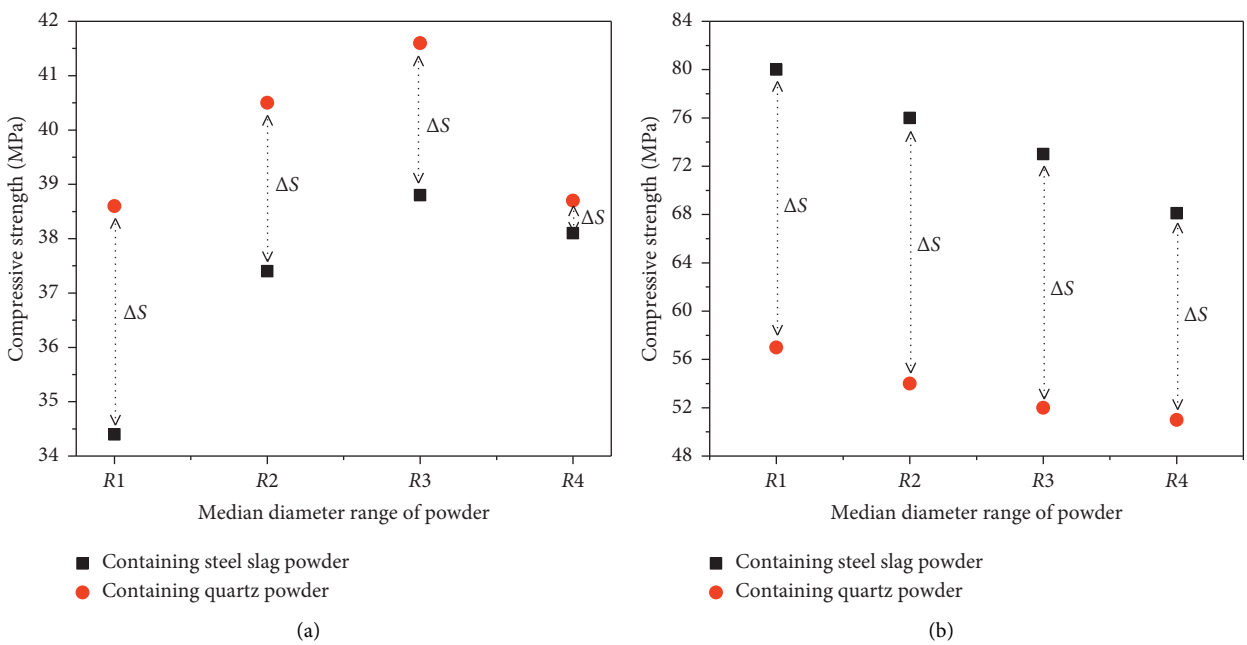

Figure 14: Compressive strength blended cement paste containing different particle size steel slag and quartz powder. (a) 3 d. (b) 28 d.

activity of steel slag is very low, and the steel slag with a large particle size basically would not participate in the hydration reaction at 3 days, which actually generates "dilution effect" to the water-cement ratio of the cement component in blended cement system. The "dilution effect," in other words, is to increase the water-cement ratio of the cement component in the blended cement system, so the hydration of the cement component in blended cement is accelerated. The smaller the steel slag particle size, the weaker the dilution effect, so the microstructure of blended cement containing steel slag powder with large particle size is relatively good at 3 days. However, with the extension of age, the hydration reaction of steel slag with a small particle size would gradually improve, and its hydration products can further fill the structure of blended cement to make it more compact in later ages. While the hydration effect of steel slag with a large particle size is lower than that of steel slag with small particle size, the blended cement containing steel slag with smaller particle size has more hydration products and a relatively compact microstructure. It also explains the effect rule of particle size of steel slag on the macroscopic properties of blended cement from the view of morphology and microstructure of hydration products.

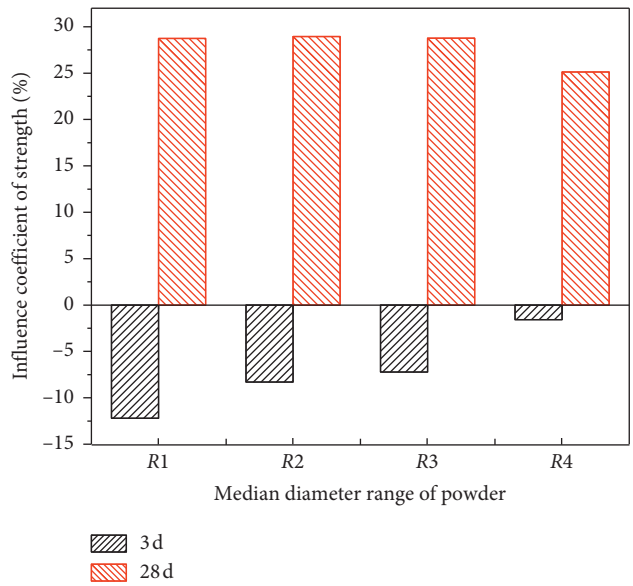

Figure 15: Strength contribution ratio of different particle size steel slag powder in blended cement.

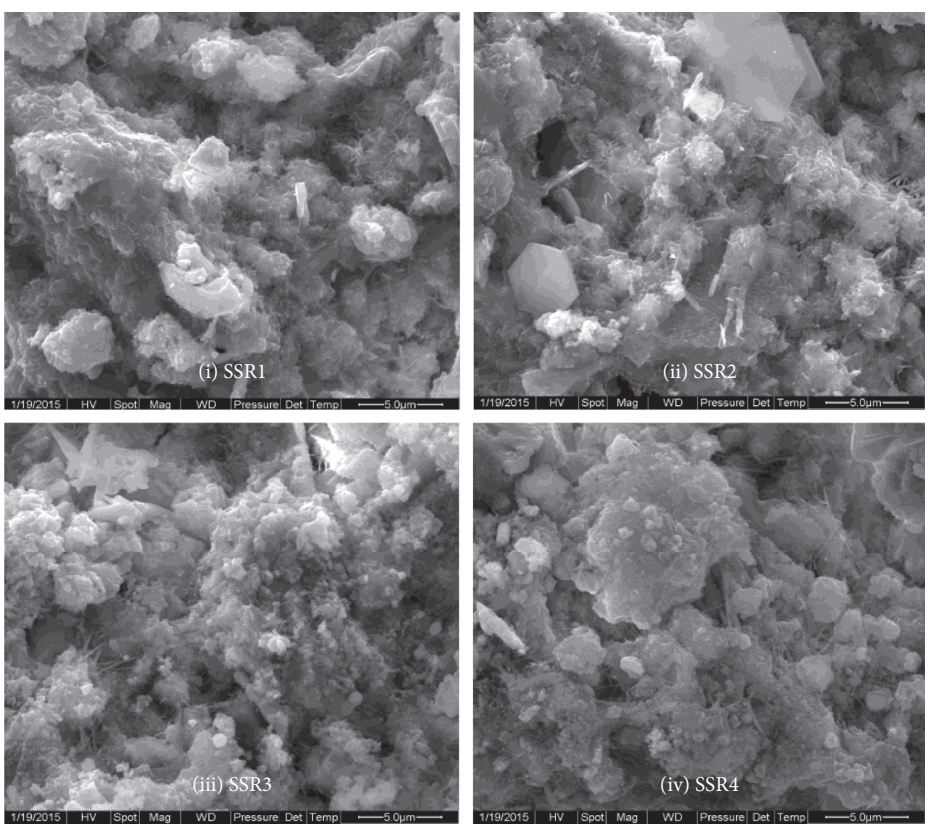

(a)

Figure 16: Continued.

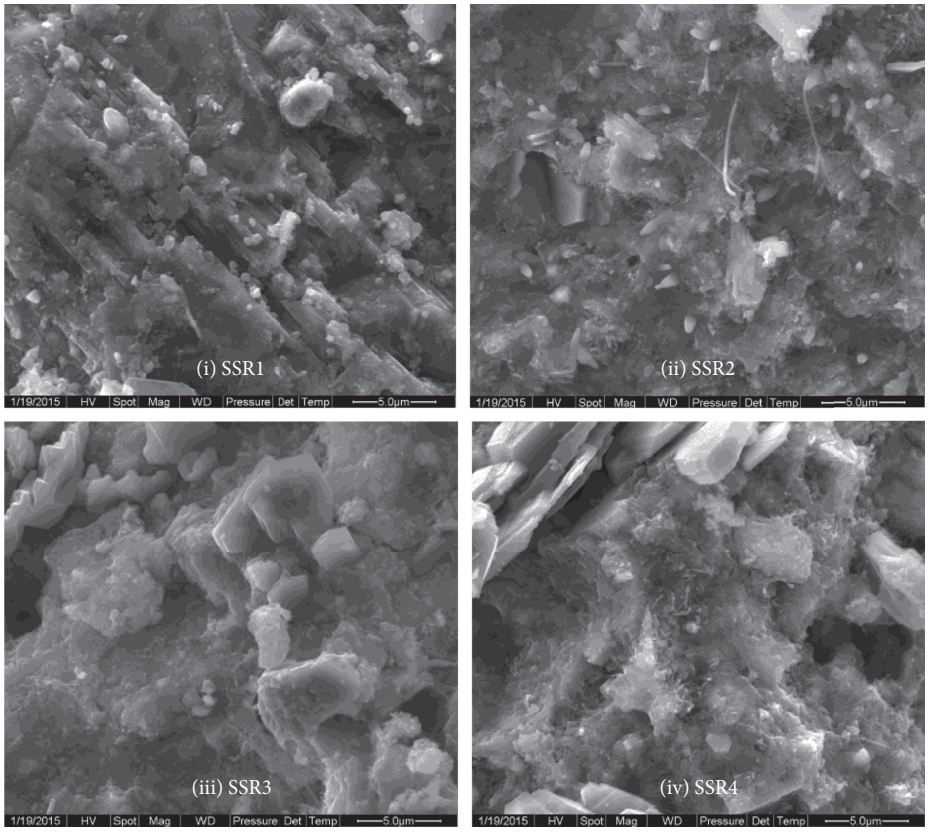

(b)

Figure 16: Morphology of blended cement containing steel slag powder with different sizes. (a) 3 d. (b) 28 d.

5. Conclusions

(1) The influence coefficient of nonevaporable water content (Φ_{Wn}) of blended cement paste is in an exponential relationship with the amount of steel slag powder. Moreover, at a dosage of 30%, Φ_{Wn} gradually decreases with the increase of the steel slag powder particle size.

(2) Both the early and late compressive strengths of blended cement paste are in a binomial relationship with the amount of steel slag powder. With the increase of particle size of the steel slag powder, the 3 d strength of the blended cement paste first increases and then decreases, while the 28 d strength gradually decreases. The influence coefficient of steel slag powder on the compressive strength of blended cement paste is negative at the age of 3 days. The greater the amount of steel slag powder or the smaller the particle size, the greater the negative influence on the compressive strength; and at the age of 28 days, the strength influence coefficient is positive.

(3) The pore size of the blended cement paste containing steel slag powder is mainly distributed in the range of 3–10 nm and 30–100 nm, and both the median pore size and porosity increase gradually with the increase of steel slag powder content. The chemical filling role of steel slag powder on the blended cement paste gradually weakens with the increase of its particle size. The chemical filling role of 30% steel slag powder with different particle sizes in the blended cement paste is only in the range of 1.13%–5.06%. The hydration products of blended cement containing steel slag powder are mainly amorphous C-S-H gel and platy $Ca(OH)_2$, and its density is consistent with the law of its porosity.

Data Availability

The data used to support the findings of this study are included within the article.

Conflicts of Interest

The authors declare that they have no conflicts of interest.

Acknowledgments

This work was financially supported by the National Natural Science Foundation of China (No. 51908568), the Natural Science Foundation of Guangdong Province (2019A1515011981), the Natural Science Foundation of Beijing (Nos. 8204058 and 2184118), and the State Key Laboratory Open fund of Marine Resource Utilization in the South China Sea (Hainan University) (201904).

References

[1] T. Honorio, B. Bary, and F. Benboudjema, "Thermal properties of cement-based materials: multiscale estimations at early-age," *Cement and Concrete Composites*, vol. 87, pp. 205–219, 2018.

[2] J. Kim, Y. C. Choi, and S. Choi, "Fractal characteristics of pore structures in GGBFS-based cement pastes," *Applied Surface Science*.vol. 428, pp. 304–314, 2017.

[3] Q. H. Nguyen, S. Lorente, and A. Duhard-Barone, "Effect of the pore size of cement based materials on ionic transport," *Construction and Building Materials*, vol. 147, pp. 160–167, 2017.

[4] P. K. Mehta and P. J. M. Monteiro, *Concrete: Microstructure, Properties, and Materials*, America, McGraw-Hill Company, Inc., New York, NY, USA, 2006.

[5] T. Zhang, Q. Yu, J. Wei, and P. Zhang, "A new gap-graded particle size distribution and resulting consequences on properties of blended cement," *Cement and Concrete Composites*, vol. 33, no. 5, pp. 543–550, 2011.

[6] X. Lu, S. X. Wang, C. H. Li, Z. M. Ye, and X. Cheng, "Properties and the hydration of portland limestone cement with diethanol-isopropanolamine," *Ceramics-Silikáty*, vol. 62, pp. 233–239, 2018.

[7] J. H. Zhao, L. Y. Tong, B. E. Li et al., "Eco-friendly geopolymer materials: a review of performance improvement, potential application and sustainability assessment," *Journal of Cleaner Production*, vol. 307, Article ID 127085, 2021.

[8] Á. Fernández, J. L. García Calvo, and M. C. Alonso, "Ordinary portland cement composition of ternary for the optimization of the synergies of supplementary cementitious materials binders in hydration processes," *Cement and Concrete Composites*, vol. 89, pp. 238–250, 2018.

[9] M. Heikal and H. El-Didamony, "Hydration and properties of blended cement systems incorporating industrial wastes," *Ceramics-Silikáty*, vol. 57, pp. 73–75, 2013.

[10] A. Aghaeipour and M. Madhkhan, "Effect of ground granulated blast furnace slag (GGBFS) on RCCP durability," *Construction and Building Materials*, vol. 141, pp. 533–541, 2017.

[11] Y. J. Zhang, *Study on the theory and method of optimization design of mineral admixtures*, Ph.D. thesis, Tongji University, Shanghai, China, 2004.

[12] C. Y. Lee, H. K. Lee, and K. M. Lee, "Strength and microstructural characteristics of chemically activated fly ash-cement systems," *Cement and Concrete Research*, vol. 33, no. 3, pp. 425–431, 2003.

[13] Y. Peng, S. Hu, and Q. Ding, "Dense packing properties of mineral admixtures in cementitious material," *Particuology*, vol. 7, no. 5, pp. 399–402, 2009.

[14] V. M. John, B. L. Damineli, M. Quattrone, and R. G. Pileggi, "Fillers in cementitious materials," *Cement and Concrete Research*, vol. 114, pp. 65–78, 2018.

[15] M. Záleská, M. Pavlíková, Z. Pavlík et al., "Physical and chemical characterization of technogenic pozzolans for the application in blended cements," *Construction and Building Materials*, vol. 160, pp. 106–116, 2018.

[16] I. Mehdipour and K. H. Khayat, "Understanding the role of particle packing characteristics in rheo-physical properties of cementitious suspensions: a literature review," *Construction and Building Materials*, vol. 161, pp. 340–353, 2018.

[17] J. Zhao, D. Wang, P. Yan, S. Zhao, and D. Zhang, "Particle characteristics and hydration activity of ground granulated blast furnace slag powder containing industrial crude glycerol-based grinding aids," *Construction and Building Materials*, vol. 104, pp. 134–141, 2016.

[18] J. Zhao, D. Wang, and P. Yan, "Design and experimental study of a ternary blended cement containing high volume steel slag and blast-furnace slag based on Fuller distribution model," *Construction and Building Materials*, vol. 140, pp. 248–256, 2017.

[19] K. E. Hassan, J. G. Cabrera, and R. S. Maliehe, "The effect of mineral admixtures on the properties of high-performance concrete," *Cement and Concrete Composites*, vol. 22, no. 4, pp. 267–271, 2000.

[20] J. J. Brooks, M. A. Megat Johari, and M. Mazloom, "Effect of admixtures on the setting times of high-strength concrete," *Cement and Concrete Composites*, vol. 22, no. 4, pp. 293–301, 2000.

[21] M. Uysal and K. Yilmaz, "Effect of mineral admixtures on properties of self-compacting concrete," *Cement and Concrete Composites*, vol. 33, no. 7, pp. 771–776, 2011.

[22] Y. Jiang, T. Ling, C. Shi, and S. Pan, "Characteristics of steel slags and their use in cement and concrete-a review," *Resources, Conservation and Recycling*, vol. 136, pp. 187–197, 2018.

[23] J. Zhao, P. Yan, and D. Wang, "Research on mineral characteristics of converter steel slag and its comprehensive utilization of internal and external recycle," *Journal of Cleaner Production*, vol. 156, pp. 50–61, 2017.

[24] J. Rosales, M. Cabrera, and F. Agrela, "Effect of stainless steel slag waste as a replacement for cement in mortars. Mechanical and statistical study," *Construction and Building Materials*, vol. 142, pp. 444–458, 2017.

[25] J. Zhao, D. Wang, P. Yan, D. Zhang, and H. Wang, "Self-cementitious property of steel slag powder blended with gypsum," *Construction and Building Materials*, vol. 113, pp. 835–842, 2016.

[26] J. Li, Q. Yu, J. Wei, and T. Zhang, "Structural characteristics and hydration kinetics of modified steel slag," *Cement and Concrete Research*, vol. 41, no. 3, pp. 324–329, 2011.

[27] M. X. Shi, Q. Wang, and Z. K. Zhou, "Comparison of the properties between high-volume fly ash concrete and high-volume steel slag concrete under temperature matching curing condition," *Construction and Building Materials*, vol. 98, pp. 649–655, 2015.

[28] J. Du and J. X. Liu, "Hydraulic properties and paste structure of basic oxygen furnace steel slag-cement blended materials," *Fresenius Environmental Bulletin*, vol. 22, pp. 3279–3286, 2013.

[29] B. Zhang, J. Hu, and M. Y. Li, "Hydration properties of steel slag under different curing temperatures," *Applied Mechanics and Materials*, vol. 507, pp. 295–299, 2014.

[30] Q. Wang, P. Yan, and J. Feng, "A discussion on improving hydration activity of steel slag by altering its mineral compositions," *Journal of Hazardous Materials*, vol. 186, no. 2-3, pp. 1070–1075, 2011.

[31] Y. M. Zhang, W. Sun, and H. D. Yan, "Hydration of high-volume fly ash cement pastes," *Cement and Concrete Composites*, vol. 22, no. 6, pp. 445–452, 2000.

Hindawi
Advances in Civil Engineering
Volume 2021, Article ID 5534002, 14 pages
https://doi.org/10.1155/2021/5534002

Research Article

Influence of Concrete Sludge Addition in the Properties of Alkali-Activated and Non-Alkali-Activated Fly Ash-Based Mortars

Fotini Kesikidou, Stavroula Konopisi, and Eleftherios K. Anastasiou

Laboratory of Building Materials, School of Civil Engineering, Aristotle University of Thessaloniki, Thessaloniki 54124, Greece

Correspondence should be addressed to Eleftherios K. Anastasiou; elan@civil.auth.gr

Received 10 February 2021; Revised 15 April 2021; Accepted 27 April 2021; Published 7 May 2021

Academic Editor: Yingzi Yang

This study investigated the use of concrete sludge, a by-product of the ready-mix concrete industry, in combination with high-calcium fly ash in binary cementless binders. Concrete sludge was used in substitution rates ranging from 0% to 60% in test fly ash-based mortars to determine potential synergy. The mortars were tested for fresh and hardened properties; workability, viscosity, strength development, open porosity, early-age shrinkage, and analytical tests were carried out. A mortar with 50% fly ash and 50% limestone filler as binders was used for comparison purposes. Furthermore, a series of mortars with fly ash and concrete sludge were alkali-activated in order to determine potential strength gain. In the activated mortars, two fractions of concrete sludge were used, under 75 μm and 200 μm, due to different silicon oxide contents, while one mortar was cured at 40°C to investigate the effect of heating on alkali activation. Results show that sludge contributes to the formation of C-S-H and strength development when used in combination with high-calcium fly ash even at high replacement rates. The alkali activation of fly ash-concrete sludge system contributed to early-age strength development and to early-age shrinkage reduction.

1. Introduction

Today, in Europe, it is estimated that fresh concrete waste, at the production stage or the cleaning/washing stage of concrete trucks, is approximately 1–4% by weight of the total concrete produced [1]. After the washing of the barrels with huge amounts of water, up to 1300 liters per truck, the material is left to settle in large sedimentation tanks. From these tanks, the water can be reused to wash the vehicles or as mixing water for new concrete, while the sediment is concentrated at the bottom in the form of sludge [2]. This wet concrete sludge is difficult to handle and also has an alkaline pH value which makes the deposit of the material a burden for the environment and human health. In some countries, like UK, Spain, and USA, sludge is classified as a corrosive hazardous material due to its high alkalinity (pH > 11.5) [3–5].

Audo et al. [2] investigated the use of sludge from ready-mixed concrete plants as a substitute for limestone fillers. It has been noted that the rheology of the fresh state mortar is altered with the addition of sludge, leading to the mixture becoming less plastic. Compressive strength varied from a reduction of 30% to an increase of 17%, which is attributed to the different fractions of the sludge (finer than 100 μm and coarser than 100 μm) and the substitution rate of the sand fraction of the mortars [2]. Xi et al. [6] have studied the use of marble and concrete sludge as supplementary cementitious material by replacing cement in mortars. The researchers have found that both materials could be used as fillers, while the use of concrete sludge showed higher compressive strength than marble sludge, probably due to its higher alkalinity.

On the other hand, fly ash is a by-product, deriving from the combustion of coal or lignite, which has been studied extensively over the last years and is already used as supplementary cementitious material [7–9]. Its chemical composition depends on the type of raw material and the methods of the combustion. Fly ashes from the burning of coal typically have low calcium oxides content and classify as siliceous fly ashes with pozzolanic

properties. On the contrary, fly ashes from the burning of lignite are rich in calcium oxides and classify as high-calcium fly ashes with both pozzolanic and self-cementing properties. European Standard EN 450-1 classifies fly ash into two categories: siliceous fly ash, which contains calcium oxides in less than 10%, and calcareous fly ash, which has a content of calcium oxides over 10% [10]. Regardless of the type, the use of fly ash in cement and concrete has both economic and environmental benefits as it enhances the service life of concrete—for example, addition of up to 30% of fly ash in concrete reduces chloride penetration [11]—and reduces the energy consumption and carbon dioxide emissions from the production of cement [12]. Calcareous fly ash is known to exhibit considerable self-cementing properties due to its reactive lime and silica contents [13]. EN 197-1 [14] requires that it must show at least 10 MPa compressive strength at 28 days when mixed with water according to EN 196-1 [15] to be used in blended cements. Researchers have shown that the hydration of calcareous fly ash can be enhanced when used in combination with other supplementary cementitious materials or when alkali-activated [16]. The process of alkali-activation is a field of study that focuses on the use of by-products like fly ash and slag. It includes a chemical reaction by polymerization of aluminosilicate oxides under the influence of silicon solutions in highly alkaline conditions by heating [17]. Over the years, many researchers have focused on the activation of binders such as several types of slag and fly ash [18], metakaolin [19], natural pozzolans [20], and red mud [21]. Extensive research has been conducted in the case of fly ash, studying the properties of siliceous and high-calcium types of fly ash [22–28].

Since cement clinker is accountable for considerable carbon dioxide emission, focus is needed to improve reduced clinker or even clinker-free binders. Although fly ash and concrete sludge have been studied separately as additives in concrete [29–31], no focus has been given so far in the combination of the two binders, in order to develop cement-free binders. Along these lines, the paper attempts to explore the potential improvement of calcareous fly ash hydration by combining it with concrete sludge. Binary mortars based on fly ash and concrete sludge were tested for strength development for an increasing rate of fly ash replacement with concrete sludge. Fresh properties such as plastic viscosity and workability of the mortars were measured and flexural and compressive strength were tested at the ages of 7, 28, and 90 days. Open porosity and volume stability were also determined. *X*-Ray Diffraction (XRD) analysis, simultaneous system of Differential Thermal-Thermogravimetric Analysis (DTA-TG), and Fourier Transform Infrared Spectroscopy (FT-IR), with the technique of Attenuated Total Reflectance (ATR), were used to characterize changes and behavior of the structure. In an effort to explore the effect of concrete sludge on fly ash hydration, a fly ash-limestone filler binary mortar was prepared for comparison purposes. Furthermore, selected fly ash-concrete sludge binary mortars were prepared with a combination of sodium hydroxide and waterglass solutions as activator and tested for strength development.

2. Materials and Methods

2.1. Raw Materials. Concrete sludge was received in wet condition and was subsequently dried, ground in a laboratory ball mill, and sieved. Initially the sieving was carried out through the 75 μm sieve, but it was concluded from the chemical analyses that a lot of the silica present in the sludge (possibly in the form of hardened C-S-H) was retained in the sieve, so the sludge was also sieved through the 200 μm mesh, resulting in testing the material in two levels of fineness (S75 and S200). Calcareous fly ash (FA) originated from a power plant in Greece and was used unprocessed, while limestone filler (LF) was received from a local quarry, already ground to adequate fineness. The particle size distribution (PSD) analyses, of the fly ash, the two concrete sludge types, and the limestone filler were measured by Malvern P.S.A Mastersizer 2000-laser scattering technique and are presented in Figures 1–4, while the mean particle diameters d10, d50, and d90 (denoting that 10%, 50%, and 90%, resp., of each sample are below the reported values) are presented in Table 1.

The total oxides of the binders were determined by Atomic Absorption Spectroscopy analysis–AAS (AAnalyst 400 Perkin Elmer) and are shown in Table 2. The gravimetric determination of total sulphates content (as SO_3) was performed by precipitation under the influence of barium chloride ($BaCl_2$) solution. The loss of ignition (LOI) was determined by combustion of the binders at 1000°C. Additionally, the pore solution pH values of fresh pastes were measured by a pH-Meter 766 Calimatic-Knick.

Natural river sand (0–4) mm was used in all test mortars. A solution of sodium hydroxide (NaOH 6 M) and waterglass in a (1 : 1) ratio in combination with water was used as an activator in the alkali-activated mortars. A polycarboxylic-based superplasticizer was added when required to achieve adequate workability.

2.2. Mix Design. Initially six mortar mixtures (Table 3) were produced with increasing rate of fly ash replacement with concrete sludge, from 0% to 60% wt.%. The finer fraction of concrete sludge (S75) had a chemical composition very close to that of LF and could be considered as filler, while the particle size distribution showed that concrete sludge was considerably finer than LF and also considerably finer than fly ash. From the literature, it is known that the increased fineness of supplementary cementitious materials can promote binder hydration and strength development by improving particle packing and also through the filler effect [32]. Thus, it was decided to use the finer fraction of sludge (S75) in the first batch of mortars, while a binary mortar with 50% fly ash and 50% limestone filler was prepared to compare the reactivity of the sludge with the limestone filler.

Alkali activation was considered at a second mortar batch as a means to enhance the reactivity of the fly ash-concrete sludge system. The fly ash used was calcareous, with free calcium oxide (CaO_{free}) equal to 5.61%, determined according to EN 451-1 [33], and with considerable amounts of silicon dioxide and aluminum oxide. Based on previous research [34], it is possible to use alkali activation to promote

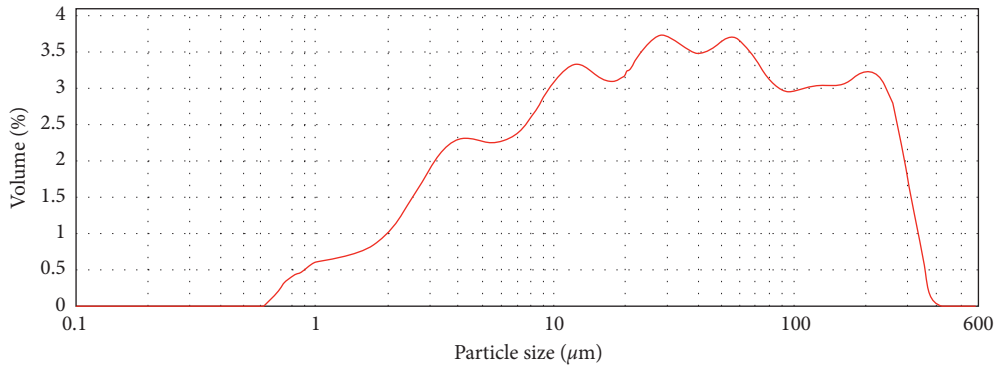

Figure 1: Particle size distribution of calcareous fly ash (FA).

the hydration of such fly ashes, and, therefore, it was decided to repeat three of the initial mortars (the ones with 0%, 20%, and 50% replacement with S75) using a combination of sodium hydroxide: waterglass solutions as activator. The three selected mixtures were decided based on the early strength results of the nonactivated mixtures. Regarding the concrete sludge, it is obvious that sieving of the material has an impact on the content of the silicon dioxide, which in the sludge under 75 μm is 2.28%, whereas in sludge under 200 μm it is 15.01% (Table 2). Since silicon dioxide content is important for the alkali activation process [17], it was decided to test a mortar using 30% replacement with the coarser, richer in silicon dioxide (SiO_2), S200 (AN30). The last mortar was repeated using heating at 40°C for 24 h after casting (AT30) in order to determine possible enhancement of the alkali activation through heating, reaching a second batch of five mortars (Table 4).

Mixing procedure followed 2 min in slow speed and 7 min in fast speed in the mixer, which was selected as appropriate for achieving adequate consistency. Workability was measured with the flow table test according to EN1015-3 [35] and plastic viscosity of the mixtures was also determined with an ICAR rheometer. Then the fresh mortars were cast in prismatic specimens $(40 \times 40 \times 160)\,\text{mm}^3$ and were cured for 24 hours in metallic molds at 25°C. Mixture AT30 was cured in an oven at 40°C to investigate the effect of early-age heating on alkali activation. After 24 hours all specimens were demolded and kept at a chamber with 90% RH and 21°C until testing.

2.3. Testing of Hardened Mortars. Compressive strength was measured at the ages of 7, 28, and 90 days according to EN 1015-11 [36]. Open porosity values at 28 days were measured following the RILEM CPC 11.3 Methodology [37] and early-age volume deformation was recorded up to 28 days, while the specimens were kept in a chamber with 50%RH and 21°C. XRD analysis, via a Bruker D2 Phaser diffractometer (CuKa1 radiation, 30 KV/10A, measurement range 5–70° 2θ, step 0,02°) was used for mineralogical characterization of phases. The content of the hydration products and the remaining compounds of calcium hydroxide and calcium carbonate were determined by DTA-TG (SDT 2960, TA Instruments) using N2 atmosphere from 10°C to 1000°C. The mid-IR spectrums (frequency range 4000–400 cm^{-1} at a resolution of 4 cm^{-1}) of samples were collected using a spectrometer (Cary 630 FTIR-Agilent Technologies) with an ATR mode, in order to record significant structural changes of the hydration products.

3. Results and Discussion

3.1. Nonactivated Mortars. Rheology of mortar is affected by multiple factors such the processing energy, the solid concentration, the paste/aggregate and mortar to aggregate/ratio, air content, and the paste composition [38]. More specifically, in terms of the paste rheology, the fineness of the binder, mineral additions, and chemical admixtures are of vital importance [39]. The chemical composition of the binder is another significant factor and, especially, its content in calcium and aluminum oxides and sulfates. Environmental conditions, such as temperature and humidity levels during mixing, also affect the measured results.

Previous work of the authors has showed that the composition of the fly ash, which is rich in calcium oxides, aluminum oxides, and sulfates, requires a different mixing procedure in order to decrease the viscosity of the mortar and achieve an appropriate workability [34]. The results of the average viscosity of all mixtures are presented in Table 5, along with the measured environmental temperature during the test and the workability of the mortars at the flow table. Viscosity was measured right after nine minutes of mixing.

Mixtures F, FS20, and FS30 did not give any results, because of their high viscosity. Due to the many factors involved in the test, more investigation is required in order to have more definite results. However, it could be said that higher percentages of concrete sludge reduce the viscosity of the mixtures. FA substitution with concrete sludge affects also the workability of the mixtures, by reducing water demand (Tables 3 and 4). High-calcium fly ash is known to have high water demand, mostly due to free calcium oxide content, and the use of concrete sludge seems to mitigate this effect, making it easier to achieve workable mortars.

Regarding strength development, Figure 5 shows the compressive strength test results for the mixtures without alkaline activation at 7, 28, and 90 days. In particular, the use of fly ash as binder showed relatively good strength results (16 MPa at 28 days) despite the high water to binder ratio.

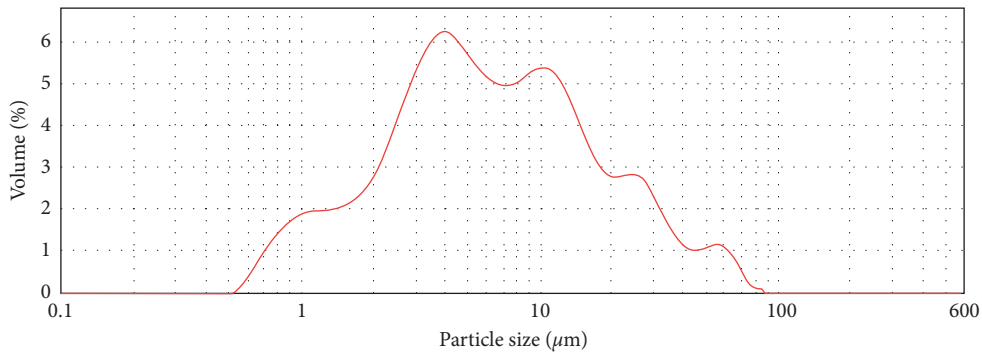

Figure 2: Particle size distribution of concrete sludge sieved under 75 μm (S75).

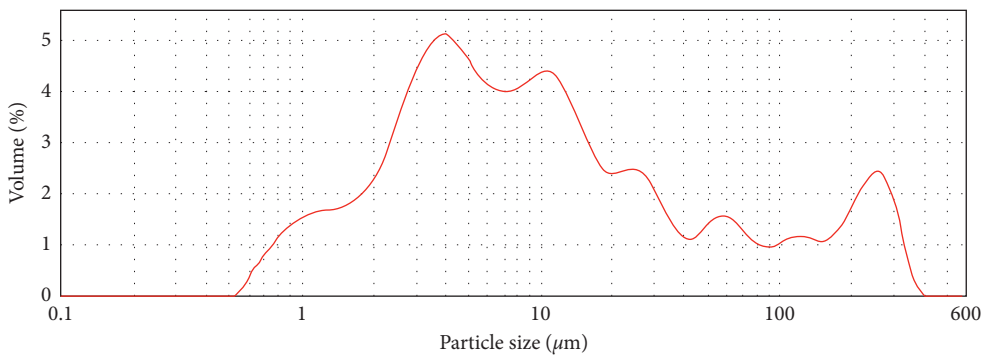

Figure 3: Particle size distribution of concrete sludge sieved under 200 μm (S200).

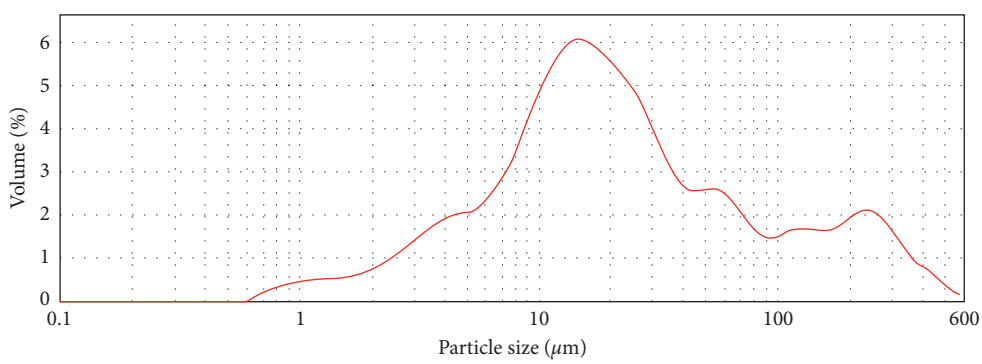

Figure 4: Particle size distribution of limestone filler (LF).

This could be attributed to the high contents of free calcium oxide and reactive silicon dioxide which are present in high-calcium fly ash. The reasonably low 7-day compressive strength of fly ash and the continued strength increase at 90 days indicate a slow rate of hydration mostly through the pozzolanic reaction. The replacement of up to 40% wt. of fly ash with concrete sludge inferred a slight 28-day compressive strength decrease (13–18%). Further increasing fly ash substitution rates to 50% and 60% resulted in considerably greater strength loss (29–43%). At earlier ages (7-day compressive strength), the differences from the various replacement rates were not very pronounced, while 90-day results showed improved results for lower replacement rates. A 22% strength increase was recorded for 20% substitution with concrete sludge, indicating an improvement in the hydration of fly ash. A smaller strength increase was observed for the 30% replacement rate, but overall increasing concrete sludge rate reduced strength proportionally.

Since the chemical composition of the concrete sludge used in these mortars (S75) was very similar to that of limestone filler (see Table 2), the improvement in the hydration of fly ash could be attributed to the filler effect. This effect is also observed when using limestone filler as cement substitution, which diminishes at higher substitution rates. However, mortar FF50 with 50% of fly ash substituted with limestone filler reached compressive strengths of 0.81 MPa at 7 days, 5.07 MPa at 28 days, and 7.92 at 90 days, a decrease of 85%, 56%, and 48% compared to mortar FS50 (50%

Table 1: Particle size distribution.

Sample	d10	d50	d90
F	3.51	29.68	191.09
S75	1.59	6.05	25.44
S200	1.82	8.35	143.82
LF	4.36	19.12	177.34

Table 2: Chemical composition (% wt) and pH values of raw materials.

Sample	Na_2O	K_2O	CaO	MgO	Fe_2O_3	Al_2O_3	SiO_2	SO_3	LOI	pH
F	0.92	1.14	22.58	1.87	5.08	17.85	46.83	3.68	2.92	13.75
S75	0.18	0.28	53.40	2.58	1.96	3.20	2.28	0.46	35.42	13.22
S200	0.18	0.09	39.95	1.56	1.18	3.55	15.01	0.50	38.17	11.87
LF	0.02	0.05	53.10	1.15	0.20	0.42	0.54	0.10	43.53	10.52

Table 3: Proportioning of test mortars.

Mixture	F (parts by mass)	CS75 (parts by mass)	LF (parts by mass)	Water/binder (parts by mass)	Natural river sand (parts by mass)	Superplasticizer (% by mass of the binder)
F	1.0	—	—	0.67	3.0	3.0
FS20	0.8	0.2	—	0.60	3.0	3.0
FS30	0.7	0.3	—	0.60	3.0	3.0
FS40	0.6	0.4	—	0.60	3.0	1.5
FS50	0.5	0.5	—	0.60	3.0	1.5
FS60	0.4	0.6	—	0.60	3.0	1.5
FF50	0.5	—	0.5	0.60	3.0	—

Table 4: Proportioning of alkali-activated mortars.

Mixture	F (parts by mass)	CS75 (parts by mass)	CS200 (parts by mass)	Liquid/binder (parts by mass)	Natural river sand (parts by mass)	Superplasticizer (% by mass of the binder)
AF	1.0	—	—	0.73	3.0	3.0
AFS20	0.8	0.2	—	0.67	3.0	3.0
AFS50	0.5	0.5	—	0.67	3.0	2.0
AN30/ AT30	0.7	—	0.3	0.67	3.0	3.0

substitution of fly ash with concrete sludge), respectively. These results indicate that concrete sludge has a different behavior than limestone filler and seems to contribute to the reaction mechanism. Another possible explanation for the higher reactivity of the mortars with concrete sludge is its high alkalinity (13.22 as opposed to 10.52 of limestone filler), which promotes hydration in the pore solution. The hydration products of the mortars with 50% fly ash replacement with either concrete sludge (FS50) or limestone filler (FF50) at 90 days were confirmed by the XRD diagrams and are presented in Figure 6.

The presence of inherent crystalline systems of calcite and quartz in all samples examined must be attributed mainly to the nature of the raw materials used (mixtures of fly ash with concrete sludge or limestone, at a ratio of 50 : 50). The phase of calcite is enhanced by the carbonation reaction of mixtures FS50 and FF50 during their exposure to atmospheric conditions for 90 days. The presence of gypsum and its anhydride is also observed in all mixtures, mainly due to the nature of the calcareous fly ash containing sulfates. The presence of crystalline phases of ettringite is due to the gradual hydration of sulfate phases of gypsum and anhydrite especially in the high alkaline environment (pH > 13) of the fly ash-concrete sludge mixture. In addition, the characteristic reflections of portlandite are identified and appear only in the diagram of FS50, as a product of long-term hydration possibly due to the nature of the concrete sludge [6]. Finally, secondary crystalline phases such as orthoclase and albite are detected, apparently due to the addition of siliceous sand.

In order to investigate further the hydration products of FS50 and FF50 mixtures at 90 days, DTA-TG analysis was applied and the thermographs presented in Figure 7 were obtained.

The peaks observed between 50°C and 200°C could be attributed to the presence of free water, as well as the bound water from the hydrated phases of calcium silicate hydrates, calcium aluminate hydrates, and sulphoaluminate hydrates [40–42]. Thus, the increase in the amount of nonevaporated water in FS50 mixture compared to FF50 mixture is probably due to an increase in the chemically bound water in C-S-H compounds in FS50 mixture [42]. The weight loss in

Table 5: Rheological properties of the mortars.

Mixture	Viscosity (Pa ∗ s)	Flow table workability (cm)	Laboratory temperature (°C)	Water/binder (parts by mass)
F	—	12.9	20.0	0.67
FS20	—	12.9	20.0	0.60
FS30	—	13.7	21.0	0.60
FS40	154.3	13.5	19.0	0.60
FS50	242.7	14.0	18.5	0.60
FS60	135.5	12.5	18.5	0.60
FF50	343.3	11.1	16.0	0.60

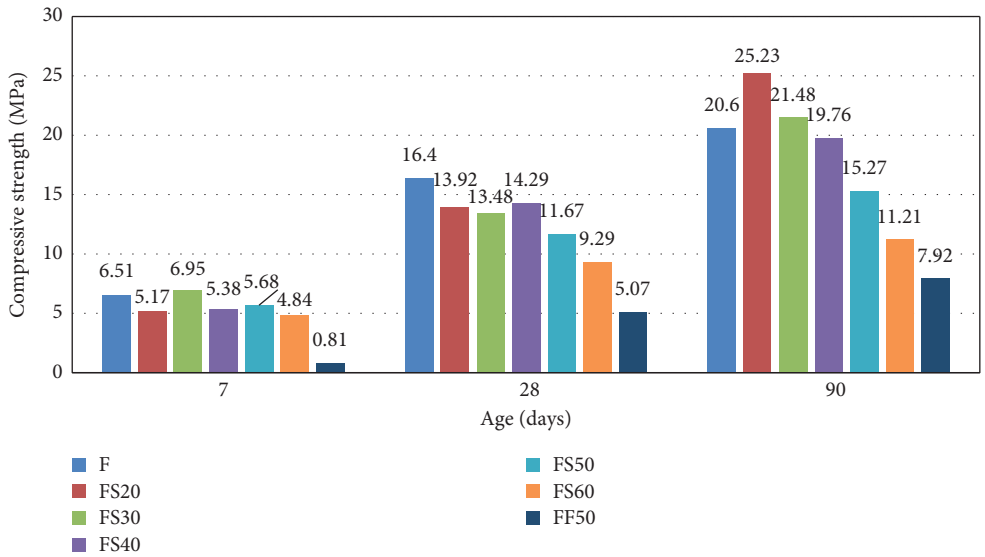

Figure 5: Compressive strength of nonactivated mortars at 7, 28, and 90 days.

the range of 400–450°C occurred mainly due to the dehydroxylation of calcium hydroxide, while the loss at 650–800°C was due to the decomposition of carbonates. The main difference between the two mortars is the loss of hydroxyls at 409–428°C for FS50 compared to FF50, interpreted as the presence of the hydration product $Ca(OH)_2$ of concrete sludge, probably increasing over time [2, 40–42].

The study of phase transformations of hydrated products at 90 days through the characteristic vibration bands and assignments (wavenumber in cm^{-1}) was conducted by taking spectra in the mid infrared by ATR technique and is presented in Figure 8 and Table 6.

The broad bands in the range of 3800–1600 cm^{-1} are generally assigned to vibration modes of bound water molecule and hydroxyls (HOH and –OH). The band at 3647 cm^{-1} observed in the hydrated product of the FS50 mixture is attributed to the hydroxyl anions of $Ca(OH)_2$. The band does not appear to the spectra of the FF50 mixture due to the nature of limestone. This agrees with the diagrams of XRD and TGA-DTA analyses, thus indicating the ability of FS50 components to give the hydration reaction possibly due to the cementitious nature of the sludge [2, 6]. The broad band at 3401 cm^{-1} in FS50 mixture was more intense compared to the FF50 mixture and this can be explained by the increased presence of hydrated products. The weak bands at 1626 cm^{-1} and at 1612 cm^{-1} in FS50 and FF50 mortars, respectively, are attributed to the bending deformation of HOH molecules. The bands at 1410 cm^{-1} and 874/711 cm^{-1} of the FS50 mortar and at 1407 cm^{-1} and 872/711 cm^{-1} of the FF50 mixture are attributed to $CaCO_3$ carbonates, which were mainly obtained from the carbonation process of the materials. The bands at 1103 cm^{-1} and 1144/1092 cm^{-1} in FS50 and FF50 mortars are attributed to the vibration of the sulphates group. Specifically, in the FS50 mortar, the band at 1103 cm^{-1} almost disappeared and was overlapped by the stretching vibration band of Si-O. The vibration strong band at 965 cm^{-1} of the FS50 mixture is worth noting, which increases in intensity and shifts to lower frequencies relative to the absorption of FF50 at 971 cm^{-1}, indicating the formation of amorphous C-S-H phase during the hydration process. Additionally, the changes observed in the region 670–450 cm^{-1} correspond to the bending vibrations from amorphous and crystalline aluminosilicates [43–47].

Porosity measurements at the age of 28 days, shown in Figure 9, confirm the compressive strength results of the mortars. When the amount of concrete sludge substitution was increased, compressive strength declined, and porosity increased accordingly. However, the measured values had a small variation overall, from 6.5% to 9.9%, and the use of

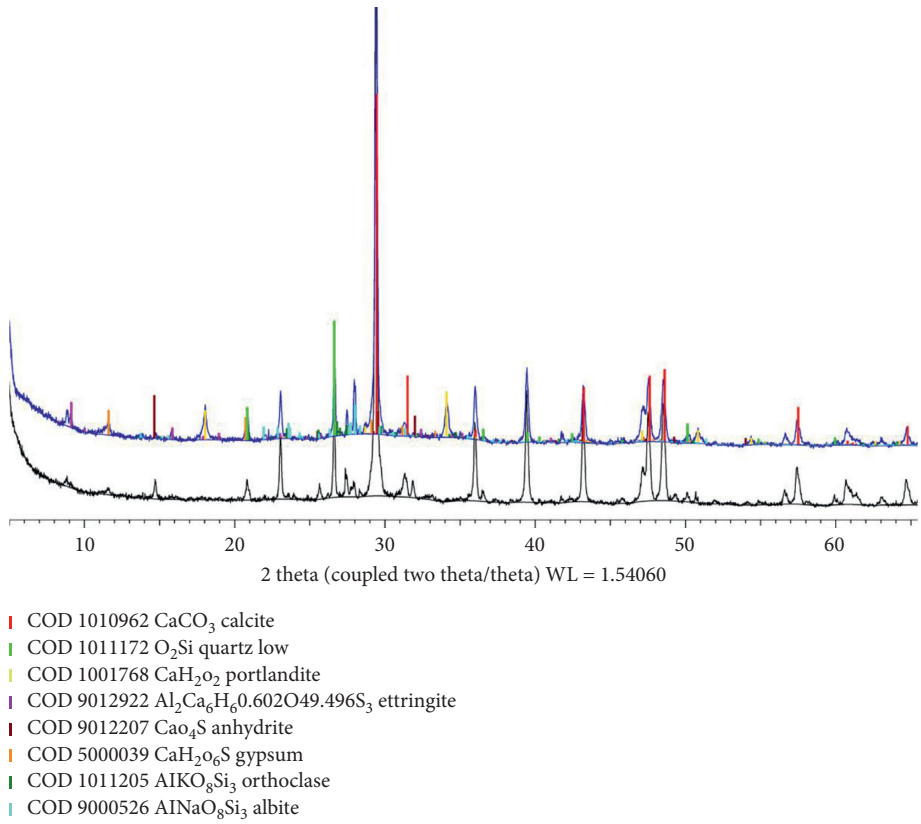

Figure 6: Diagrams of XRD analysis of mixtures FS50 (up) and FF50 (down) at 90 days.

concrete sludge did not alter mortar porosity considerably. Also, substitution of fly ash with limestone filler compared to concrete sludge did not change mortar porosity considerably either. Regarding early-age shrinkage measurements (Figure 10), the rate of volume shrinkage and percentile volume change was similar for all mortars and seems to stabilize at 25–30 days. This indicates that there were no significant early-age deformations arising from the combination of fly ash and concrete sludge; however, long-term shrinkage measurements should be made to establish adequate durability regarding deformation.

3.2. Alkali-Activated Mortars. The fresh properties of the selected mortar mixtures which were repeated with the addition of the alkaline activator are shown in Table 7. Compared to the nonactivated mortars (Table 5), the use of the activator seems to increase water demand regardless of the use of concrete sludge. However, the substitution of fly ash with concrete sludge still seems to improve the workability and viscosity of the mixtures, taking also into account the lower liquid/binder ratio. The coarser concrete sludge (S200) used in activated mortars AN30 and AT30 seemed to improve mostly viscosity rather than flow table workability, which could be attributed to its particle size distribution.

Figure 11 shows the values from the compressive strength tests of the alkali-activated mortars. Regarding the 100% high-calcium fly ash mortar, the addition of the alkaline activator enhanced compressive strength at early ages (15.29 MPa at 7 d) compared to the mixture with plain water (6.51 MPa at 7 d, Figure 5). This increase continued at the age of 28 days, where strength level of AF and F mixtures was around 19.99 MPa and 16.40 MPa, respectively. Again, the replacement of fly ash with concrete sludge (S75) at rates of 20% (AFS20) and 50% (AFS50) reduced the compressive strength up to 50%. However, the use of S200 concrete sludge had a great impact on the development of strength, since for mortar AN30, a 28-day compressive strength increase of 30% was observed. This is attributed to the chemical composition of S200 (Table 1), since S200 (<200 μm) had 15.01% content of silicon oxides, while S75 (<75 μm) had only 2.28% and the extra silicon oxide present is considered to contribute to this strength increase. When curing at 40°C for 24 hours was used to further enhance the alkali activation process (AT30), it was clear that it did not improve the mechanical characteristics of the mortar, as it appeared to reduce strength over 15% in all ages compared to AN30 (cured at 25°C). This has also been reported before by the authors, as it is proven that binders with a high lime content, such as fly ash and ladle furnace slag, do not require heating in order to develop high strength levels [34, 48]. However, the relative 28-day compressive strength increase for the alkali-activated mortars with

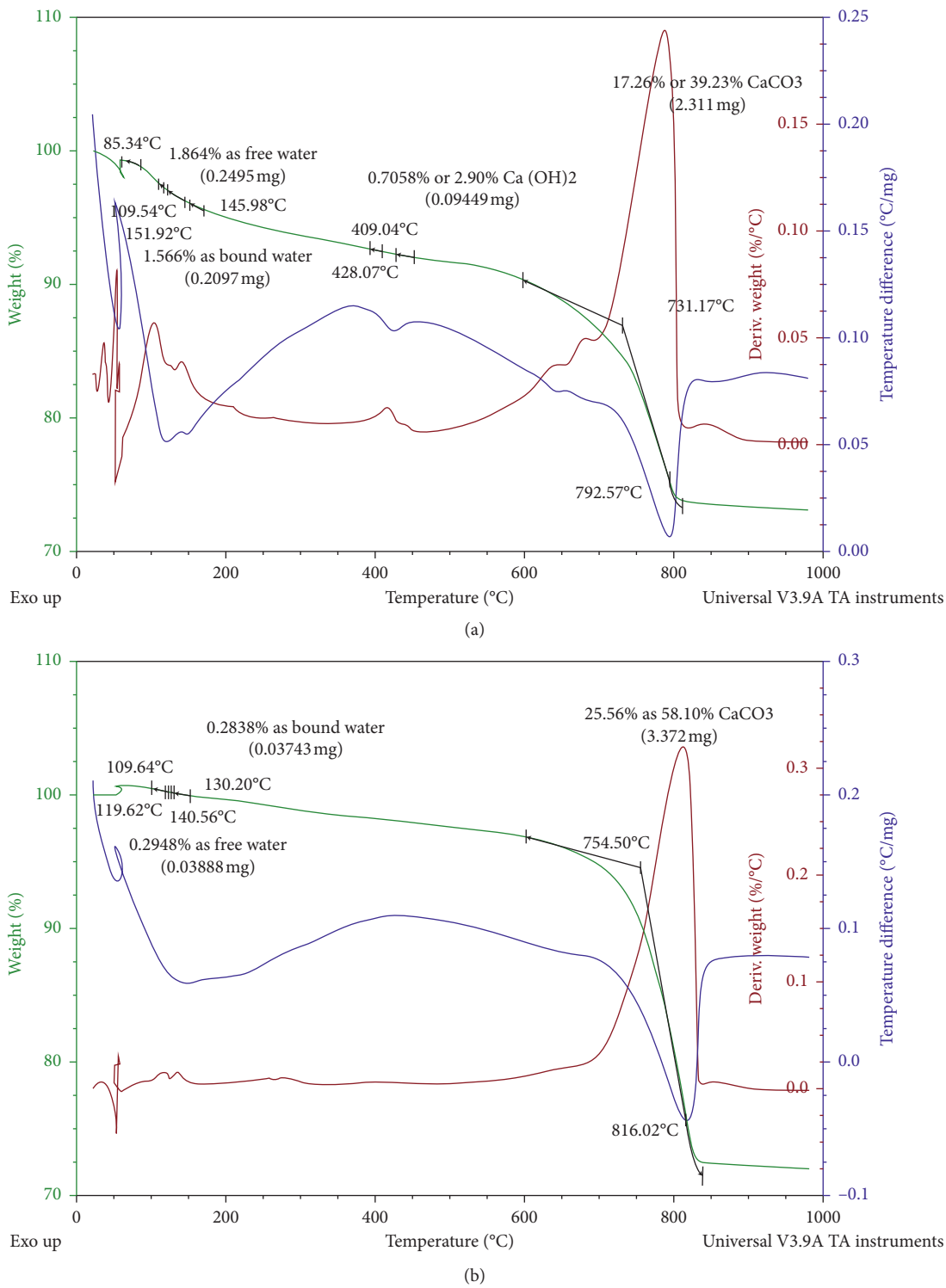

Figure 7: Thermographs of DTA-TG analysis of mixtures (a) FS50 and (b) FF at 90 days.

S200 was followed by a marked decrease at 90 days for both AN30 and AT30 mixtures, which shows limited gains by the activation process.

Porosity values of the alkali-activated mortars are presented in Figure 12 and the mortars with fly ash and S75 concrete sludge showed a reduction of around 30% compared to the same mixtures without alkali activation (Figure 9), which complies with the elevated compressive strength results. Alkali-activated mortars AN30 and AT30, however, showed considerably higher porosity values, despite the higher compressive strength results. This occurrence confirms the diverse performance of S75 and S200,

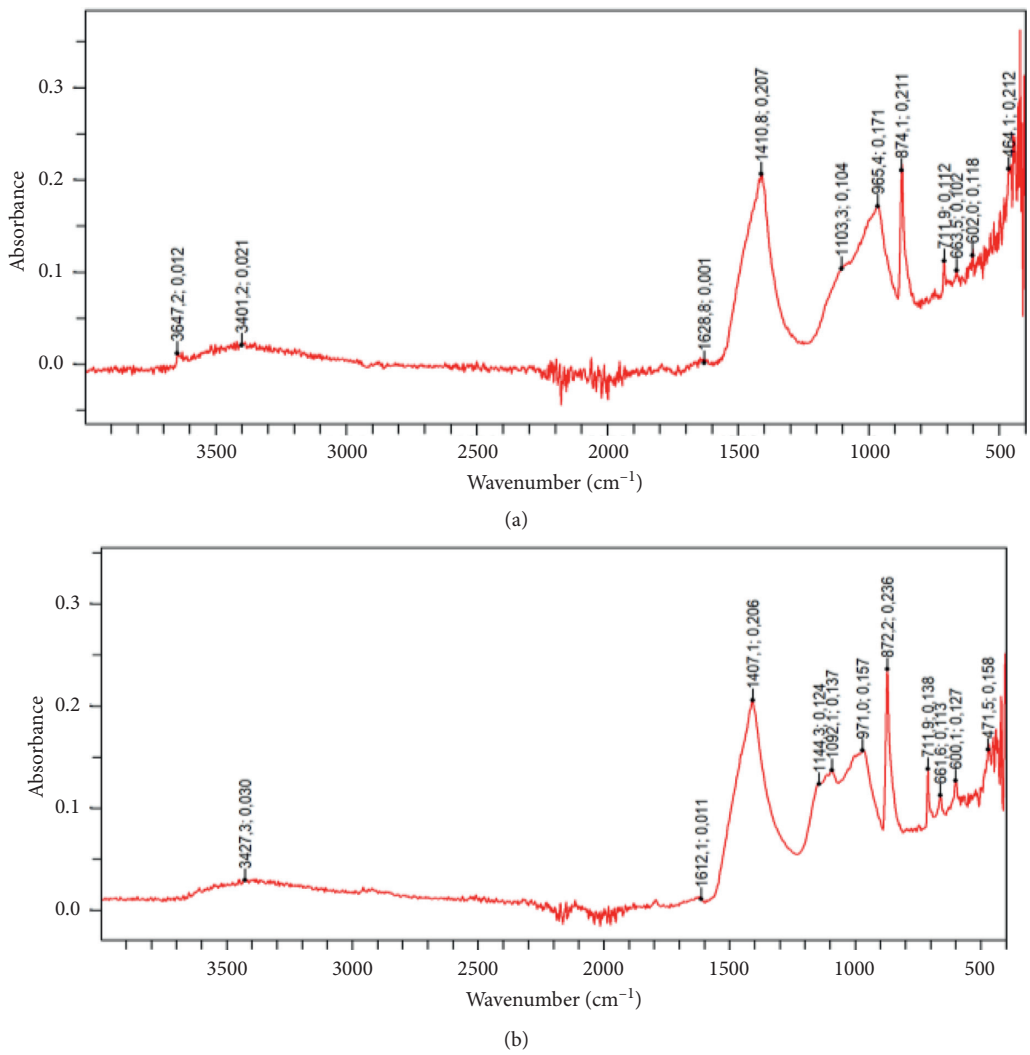

Figure 8: ATR-FTIR spectra analysis of mixtures (a) FS50 and (b) FF50 at 90 days.

Table 6: FTIR assignments (wavenumber in cm^{-1}) for the FS50 and FF50 mixtures at 90 days.

Assignments	FS50	FF50
Hydrogen bonds O-H ($Ca(OH)_2$) (stretching vibration)	3647	—
Hydrogen bonds O-H (H_2O) (stretching vibration)	3401	3427
HOH (bending vibration)	1626	1612
Carbonates, O-C-O (stretching vibration)	1410	1407
Sulphates, SO_4 = (anhydrite)	1103	1144/1092
Si-O (C-S-H) (stretching vibration)	965	971
Carbonates, O-C-O (stretching vibration)	874/711	872/711
Si-O-Si, Si-O-Si/Si-O-Al (bending vibration)	663, 602	661, 600
Si-O (SiO_4) (bending vibration)	464	471

owing to either different granulometry or different activity. The same pattern was observed regarding the early-age volume shrinkage test results (Figure 13). While the activated mortars with S75 showed a 28-day volume reduction of 5%–7%, higher than the nonactivated mortars (3.5–5%), the mortars with S200 had 28-day volume reduction limited to 2.5%. The volume reduction of all mortars gradually stabilized, while curing at 40°C (AT30) for 24 hours seem to affect the results neither of early-age shrinkage nor of porosity.

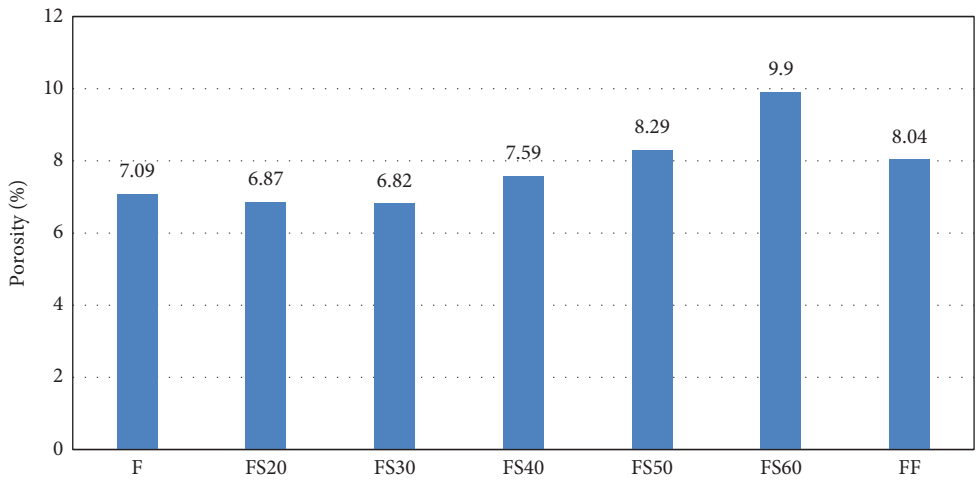

Figure 9: Porosity of the nonactivated mortars at 28 days.

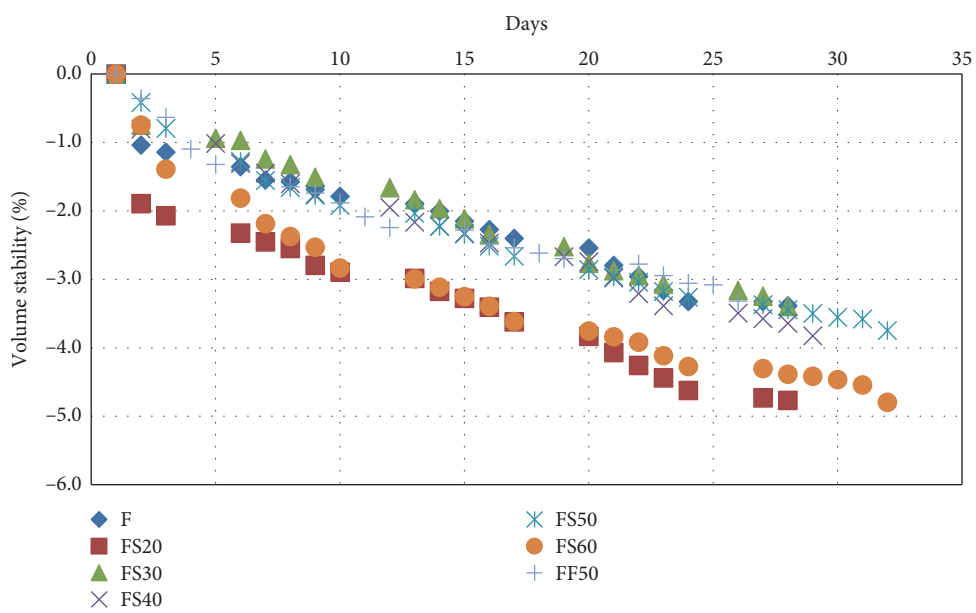

Figure 10: Volume stability of the nonactivated mortars.

Table 7: Rheological properties of alkali-activated mortars.

Mixture	Viscosity (Pa ∗ s)	Flow table workability (cm)	Laboratory temperature (°C)	Liquid/binder (parts by mass)
AF	385.2	11.8	16	0.73
AFS20	91.6	15.1	16	0.67
AFS50	63.1	16.1	16	0.67
AN30/AT30	29.5	12	15.5	0.67

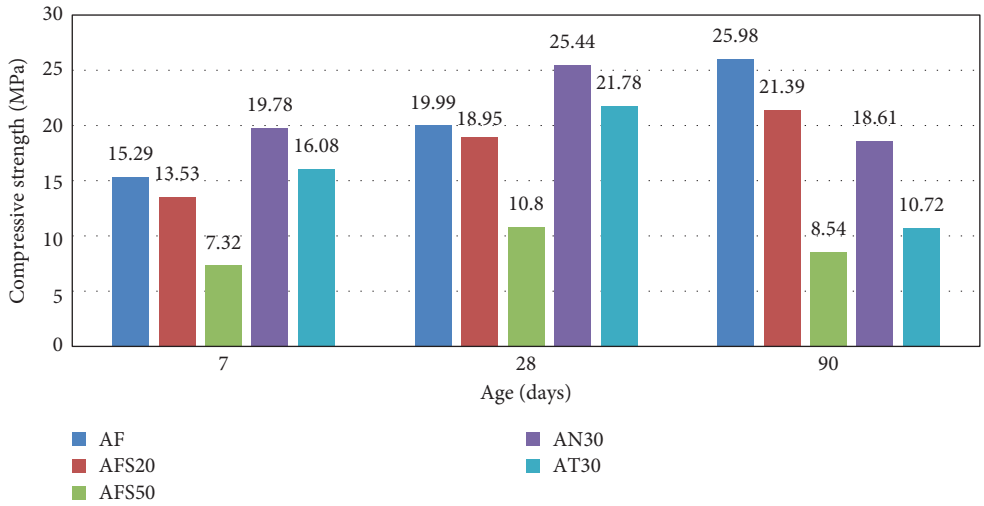

Figure 11: Compressive strength of alkali-activated mortars at 7, 28, and 90 days.

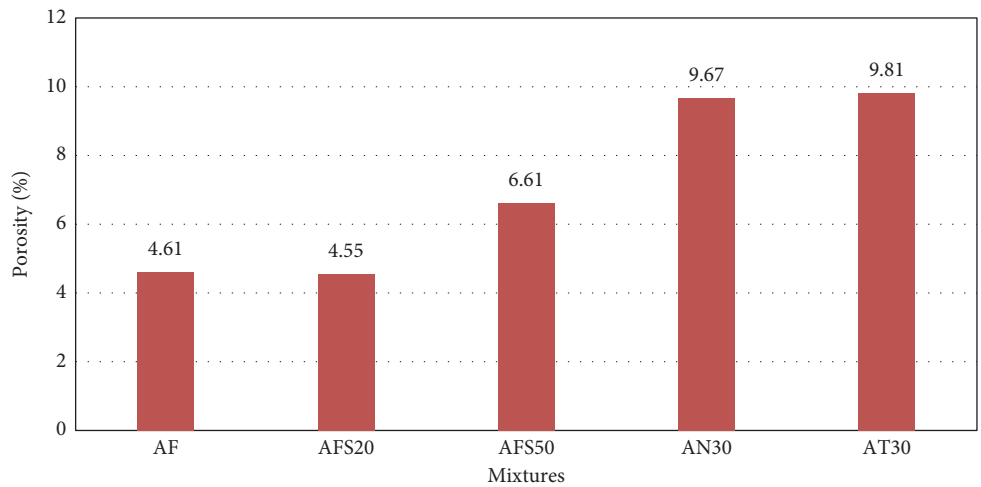

Figure 12: Porosity of alkali-activated mortars at 28 days.

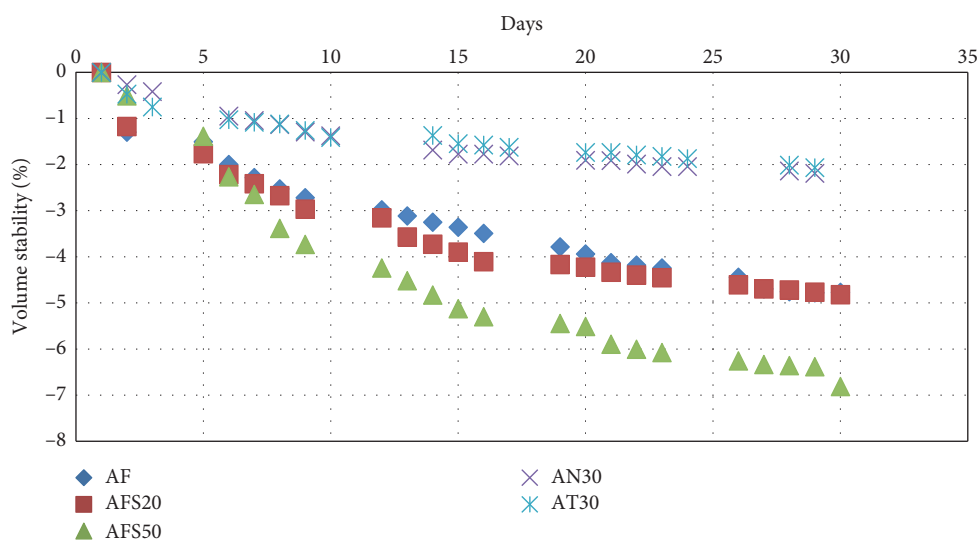

Figure 13: Volume stability of alkali-activated mixtures.

4. Conclusions

The present research investigated the potential combination of concrete sludge and high-calcium fly ash for mortar production.

(i) The high-calcium fly ash tested showed a slow but considerable strength development rate, reaching 16 MPa compressive strength at 28 days.

(ii) Fly ash substitution with concrete sludge had a positive effect on the rheology of mortars, since it reduced viscosity, improved workability, and reduced water demand.

(iii) Fly ash substitution rates of 20% and 30% showed the best results regarding strength development, starting with a slight reduction at 28 days and eventually improving strength at 90 days. Higher replacement rates, however, showed a decrease in strength development, proportional to the concrete sludge used.

(iv) Analytical tests in comparison with fly ash-limestone filler mortars confirmed that concrete sludge promotes the hydration of fly ash and the formation of C-S-H. XRD analysis confirmed the presence of crystalline phases of ettringite and the characteristic reflections of portlandite in the mortar with 50% concrete sludge. According to the DTA-TG analysis, the main difference between the fly ash-concrete sludge and the fly ash-limestone filler mortars was the loss of hydroxyls at 409–428°C, as a presence of hydration product $Ca(OH)_2$ of concrete sludge which probably increases with time. The cementitious nature of the sludge is also certified through the ATR-FTIR spectra analysis. Porosity and early-age shrinkage did not alter significantly when concrete sludge was used in the mortars.

(v) The alkali-activation mechanism increases water demand of the mortars, but the inclusion of concrete sludge still improves its rheological properties and decreases plastic viscosity of high-calcium fly ash-based mortars.

(vi) Regarding the mechanical properties, an improvement of earlier-age (7 and 28 days) compressive strength was observed with the addition of the alkaline activator in all cases. The same as in nonactivated mortars, increasing rates of concrete sludge replacement resulted in proportionally lower compressive strengths.

(vii) Thermal curing of the alkali-activated mortar at 40°C did not seem to promote compressive strength development, but rather decreased strength.

(viii) The chemical composition of the concrete sludge played an important role to the mechanism. This difference in chemical composition was obtained through sieving of the material under 75 μm or under 200 μm and thus obtaining a finer fraction of concrete sludge with low silicon oxide content (S75) and a coarser fraction with higher silicon oxide content (S200).

(ix) The mortars with 30% fly ash replacement with S200 sludge developed higher 28-day compressive strength, but strength decreased at 90-days.

(x) Overall, the alkali-activated mortars using the coarser concrete sludge with higher silicon oxide content had higher porosity and reduced early-age shrinkage S200, but further investigation is required regarding the alkali activation of concrete sludge.

(xi) After further research, especially regarding long-term properties and durability, these mortars could be used as masonry mortars and in low strength applications such as renders, paving slabs, and blocks. Studies regarding the environmental footprint of the mortars with fly ash and concrete sludge, such as comparative life cycle assessment, would highlight their environmental benefits.

Data Availability

The underlying data supporting the results of our study are available by the authors upon request.

Conflicts of Interest

The authors declare that they have no conflicts of interest.

References

[1] D. Xuan, B. Zhan, C. S. Poon, and W. Zheng, "Innovative reuse of concrete slurry waste from ready-mixed concrete plants in construction products," *Journal of Hazardous Materials*, vol. 312, pp. 65–72, 2016.

[2] M. Audo, P.-Y. Mahieux, and P. Turcry, "Utilization of sludge from ready-mixed concrete plants as a substitute for limestone fillers," *Construction and Building Materials*, vol. 112, pp. 790–799, 2016.

[3] B. J. Sealey, P. S. Phillips, and G. J. Hill, "Waste management issues for the UK ready-mixed concrete industry," *Resources, Conservation and Recycling*, vol. 32, no. 3-4, pp. 321–331, 2001.

[4] J. A. Férriz Papí, "Recycling of fresh concrete exceeding and wash water in concrete mixing plants," *Materiales de Construcción*, vol. 64, no. 313, p. e004, 2014.

[5] M. Paolini and R. Khurana, "Admixtures for recycling of waste concrete," *Cement and Concrete Composites*, vol. 20, no. 2-3, pp. 221–229, 1998.

[6] Y. Xi, E. Anastasiou, A. Karozou, and S. Silvestri, "Fresh and hardened properties of cement mortars using marble sludge fines and cement sludge fines," *Construction and Building Materials*, vol. 220, pp. 142–148, 2019.

[7] V. M. Malhotra, "High-performance high-volume fly ash concrete," *Concrete International*, vol. 24, no. 7, pp. 30–34, 2002.

[8] I. Papayianni and E. Anastasiou, "Production of high-strength concrete using high volume of industrial by-products," *Construction and Building Materials*, vol. 24, no. 8, pp. 1412–1417, 2010.

[9] F. Faleschini, M. A. Zanini, K. Brunelli, and C. Pellegrino, "Valorization of co-combustion fly ash in concrete production," *Materials & Design*, vol. 85, pp. 687–694, 2015.

[10] European Committee, *EN 450-1: 2012. Fly Ash for Concrete. Definition, Specifications and Conformity Criteria*, European Committee, Brussels, Belgium, 2012.

[11] Q. Zhou, C. Lu, W. Wang, S. Wei, C. Lu, and M. Hao, "Effect of fly ash and sustained uniaxial compressive loading on chloride diffusion in concrete," *Journal of Building Engineering*, vol. 31, Article ID 101394, 2020.

[12] E. K. Anastasiou, A. Liapis, and I. Papayianni, "Comparative life cycle assessment of concrete road pavements using industrial by-products as alternative materials," *Resources, Conservation and Recycling*, vol. 101, pp. 1–8, 2015.

[13] I. Papayianni and E. K. Anastasiou, "An investigation of the behavior of raw calcareous fly ash in mortar mixtures," *CCGP Journal*, vol. 2, no. 1, 2010.

[14] European Committee, *EN 197-1:2011. Cement—Part 1: Composition, Specifications and Conformity Criteria for Common Cements*, European Committee, Brussels, Belgium, 2011.

[15] European Committee, *EN 196-1:1995. Methods of Testing Cement—Part 1: Determination of Strength*, European Committee, Brussels, Belgium, 1995.

[16] I. Papayianni, S. Konopisi, K. Datsiou, and F. Kesikidou, "Products of alkali-activated calcareous fly ash and glass cullet," *International Journal of Research in Engineering and Technology*, vol. 3, no. 25, pp. 43–51, 2014.

[17] C. Shi, P. Krivenko, and D. Roy, *Alkali-activated Cements and Concrete*, Taylor & Francis, Abingdon-on-Thames, UK, 2006.

[18] J. L. Provis and J. S. J. van Deventer, "Alkali-activated materials," *State of the Art Report, RILEM TC 224-AAM*, Vol. 13, Springer, Berlin, Germany, 2014.

[19] S. Alonso and A. Palomo, "Alkaline activation of metakaolin and calcium hydroxide mixtures: influence of temperature, activator concentration and solids ratio," *Materials Letters*, vol. 47, no. 1-2, pp. 55–62, 2001.

[20] D. Bondar, C. J. Lynsdale, N. B. Milestone, N. Hassani, and A. A. Ramezanianpour, "Effect of type, form, and dosage of activators on strength of alkali-activated natural pozzolans," *Cement and Concrete Composites*, vol. 33, no. 2, pp. 251–260, 2011.

[21] X. Ke, S. A. Bernal, N. Ye, J. L. Provis, and J. Yang, "One-part geopolymers based on thermally treated red mud/NaOH blends," *Journal of the American Ceramic Society*, vol. 98, no. 1, pp. 5–11, 2015.

[22] M. Palacios, M. M. Alonso, C. Varga, and F. Puertas, "Influence of the alkaline solution and temperature on the rheology and reactivity of alkali-activated fly ash pastes," *Cement and Concrete Composites*, vol. 95, pp. 277–284, 2019.

[23] A. Fernández-Jiménez and A. Palomo, "Composition and microstructure of alkali activated fly ash binder: effect of the activator," *Cement and Concrete Research*, vol. 35, no. 10, pp. 1984–1992, 2005.

[24] D. W. Law, A. A. Adam, T. K. Molyneaux, I. Patnaikuni, and A. Wardhono, "Long term durability properties of class F fly ash geopolymer concrete," *Materials and Structures*, vol. 48, no. 3, pp. 721–731, 2015.

[25] C. D. Atiş, E. B. Görür, O. Karahan, C. Bilim, S. Ilkentapar, and E. Luga, "Very high strength (120 MPa) class F fly ash geopolymer mortar activated at different NaOH amount, heat curing temperature and heat curing duration," *Construction and Building Materials*, vol. 96, pp. 673–678, 2015.

[26] P. Chindaprasirt, T. Chareerat, and V. Sirivivatnanon, "Workability and strength of coarse high calcium fly ash geopolymer," *Cement and Concrete Composites*, vol. 29, no. 3, pp. 224–229, 2007.

[27] X. Guo, H. Shi, and W. A. Dick, "Compressive strength and microstructural characteristics of class C fly ash geopolymer," *Cement and Concrete Composites*, vol. 32, no. 2, pp. 142–147, 2010.

[28] A. Fernandez-Jimenez, I. García-Lodeiro, and A. Palomo, "Durability of alkali-activated fly ash cementitious materials," *Journal of Materials Science*, vol. 42, no. 9, pp. 3055–3065, 2007.

[29] D. Xuan, C. S. Poon, and W. Zheng, "Management and sustainable utilization of processing wastes from ready-mixed concrete plants in construction: a review," *Resources, Conservation and Recycling*, vol. 136, pp. 238–247, 2018.

[30] M. U. Hossain, D. Xuan, and C. S. Poon, "Sustainable management and utilisation of concrete slurry waste: a case study in Hong Kong," *Waste Management*, vol. 61, pp. 397–404, 2017.

[31] M. Zervaki, C. Leptokaridis, and S. Tsimas, "Reuse of by-products from ready-mixed concrete plants for the production of cement mortars," *Journal of Sustainable Development of Energy, Water and Environment Systems*, vol. 1, no. 2, pp. 152–162, 2013.

[32] I. Mehdipour, A. Kumar, and K. H. Khayat, "Rheology, hydration, and strength evolution of interground limestone cement containing PCE dispersant and high volume supplementary cementitious materials," *Materials & Design*, vol. 127, pp. 54–66, 2017.

[33] European Committee, *EN 451-1:1995.Method of testing fly ash—Part 1: Determination of free calcium oxide content*, European Committee, Brussels, Belgium, 1995.

[34] I. Papayianni, S. Konopisi, and F. Kesikidou, "Physico-mechanical properties and durability aspects of alkali-activated calcareous fly ash/slag mortars," *Key Engineering Materials*, vol. 761, pp. 87–91, 2018.

[35] European Committee, *EN 1015-3:2003, Methods of Test for Mortar for Masonry—Part 3: Determination of Consistence of Fresh Mortar*, European Committee, Brussels, Belgium, 2003.

[36] European Committee, *EN 1015-11:2006 Methods of Test for Mortar for Masonry—Part 11: Determination of Flexural and Compressive Strength of Hardened Mortar*, European Committee, Brussels, Belgium, 2006.

[37] RILEM TC, "CPC 11.3 absorption of water by concrete by immersion under vacuum," *RILEM Recommendations for the Testing and Use of Constructions Material*, pp. 36-37, RILEM, Paris, France, 1984.

[38] P. C. Aïtcin and R. J. Flatt, *Science and Technology of Concrete Admixtures, Series in Civil and Structural Engineering*, Woodhead Publishing, Cambridge, UK, 59th edition, 2016.

[39] M. M. Alonso, S. Gismera, M. T. Blanco, M. Lanzón, and F. Puertas, "Alkali-activated mortars: workability and rheological behaviour," *Construction and Building Materials*, vol. 145, pp. 576–587, 2017.

[40] G. Liptay, *Atlas of Thermoanalytical Curves: (TG-, DTG-, DTA-Curves Measured Simultaneously)*, Heyden and Son, Hoboken, NJ, USA, 1971.

[41] F. Deschner, F. Winnefeld, B. Lothenbach et al., "Hydration of Portland cement with high replacement by siliceous fly ash," *Cement and Concrete Research*, vol. 42, no. 10, pp. 1389–1400, 2012.

[42] P. Hewllet, *Lea's Chemistry of Cement and Concrete*, Elsevier Science & Technology Books, London, UK, 4th edition, 2004.

[43] H. F. W. Taylor, *Cement Chemistry*, Academic Press, Cambridge, MA, USA, 1990.
[44] V. C. Farmer, *The Infrared Spectra of Minerals*, Mineralogical Society, London, UK, 1974.
[45] W. Mozgawa, M. Sitarz, and M. Rokita, "Spectroscopic studies of different aluminosilicate structures," *Journal of Molecular Structure*, vol. 511-512, pp. 251–257, 1999.
[46] Y. Ping, R. J. Kirkpatrick, B. Poe, P. F. McMillan, and X. Cong, "Structure of calcium silicate hydrate (C-S-H): near-, mid-, and far-infrared sprectoscopy," *Journal of the American Ceramic Society*, vol. 82, no. 3, pp. 742–748, 2004.
[47] I. García Lodeiro, A. Fernández-Jimenez, A. Palomo, and D. E. Macphee, "Effect on fresh C-S-H gels of the simultaneous addition of alkali and aluminium," *Cement and Concrete Research*, vol. 40, no. 1, pp. 27–32, 2010.
[48] I. Papayianni, S. Konopisi, and F. Kesikidou, "Alkali activation of ladle furnace slag (LFS). effect of fineness, curing regime and concentration of activator on mechanical and physical characteristics of LFS pastes," in *Proceedings of the 10th European Slag Conference*, Thessaloniki, Greece, October 2019.

Hindawi
Advances in Civil Engineering
Volume 2021, Article ID 5513303, 11 pages
https://doi.org/10.1155/2021/5513303

Research Article

Study on the Properties of an Ecotype Mortar with Rice Husks and Sisal Fibers

Xiaofan Liu, Jixiang Li, Fengyun Li, Junguang Wang, and Haijun Lu

School of Civil Engineering and Architecture, Wuhan Polytechnic University, Wuhan 430023, China

Correspondence should be addressed to Xiaofan Liu; hnsfine@163.com

Received 26 February 2021; Revised 16 April 2021; Accepted 24 April 2021; Published 5 May 2021

Academic Editor: Xianming Shi

Adding plant fibers such as rice husks or sisals to the mortar is one of the main methods to reuse the agricultural wastes and reduce the energy consumption of building industry. However, recent research showed some limitation of the mortar mixed with plant fibers. In this paper, sisal fibers and rice husks were added together into cement mortar to investigate its mechanical properties and the optimum mixture ratio of sisal fiber and rice husk by mix ratio test and orthogonal test. The microstructure of the sisal fiber was observed using scanning electron microscopy (SEM) to understand how the properties of the mortar were affected. Results showed that adding sisal fiber and rice husk into cement mortar significantly improved the mechanic property, anticrack performance, and impermeability of the mortar. The highest compressive strength and flexural strength can reach 17.1 MPa and 3.3 MPa. The area of early cracks was reduced by 100%, and the maximum seepage pressure was 0.36 MPa. The microstructure analysis also indicated that adding rice husk and sisal fiber have a positive effect on the mortar. These results support that adding 0.1% volume admixture of 16 mm length sisal fiber with 35% rice husk into mortar is helpful for engineering application.

1. Introduction

The rapid slumping of resources is attracting increasing social attention to environmental protection and sustainable development. In China, the energy consumption from building accounts for a large proportion [1, 2]. Lightweight concrete, which contains rice husk instead of sand, is a well-known material that can reduce the building energy consumption. The application of this material can not only save resources and protect the environment but also promote the research on reusing rice husk to produce economic benefits [3, 4]. In the last century, H. F. Porter proposed the concept of fiber concrete. From then on, adding various kinds of fiber to the concrete has become a promising research field to improve the performance of the concrete. Natural plant fibers, such as sunflower, sisal, and bamboo [5–7], are very popular in developing countries due to their low cost and high reproducibility [8]. Many research studies have been done to energy-saving and environment-friendly concrete.

There is a long history of the research studies on adding rice husk to mortar. Sun et al. [9] studied the mechanical properties of mortar prepared from rice husk and cement treated with saturated lime water and tap water. According to their research, the mortar prepared from pretreated rice husk, which were soaked with saturated lime water, was greatly improved in performance. António et al. [10] studied the practical application of new type of rice husk wallboard. Their research studies indicated that the new wallboards prepared with rice husk had a better performance. Morgan et al. [3] studied the application of rice husks as lightweight aggregates in low-cost housing.

Sisal fiber also has a significant effect on improving the mortar performance. Huang et al. [11] added sisal fibers with different amounts of mixture into mortar, indicating that the mechanical properties of cement concrete were obviously improved when the amount of admixture of sisal fibers was 3.5 kg/m^3. Silva et al. [12] studied the bond strength and crack resistance of sisal fibers with different shapes in cement. The bending arch exhibited the highest bond stress and the greatest improvement in crack resistance. Besides, adding sisal fibers was shown to greatly improve the crack resistance of the cement by Balaguru [13]. Even when the amount of admixture of fibers was only 0.1%, the reduction of early cracks was obvious.

According to previous studies, adding rice husk or sisal fiber to mortar can greatly improve the performance of the mortar. However, the low strength and easy cracking feature of the rice husk mortar limited its application. In order to solve this problem, rice husk and sisal fiber were added together into mortar in this study to search for the optimal mixture ratio that could meet the performance requirements of practical projects. The effects of sisal fiber and rice husk on the properties of mortar were discussed, and the mechanism of the hybrid fibers was studied.

2. Test Scheme

2.1. Raw Material. The test raw materials are ordinary Portland cement P·O42.5; the maximum particle size of the engineering sand is 2.36 mm with modulus coefficient of 2.1; the rice husk is from Hubei Province, and its physical properties are shown in Table 1. The lengths of the sisal fibers are 8 mm, 12 mm, and 16 mm, respectively. Physical properties of raw material are shown in Tables 1 and 2.

2.2. Mixture Ratio of Test Mortar and Specimen Forming. The mixture ratios of test mortar are shown in Table 3. Sisal fiber's length of 8 mm, 12 mm, and 16 mm with volume admixture of 0.10%, 0.15%, and 0.20% are tested. The replacement rates of rice husk volume are 35%, 40%, and 45%. Because the volume of mortar is mainly composed of sands, the replacement of sands is the same volume of rice husk. Moreover, rice husk has high water absorption property; a relatively high water to cement ration was used to ensure the working performance of mixing mortar.

Sisal fiber is easy to agglomerate when mixed into cement-based materials, which will result in uneven fiber distribution. In order to ensure the uniformity, continuity, and good workability of the material, after many attempts, the technological mixing process of sisal fiber rice husk mortar is formulated. Pour the sand and rice husk into the blender and keep stirring. Sisal fiber is added during stirring. Cement and water are added together and stirred in reverse direction for 2 minute. After mixing, the material is divided into three layers to cover the specimen mold, and a vibrator with the diameter of about 2 cm is used to slightly insert the vibrator layer by layer for 20 second. After smoothing, gently vibrate with both hands for 20 times and then rest. This process can effectively avoid the phenomenon of uneven mixing and floating of rice husk.

2.3. Test Methods

2.3.1. Compression Test. The size of sisal fiber husk mortar compression specimen is 70.7 mm × 70.7 mm × 70.7 mm. The specimens were loaded after 28 days of curing. The test was carried out in accordance with the requirements of JGJ-T70-2009 [14], using miniature controlled electronic universal testing machine. The loading device and the situation of the specimen are shown in Figure 1.

2.3.2. Flexural Test. The sisal fiber husk mortar flexural test specimen is a prism of 100 mm × 100 mm × 400 mm. The test was carried out in accordance with the requirements of GB/T50081-2002) [15], using miniature controlled electronic universal testing machine, as shown in Figure 2.

2.3.3. Early Plastic Shrinkage Crack Test of Sisal Fiber Rice Husk Mortar. The test molds are shown in Figure 3. The displacement of mortar periphery is restrained by the steel frame and steel bolt. Internal mortar shrinkage may produce cracks. The test was carried out in accordance with the requirements of CECS38:2004 [16].

2.3.4. Antipenetrability Performance Test of Sisal Fiber Rice Husk Mortar. The test was carried out in accordance with the requirements of JGJ-T70-2009 [14]. Six specimens of sisal fiber rice husk mortar in each group were prepared to carry the antipenetrability performance test. The location form of the specimens is shown in Figure 4.

3. Test Results and Analysis of Sisal Fiber Rice Husk Mortar

3.1. Mechanical Properties of the Sisal Fiber Rice Husk Mortar. The results of the mechanical test are shown in Table 4. Table 5 and Figures 5 and 6 are the k value calculated results of the compressive strength and flexural strength of the sisal fiber husk mortar, respectively.

It can be seen from Table 4 that the optimal mixture ratio of sisal fiber rice husk mortar for compressive resistance is 0.10% volume admixture with 8 mm length of sisal fiber and 35% rice husk volume replacement rate. The rice husk volume replacement rate has a dominant contribution to compressive strength, while sisal fiber volume admixture shows smaller effect. The contribution from sisal fiber length is the minimum. The optimal mixture ratio of sisal fiber rice husk mortar for flexural strength is 0.10% volume admixture with 8 mm length of sisal fiber and 35% rice husk volume replacement rate. Sisal fiber length has a dominant contribution to flexural strength, while sisal fiber volume admixture shows smaller effect. The contribution from sisal fiber volume is the minimum.

As shown in Figure 5, the compressive strength of mortar decreases with the increase of sisal fiber length and sisal fiber volume admixture. The sisal fiber length exhibits the greatest influence on the compressive strength.

Figure 6 shows that the flexural strength of the mortar decreases with the increasing of volume admixture of the sisal fiber. The increase of the rice husk volume replacement rate also gradually reduces the flexural strength of the mortar. The length of the sisal fiber exerts little influence on the flexural strength. The volume replacement ratio of the rice husk and the sisal fiber admixture has similar effects on the mortar.

Stress failure of cement can be considered to be a process in which the stress expansion of tiny cracks inside the specimen leads to gradual connection of internal cracks until a complete failure [17]. In the compression test, the overlong sisal fibers in the process of specimen compression cannot be completely stressed due to their low stiffness. However,

Table 1: Physical properties of the rice husk.

Category	Length (mm)	Width (mm)	Density (g/cm^3)	Bulk density (g/cm^3)	Thermal conductivity (W/m·K)
Rice husk	5~8	2.5~5	720	83~160	0.084~0.209

Table 2: Physical properties of the sisal fiber.

Fiber category	Density (g/cm^3)	Elongation (%)	Tensile strength (MPa)	Tensile elasticity modulus (GPa)
Sisal fiber	1.45	2.0~2.5	511~635	9.4~22.0

Table 3: Mixture ratio of test mortar.

Sample	Sisal fiber content (%)	Sisal fiber length (mm)	Sisal fiber quality (kg)	Rice husk content (%)	Rice husk quality (kg)	Sand (kg)	Cement (kg)	Water (kg)
A0	0	—	0	0	0	1500	400	300
A1	0.10	8	1.45	35	35	975	400	300
A2	0.10	12	1.45	40	40	900	400	300
A3	0.10	16	1.45	45	45	825	400	300
A4	0.15	8	2.18	40	40	900	400	300
A5	0.15	12	2.18	45	45	825	400	300
A6	0.15	16	2.18	35	35	975	400	300
A7	0.20	8	2.90	45	45	825	400	300
A8	0.20	12	2.90	35	35	975	400	300
A9	0.20	16	2.90	40	40	900	400	300

Figure 1: Compression test of sisal fiber husk mortar.

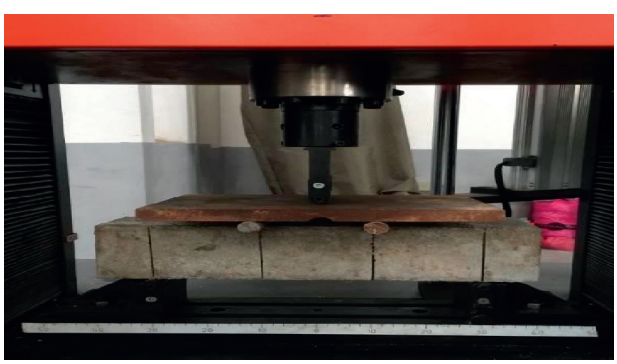

Figure 2: Flexural test of sisal fiber husk.

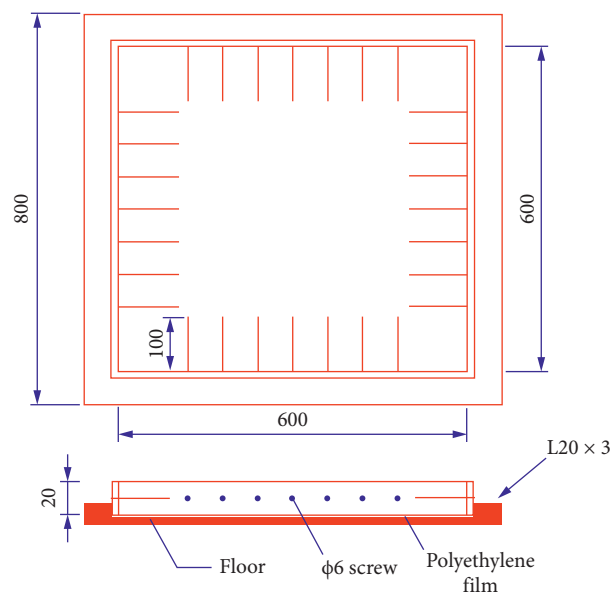

Figure 3: Test mold of early plastic shrinkage crack.

adding too many sisal fibers may contribute to the failure of producing weak areas in the cement mortar test and therefore limit the strength of cement mortar. In the flexural test, the rice husk and sisal fiber can promote the cement hydration due to their high water retention, which could increase the compactness and integrity of the cement material. However, the water storage capacity of the rice husk and sisal fiber is inhomogeneous inside the specimen, which results in humidity gradients due to the drying shrinkage of the material itself. When the sisal fiber admixture is increased, the strength of the cement matrix material is lower than that of the cement matrix material with the low volume admixture. The low density of sisal fiber and rice husk will reduce the strength of the cement matrix material when the two materials are overmixed.

3.2. Mechanism Analysis. In 1962, Lyubimove et al. [18] studied mortar on a microscopic scale and proposed the concept of interfacial transition zone (ITZ). They found that

Figure 4: Antipenetrability performance test of sisal fiber rice husk mortar.

Table 4: Experimental results of test blocks.

Sample	Average compressive load (kN)	Compressive strength (MPa)	Average flexural load (kN)	Flexural strength (MPa)
A1	63.48	17.14	13.04	3.26
A2	52.12	14.07	10.87	2.72
A3	51.29	13.85	10.50	2.63
A4	54.67	14.77	8.60	2.15
A5	57.41	15.51	10.20	2.55
A6	52.21	14.09	10.88	2.72
A7	56.31	15.21	8.58	2.15
A8	53.38	14.41	9.11	2.28
A9	46.23	12.48	9.68	2.42

Table 5: k value of compressive strength and flexural strength.

	Compressive strength			Flexural strength		
	Sisal fiber content	Sisal fiber length	Rice husk content	Sisal fiber content	Sisal fiber length	Rice husk content
K1	8.78	7.71	8.39	8.78	7.71	8.39
K2	7.65	7.69	7.73	7.65	7.69	7.73
K3	7.48	7.93	7.2	7.48	7.93	7.2
k1	2.93	2.57	2.80	2.93	2.57	2.80
k2	2.55	2.56	2.58	2.55	2.56	2.58
k3	2.49	2.64	2.4	2.49	2.64	2.4
R	0.43	0.078	0.4	0.43	0.078	0.4

the hardness is minimum near the surface of the aggregate and is increasing towards the direction of the matrix. According to Songshan's model [19] (as shown in Figure 7), the height of interface transition zone [20] is about 15 to 25 μm.

Measured from the SEM images, as shown in Figures 8(a) and 8(b) , the pore size of rice husk and the pore diameter of the rice husk cross section are larger than that of the interface transition zone. Therefore, the cement slurry will enter the interior of the rice husk through these pores, increasing the friction produced by the mortar and the husk's uneven surface. Furthermore, the cement mortar will enter the pores on the surface of the rice husk, fixing the rice husk on the surface as the "nail plate," thus forming a hardened cement adhere to rice husk structure (as shown in Figures 8(c) and 8(d)).

The hardness gradient of the ITZ can be explained from its formation process. The infiltration of moisture will be blocked at the surface of the aggregate to form a thicker water film. When the water enters the pores, most of the ions with strong diffusion ability during hydration will be combined with the water in the pores to form crystals. Based on these assumptions, an interface area model around the holes in rice husk is presented, as shown in Figure 9. According to the research of Hu et al. [21], the internal conservation of moisture in rice husk is fully hydrated in the interface area of cement minerals. As a result, the microhardness of the interface area is higher than that of the cement paste matrix. Because the solution concentration between the husk and the cement is different, the interface area transfers to the lower concentration area, which results in higher silicon-calcium ratio in interface area than that of the cement matrix. Due to its internal porous structure, rice husk releases water in the hydration process of cement and internally maintains the structure of the cement matrix.

According to current research, the strengthening effect of the fiber in the cement matrix mainly includes the following aspects [22]: (1) improving the ductility of the mortar

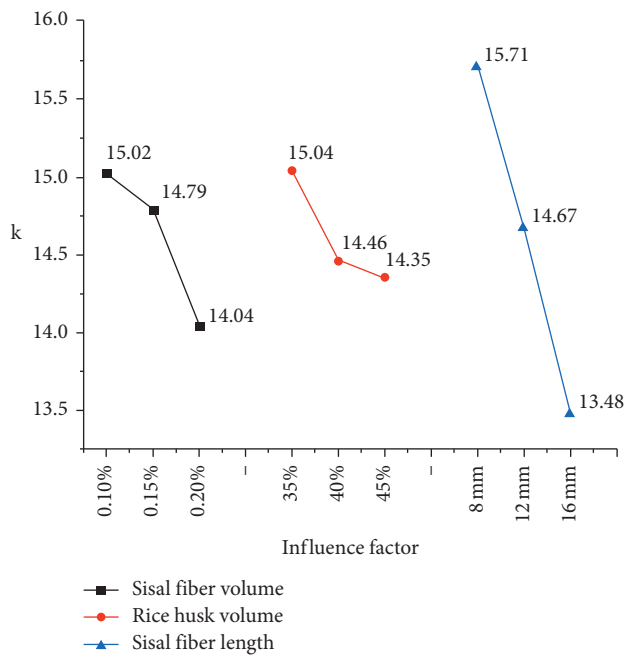

Figure 5: k value diagram of the compressive strength.

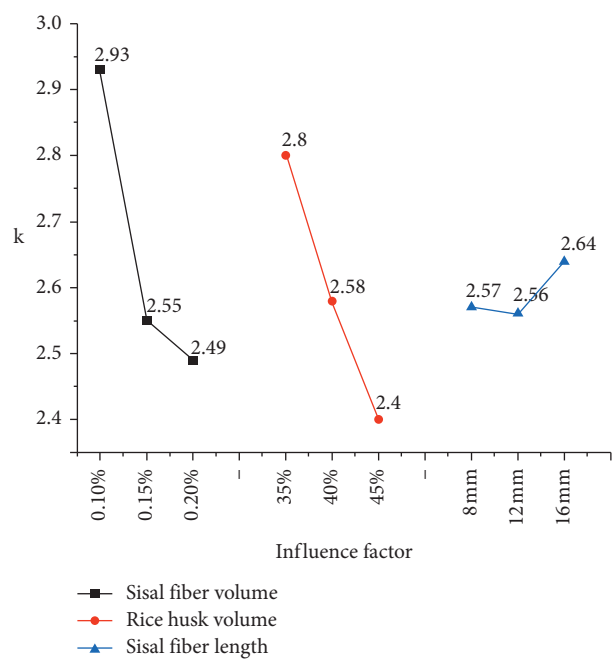

Figure 6: k value diagram of the flexural strength.

matrix, thereby effectively reducing its brittleness and improving its toughness, (2) improving the stress level of cement mortar, and (3) reducing the sedimentation of aggregates. The failure stage of the mortar is divided into two types: mortar failure and hard cement ingredient failure. However, in these two kinds of failure, adding sisal fiber, which has high elastic modulus, high extension strength, and high ultimate deformation property, can disperse parts of the internal force and thereby prevent the failure of the mortar. In the process of the crack expansion, there is the third failure stage of sisal fiber concrete: sisal fiber pull-out failure. During the failure stage of the mortar, the interface between sand and hardened cement be disintegrated and destroyed ultimately. In this process, the sisal fiber plays a reinforcing role which slows down the expansion of cracks. During the failure of hardened cement slurry, macroscopic cracks appear and grow significantly. A large number of sisal fibers can slow down the propagation process of the cracks. In the pulling out stage of sisal fiber and macrocrack expansion, due to the retardation of the sisal fiber, the

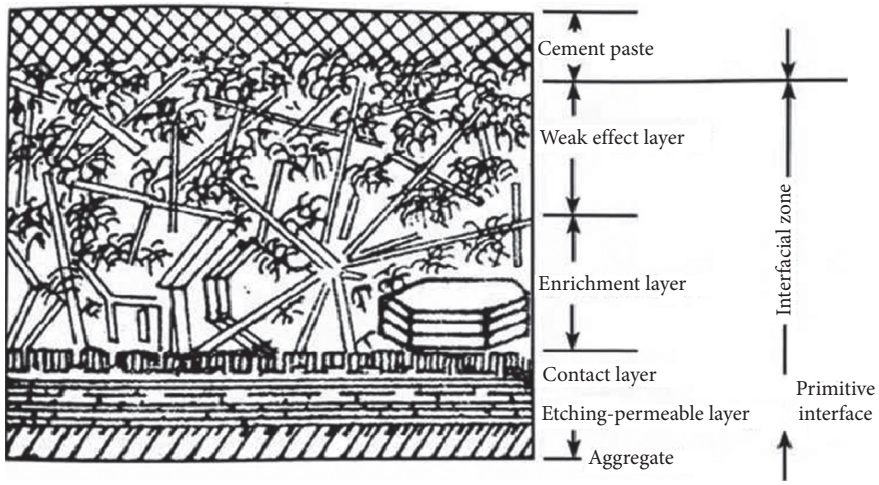

Figure 7: Songshan Jie's model.

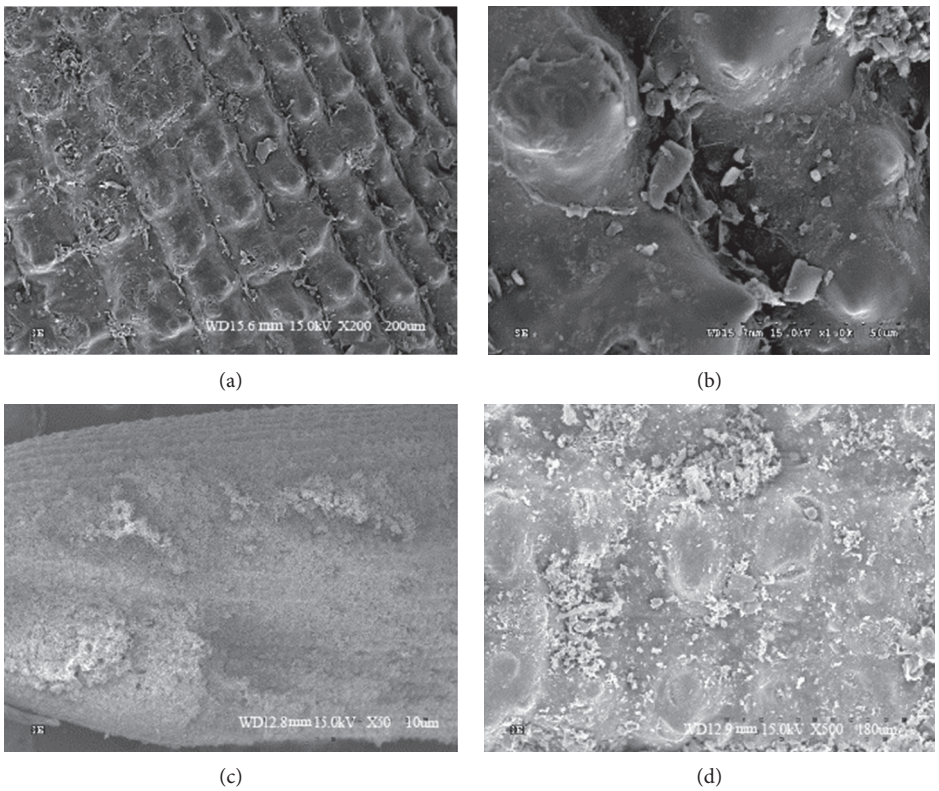

Figure 8: SEM of rice husk mortar surface. (a) Rice husk in mortar magnified 100 times. (b) Rice husk in mortar magnified 1000 times. (c) Rice husk in mortar magnified 50 times. (d) Rice husk in mortar magnified 500 times.

expansion speed becomes slower. However, in this situation, the construction degenerates faster. The bond between the sisal fiber and hardened cement gradually weakens, until the sisal fibers are pulled out and the final components are completely destroyed.

There is also a fiber spacing theory represented by Romualdi and Batson [23]. Based on the fracture mechanics, the sisal fiber is used as a constraint of cracks to explain the fiber spacing theory formed by the crack enhancement. When the fiber length is relatively short, the larger the fiber volume per unit volume is, the smaller the average fiber spacing is. The compressive strength reaches its maximum when the average fiber spacing reaches the optimal fiber spacing. When the fiber length is relatively long, the volume ratio of the fibers is relatively small. When the average spacing of the fibers increases beyond the optimum fiber spacing, the strength enhancement effect of the fiber will be weakened. Figures 10(a) and 10(b) show the interface area between the sisal fiber and the cement mortar. The sisal fibers are distributed in the cement mortar being closely

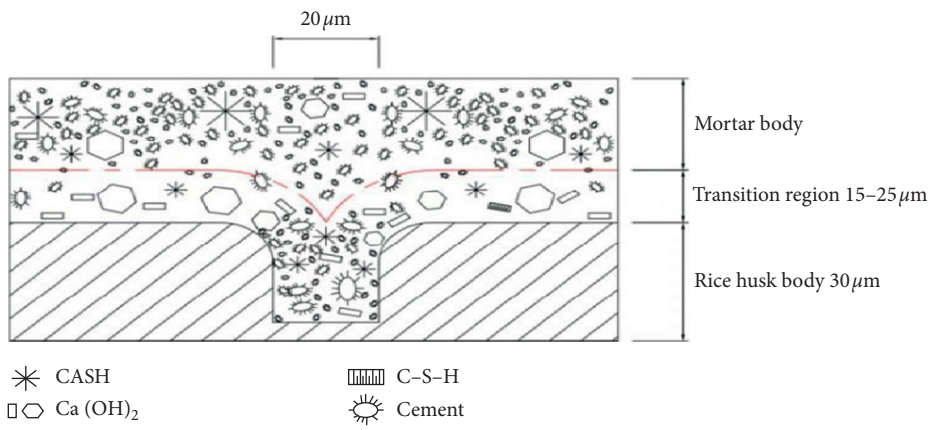

Figure 9: Interface area model with the holes in rice husk.

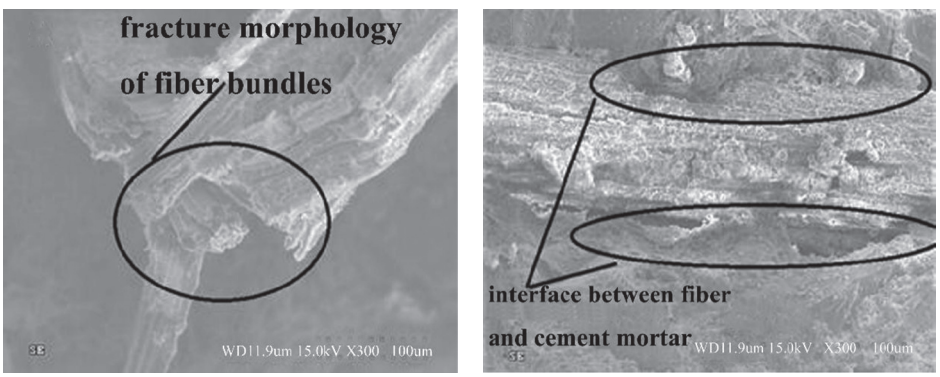

(a) (b)

Figure 10: Interface area of the sisal fiber and the cement mortar.

wrapped, filling up the internal gaps, which effectively make up for the defects of the cement mortar. Adding sisal fibers into the cement mortar of brittle material with internal defects can greatly reduce the size of the internal detects and form a compact structure to improve the performance.

3.3. Test Results and Analysis of Early Plastic Shrinkage Crack Performance and Impermeability. Test results of early plastic shrinkage crack performance and impermeability are shown in Table 6. A0 is the pure mortar specimen. Figure 11 shows the k value diagram of factors affecting crack area. Figure 12 shows the k value diagram of the factors affecting the maximum seepage pressure. Figures 13–15 show the crack distribution map of typical specimens.

As shown in Table 6, the early crack area of mortar blocks has been significantly reduced in the samples with sisal fiber and rice husk. The reduction coefficients are above 94%. Conclusion can be drawn from Figure 11 that the admixture amount of sisal fiber has a dominant contribution to the crack area, while the length of sisal fiber contributes the least. The optimal mixture ratio of crack resistance is 0.10% 16 mm sisal fiber volume admixture and 35% rice husk volume replacement rate.

According to the k value in Figure 12, the admixture amount of sisal fiber affects the antipermeability property most, while the length of sisal fiber affects least. The optimal mixture ratio of impermeability is 0.10% 16 mm sisal fiber volume admixture and 35% rice husk volume replacement rate.

The test results showed in Table 5 indicate that the sisal fiber and rice husk improve the impermeability and crack resistance of mortar significantly. The impermeability and crack resistance of sisal fiber rice husk mortar show a positive correlation: the stronger the impermeability is, the stronger the fission resistance is. After being added into the mortar, the sisal fiber and the rice husk form a closely connected net, which have strong water-locking capacity and ability to prevent the uneven settlement of the aggregate. Therefore, adding sisal fiber, the rice husk is helpful to improve the crack resistance and impermeability. However, adding too much fiber and rice husk into mortar has an opposite effect on the impermeability and anticracking performance: the sisal fiber and rice husk will create excessive "channels" along sisal fiber and rice husk. When the seepage pressure increases, these "channels" will connect with each other and lead to the failure of the specimen. In the SEM image of sisal fiber, cavities can be clearly observed in low density, as shown in Figures 16(a) and 16(b). These cavities are evenly distributed in the mortar and therefore effectively prevent the settlement of the mortar and improve the internal bleeding of the mortar.

Table 6: Experimental results of anticrack performance and impermeability.

Sample	Crack area/mm^2	Fracture reduction factor (%)	Maximum seepage pressure (MPa)
A0	3016.33		0.19
A1	0	100	0.36
A2	38.68	98.72	0.33
A3	53.36	98.23	0.35
A4	116.81	96.13	0.23
A5	122.36	95.94	0.22
A6	66.61	97.79	0.24
A7	179.85	94.04	0.17
A8	132.14	95.62	0.21
A9	158.34	94.75	0.19

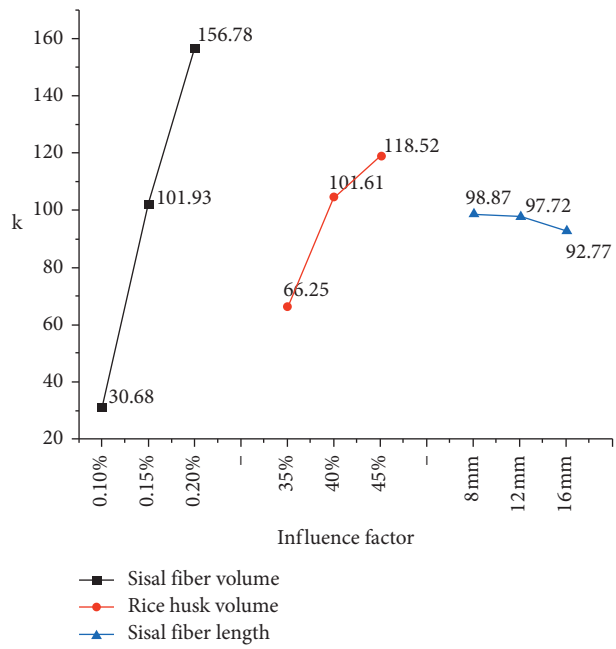

Figure 11: The k value diagram of factors affecting crack area.

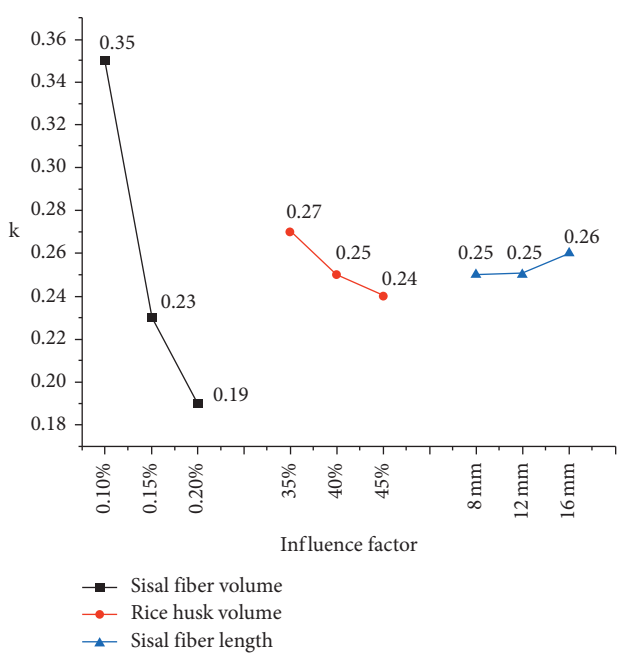

Figure 12: The k value diagram of the factors affecting the maximum seepage pressure.

Figure 13: Test A1.

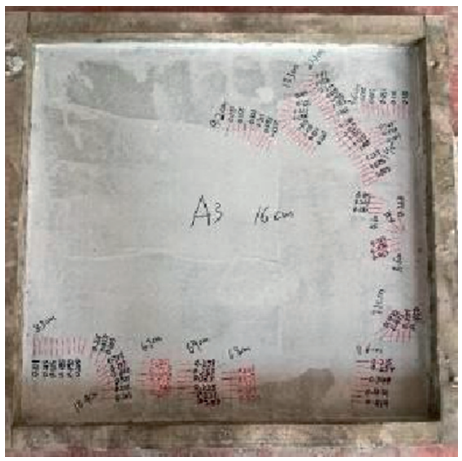

Figure 14: Test A3.

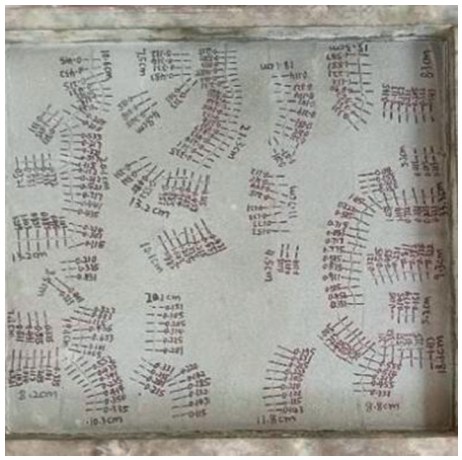

Figure 15: Test A4.

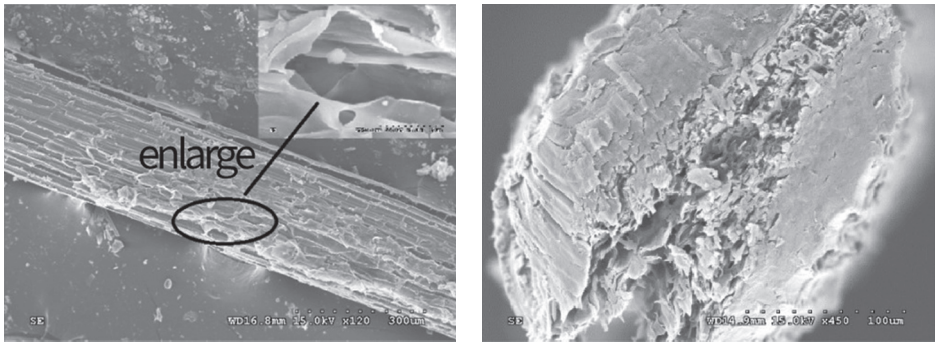

(a) (b)

Figure 16: Cavities in the mortar created by too many fibers.

4. Conclusion

In this paper, the effects of sisal fiber and rice husk on mechanical properties, early crack shrinkage, and impermeability of cement mortar were studied. The following conclusions were obtained from the experiments:

(1) The order of influence on compressive strength, from large to small, is the sisal fiber length, sisal fiber content, and rice husk content. The optimal mixture ratio of compressive strength is 0.10% volume admixture of 8 mm sisal fiber with 35% volume admixture of rice husk. The highest compressive strength can reach 17.1 MPa.

(2) The order of influence on flexural strength, from large to small, is the sisal fiber content, rice husk content, and sisal fiber length. The optimal mixture ratio is 0.10% volume admixture of 16 mm sisal fiber with 35% rice husk.

(3) The admixture amount of sisal fiber has a dominant contribution to the crack area and antipermeability property, while the length of sisal fiber contributes the least. The optimal mixture ratio of crack resistance and antipermeability property is 0.10% 16 mm sisal fiber volume admixture and 35% rice husk volume replacement rate. The area of early cracks is reduced by 100%, and the maximum seepage pressure is 0.36 MPa.

(4) Microstructure analysis showed that rice husk and sisal fiber release water in hydration process of cement which could improve the mechanical properties of the mortar. The water retention of rice husk and sisal fiber with high elastic modulus can support the interior structure of the mortar and improve its ductility.

Data Availability

All the data used to support the findings of this study are included within the article.

Conflicts of Interest

The authors declare that they have no conflicts of interest.

Acknowledgments

This study was financially supported by the National Natural Science Foundation of China (51474168).

References

[1] T. Huo, W. Cai, H. Ren et al., "China's building stock estimation and energy intensity analysis," *Journal of Cleaner Production*, vol. 207, pp. 801–813, 2019.

[2] Y. Lu, "*Application analysis and countermeasures of new wall materials*," Master's thesis, pp. 9–10, Shandong University, Jinan, China, 2006.

[3] C. Morgan, J.-C. Bénézet, L. Clerc, and E. Garcia-Diaz, "Use of raw rice husk as natural aggregate in a lightweight insulating concrete: an innovative application," *Construction and Building Materials*, vol. 70, pp. 428–438, 2014.

[4] J. Salas, M. Alvarez, and J. Veras, "Lightweight insulating concretes with rice husk," *The International Journal of Cement Composites and Lightweight Concrete*, vol. 8, no. 3, pp. 171–180, 1986.

[5] H. Binici, M. Eken, M. Kara, and M. Dolaz, "An environment-friendly thermal insulation material from sunflower stalk, textile waste and stubble fibers," in *Proceedings of the 2013 International Conference on Renewable Energy Research and Applications (ICRERA)*, October 2013.

[6] H. Jr Savastano, A. Turner, C. Mercer, and W. O. Soboyejo, "Mechanical behavior of cement-based materials reinforced with sisal fibersfibers," *Journal of Materials Science*, vol. 41, no. 21, pp. 6938–6948, 2006.

[7] R. S. P. Coutts and Y. Ni, "Autoclaved bamboo pulp fibre reinforced cement," *Cement and Concrete Composites*, vol. 17, no. 2, pp. 99–106, 1995.

[8] T. Yoshio, K. Masaaki, and J. John, "Properties and applications of slag-gypsum construction materials," in *Proceedings of the 8th Conference on Inorganic-Bonded Wood and Fiber Composite Materials*, pp. 23–25, Boise, ID, USA, 2008.

[9] Z. Sun and L. Zhang, "Effect of rice husk pretreatment process on properties of rice husk mortar," *Journal of Tongji University (Natural Science)*, vol. 43, no. 3, pp. 430–435, 2015.

[10] J. António, A. Tadeu, B. Marques, J. A. S. Almeida, and V. Pinto, "Application of rice husk in the development of new composite boards," *Construction and Building Materials*, vol. 176, pp. 432–439, 2018.

[11] Q. Huang, F. Qin, F. Ma, and M. Li, "Experimental study on the composites performance of sisal fiber-cement concrete,"

Journal of Guangxi University (National Science Education), vol. 33, no. 1, pp. 27–30, 2008.

[12] F. D. A. Silva, B. Mobasher, C. Soranakom, R. D. T. Filho, and R. D. T. Filho, "Effect of fiber shape and morphology on interfacial bond and cracking behaviors of sisal fiber cement based compositesfiber shape and morphology on interfacial bond and cracking behaviors of sisal fiber cement based composites," *Cement and Concrete Composites*, vol. 33, no. 8, pp. 814–823, 2011.

[13] P. Balaguru, "Contribution of fibers to crack reduction of cement composites during the initial and final setting period," *ACI Materials Journal*, vol. 91, no. 3, pp. 280–288, 1994.

[14] Standard for Test Method of Basic Properties of Construction Mortar (JGJ-T70-2009) [S].

[15] Standard for Test Method of Mechanical Property on Ordinary Concrete (GB/T50081-2002) [S].

[16] Technical Specification for Fiber Reinforced Concrete Structures (CECS38:2004) [S].

[17] J. Jiang, J. Li, and W. Jin, *Master of Civil Engineering*, China Architecture & Building Press, Beijing, China, 2007.

[18] T. Y. Lyubimova and E. R. Pinus, "Crystallization structure in the contact zone between aggregate and cement in concrete," *Colloid Journal*, vol. 24, no. 5, pp. 491–498, 1962.

[19] J. Songshan, "Study on interfacial bonding in cement-based composites," *Journal of the Chinese Ceramic Society*, vol. 11, no. 4, pp. 489–497, 1983.

[20] H. Savastano Jr. and V. Agopyan, "Transition zone studies of vegetable fibre-cement paste composites," *Cement and Concrete Composites*, vol. 21, no. 1, pp. 49–57, 1999.

[21] S. Hu, "Advanced cement-based composite materials," *Science Press*, 2009.

[22] P. Soroushian, F. Mirza, and A. Alhozaimy, "Plastic shrinkage cracking of polypropylene fiber reinforced concrete," *Materials Journal*, vol. 91, no. 3, pp. 280–288, 1994.

[23] J. P. Romualdi and G. B. Batson, "Mechanics of crack arrest in concrete," *Journal of the Engineering Mechanics Division*, vol. 89, no. 3, pp. 147–168, 1963.

Hindawi
Advances in Civil Engineering
Volume 2021, Article ID 6681429, 11 pages
https://doi.org/10.1155/2021/6681429

Research Article

The Role of Iron Tailing Powder in Ultra-High-Strength Concrete Subjected to Elevated Temperatures

Kexin Huang,[1] Xindan Zhang,[2] Dong Lu,[3] Ning Xu,[4] Yingxin Gan,[5] and Xin Han[5]

[1]*Xi'an University of Architecture and Technology Ande College, Xi'an 710064, China*
[2]*Chang'an University Weishui Campus Chang'an Dublin Institute of International, Xi'an 710064, China*
[3]*School of Materials Science and Engineering, Chang'an University, Xi'an 710064, China*
[4]*School of Highway, Chang'an University, Xi'an 710064, China*
[5]*Zhengping Road and Bridge Construction Co., Ltd., Xining 810000, China*

Correspondence should be addressed to Dong Lu; dongluhit@163.com and Ning Xu; xn@chd.edu.cn

Received 27 December 2020; Revised 19 January 2021; Accepted 19 February 2021; Published 16 March 2021

Academic Editor: Yushi Liu

Iron tailing powder (ITP) is considered to have the potential to replace cement to manufacture ultra-high-performance concrete (UHPC). However, the performance of UHPC with the addition of ITP after exposure to high temperatures is more complex. This investigation prepares seven UHPC formulations by introducing different contents of ITP and investigates the mechanical behavior (residual strength), bound water content, and microstructural properties (crystalline and amorphous phases, chemical structure, and morphology) of UHPC subjected to elevated temperatures. The experimental results show that the addition of ITP postpones the spalling of concrete when exposed to high temperatures. The concrete incorporating 15% ITP maintains 53.8% of its original strength at 800°C, unlike the concrete without ITP that maintains 31.6% of its original strength. The addition of ITP increases the number of micropores/cracks in concrete and helps release the vapor pressure caused by water evaporation. The findings of this investigation highlight the potential application of ITP for future UHPC design and manufacture.

1. Introduction

Concrete can endure high temperatures owing to its high specific heat and low thermal conductivity [1], which, however, does not imply that its performance is not degraded at all. Its compact microstructure is susceptible to explosive spalling due to the build-up of thermal stress at approximately 100°C of the release of vapor [2, 3]. Moreover, the internal physical/chemical changes of concrete at high temperatures affect its mechanical strength [3, 4]. It has been reported that the residual strength of concrete could significantly reduce when subjected to elevated temperatures [5]. In particular, ultra-high-performance concrete (UHPC) has extremely low permeability and porosity [6, 7], which means that the build-up of thermal pressure that existed in the pores is extremely high. Correspondingly, the high thermal pressure could cause the concrete to explosive spalling [8]. Therefore, it is essential and urgent to address or avoid the negative impacts of elevated temperatures on the performance of concrete by taking preventive measures.

An effective approach towards improving the performance of concrete at high temperatures is the accurate selection of supplementary cementitious materials (SCMs) [9, 10]. For instance, Karahan [11] developed a high volume (0–90%) of fly ash/slag concrete and reported that the concrete incorporating ~30% fly ash and ~50% slag achieved the optimal performance at 800°C. Anwar [12] found that the concrete with 20% volcanic ash behaved a higher residual strength than the Portland cement concrete. However, the residual strength of concrete deteriorated sharply at 800°C due to a weakened interfacial transition zone. Burciaga-Díaz and Escalante-García [13] found that the concrete containing metakaolin obtained the highest strength losses of 42%, while the samples with 50% granulated blast furnace slag showed minor losses of ~20%. Most recently, Manjunath et al. [14] prepared alkali-activated slag concrete by

introducing 15% activated slag and pointed out that the concrete behaved better residual strength-sustaining than the ordinary concrete at 800°C. SCMs, especially fly ash [5], metakaolin [15], and slag [16], have recently attracted much attention due to their unique characteristics, such as the stabilization of calcium hydroxide (CH) released by pozzolanic reaction [1]. More importantly, the high temperature is conducive to the sintering of some components in concrete containing SCMs and enhances its strength [17].

The increasing demand for SCMs and effective recycling of industrial waste has been attracting wide attention for sustainability in high-performance concrete and green concrete [18]. The use of iron tailing powder (ITP) could be considered an ideal alternative cementitious material in concrete-related applications [19], because of its abundant storage [20] and low-cost [19]. Meanwhile, the outstanding pozzolanic reactivity [21, 22] and the filling effect of ITP particles enable it to replace cement partially, thereby reducing the CO_2 emission caused by Portland cement in concrete production. Additionally, the fine ITP particles had a large surface area, which conduces to accelerating the cement hydration and helps to generate a compact cement matrix with more calcium silicate hydrates (C-S-H gel) and less CH [20]. Therefore, the application of ITP in concrete is regarded as a promising way to improve its performance. Besides, silica fume, as a typical pozzolanic material, is one of the mandatory raw materials in UHPC production and has been proved to have the potential to improve the high-temperature resistance of concrete [7]. However, the combined effect of variable dosages of ITP with silica fume on mechanical and microstructural properties of UHPC at high temperatures is still not clear.

This investigation aims to investigate the combined effects of variable dosages of ITP with silica fume on the mechanical and microstructural properties of UHPC at high temperatures by (1) designing seven concrete formulations by introducing different contents of ITP (0–30%) and constant dosage of silica fume (20%); (2) characterizing their macro-performance by mechanical properties, residual strength, and bound water content; and (3) analyzing their microstructure properties by crystalline phases analysis, amorphous characterization, chemical structure detection, and morphology observation.

2. Experimental

2.1. Materials. Ordinary Portland cement, silica fume, and ITP were used to prepare the UHPC mortar. The cement was produced by Qinling Factory (Shaanxi, China), whose physical properties were tested and presented in Table 1, meeting the requirements of Chinese National Standards GB 175-2007 [23]. The ITP was obtained from iron tailings after grinding for 45 minutes. The chemical composition analysis of ITP demonstrates that it has abundant calcium and silicon phase (Table 2). Particle size distribution (Malvern Instrument, Mastersizer 3000E, UK) of the raw materials showing that the ITP powder has the finest particle size (Figure 1(a)), indicating that the introduction of ITP particles help to form dense particle packing and has the potential to improve the strength of concrete [23]. The XRD patterns of ITP are presented in Figure 1(b). The silica fume had moisture of 0.58% and a density of 2.21 g/cm^3.

Fine quartz sand had a maximum particle diameter of 0.80 mm and an apparent density of 2.542 g/cm^3. Polycarboxylic superplasticizer (SP) was used to adjust the fluidity of the mixture [24]. It had a water-reducing of 35% and a solid content of 30%.

2.2. Mix Preparations. In this study, seven concrete formulations were mixed to investigate the combined effects of variable dosages of ITP with silica fume on the performance of UHPC mortars. It should be noted that the UHPC mortars were prepared to simulate the UHPC matrix, as recommended by Mo et al. [7]. Portland cement was substituted by ITP particles (wt. %) to prepare UHPC mortars, as presented in Table 3. For manufacturing UHPC mortars, all dry materials, including binders and sand, were firstly mixed at a low speed of 62 rpm for 2 min. Subsequently, the water containing dissolved SP was poured into the mixing pot and mixed at the same speed for another 3 min. Finally, another 5 min mixing was performed at a high speed of 125 rpm until a homogeneous fresh mixture was obtained.

2.3. Test Methods

2.3.1. Mechanical Properties of Concrete at Room Temperature. Mechanical properties of UHPC mortars at room temperature (RT) were tested according to GB/T 17671-1999 [25]. The UHPC samples were prepared with a dimension of 40 mm × 40 mm × 160 mm. A three-point bending test was adopted to identify their flexural strength, and the loading rate was 50 N/s. The final recorded value was obtained by the average of the three samples. After that, the compressive strength test of UHPC was conducted based on six broken specimens from the flexural strength test, and the average of the six reading was used to define the ultimate compressive strength.

2.3.2. Chemically Bound Water Content. The hardened cement paste specimens were obtained from the broken samples, as recommended by Han et al. [26]. The chemically bound water content of the specimen was determined as follows:

$$W_{\mathrm{ne}} = \frac{((M_1 - M_2)/M_1) - L_B}{1 - L_B}, \quad (1)$$

$$L_B = F_c \times W_c + F_{\mathrm{ITP}} \times W_{\mathrm{ITP}} + F_{\mathrm{SF}} \times W_{\mathrm{SF}}, \quad (2)$$

where M_1 and M_2 are the weight of hardened paste subjected to 80°C and 1050°C (g), respectively; F_c, F_{ITP}, and F_{SF} are the mass fractions of cement, ITP, and silica fume (%), respectively; W_c, W_{ITP}, and W_{SF} are the loss on ignition of cement, ITP, and silica fume (%), respectively.

Table 1: Physical properties of cement.

Flexural strength (MPa)		Compressive strength (MPa)		Specific surface area (m^2/kg)	Density (g/cm^3)
3 d	28 d	3 d	28 d		
4.3	8.2	23.8	46.8	350	2.875

Table 2: Composition analysis of raw materials (%).

Specimens	CaO	SiO_2	Al_2O_3	Fe_2O_3	SO_3	MgO	Loss on ignition
Cement	57.58	20.35	6.12	4.23	2.19	2.59	2.59
Silica fume	0.41	94.02	0.27	0.11	0.11	0.34	2.86
Iron tailing powder	12.12	51.85	11.24	9.34	0.41	4.86	2.41

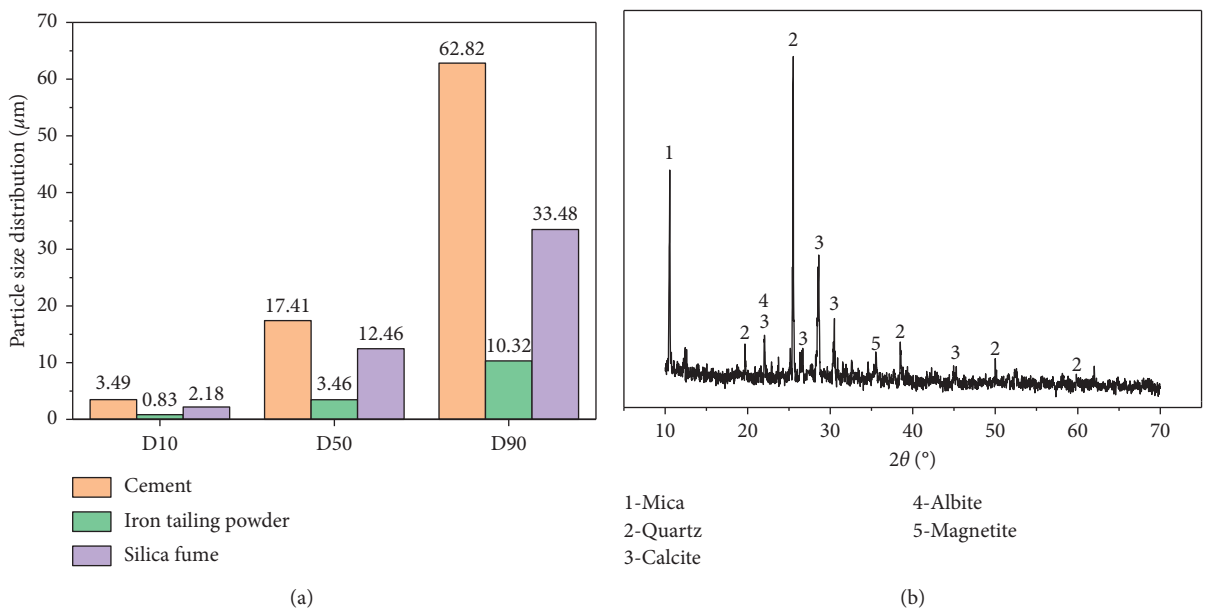

Figure 1: (a) The particle size distribution of raw materials and (b) the XRD patterns of iron tailing powder.

Table 3: Mix proportions of UHPC mortar*.

Concrete ID	Cement was substituted by ITP (wt. %)		Mix proportion of concrete (kg/m^3)		
	Cement	ITP	SF	Quartz sand	SP
CITP0	100	0	168	1330	21
CITP5	95	5	168	1330	21
CITP10	90	10	168	1330	21
CITP15	85	15	168	1330	21
CITP20	80	20	168	1330	21
CITP25	75	25	168	1330	21
CITP30	70	30	168	1330	21

*$w/b = 0.37$.

2.3.3. Residual Strength Testing. Residual strengths of UHPC mortars after exposure to high temperatures were determined by residual flexural strength and residual compressive strength, as recommended by Abaeian et al. [27]. For this purpose, the UHPC specimens (40 mm × 40 mm × 160 mm) were cured in water (20 ± 3°C) until 28 days age. After that, they were placed in an oven for heating at 60°C for 48 hours. Subsequently, an electrically controlled furnace (KRX, Henan, China) was employed to heat the UHPC mortars from RT to the set temperature of 200°C, 400°C, 600°C, and 800°C, respectively, with a heating rate of 3°C/minute. Finally, the specimens were kept in the target temperature for another 3 hours, and then the electrically controlled furnace was turned off and naturally cooled to the ambient temperature [28].

2.3.4. Microscopic Investigation. The specimens were soaked in ethanol and sealed continuously for seven days to stop the cement hydration. After that, these specimens were dried in a vacuum oven at 60°C for 48 h before testing.

X-ray diffraction (XRD, 6000, Daojin, Japan) was adopted to analyze the constituent of UHPC after exposure to elevated temperatures. For this purpose, the dry powders (<45 μm) were produced by grinding the selected crushed samples. XRD measurements were performed with Cu Kα radiation ($\lambda = 1.54$ Å) and carried out using constant pass energy (40 kV and 30 mA). The diffraction patterns were

obtained with a scanning rate of 10 degrees/min in a 2θ range of 10–70 degrees. Thermogravimetric analysis (TGA) was applied to characterize the amorphous phases of UHPC. TGA experiment was conducted using a Discovery SDT 650 thermal analyzer (TA Instruments, USA). The dry powders were tested under an oxygen atmosphere, and the heating rate was 20°C/min. Fourier-transform infrared spectrometer (FTIR, BRUKER TENSOR II, Germany) was adopted to measure the chemical structures of UHPC. For this purpose, the test powder samples (<45 μm) were carried out in the wavenumber range of 400–4000 cm^{-1} [29].

Scanning electron microscopy (SEM, S4800, Hitachi, Japan) was adopted to explain the internal microstructure and morphology of UHPC. For this purpose, the surface of the samples was coated with Au to prevent charging effects before testing. The samples were dried under vacuum conditions, and the test voltage was 15 kV.

3. Results and Discussion

3.1. Compressive Strength. The compressive strength of UHPC mortars at 28 days all exceeds 120 MPa (Figure 2(a)); it can be concluded that the addition of ITP (within 30%) could obtain an excellent compressive strength. Moreover, the sample CITP15 reaches the highest strength value at 28 days (148.8 MPa). The addition of ITP accelerated the hydration of cement [22] and promoted the generation of hydration products [30]. Also, the fine ITP particles filled the voids and contributed to the strength of concrete [24, 26].

The compressive strength of CITP30 was lower than the CITP15 sample and even lower than the reference sample CITP0. Interestingly, the compressive strength of CITP30 slightly decreased by 3.2%, compared to the CITP0 at 28 days. The high substitution level of ITP adsorbed a lot of free water [18], increased the amount of unhydrated cement particles, and limited the strength formation of concrete [30]. Also, the hydration products generated by ITP were very limited due to the low reactivity as compared to the Portland cement [26].

3.2. Flexural Strength. The flexural strength of samples at 28 days all exceeds 20 MPa (Figure 2(b)). In particular, the flexural strength of the CITP10 sample slightly increased by 7.7%, compared to the sample CITP0 at 28 days. As 15% ITP was added, the flexural strength of UHPC mortars could be further increased by 26.1%. Besides, the flexural strength value of the CITP30 sample dropped to 20.3 MPa, a decrease by 1.5% compared to the reference sample CITP0.

3.3. Chemically Bound Water Content. As presented in Figure 3, the CITP15 obtains the highest chemically bound water content value (17.32%), slightly increased by 4.2% compared to the reference sample CITP0. The result was mainly because the sample CITP15 had the largest amount of C-S-H gel [19]. However, lower bound water content could be achieved in the CITP30 sample. The high replacement level of ITP (30%) decreased the number of hydration products. These results further verified that the optimal addition of ITP was 15% in concrete production.

It can be found that there was a subtle difference in the bound water content between the UHPC mortars with and without ITP. Also, for the CITP0 sample, the bound water content was slightly higher than that of the CITP25 and CITP30 samples, but slightly lower than that of samples CITP5, CITP10, and CITP15 samples. The result was consistent with the above compressive strength (Figure 2(a)). It indicated that the addition of ITP mainly exerted the nucleation effect and the filling effect.

3.4. Residual Strength. Two obvious stages of evolution of residual strength with temperature could be observed (Figure 4). The first stage corresponds to between RT and 200°C, and the second phase corresponds to the temperature between 200°C and 800°C.

3.4.1. Residual Compressive Strength. The first stage (below 200°C) shows a slight increase in residual compressive strength (Figure 4(a)). For example, the residual strength of CITP0 at 200°C increased by 9.7%, compared with the reference sample at RT. Some cement hydrates were decomposed at 200°C, which provided water to unhydrated cement particles that existed in capillary pores and contributed to the strength development [31]. As Portland cement was substituted by 10% ITP, the residual compressive strength increased to 149.5 MPa. Since the filling effect of ITP particles, as well as their chemical reactivity, was greatly stimulated by the high temperatures [1], some additional hydration products were generated and the denser microstructure was formed [32]. Residual compressive strength of CITP15 sample further increased to 156.3 MPa, which was caused by the outstanding filling effect of ITP. Similar conclusions pointed out that the additional amount of C-S-H gel with low Ca/Si was generated due to the presence of amorphous aluminosilicate in ITP [33]. Interestingly, the residual compressive strength of sample CITP30 decreased to 143.9 MPa, which suggested the importance of the replacement level of ITP in concrete preparation.

In the second stage (400–800°C), the residual compressive strength decreased with temperatures. The decreasing trend was roughly linear below 400°C. In comparison, a significant drop of residual strength was observed beyond 400°C, which was caused by the decomposition of CH and the desiccation of the pore system [13]. The CITP15 maintained 53.8% of its original strength after 3 hours of annealing at 800°C. While the CITP0 and CITP30 samples maintained 31.6% and 39.7% of their original strength, respectively. The addition of ITP significantly increased the number of micropores, microvoids, and microcracks, which helped to release the accumulated vapor pressure, thereby improving the residual strength of concrete [8]. Besides, the high strength of UHPC postponed the degradation of the microstructure caused by the free evaporation of water at high temperatures.

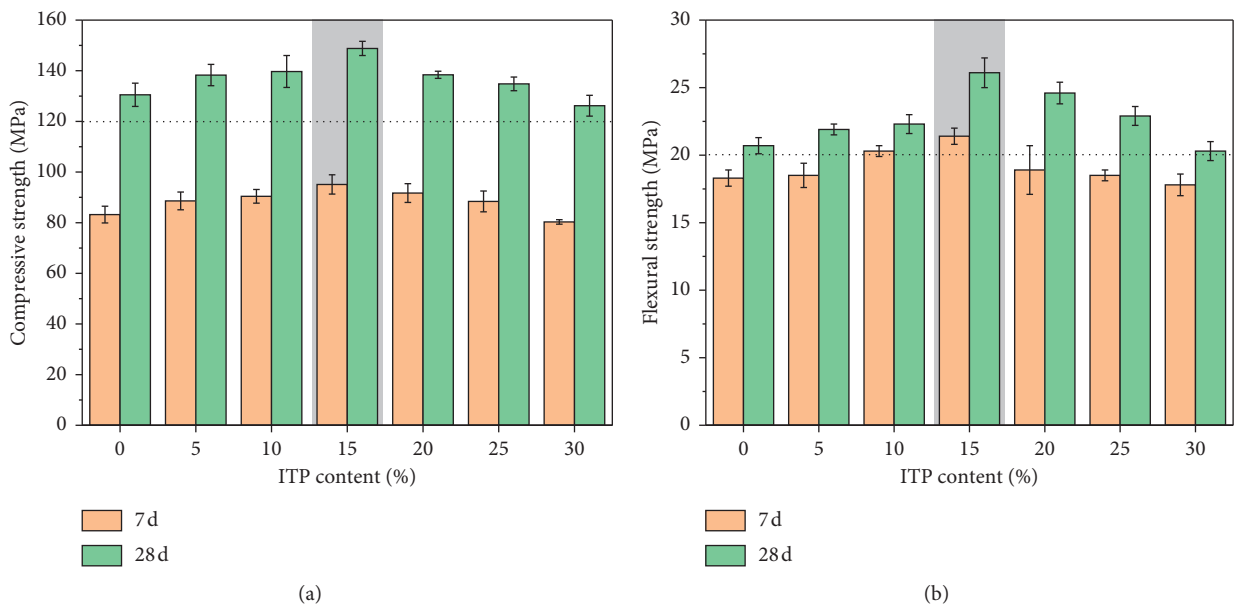

Figure 2: Mechanical properties of UHPC mortar: (a) compressive and (b) flexural strength.

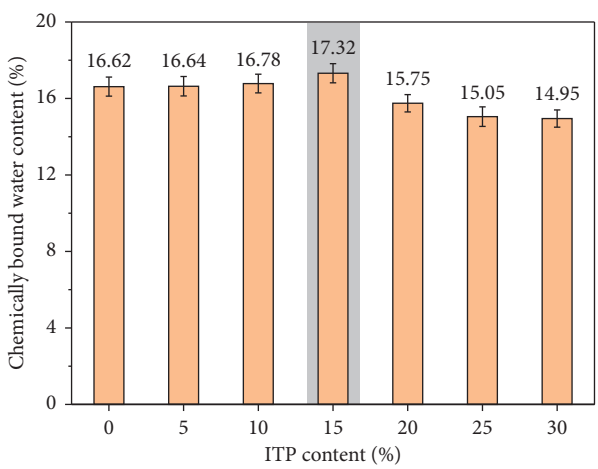

Figure 3: The bound water content of samples containing different contents of ITP.

3.4.2. Residual Flexural Strength. Residual flexural strength of concrete at 200°C increased by approximately 15%, compared to the UHPC mortars at RT (Figure 4(b)). At 800°C, the residual flexural strength of samples significantly dropped to approximately 6.7–7.1 MPa, except for the CITP15 sample, which can still retain almost 8 MPa after 3 hours of annealing. This could also confirm that the addition of 15% ITP was most effective for improving the high-temperature resistance of concrete.

3.5. XRD. Typical reflections, such as portlandite (CH), alite (C_3S), and belite (C_2S), can be observed in Figure 5. Note that, C-S-H gel cannot be found due to its amorphous phase [26], which will be analyzed in TGA and FTIR discussions (will be illustrated in Sections 3.6 and 3.7).

The diffraction peak of CH of CITP15 is slightly stronger than the CITP0 sample. The introduction of ITP promoted the hydration of cement particles and generated more hydration crystals [34]. While the reactivity of ITP was lower as compared to the cement. Therefore, the number of hydration products was decreased when a higher portion of cement was replaced by ITP [30]. As a result, the addition of 30% ITP limited the further hydration of cement and resulted in the reduction of strength (Figure 2). The diffraction peaks C_2S and C_3S in sample CITP15 at 200°C became weaker than those of the sample CITP0 at RT. This was mainly due to some of the unhydrated cement particles that existed in the capillary pores rehydrated at 200°C [35]. In this process, the additional gel-like hydration products were formed [36]. The diffraction peak intensity of CH crystal gradually decreased at 400°C and disappeared at 800°C because the CH crystal began to decompose over a temperature range between 350°C and 600°C [37]. Therefore, the residual strength of concrete decreased in this stage (Figure 4).

3.6. TGA. As presented in Figure 6(a), the first absorption peak (#1) that appears at approximately 90°C was mainly caused by the loss of free water and physically bound water [8]. Furthermore, a mass loss below 120°C was attributed to the decomposition of nearly amorphous C-S-H gel [13]. In the range of 120–200°C (#2), the mass loss was due to the dehydration of the C-S-H gel [8]. Note that, the second peak (#2) of CITP30 was lower than the CITP0, which suggested that the CITP30 sample had less C-S-H gel content than the sample CITP0. It was attributed to the less cement consumption and the limited pozzolanic reaction of ITP. The peaks were located at about 430°C (#3) and 690°C (#4) which corresponded to dehydration of CH and decarbonization of $CaCO_3$ [13], respectively. The CH content in the CITP15

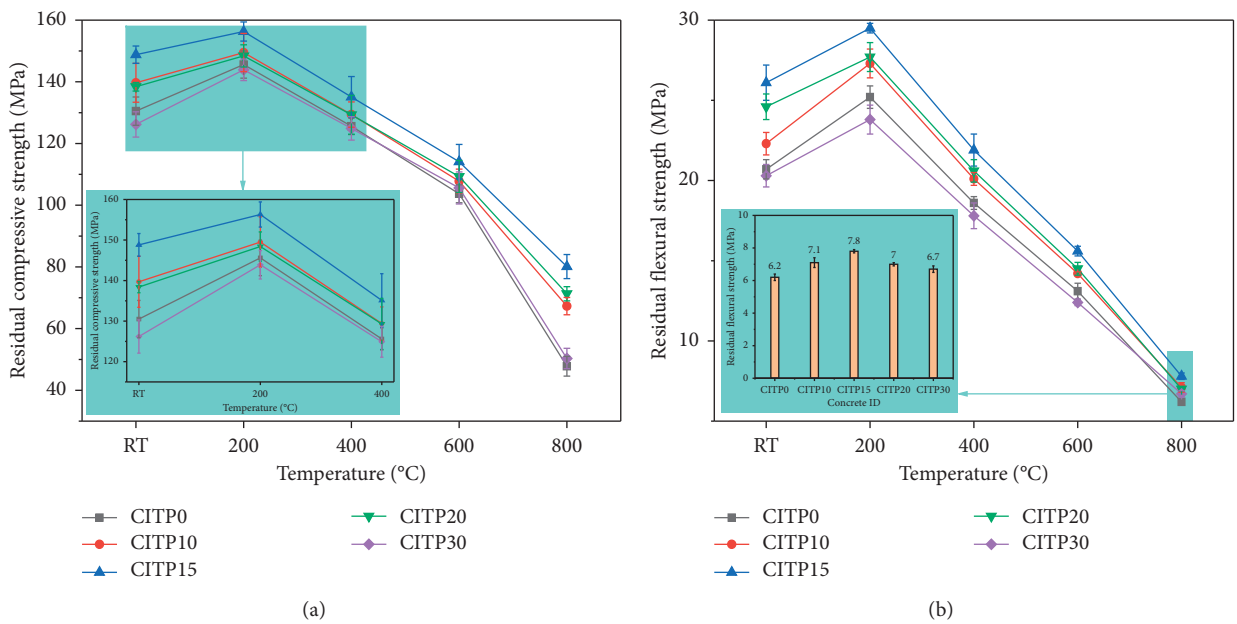

Figure 4: Residual strength of concrete: (a) residual compressive and (b) residual flexural strength.

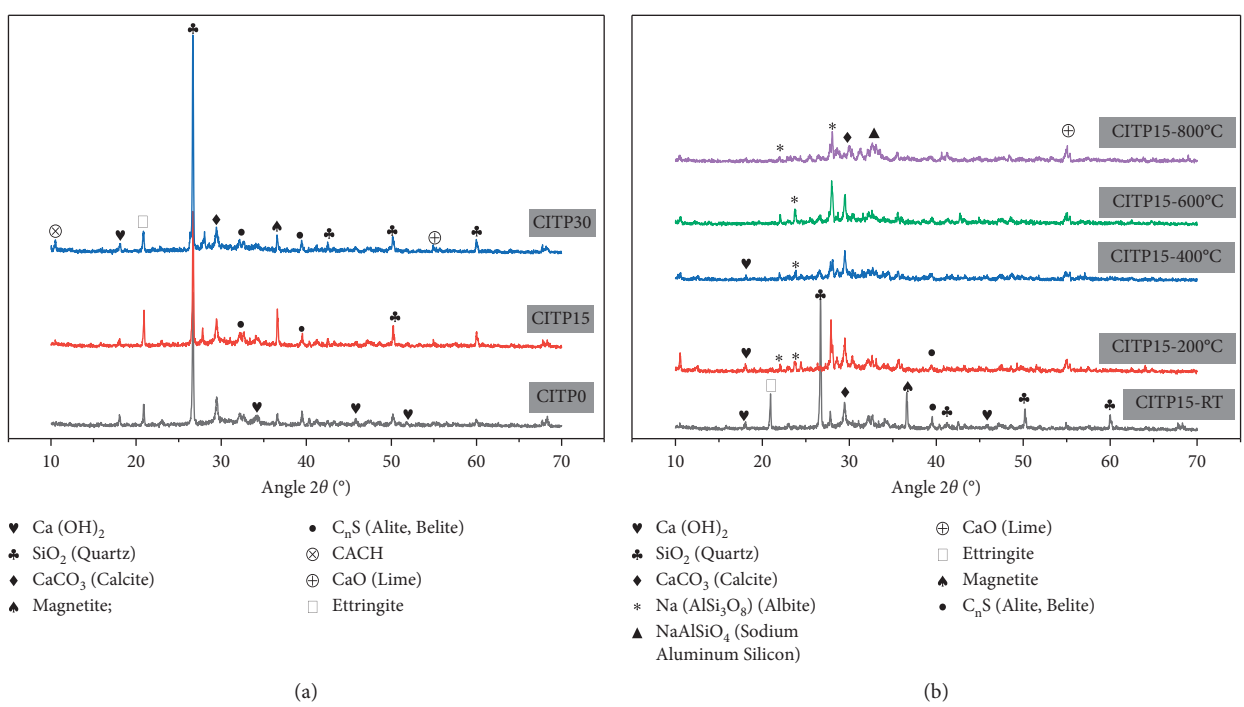

Figure 5: XRD patterns of concrete: (a) the reference sample CITP0, CITP15, and CITP30 at RT and (b) the sample CITP15 after exposure to high temperatures.

sample was slightly higher compared to CITP30; it indicated that the addition of ITP was involved in the chemical reaction. A similar conclusion has been confirmed by the earlier work [19], which indicated that if ITP does not participate in the chemical reaction; the sample incorporating ITP will show higher CH content than that of the sample without ITP. This result further demonstrated that the ITP participated in the reaction and some CH was consumed.

As evident from Figure 6(b), the first peak (#1) of sample CITP15-200°C is lower than that of the sample CITP15-RT. Note that, the water content further decreased with temperature and almost disappeared at 800°C. The content of CH (#3) showed a significant decrease at 400°C and

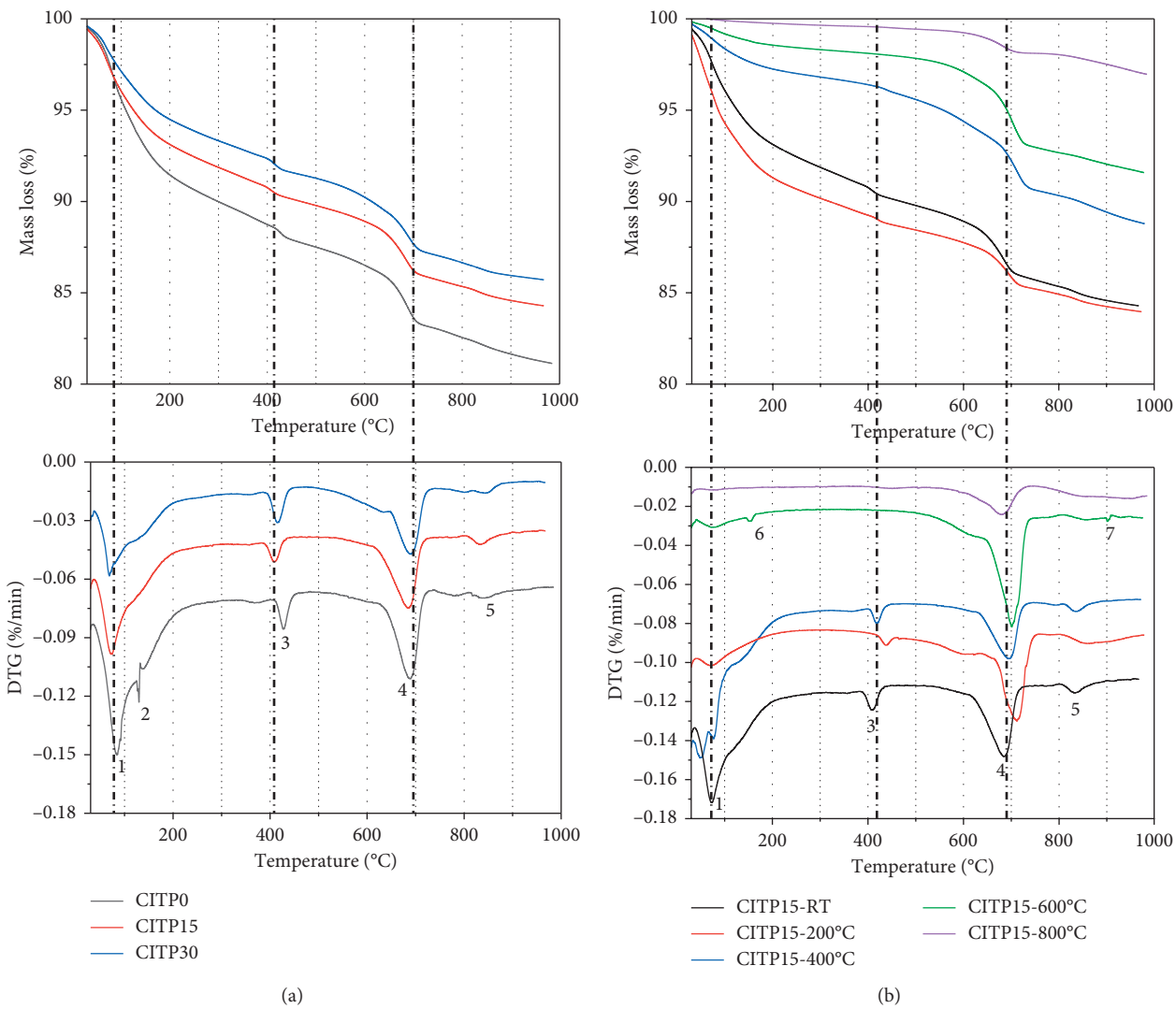

Figure 6: DTA curves and mass loss of concrete: (a) the reference sample CITP0, CITP15, and CITP30 at RT; (b) the CITP15 exposed to high temperatures.

disappeared at temperatures above 600°C. This was mainly because the CH crystal began to decompose over a temperature range between 350°C and 600°C [37]. These results were consistent with the above-discussed XRD results (Figure 5).

3.7. FTIR. The band around 3576.21 cm^{-1} corresponds to the vibration of [O-H] in CH [30], as seen in Figure 7(a). The bands at 3380.04 cm^{-1} and 1617.37 cm^{-1} were attributed to the [O-H] stretching vibration of structural water and the vibration of [H-O-H] of interlayer water in hydration products, respectively [29]. The bands of [SiO_4] around 968.71 cm^{-1} and 871.55 cm^{-1} confirmed that some hydration products were formed in UHPC incorporating ITP [30]. It suggested that the ITP particles that participated in the chemical reaction and generated the additional hydration products.

For the CITP15 sample at RT, the band can be observed at about 3380.04 cm^{-1}, while it was not detected in sample CITP15 at high temperatures (Figure 7(b)). This indicated that the decomposition of AFt and some C-S-H gel in concrete after exposure to elevated temperatures. Besides, the bands of [SiO_4] at 968.71 cm^{-1} and 871.55 cm^{-1} in sample CITP15 became weaker. This also confirmed that the hydration products of concrete gradually disappeared.

3.8. Microstructure Observation. As presented in Figure 8, the CTIP15 sample achieves a remarkably dense microstructure at RT. Several voids, microcracks, and unhydrated cement particles could be found in the CITP0 sample (Figure 8(a)) and CITP30 (Figure 8(c)). The fine ITP particles with high specific surface area (see Section 2.1) and adsorbed a lot of free water, which resulted in an increase in the amount of unhydrated cement in the CITP30 sample. On further magnification, some needle-like AFt could be observed in the reference sample (Figure 8(d)). The needle-like crystals overlapped each other and formed a network structure (Figure 8(e)). This could at least partially explain the CITP15 sample demonstrating the highest compressive

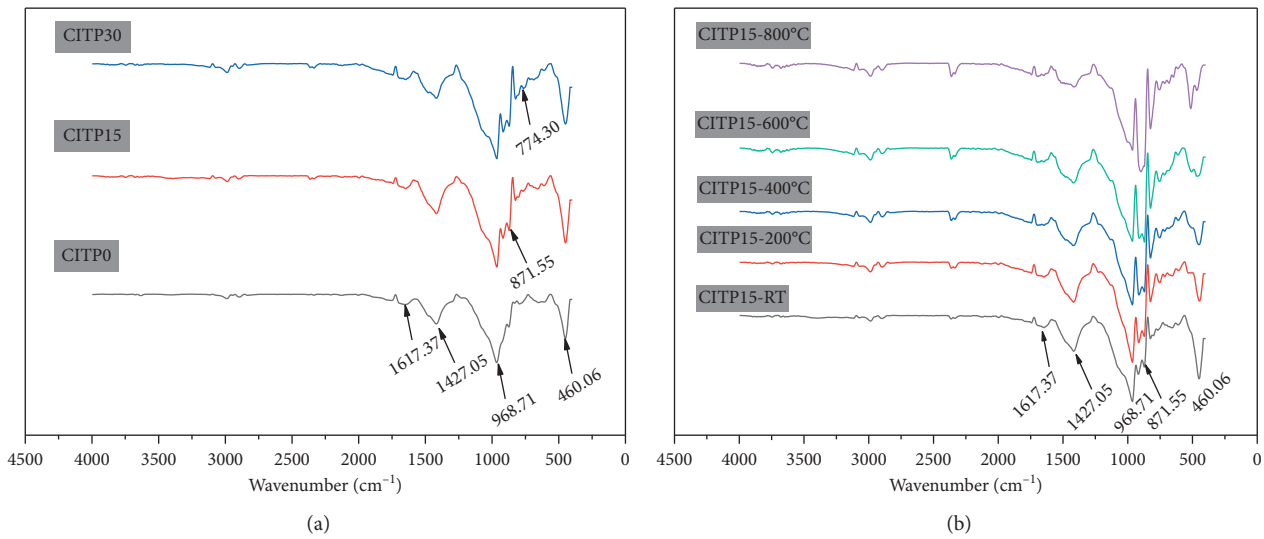

Figure 7: FTIR spectrum of concrete: (a) the reference sample CITP0, CITP15, and CITP30 at RT; (b) the sample CITP15 after exposure to high temperatures.

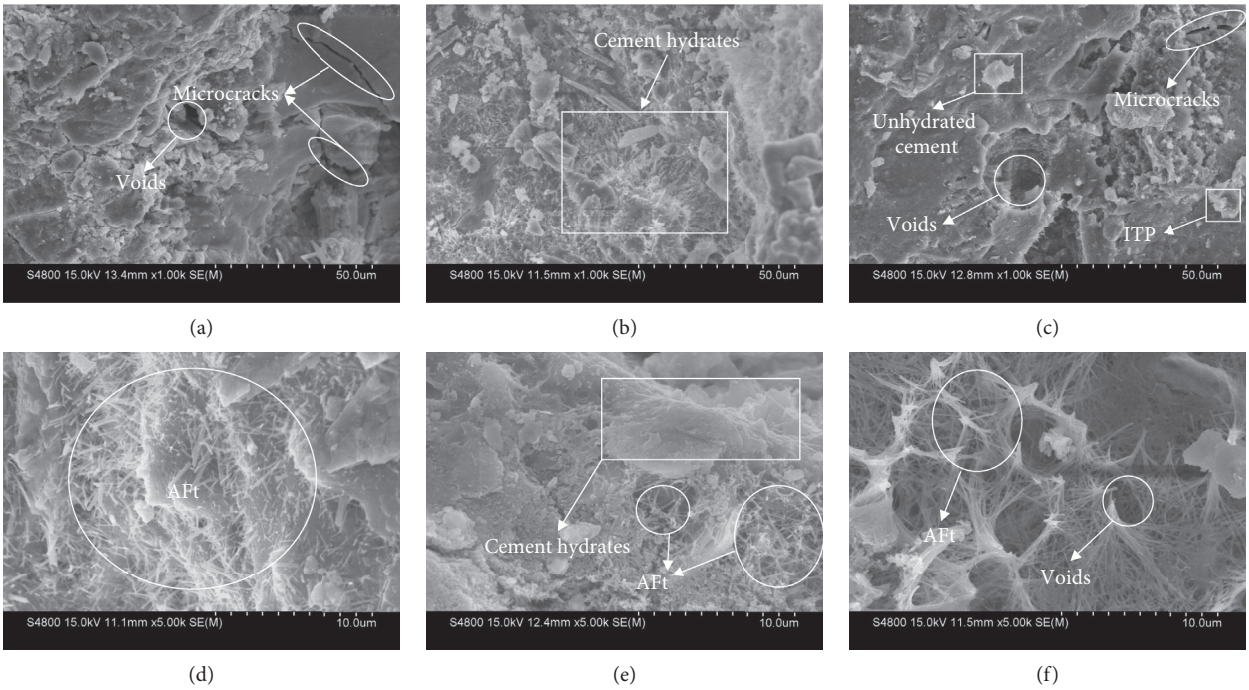

Figure 8: Microstructure of concrete: (a) sample CIP0, (b) CIP15, and (c) CIP30 with magnification of ×1,000; (d) sample CIP0, (e) CIP15, and (f) CIP30 with magnification of ×5,000.

strength (Figure 2). Interestingly, several voids were observed in the CITP30 sample and some voids were filled with cement hydrates (Figure 8(f)). This was mainly due to the surface of the ITP particle was not smooth and linked with the cement hydrates.

Numerous micropores and microcracks were found in UHPC specimens at high temperatures (Figure 9). Besides, the hydration products gradually disappeared, unlike the CITP15 sample under RT that had several needle-like AFt (Figure 9(a)). The microstructure of the CITP15 sample at 200°C (Figure 9(b)) showed a denser structure compared with the sample at RT (Figure 9(a)). This was mainly because the hydration products were generated at 200°C and filled the pores [8, 14]. Up to 800°C, the CITP15 sample presented a relatively complete structure and had a small number of microcracks (Figure 9(e)), which helped to release the thermal stress and improved the high-temperature resistance of

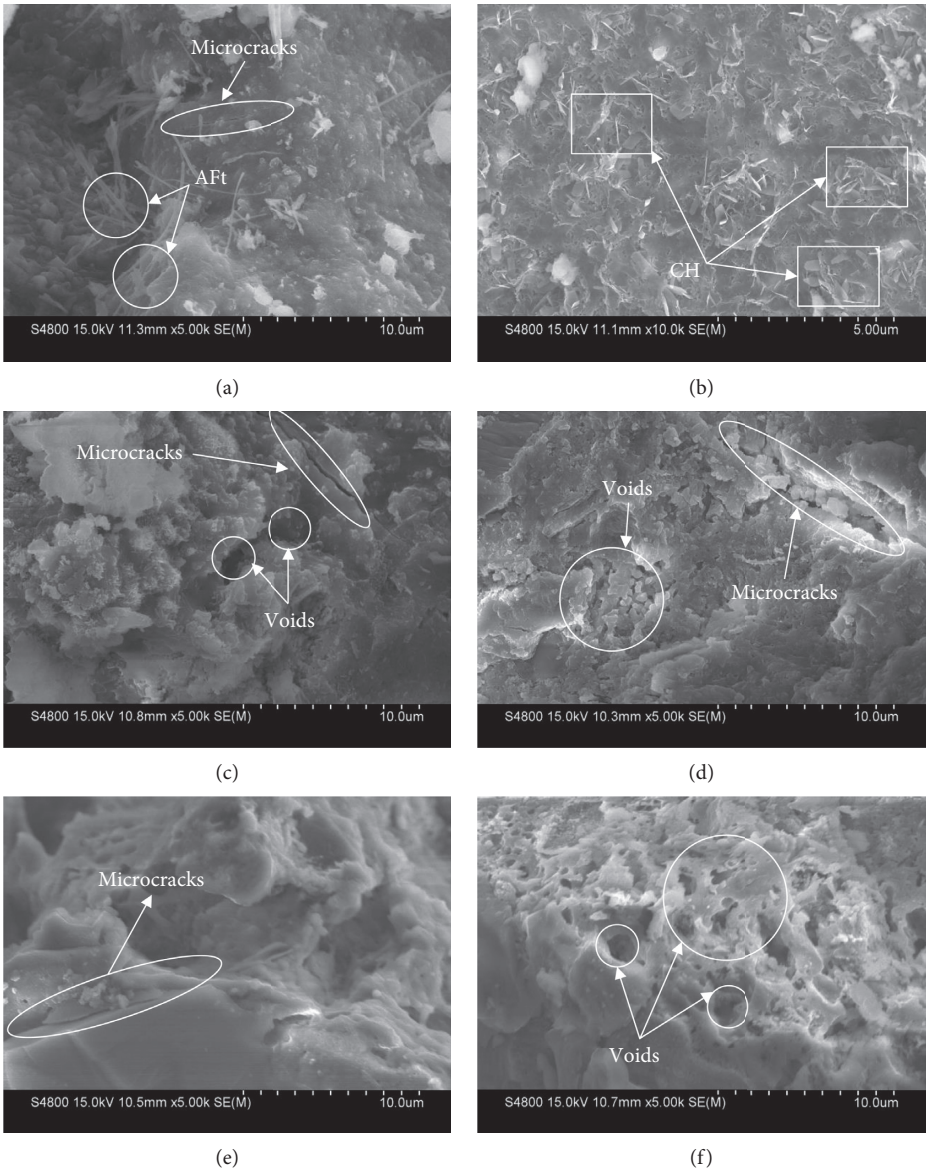

Figure 9: Microstructure of CITP15 (a) at room temperature; (b) at 200°C; (c) at 400°C; (d) at 600°C; (e) at 800°C; and (f) the sample CITP30 at 800°C.

concrete. Some micropores/cracks could be observed in the CITP30 sample at 800°C (Figure 9(f)), which improved the high-temperature resistance of concrete [8]. Therefore, the concrete containing 30% ITP maintained 39.7% of its original strength at 800°C, higher than that of the concrete without ITP (Figure 4).

4. Conclusions

Mechanical behavior and microstructural properties of UHPC containing ITP at high temperatures were investigated in this study. Residual strength and bound water content of UHPC mortars were discussed. Also, their microscopic investigation was studied by XRD, TGA, FTIR, and SEM techniques. The main findings can be concluded as follows:

(1) The addition of ITP particles has accelerated the hydration of cement and the filling effect of ITP refined the pore structure, which contributed to the strength development of UHPC mortars. As a result, the concrete with the addition of 15% ITP achieved the highest compressive strength of 148.8 MPa at 28 days.

(2) The addition of ITP has postponed the spalling of UHPC mortars at high temperatures, because the number of micropores, microvoids, and microcracks has increased, which helped to release the accumulated vapor pressure, thereby improving the residual strength of concrete.

(3) Some water released by the hydration products can be used to rehydrate the unhydrated cement particles, thereby slightly enhanced the strength of the

UHPC mortars at 200°C. Amorphous phases and microstructure results demonstrated that the ITP particles have participated in the chemical reaction and some CH has consumed.

(4) The outstanding mechanical strength of UHPC mortars due to the addition of ITP particles has alleviated the microstructure degradation caused by free water evaporation, thereby improving the high-temperature resistance of concrete.

Data Availability

The residual strength data used to support the findings of this study have not been made available because another work, we are doing, has not yet been published.

Conflicts of Interest

The authors declare that there are no conflicts of interest regarding the publication of this paper.

Acknowledgments

This work was supported by the Natural Science Foundation of Qinghai Province (No. 2020-ZJ-736).

References

[1] M. S. Morsy, Y. A. Al-Salloum, H. Abbas, and S. H. Alsayed, "Behavior of blended cement mortars containing nano-metakaolin at elevated temperatures," *Construction and Building Materials*, vol. 35, pp. 900–905, 2012.

[2] W. Wang, C. Lu, Y. Li, and Q. Li, "An investigation on thermal conductivity of fly ash concrete after elevated temperature exposure," *Construction and Building Materials*, vol. 148, pp. 148–154, 2017.

[3] X. Liang, C. Wu, Y. Yang, and Z. Li, "Experimental study on ultra-high performance concrete with high fire resistance under simultaneous effect of elevated temperature and impact loading," *Cement and Concrete Composites*, vol. 98, pp. 29–38, 2019.

[4] F. Lo Monte, R. Felicetti, and M. J. Miah, "The influence of pore pressure on fracture behaviour of normal-strength and high-performance concretes at high temperature," *Cement and Concrete Composites*, vol. 104, 2019.

[5] A. M. Rashad, "Potential use of phosphogypsum in alkali-activated fly ash under the effects of elevated temperatures and thermal shock cycles," *Journal of Cleaner Production*, vol. 87, pp. 717–725, 2015.

[6] X. Liang, C. Wu, Y. Yang, C. Wu, and Z. Li, "Coupled effect of temperature and impact loading on tensile strength of ultra-high performance fibre reinforced concrete," *Composite Structures*, vol. 229, 2019.

[7] Z. Mo, R. Wang, and X. Gao, "Hydration and mechanical properties of UHPC matrix containing limestone and different levels of metakaolin," *Construction and Building Materials*, vol. 256, Article ID 119454, 2020.

[8] N. K. Lee, K. T. Koh, S. H. Park, and G. S. Ryu, "Microstructural investigation of calcium aluminate cement-based ultra-high performance concrete (UHPC) exposed to high temperatures," *Cement and Concrete Research*, vol. 102, pp. 109–118, 2017.

[9] T. Xie, C. Fang, M. S. Mohamad Ali, and P. Visintin, "Characterizations of autogenous and drying shrinkage of ultra-high performance concrete (UHPC): an experimental study," *Cement and Concrete Composites*, vol. 91, pp. 156–173, 2018.

[10] C. Fang, M. Ali, T. Xie, P. Visintin, and A. H. Sheikh, "The influence of steel fibre properties on the shrinkage of ultra-high performance fibre reinforced concrete," *Construction and Building Materials*, vol. 242, 2020.

[11] O. Karahan, "Transport properties of high volume fly ash or slag concrete exposed to high temperature," *Construction and Building Materials*, vol. 152, pp. 898–906, 2017.

[12] K. M. Anwar Hossain, "High strength blended cement concrete incorporating volcanic ash: performance at high temperatures," *Cement and Concrete Composites*, vol. 28, no. 6, pp. 535–545, 2006.

[13] O. Burciaga-Díaz and J. I. Escalante-García, "Comparative performance of alkali activated slag/metakaolin cement pastes exposed to high temperatures," *Cement and Concrete Composites*, vol. 84, pp. 157–166, 2017.

[14] R. Manjunath, M. C. Narasimhan, and K. M. Umesha, "Studies on high performance alkali activated slag concrete mixes subjected to aggressive environments and sustained elevated temperatures," *Construction and Building Materials*, vol. 229, 2019.

[15] H. K. Shehab El-Din, A. S. Eisa, B. H. Abdel Aziz, and A. Ibrahim, "Mechanical performance of high strength concrete made from high volume of Metakaolin and hybrid fibers," *Construction and Building Materials*, vol. 140, pp. 203–209, 2017.

[16] D. Shen, Y. Jiao, J. Kang, Z. Feng, and Y. Shen, "Influence of ground granulated blast furnace slag on early-age cracking potential of internally cured high performance concrete," *Construction and Building Materials*, vol. 233, 2020.

[17] W. G. Valencia Saavedra and R. Mejía de Gutiérrez, "Performance of geopolymer concrete composed of fly ash after exposure to elevated temperatures," *Construction and Building Materials*, vol. 154, pp. 229–235, 2017.

[18] P. Zhu, S. Brunner, S. Zhao et al., "Study of physical properties and microstructure of aerogel-cement mortars for improving the fire safety of high-performance concrete linings in tunnels," *Cement and Concrete Composites*, vol. 104, 2019.

[19] F. Han, A. Luo, J. Liu, and Z. Zhang, "Properties of high-volume iron tailing powder concrete under different curing conditions," *Construction and Building Materials*, vol. 241, 2020.

[20] F. Han, L. Li, S. Song, and J. Liu, "Early-age hydration characteristics of composite binder containing iron tailing powder," *Powder Technology*, vol. 315, pp. 322–331, 2017.

[21] W. C. Fontes, J. M. Franco de Carvalho, L. C. R. Andrade, A. M. Segadães, and R. A. F. Peixoto, "Assessment of the use potential of iron ore tailings in the manufacture of ceramic tiles: from tailings-dams to "brown porcelain," *Construction and Building Materials*, vol. 206, pp. 111–121, 2019.

[22] G. Yao, Q. Wang, Z. Wang, J. Wang, and X. Lyu, "Activation of hydration properties of iron ore tailings and their application as supplementary cementitious materials in cement," *Powder Technology*, vol. 360, pp. 863–871, 2020.

[23] GB175-2007, *Common Portland Cement*, Chinese National Standard, Beijing, China, 2007, in Chinese.

[24] T. Zhang, Q. Yu, J. Wei, P. Zhang, and P. Chen, "A gap-graded particle size distribution for blended cements: analytical approach and experimental validation," *Powder Technology*, vol. 214, no. 2, pp. 259–268, 2011.

[25] GB/T17671-1999, *Method of Testing Cements-Determination of Strength*, BSI Standards, London, UK, 1999, in Chinese.
[26] F. Han, S. Song, J. Liu, and S. Huang, "Properties of steam-cured precast concrete containing iron tailing powder," *Powder Technology*, vol. 345, pp. 292–299, 2019.
[27] R. Abaeian, H. P. Behbahani, and S. J. Moslem, "Effects of high temperatures on mechanical behavior of high strength concrete reinforced with high performance synthetic macro polypropylene (HPP) fibres," *Construction and Building Materials*, vol. 165, pp. 631–638, 2018.
[28] D. Lu, Z. Tang, L. Zhang et al., "Effects of combined usage of supplementary cementitious materials on the thermal properties and microstructure of high-performance concrete at high temperatures," *Materials*, vol. 13, no. 8, 2020.
[29] X. Li, N. Zhang, J. Yuan et al., "Preparation and microstructural characterization of a novel 3D printable building material composed of copper tailings and iron tailings," *Construction and Building Materials*, vol. 249, 2020.
[30] F. Han, Y. Zhou, and Z. Zhang, "Effect of gypsum on the properties of composite binder containing high-volume slag and iron tailing powder," *Construction and Building Materials*, vol. 252, 2020.
[31] T. G. G. Molay, M. N. L. Leroy, T. Fidele, H. G. Franck, and N. J.-M. Bienvenu, "Mechanical and physical performances of concretes made from crushed sands of different geological nature subjected to high temperatures," *Engineering Science and Technology, an International Journal*, vol. 22, no. 4, pp. 1116–1124, 2019.
[32] D. Lu, J. Zhong, B. Yan et al., "Effects of curing conditions on the mechnical and microstructural properties of ultra-high-performance concrete (UHPC) incorporating iron tailing powder," *Materials*, vol. 14, no. 1, 2021.
[33] S. Pourchet, L. Regnaud, J. P. Perez, and A. Nonat, "Early C3A hydration in the presence of different kinds of calcium sulfate," *Cement and Concrete Research*, vol. 39, no. 11, pp. 989–996, 2009.
[34] L. Luo, K. Li, W. Fu, C. Liu, and S. Yang, "Preparation, characteristics and mechanisms of the composite sintered bricks produced from shale, sewage sludge, coal gangue powder and iron ore tailings," *Construction and Building Materials*, vol. 232, 2020.
[35] K. Do Carmo e Silva Defáveri, L. F. Dos Santos, J. M. Franco de Carvalho, R. A. F. Peixoto, and G. J. Brigolini, "Iron ore tailing-based geopolymer containing glass wool residue: a study of mechanical and microstructural properties," *Construction and Building Materials*, vol. 220, pp. 375–385, 2019.
[36] J. Yang, G.-F. Peng, J. Zhao, and G.-S. Shui, "On the explosive spalling behavior of ultra-high performance concrete with and without coarse aggregate exposed to high temperature," *Construction and Building Materials*, vol. 226, pp. 932–944, 2019.
[37] B. Zhang, "Effects of moisture evaporation (weight loss) on fracture properties of high performance concrete subjected to high temperatures," *Fire Safety Journal*, vol. 46, no. 8, pp. 543–549, 2011.

Hindawi
Advances in Civil Engineering
Volume 2021, Article ID 6692729, 10 pages
https://doi.org/10.1155/2021/6692729

Research Article

Research on the Infrared Thermographic Detection of Concrete under Solar Heating

Dan Zheng,[1] **Shuaishuai Tan**,[1] **Xinxin Li**,[1,2] **and Haonan Cai**[1]

[1]*College of River and Ocean Engineering, Chongqing Jiaotong University, Chongqing 400074, China*
[2]*College of Water Conservancy and Environmental Engineering, Zhengzhou University, Zhengzhou 450001, China*

Correspondence should be addressed to Xinxin Li; 990201600023@cqjtu.edu.cn

Received 10 December 2020; Revised 14 January 2021; Accepted 21 January 2021; Published 4 February 2021

Academic Editor: Xianming Shi

Infrared thermography for detecting defects in concrete structures is closely related to the heat source and the optimized method of the thermal image. Due to the limitation of the irradiation area of the heat source, it is inefficient to detect the defects in large concrete structures. In this paper, sunlight was employed as a heat source to detect the defects with different sizes and depths in concrete, and the measured infrared images were processed and optimized by an enhancement algorithm. The experimental results showed that the defects in concrete could be rapidly identified under sunlight. The effect of environment, view angle, and boundary can be eliminated by image preprocessing, and the histogram equalization algorithm can increase the detection depth of the defects. The research results can also provide a reference for the infrared detection technology of concrete under the weak heat source.

1. Introduction

Nondestructive testing (NDT) of concrete is critical to evaluate the safety of structures, and infrared thermography (IRT) is one of the most important internal defect detection methods available. When the heating source is applied on the concrete, due to the poor thermal conductivity of the gas contained in the internal defects, energy could not pass through and accumulate on the top region of the defect, causing the surface temperature above the defect higher than the intact area. Therefore, infrared thermography can be used to collect the surface temperature information and detect the internal defects in concrete [1, 2]. The variation of temperature in different parts of the concrete depends on the depth and size of the defects. However, this method is not effective for detecting deep defects [3–5]. Maierhofer studied the influence of the size and depth of the cavity on the transient temperature curve under different heating times, realizing the locating of the internal defects in concrete [6]. Patricia further observed that the maximum detection depth is related to the horizontal dimensions of the defects [7].

Although the thermal conductivity of concrete is two orders of magnitude higher than that of gas, its value is still low, and identification of defects may take a long time. Thus, researchers began to focus on improving the heating mode and optimizing the thermal image. The test results show that a clear thermal image can be obtained by heating the specimen with a strong heat source [8, 9]. Krishnendu compared the infrared inspection results of concrete under various heating methods and found that the high-resolution infrared images can be obtained by frequency modulation heating mode [10].

For large concrete structures, the defects are randomly distributed in the structure. Owing to the limitation of the heat source, it is inefficient to divide the structure into small parts for detection. As a natural heat source, sunlight can be evenly applied to the structure, and the heating range could be effectively expanded [11]. However, the radiant intensity of sunlight applied to the structure is small, and a stable environment is needed to reduce the influence of external factors (e.g., wind, moisture evaporation, and boundary) on the surface temperature of the inspected object [12].

Therefore, it is necessary to optimize the measured results under solar heating.

Digital image processing is an applied science, which can realize image nonuniformity correction and contrast enhancement [13]. Existing studies have shown that the processing method based on color histogram is widely applied to infrared image optimization, which can achieve the purpose of expanding the gray range and improving contrast, and the types of derived algorithms are gradually enriched, such as the global histogram equalization (GHE) and the contrast limit adaptive histogram equalization (CLAHE) [14, 15]. Scholars have used this enhancement method to reduce the limit of contrast in infrared images for visual observation and improve the recognition effect [16].

This paper aims to present an experimental investigation into the surface temperature distribution of concrete under solar heating. The effect of the depth and size of the defects, the heat source, the boundary condition, and the optimized method on the temperature variation are evaluated. Finally, the proper optimized method for the recorded images under different heat sources is proposed.

2. Experimental Program

2.1. Specimens and Material. To analysis the surface temperature distribution above the defect, two groups of specimens with dimensions of $400 \times 170 \times 70$ mm and $1000 \times 540 \times 170$ mm were adopted in the test. In group A, two specimens with four defects were tested to evaluate the depth of the defect on the temperature distribution under pulse heating. In group B, a specimen with eight defects was used to study the effect of the size and depth of the defects on the temperature distribution under solar heating. The detailed dimension and distribution of defects are depicted in Figure 1. Concrete with a designed strength of 30 MPa was adopted in the test and the mix proportion was cement: water: sand: coarse aggregate = 1 : 0.62 : 1.81 : 4.20. Before pouring the concrete, polyurethane foam with the same size as the defect was fixed in the design position by steel wire. As the thermal conductivity of the foam is close to that of air, the polyurethane foam can be used to simulate the defects in concrete [17].

2.2. Test Apparatus and Test Procedure. To analyze the application range of infrared thermography in nondestructive testing of concrete structures, quartz plate and sunlight were both used as heating sources to apply thermal energy to the specimens, as shown in Figure 2.

The pulse heating tests were carried out in the laboratory at a temperature of 25°C. During the test, the quartz heating plate was first preheated for 2 min to keep the heating power stable and then placed above the specimen with a distance of 400 mm. The heating power maintained 3000 W during the heating stage. After heating for 6 min, the quartz plate was removed from the supports. In the meantime, an A300 infrared thermal imaging camera with a precision of 0.1°C and measuring range of −20°C~350°C was employed to record the surface temperature field. Considering the heat reflection generated in the heating stage is violent and the heat conduction is insufficient, it is not suitable to carry out defect identification in this period. At present, active heating research generally adopts the cooling stage, and the detection results are more accurate.

The solar heating tests were conducted under sunlight with a radiation intensity of about 800 W/m^2 and an ambient temperature of 33°C. Generally, it is appropriate to apply solar heating in the morning because of the large temperature gradient of sunlight [18, 19]. Before testing, the specimen was shaded to an ambient temperature of 25°C to eliminate the temperature difference and then exposed to sunlight for 30 min. Meanwhile, the variation of surface temperature was recorded by the infrared thermal imaging camera. Since the sunlight is not controllable, it is inconvenient to conduct shading treatment in the signal acquisition process. No data on the cooling period was recorded, meaning that defects need to be identified during the heating phase.

2.3. Experimental Results. Figure 3 shows the surface temperature distribution of each specimen under the maximum temperature difference between the defect area and the intact area. It can be seen that the infrared thermal image detection method can be well used to detect the shallow defect in concrete.

In the pulse heating test, it is obvious that the brightness of deep defects A2-1 and A2-2 is higher than that of A1-2. This unexpected phenomenon is caused by the working principle of the thermal imager. The brightness of the infrared image is directly proportional to the temperature. The thermal imager assigns the brightest color to the highest temperature and the darkest color to the lowest temperature. However, the temperature range will change with time, and the brightness range remains unchanged, which means that the proportional coefficient of brightness and temperature is constantly changing. When there is an extremely high-temperature part (A1-1) in the image, the brightness range allocated to the relatively low-temperature area (A1-2) will be compressed, resulting in the brightness lower than A2-1 and A2-2, whose temperature is high and relatively close. The location of all the defects can be accurately determined; however, with the increase of the depth, the contours will be harder to distinguish.

In the solar heating test, the brightness corresponds well with the defect depth because the defects are located in the same image. When the defect depth is higher than 32 mm, it is difficult to recognize the existence of the defect.

The subjective defect-recognition depends on the color difference between the defect area and the intact area. When the temperature difference is small, it is difficult for the naked eye to identify the defect, limiting the application of IRT. To further analyze the application range under pulse heating and solar heating manners, the average temperatures (T) of defect area and intact area were extracted, and the temperature difference (ΔT) curves are shown in Figure 4.

Under pulse heating, it can be seen from Figure 3 that ΔT increases steadily in the early stage of cooling and then rises

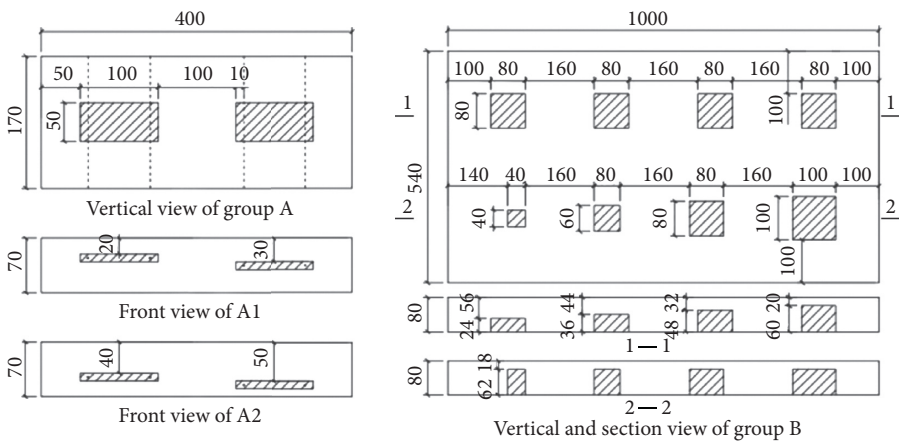

Figure 1: Defect layout of specimens.

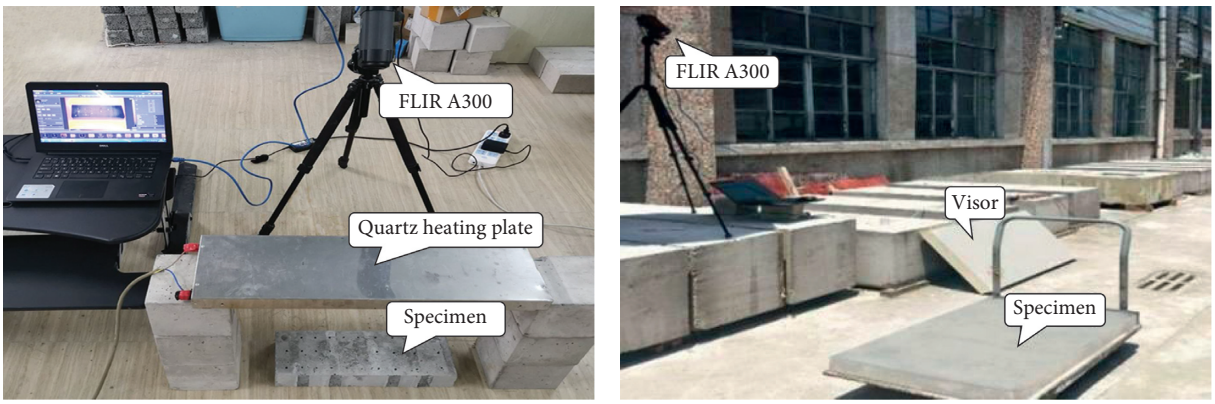

(a) (b)

Figure 2: Equipment layout. (a) Pulse heating. (b) Solar heating.

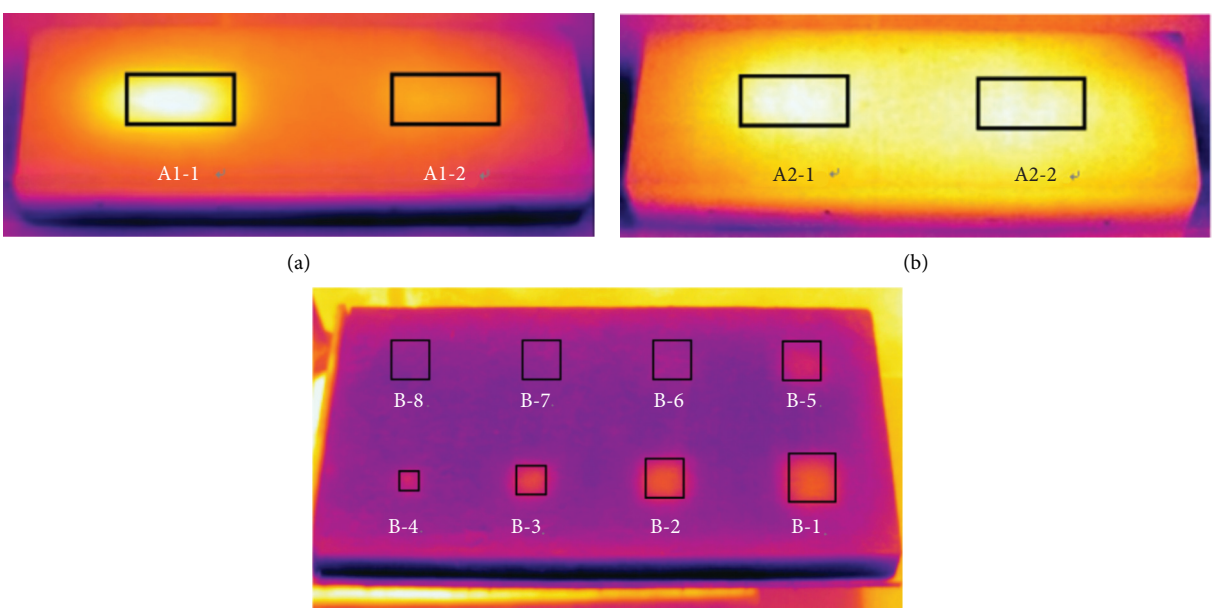

(a) (b)

(c)

Figure 3: Temperature distribution. (a) A1-cool down for 12 minutes. (b) A2-cool down for 12 minutes. (c) B-heat up for 20 minutes.

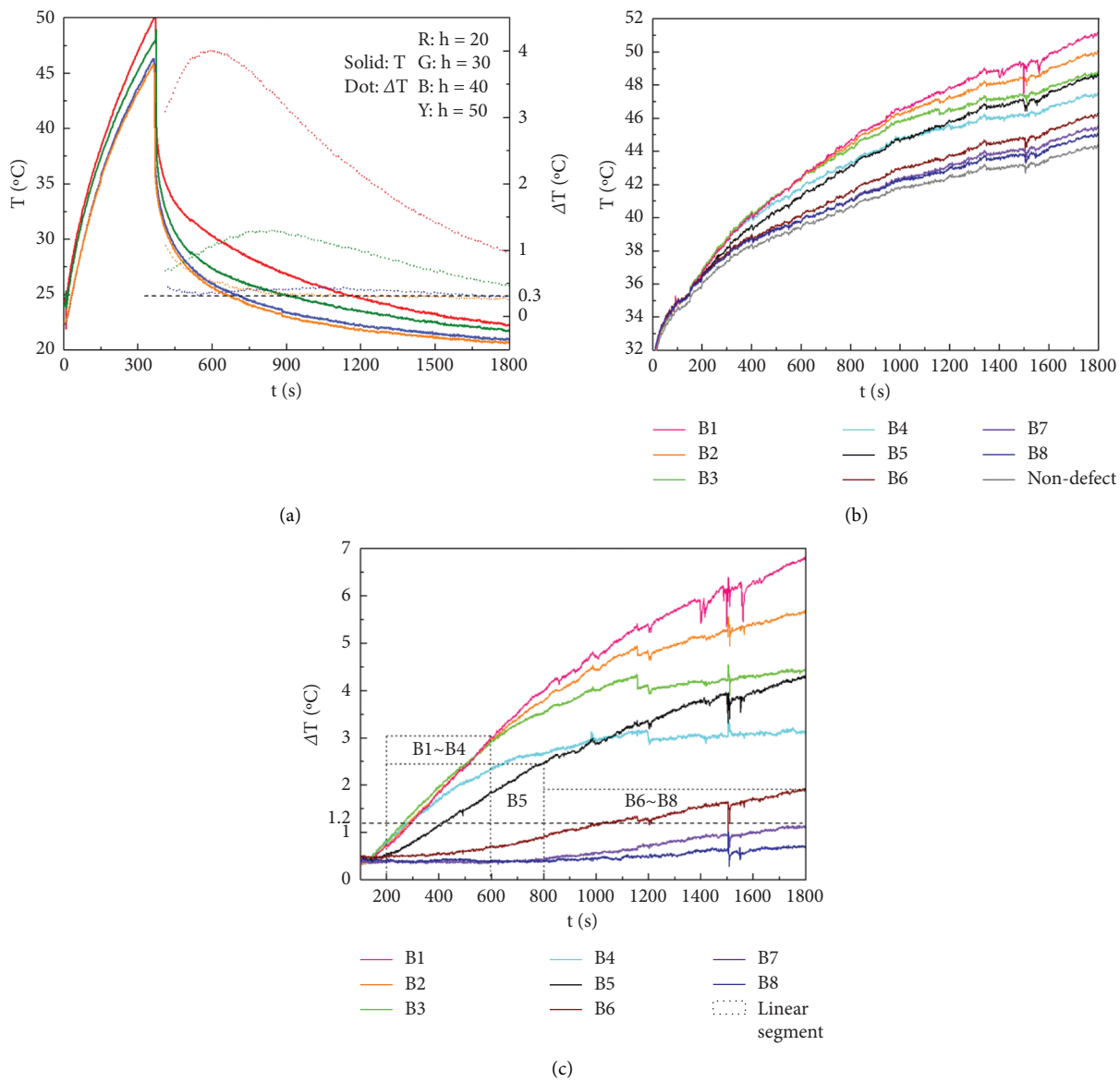

Figure 4: Temperature and temperature difference curve. (a) Pulse heating-T, ΔT; (b) solar heating-T; (c) solar heating-ΔT.

to the maximum value. However, it is difficult to distinguish the outline of deep defects when the temperature difference is less than 0.3°C (A2-1, A2-2). For solar heating, it can be found from Figure 4 that when the temperature difference is less than 1.2°C (B-7, B-8), the defects cannot be accurately identified with naked eyes. To analyze the influence of dimension and depth of the defect on ΔT, the ratio (R) of side length (L) to depth (D) and the corresponding temperature difference is listed in Table 1 and Figure 5.

It can be seen from Figure 5 that it is hard to distinguish the defect when the ratio is less than 1.8. Therefore, it is necessary to optimize for this type of defect.

Meanwhile, to make infrared thermography detection more accurate in depth judgment, the temperature difference growth rate (S) and the corresponding time of the linear segment of the temperature difference curve in Figure 4 are extracted in Table 2.

Table 1: Growth rate of temperature difference.

Def.	B1	B2	B3	B4	B5	B6	B7	B8
L(mm)	100	80	60	40	80	80	80	80
D(mm)	18	18	18	18	20	32	44	56
R	5.6	4.4	3.3	2.2	4.0	2.5	1.8	1.4
ΔT(°C)	5.32	4.73	4.02	2.99	3.28	1.22	0.68	0.48

It can be seen from Table 2 that when $D = 18$ mm (B1~B4), L has little influence on S, which remains nearly 0.0058. When $L = 80$ mm (B2, B5~B8), with the increase of D, S decreases significantly. As a result, S is mainly related to D, and L exerts a minor influence on it. It can be seen from Figure 6 that a power function can represent the relationship between S and D and be used to judge the depth of the defects. The maximum detection depth can also be obtained.

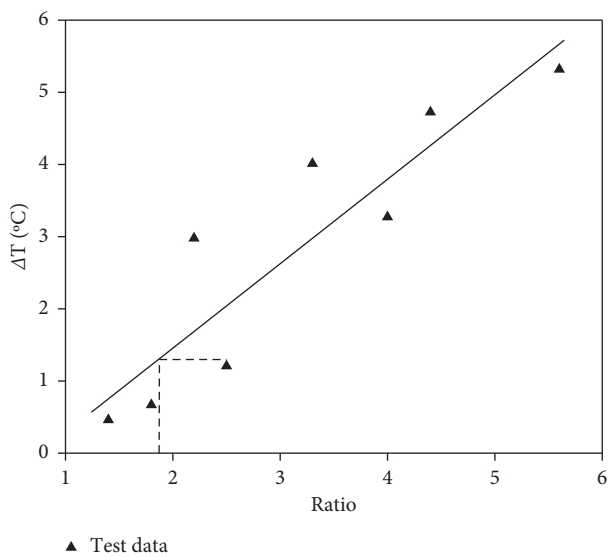

Figure 5: Ratio fitting.

Table 2: Growth rate of temperature difference.

Def.	B1	B2	B3	B4	B5	B6	B7	B8
L[mm]	100	80	60	40	80	80	80	80
D(mm)	18	18	18	18	20	32	44	56
Time range(s)	200~600				200~800		>800	
S	0.0058	0.0058	0.0059	0.0050	0.0034	0.0014	0.0009	0.0005

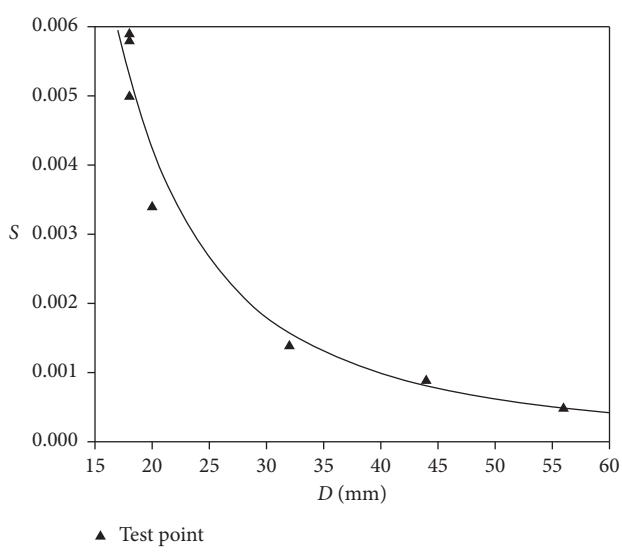

Figure 6: Slope fitting.

3. Optimized Method of Image

3.1. Interference Cancellation. Generally, the IRT detection mainly uses the temperature field at a single moment to identify defects [20], but the recorded information is easily disturbed by the external noise. During the tests, the thermal imaging camera can record the whole variety of the surface temperature. To make full use of the recorded data and reduce the influence of external noise on images, the video was decomposed into single-frame images with equal interval time. After that, the gray value of each pixel point is fitted with n times polynomial equation in chronological order [10, 16], and the fitting value of surface temperature $T(t)$ can be expressed as follows:

$$T(t) = \sum_{(i=0)}^{n} a_i t^i = a_0 + a_1 t + a_2 t^2 + \cdots + a_n t^n. \quad (1)$$

The experimental material is not an ideal semi-infinite body. In the process of solar heating, the deviation of illumination angle and ambient temperature will affect the boundary temperature of the sample. However, in the process of active heating, the pulse intensity is much greater than the environmental impact which can be ignored. As shown in Figure 7, to study the temperature variation at the material boundary and propose an effective correction method, the image is corrected by perspective transformation to ensure the authenticity of the defect information [21–23], and two measuring lines are arranged in the detection image to extract the gray value (proportional to the temperature) along the line.

It can be seen from Figure 7 that the temperature around the boundary region is higher than the central part of the specimen. Moreover, the temperature above the defect is larger than the intact area—the deeper the defect, the lower the temperature. Therefore, the temperature of the specimen is influenced by solar radiation, defects, and boundaries. To obtain the actual temperature above the defect, the effect of the boundary should be eliminated. For an intact area, the

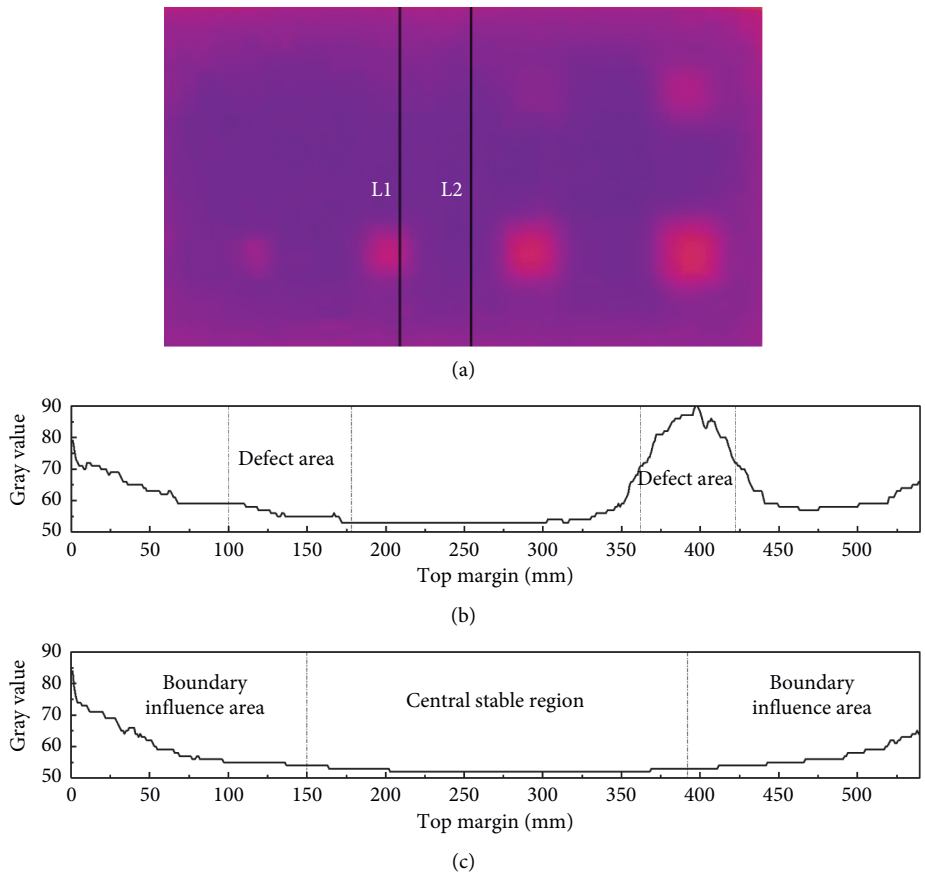

Figure 7: Line layout and gray level. (a) Line layout. (b) L1-gray level. (c) L2-gray level.

surface temperature is related to the solar radiation and boundary. During the test, the radiation was uniformly applied to the concrete. The influence of solar radiation on the temperature can be regarded as a fixed value at a particular moment. The boundary effect mainly controls the variation of temperature around the boundary region. Therefore, the average temperature on the left side of Figure 7(c) can be described in Figure 8.

As illustrated in Figure 8, the horizontal asymptote of the fitting curve can be regarded as the dividing line between the effect of solar radiation and boundary, and the influence of boundary effect can be eliminated by subtracting the part enclosed by the horizontal asymptote and the fitting curve. Therefore, the infrared 3D image of the specimen B after subtracting can be obtained in Figure 9.

The image preprocessing effectively eliminates external interference and makes the temperature in the nondefect area more stable, but the deep defects are still not highlighted, so it is necessary to further optimize the preprocessed image.

3.2. Image Enhancement. The infrared detection image is different from the ordinary image by reason of the simple distribution of color blocks, no sudden change in brightness, and few details available. When processing this kind of image, the effect of many algorithms based on visual and multiscale information is close to that of histogram equalization. However, the histogram algorithm has the advantages of convenient adjustment and fast operation speed, so the global histogram equalization (GHE) and the contrast limit adaptive histogram equalization (CLAHE) method were adopted in this passage [24–29].

GHE is a method of applying histogram equalization directly to the whole image by broadening the gray value that occupies most of the image and merges the gray value with a small number to enhance image contrast. The transform function can be obtained through the histogram information of the image. CLAHE first subdivides the image into a square subarray. Then, the exceeding default gray values are distributed to each pixel to make the high-temperature area's gray value tend to be consistent. This approach abandons the idea of uniform transition and transforms the region into a ladder form so that the contours of the high-temperature parts can be highlighted. The optimization results of pulse heating and solar heating under different enhancement image algorithms are shown in Figures 10 and 11.

It can be seen from Figure 10 that the enhanced image algorithm can improve defect-recognition resolution. For pulse heating, the heat around the defect was continuously transmitted to the surrounding parts during the cooling stage. For shallow defect, as shown in Figures 10(b) and 10(e), the GHE method results in a large red speckle formed above the defect, and the shape of the defect is hard to be

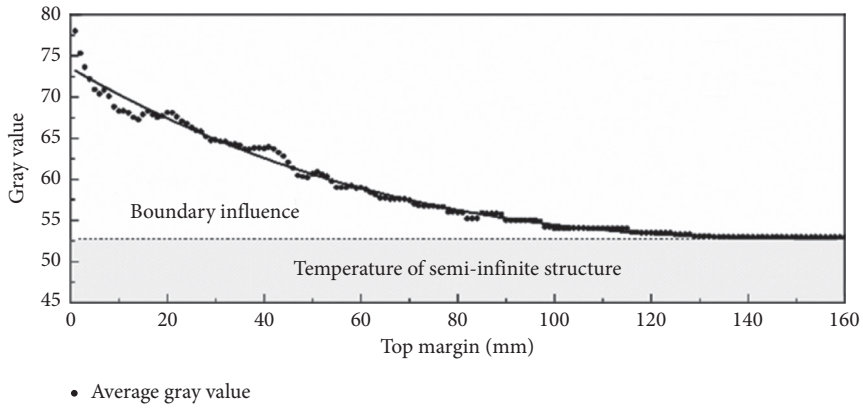

Figure 8: Edge temperature fitting.

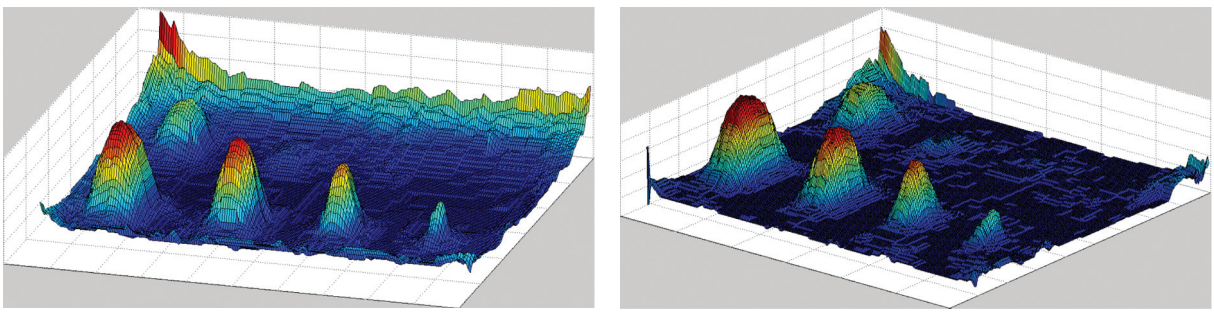

(a) (b)

Figure 9: Preprocessing effect of specimen B. (a) Before preprocessing. (b) After preprocessing.

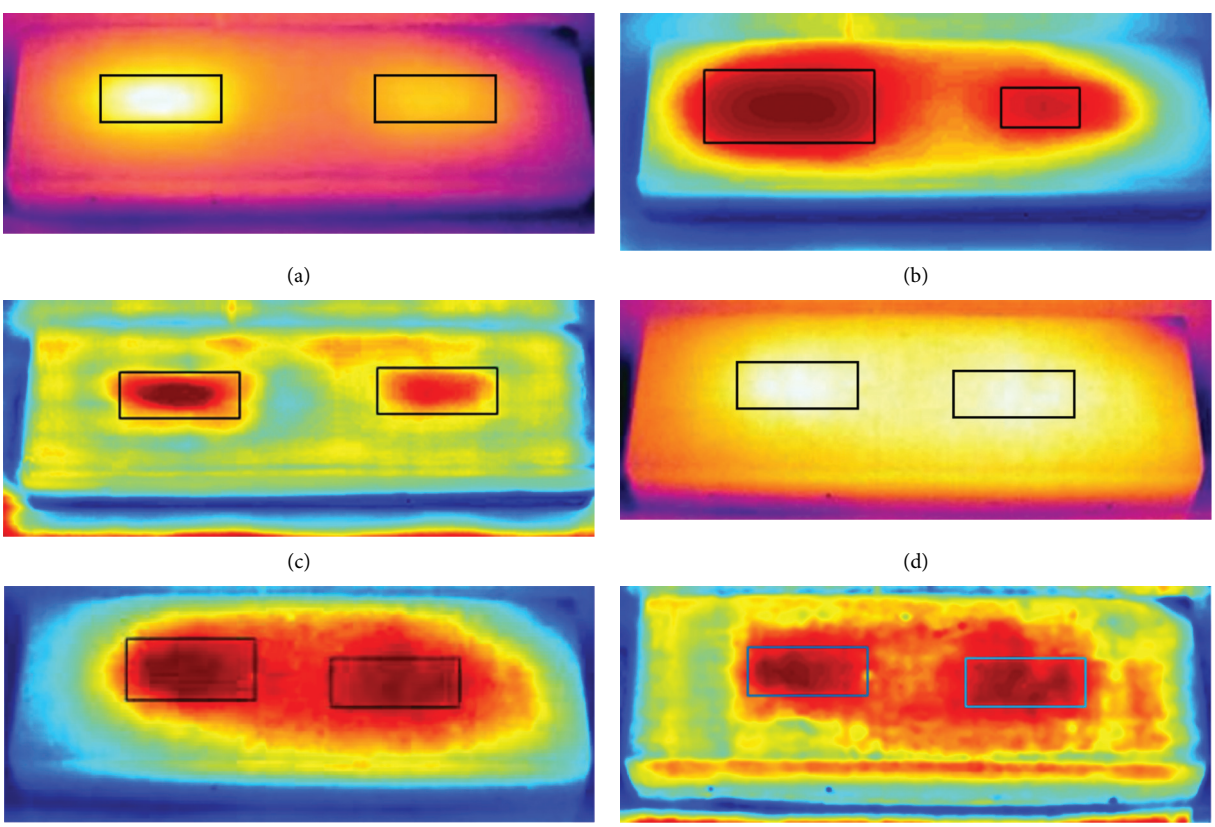

(a) (b) (c) (d) (e) (f)

Figure 10: Comparison image enhancement of A1 and A2. (a) A1-before enhancement. (b) A1-GHE enhancement. (c) A1-CLAHE enhancement. (d) A2-before enhancement. (e) A2-GHE enhancement. (f) A2-CLAHE enhancement.

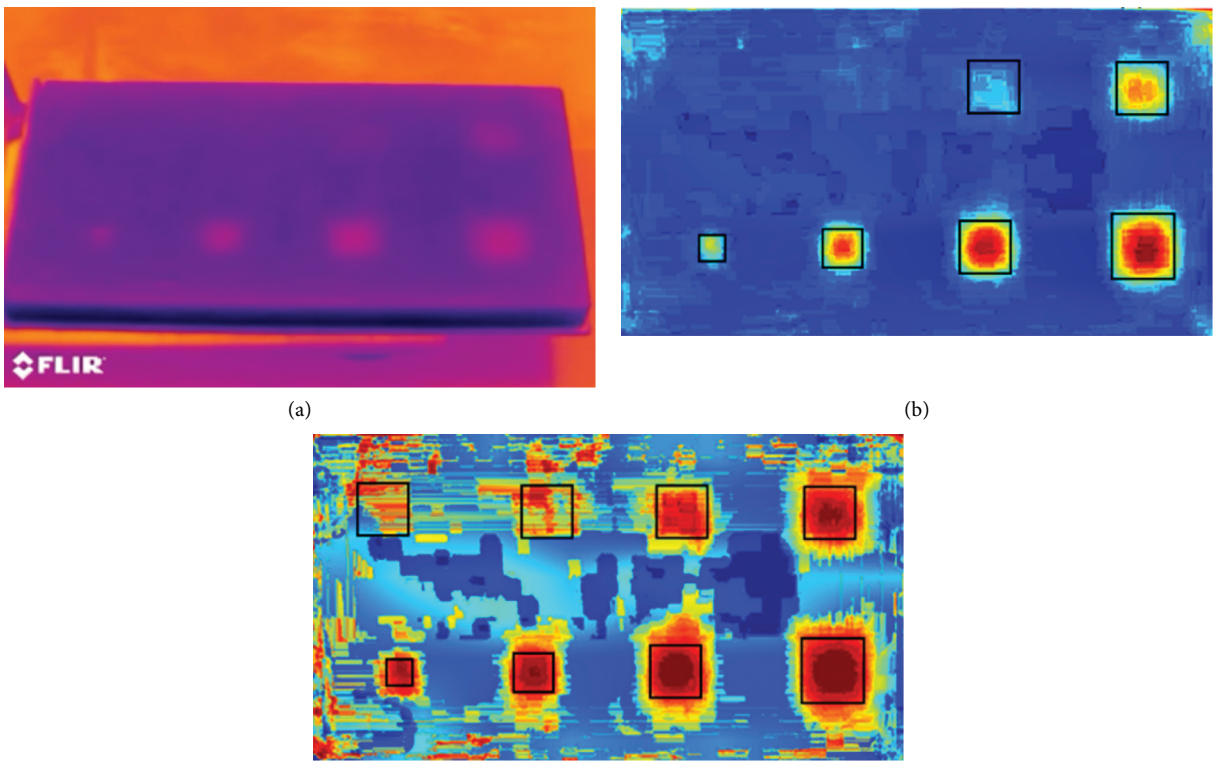

(a) (b) (c)

Figure 11: Comparison image enhancement of B. (a) B-before image enhancement. (b) B-CLAHE enhancement. (c) B-GHE enhancement.

discriminated. However, it can be seen from Figure 10(c) that the location and the shape of the defect are easy to be distinguished after the image was enhanced by the CLAHE method. At this point, the use of CLAHE was more effective in shaping defect contours.

As shown in Figure 11, it is difficult to identify deeper defects after the optimization by the CLAHE algorithm. However, the GHE algorithm can equalize the whole image and extend the range of compressed pixels, which could effectively improve the contrast of the deep defects.

Root mean square contrast σ_I and area ratio z_s are used to measure the identification effect and accuracy of defects to objectively compare the advantages of different image enhancement algorithms and image quality after processing. The calculation method is as follows [30]:

$$\sigma_I = \sqrt{\frac{1}{(m \times n)} \cdot \sum_{I_{m \times n}} \left(I(x, y) - a^2 \right)}, \tag{2}$$

$$z_s = \frac{s_0}{s_d}, \tag{3}$$

where $I(x, y)$ is gray value at point (x, y); s_0 is area of the embedded defect; and s_d is area of the actual detection.

According to equations (2) and (3), the optimization parameters of each defect area before and after using different enhanced image algorithms in Figures 10 and 11 are shown in Table 3.

Table 3: Optimization parameters.

Def.	ΔT (°C)	σ_I			z_s		
		Initial	CLAHE	GHE	Initial	CLAHE	GHE
A1-1	3.5	32.6	56.5	60.4	0.86	1.04	—
A1-2	1.2	14.8	39.0	54.5	1.18	0.93	0.81
A2-1	0.4	22.3	65.0	60.3	—	0.73	0.80
A2-2	0.4	16.6	53.7	51.2	—	0.77	0.85
B-1	5.7	12.1	56.5	61.6	1.08	1.24	1.30
B-2	4.3	10.2	54.5	65.2	1.14	1.36	1.27
B-3	4.0	7.8	48.3	59.8	1.35	1.27	1.23
B-4	3.0	4.4	45.5	55.9	0.71	1.26	1.29
B-5	3.3	5.6	31.1	61.0	0.89	1.16	1.28
B-6	1.2	1.9	29.5	58.5	—	0.94	1.13
B-7	0.7	—	15.8	55.2	—	0.88	1.10
B-8	0.5	—	—	51.3	—	—	1.03

It can be seen from Table 3 and Figures 10 and 11 that both CLAHE and GHE algorithms can effectively improve the recognition effect of internal defects in infrared thermal images. CLAHE algorithm makes temperature ladder-type through local processing, which better shapes the defect profile without causing defect distortion. However, it is not suitable for areas with low initial contrast (σ_I <5.6) or low-temperature gradient, so that the optimization effect of deep defects (h >32 mm) under solar heating is not good enough.

GHE algorithm, by expanding the pixel interval of the full image, increases the gray value of the small proportion of the defected part. The increase of defect depth has little influence on the optimization effect. After application, the

defect area is enlarged by 1.0~1.3 times while the line error is kept between 0 and 15%. Under the experimental conditions in this paper, the effective detection depth under solar heating can be increased from 30 mm to 55 mm, with an increase of more than 80%.

3.3. Discussion. In this paper, we combine some simple image processing algorithms with infrared defect detection of concrete and obtain some positive results.

In the past, the optimization of infrared detection of concrete mainly focuses on the improvement of heating mode and instruments. The continuous optimization of hardware facilities is pleasant, but it may face some limitations in the practical application process. Therefore, this paper adopts a common heat source for assistance and combines the algorithm to optimize the detection results. For simple detection images, some commonly used algorithms, such as histogram equalization, can play a good processing effect and are not inferior to the complex algorithm. At the same time, the algorithm principle determines its applicable scope. We tentatively put forward that GHE can improve the contrast and is more suitable for highlighting deep defects, while CLAHE can shape the defect contour better. The results of the experiment can also prove this point.

Although there are important discoveries revealed by these studies, there are also limitations. First, there are few types of defects arranged, and the influence of environmental humidity, air convection, and other potential influencing factors is not considered in the test process, so the simulation is not comprehensive enough. At the same time, the quantification of defect depth requires a large number of tests to determine the query parameters. Therefore, we hope to share more research data and further subdivide the experimental conditions according to different working conditions in order to draw more general conclusions. Second, the intelligent degree is not satisfactory, and subjective judgment is required in many aspects. Neural network learning may be a good solution.

4. Conclusion

Experimental research has been carried out to detect the internal defects in concrete by infrared thermography, and the thermograph was optimized by image preprocessing and enhancement algorithm. The main conclusions from the results are summarized as follows:

(1) Under sunlight heating, the defect can be easily distinguished when the ratio of side length to depth is larger than 1.8.

(2) The depth of defects can be preliminarily determined according to the combination of heating rate and set parameters.

(3) The impact of view angle, temperature fluctuation, and boundary conditions on the thermal image can be reduced by image preprocessing, such as signal reconstruction and transformation and temperature division.

(4) GHE can stretch the temperature scale and is more suitable for deep defect-recognition under solar heating. The ladder processing of CLAHE is more suitable for pulse heating images with blurred defect contours.

Data Availability

The data used to support the findings of this study are available from the corresponding author upon request.

Conflicts of Interest

The authors declare that there are no conflicts of interest regarding the publication of this paper.

Acknowledgments

This work was supported by the National Natural Science Foundation of China (51479013 and 51809025) and Chongqing Youth Science and Technology Talent Training Program (CSTC2014KJRC-QNRC30001).

References

[1] G. J. Weil, "Nondestructive testing of airport concrete structures: runways, taxiways, roads, bridges, and building walls and roofs," *Nondestructive Evaluation of Aging Aircraft, Airports, and Aerospace Hardware II*, The International Society for Optical Engineering, vol. 3397, 1998.

[2] C. Ibarra-Castanedo, J. R. Tarpani, and X. P. V. Maldague, "Nondestructive testing with thermography," *European Journal of Physics*, vol. 34, no. 6, pp. 91–109, 2013.

[3] C. C. Cheng, T. M. Cheng, and C. H. Chiang, "Defect detection of concrete structures using both infrared thermography and elastic waves," *Automation in Construction*, vol. 18, no. 1, pp. 87–92, 2009.

[4] N. P. Avdelidis, C. Ibarra-Castanedo, X. Maldague, Z. P. Marioli-Riga, and D. P. Almond, "A thermographic comparison study for the assessment of composite patches," *Infrared Physics & Technology*, vol. 45, no. 4, pp. 291–299, 2004.

[5] B. Z. Wang, L. H. Dong, H. D. Wang et al., "Research and application of laser infrared thermography in material defect detection," *Materials Reports*, vol. 34, no. 3, pp. 127–132, 2020.

[6] C. Maierhofer, A. Brink, M. Röllig, and H. Wiggenhauser, "Detection of shallow voids in concrete structures with impulse thermography and radar," *NDT & E International*, vol. 36, no. 4, pp. 257–263, 2003.

[7] P. Cotič, D. Kolaric, V. B. Bosiljkov, V. Bosiljkov, and Z. Jagličića, "Determination of the applicability and limits of void and delamination detection in concrete structures using infrared thermography," *NDT & E International*, vol. 74, no. 9, pp. 87–93, 2015.

[8] Y. P. Tian, K. Y. Zhou, H. Liang et al., "Research on quantitative evaluation of infrared thermography," *Chinese Journal of Scientific Instrument*, vol. 29, no. 11, pp. 2413–2418, 2008.

[9] X. P. Maldague, "Theory and practice of infrared technology for nondestructive testing," *Chapter*, vol. 4, no. 3, p. 307, 2001.

[10] K. Chatterjee, S. Tuli, S. G. Pickering, and D. P. Almond, "A comparison of the pulsed, lock-in and frequency modulated thermography nondestructive evaluation techniques," *NDT & E International*, vol. 44, no. 7, pp. 655–667, 2011.

[11] R. Krankenhagen and C. Maierhofer, "Pulse phase thermography for characterising large historical building façades after solar heating and shadow cast-a case study," *Quantitative InfraRed Thermography Journal*, vol. 11, no. 4, pp. 10–28, 2014.

[12] M. R. Clark, D. M. Mccann, and M. C. Forde, "Application of infrared thermography to the non-destructive testing of concrete and masonry bridges," *NDT & E International*, vol. 36, no. 4, pp. 265–275, 2003.

[13] Z. Wang and A. C. Bovik, *Modern Image Quality Assessment*pp. 1–10, National Defense Industry Press, Beijing, China, 1st edition, 2015.

[14] K. Singh, D. K. Vishwakarma, G. S. Walia, and R. Kapoor, "Contrast enhancement via texture region based histogram equalization," *Journal of Modern Optics*, vol. 63, no. 15, pp. 1–7, 2016.

[15] Z. G. Xu, X. M. Zhao, H. S. Song, T. Lei, and N. Wei, "Asphalt pavement crack recognition algorithm based on histogram estimation and shape analysis," *Chinese Journal of Scientific Instrument*, vol. 31, no. 10, pp. 2260–2266, 2010.

[16] S. B. Tian, Y. Yang, Z. Liu, C. Wang, and R. H. Pan, "Enhancement of infrared images based on efficient histogram processing," *Wireless Personal Communications*, vol. 99, no. 2, pp. 619–636, 2018.

[17] P. Cotič, Z. Jagličić, E. Niederleithinger, M. Stoppel, and V. Bosiljkov, "Image fusion for improved detection of near-surface defects in NDT-CE using unsupervised clustering methods," *Journal of Nondestructive Evaluation*, vol. 33, no. 3, pp. 384–397, 2014.

[18] J. H. A. Rocha and Y. V. Póvoas, "Detección de delaminaciones en puentes de concreto armado usando Termografía Infrarroja," *Revista ingeniería de construcción*, vol. 34, no. 1, pp. 55–64, 2019.

[19] S. Sfarra, E. Marcucci, D. Ambrosini, and D. Paoletti, "Infrared exploration of the architectural heritage: from passive infrared thermography to hybrid infrared thermography (HIRT) approach," *Materiales de Construcción*, vol. 66, no. 323, p. e094, 2016.

[20] C. Maierhofer, H. Wiggenhauser, A. Brink, and M. Röllig, "Quantitative numerical analysis of transient IR-experiments on buildings," *Infrared Physics and Technology*, vol. 46, no. 1, pp. 73–80, 2004.

[21] H. Zhen, J. Li, H. X. Chen, and Z. Li, "Research on fast algorithm for parallel correction of distorted infrared image," *Chinese Journal of Scientific Instrument*, vol. 32, no. 11, pp. 2530–2535, 2011.

[22] D. J. Titman, "Applications of thermography in non-destructive testing of structures," *NDT & E International*, vol. 34, no. 2, pp. 149–154, 2001.

[23] M. Weiser, M. Roellig, R. Arndt, and B. Erdmann, "Development and test of a numerical model for pulse thermography in civil engineering," *Heat & Mass Transfer*, vol. 46, no. 11-12, pp. 1419–1428, 2010.

[24] Z. Q. Feng, B. Gao, Y. Yang, and G. Y. Tian, "Debonding defect detection of CFRP based on thermal signal reconstructed region growing algorithm," *Nondestructive Testing*, vol. 9, pp. 29–34, 2017.

[25] Y. T. Liu, Z. Chen, Z. F. Fu, and F. X. Zheng, "Infrared image enhancement algorithm based on CLAHE," *Laser & Infrared*, vol. 46, no. 10, pp. 1290–1294, 2016.

[26] M. Abdullah-Al-Wadud, M. Kabir, M. Akber Dewan, and O. Chae, "A dynamic histogram equalization for image contrast enhancement," *IEEE Transactions on Consumer Electronics*, vol. 53, no. 2, pp. 593–600, 2007.

[27] R. C. Gonzalez, R. E. Woods, and S. L. Eddins, *Digital Image Processing Using MATLAB*, pp. 197–199, Prentice Hall, Upper Saddle River, CF, USA, 2010.

[28] K. Liang, Y. Ma, Y. Xie, B. Zhou, and R. Wang, "A new adaptive contrast enhancement algorithm for infrared images based on double plateaus histogram equalization," *Infrared Physics & Technology*, vol. 55, no. 4, pp. 309–315, 2012.

[29] C. Y. Wong, G. Jiang, M. A. Rahman et al., "Histogram equalization and optimal profile compression based approach for colour image enhancement," *Journal of Visual Communication and Image Representation*, vol. 38, no. 7, pp. 802–813, 2016.

[30] A. A. Bhuiyan and A. R. Khan, "Image quality assessment employing RMS contrast and histogram similarity," *International Arab Journal of Information Technology*, vol. 15, no. 6, pp. 983–989, 2018.